Arctic Ocean Circulation Patterns Revealed by Ocean Bottom Pressure Anomalies

Ana Cecilia Peralta Ferriz

A dissertation
submitted in partial fulfillment of the
requirements for the degree of

Doctor of Philosophy

University of Washington

2012

Reading Committee:

James H. Morison, Chair

LuAnne Thompson

Peter B. Rhines

Program Authorized to Offer Degree:

Oceanography

University of Washington

Abstract

Arctic Ocean Circulation Patterns Revealed by
Ocean Bottom Pressure Anomalies

Ana Cecilia Peralta Ferriz

Chair of the Supervisory Committee:
Professor James H. Morison
Polar Science Center, Applied Physics Laboratory, UW

Over the last few decades, the Arctic Ocean has experienced drastic changes that include increased temperature, changes in freshwater distribution, and decrease in sea ice extent and thickness. These changes, which potentially affect global climate, are intimately linked to changes in the Arctic Ocean circulation. Thus, understanding Arctic Ocean circulation patterns is fundamental to monitoring and predicting the fate of the Arctic System.

Since 2002, NASA's Gravity Recovery and Climate Experiment (GRACE) has provided continuous measurements of the time-varying gravity field of the Arctic Ocean. The gravitational variations represent mass variations, or the time-varying ocean bottom pressure (OBP) field. OBP variations are the sum of the mass change due to the sea surface height change and the integrated density variations through the water column.

In this dissertation, *in situ* and GRACE measurements of OBP anomalies, complemented by information from ocean models, are used to investigate the relative contribution of sea surface height and density-variations on the Arctic OBP field. The dynamics associated with the observed OBP changes are investigated. Major

findings include the identification of three primary temporal-spatial modes of OBP variability at monthly to inter-annual timescales with the following characteristics:

- Mode 1 is a wintertime basin-coherent Arctic mass change forced by southerly winds through Bering and Fram Straits.

- Mode 2 reveals mass change along the Siberian shelves, driven by surface Ekman dynamics and associated with the Arctic Oscillation.

- Mode 3 reveals a mass drop in Western Arctic shelves forced by the strengthening of the anticyclonic Beaufort Gyre, and wintertime along-shore westerly winds that increase OBP in the Eastern Arctic shelves.

The OBP changes in the Kara Sea reveal a more baroclinic ocean character than modeling results have previously suggested, due to the complex bathymetry of this region and runoff-derived large density changes through the water column.

This work integrates the character of the Arctic mass changes at different timescales, and provides information about the ocean mass re-distribution during years of rapidly thinning and disappearing seasonal sea ice.

TABLE OF CONTENTS

Page

List of Figures iii

List of Tables vi

Chapter 1: Introduction 1
1.1 The Changing Arctic 1
1.2 Objectives 6

Chapter 2: Background 9
2.1 Ocean bottom pressure 9
2.2 Barotropic vs baroclinic contributions to OBP 12
2.3 The Gravity Recovery and Climate Experiment: GRACE 15
2.4 GRACE in other relevant studies 21

Chapter 3: Data description and analysis technique 25
3.1 GRACE ocean bottom pressure 25
3.2 In situ ocean bottom pressure at the North Pole 26
3.3 Other Arctic pressure and tide gauges 36
3.4 Atmospheric data 41
3.5 Bathymetry data 42
3.6 Model output 42
3.7 Methods 43

Chapter 4: Results 45
4.1 Evaluation of optimized GRACE solutions 45
4.2 GRACE-model inter-comparison 55

4.3 Spatial and temporal variations of Arctic OBP 64
4.4 Inter-annual mass changes before and after the year of minimum summer sea-ice extent, 2007 88
4.5 Assessing the barotropic vs baroclinic character of the Siberian Arctic shelves 97

Chapter 5: Summary and conclusions 107
5.1 Timescales of Arctic OBP variations 108
5.2 The role of the models to understand Arctic Ocean circulation 115
5.3 Perspective and speculations for the future Arctic Ocean 116
5.4 Suggested future work 118

Bibliography 121

Appendix A: Sub-monthly variability in Arctic Ocean bottom pressure 139
A.1 Supplementary information of peer-reviewed work 147
A.2 Daily SLP, SSH and transport within the sub-monthly OBP mode . . 148

Appendix B: Seasonal variability of Arctic Ocean bottom pressure 155
B.1 Supplemental information of seasonal variability in Arctic OBP . . . 162

Appendix C: Tidal analysis of ABPRs near the North Pole 165
C.1 ABPR1 165
C.2 ABPR3 166
C.3 ABPR4 168
C.4 ABPR5 170

LIST OF FIGURES

Figure Number		Page
1.1	Arctic Ocean map and general circulation patterns	2
1.2	The Arctic Oscillation pattern and effects on sea-ice	5
2.1	Barotropic versus baroclinic conditions	13
2.2	OBP-SSH relationship from an eddy-permitting model	14
2.3	The GRACE satellite system	16
3.1	ABPR-1 general constituents	28
3.2	ABPR-1 data recovery in 2008	29
3.3	Deployment of ABPR-5	30
3.4	ABPR-1 record	32
3.5	ABPR-3 record	34
3.6	ABPR-4 record	35
3.7	ABPR-5 record	37
3.8	Representative 6-year record of North Pole OBP	38
3.9	Map with locations of Arctic pressure and tide gauges	39
4.1	Optimized leakage-reduced GRACE solutions	46
4.2	Modeled OBP, SSH, and in situ tide gauges in Amderma	49
4.3	Validation with *in situ* data at the North Pole	51
4.4	Validation with *in situ* data at Fram Strait	52
4.5	Validation with *in situ* data in the Kara Sea	53
4.6	Validation with *in situ* data in the Laptev Sea	54
4.7	Validation with *in situ* data in a Canadian Arctic shelf	55
4.8	Test for land-hydrology contamination in Kara and Barents Seas	56
4.9	GRACE OBP climatology 2002 to 2011	57
4.10	Effects of gaussian filtering on the modeled OBP and SSH	59

4.11 Correlation maps of GRACE and models 60
4.12 Variance and significance of EOF modes 66
4.13 First three EOF modes of GRACE 67
4.14 GRACE PC1 and in situ OBP from ABPR-1 68
4.15 Winds and SLP regressed on GRACE PC1 70
4.16 Mid- to high-latitude GRACE-300 projected on PC1 72
4.17 Modeled OBP and SSH from PIOMAS, projected on PC1 73
4.18 Modeled OBP and SSH from ECCO2, projected on PC1 74
4.19 GRACE PC2 and the Arctic Oscillation Index 76
4.20 Winds and SLP regressed on GRACE PC2 77
4.21 Modeled OBP and SSH from PIOMAS, projected on PC2 79
4.22 Modeled OBP and SSH from ECCO2, projected on PC2 80
4.23 GRACE PC3 81
4.24 Winds and SLP regressed on GRACE PC3 82
4.25 Modeled OBP and SSH from PIOMAS, projected on PC3 84
4.26 Modeled OBP and SSH from ECCO2, projected on PC3 85
4.27 Curl of the wind field regressed on PC 1, 2 and 3 88
4.28 Curl of the wind and wind velocity difference relative to 2007 90
4.29 Modeled OBP, SSH, and GRACE OBP difference 92
4.30 Post-2007 minus pre-2007 OBP and SSH for all months 94
4.31 Post-2007 minus pre-2007 steric pressure and FWC 96
4.32 Largest rivers discharging into the Arctic Ocean 98
4.33 Bathymetry of the Arctic Siberian shelves 100
4.34 Magnitude squared coherence between modeled OBP and SSH for different Arctic shelves 101
4.35 RMS variability of OBP, SSH, steric pressure and salinity field 104

A.1 Energy increased during winters 149
A.2 Atmospheric forcing through the North Pacific side 150
A.3 Transfer function OBP / SLP forcing 151
A.4 Composite maps of daily progression before maximum OBP 152
A.5 Composite maps of daily progression after maximum OBP 153

B.1 MCA analysis on seasonal mass distribution 164

LIST OF TABLES

Table Number Page

3.1 Stations of *in situ* Arctic pressure and tide gauges 40

4.1 Correlation and RMS error between *in situ* Arctic pressure/tide gauge records and GRACE and models 47

4.2 Correlation and RMS error between *in situ* Arctic pressure/tide gauge records and GRACE and models, with the climatology removed . . . 50

A.1 Correlation Coefficient R among *in situ* Arctic OBP records 147

A.2 Net volume flow into Arctic within sub-monthly OBP mode 148

C.1 Tidal constituents of ABPR 1 (5 years) 166

C.2 Tidal constituents of ABPR 3 (3 years) 168

C.3 Tidal constituents of ABPR 4 (1 year) 170

C.4 Tidal constituents of ABPR 5 (1 year) 172

ACKNOWLEDGMENTS

I wish to express sincere gratitude to my research adviser, Dr. James Morison, for his guidance and support throughout my graduate studies. I deeply thank Dr. John M. Wallace for his immense help and valuable suggestions that proved essential for the completition of this dissertation. I am very thankful for the suggestions, time and continuous support of my committee members, Dr. LuAnne Thompson, Dr. Peter B. Rhines, Dr. Michael Steele and Dr. Jody Deming.

The Faculty of the School of Oceanography and Applied Physics Laboratory are greatly acknowledged for their instruction, teaching opportunities and support on diverse discussions and organized activities. This dissertation would not have been possible without the engagement in science discussions, outreach participation, technical, administrative and moral support of the Polar Science Center group, especially to Dr. Rebecca Woodgate, Dr. Ignatius Rigor, Dr. Camille Lique, Mark Ortmeyer, Wendy Ermold, Dr. Harry Stern, Dr. Axel Schweger, Mari Litzenberger and Lisa Isozaki.

I want to express gratitude to the GRACE team members, particularly Dr. Don Chambers and Dr. Jennifer Bonin, for providing the high quality GRACE data of the Arctic Ocean and for their valuable discussions and collaboration for improving the satellite solutions in the Arctic. I am sincerely thankful for the support and instruction received from APL members during polar ocean fieldwork campaigns, with especial mention to Jim Johnson. I would like to thank Dr. Jinlun Zhang for providing the output of the PIOMAS sea-ice model, and for his willingness to discuss specific

details on the model forcing, performance and output, whenever needed. I also thank Dr. Ron Kwok and Dr. An Nguyen for providing the ECCO2 model output and for their collaboration and discussion throughout this work. NOAA's engineers and technical support are greatly acknowledged for the development, testing and training on the Arctic bottom pressure sensors. I thank researchers from diverse programs and institutions such as RUSALCA, BGEP/WHOI, AWI (specially Dr. Agnieszska Beszczynska-Möller), the Permanent Service for Monitoring Sea Level, UK, and the Dept. of Fisheries and Oceans, Canada, for providing high quality *in situ* data for this dissertation.

The research in this dissertation was funded by NASA Grant NNX08AH62G and by NSF Grant ARC 0856330.

I am very thankful for the continuous support and encouragement from my husband, Greg Curtiss; my parents, Tere Ferriz and Enrique Peralta; and my beloved sister, Tere Peralta, and her family. My fellow graduate students –with special mention to Tom Connolly and Sally Warner– and my wonderful friends, who made of my grad school experience an amazing and unforgettable one.

DEDICATION

To my mother, María Teresa Ferriz

and to the memory of my grandfather, Alfonso Ferriz

Chapter 1
INTRODUCTION

In this dissertation, the changes in the Arctic Ocean circulation are investigated using *in situ* and remote sensing measurements of ocean bottom pressure. These observations are complemented with OBP and SSH output from ocean models, which in turn are used to identify and understand the physical mechanisms that drive the observed changes in the bottom pressure field at different timescales.

1.1 The Changing Arctic

The Arctic Ocean connects to the Atlantic and Pacific Oceans through relatively narrow paths. Relatively fresh and cold water –characteristic of Pacific water (PW) masses– enters the Arctic through the shallow ($\sim$ 50 m deep) and narrow ($\sim$ 80 km wide) Bering Strait. Forced by the wind, most of the PW tends to circulate into the anticyclonic (clockwise) Beaufort Gyre in the upper ocean, typically between 50 to 200 m. Another portion of the PW flows eastward with the Alaskan Coastal Current (*Aagaard and Carmack*, 1989; *Woodgate and Aagaard*, 2005). Relatively warm and salty water –characteristic of the Atlantic water (AW) masses– enters the Arctic through Fram Strait and the Barents Sea. As it enters the Arctic, it cools and subducts underneath the lighter PW. AW typically circulates cyclonically (counterclockwise) around the Eurasian and Canadian Basin in a pan-Arctic boundary current that is topographically steered along the slope (*Rudels et al.*, 1999). AW water circulates in the Arctic Basin between 200 and 800 m depth (Figure 1.1).

The Arctic Ocean has experienced drastic changes over the last few decades. Arc-

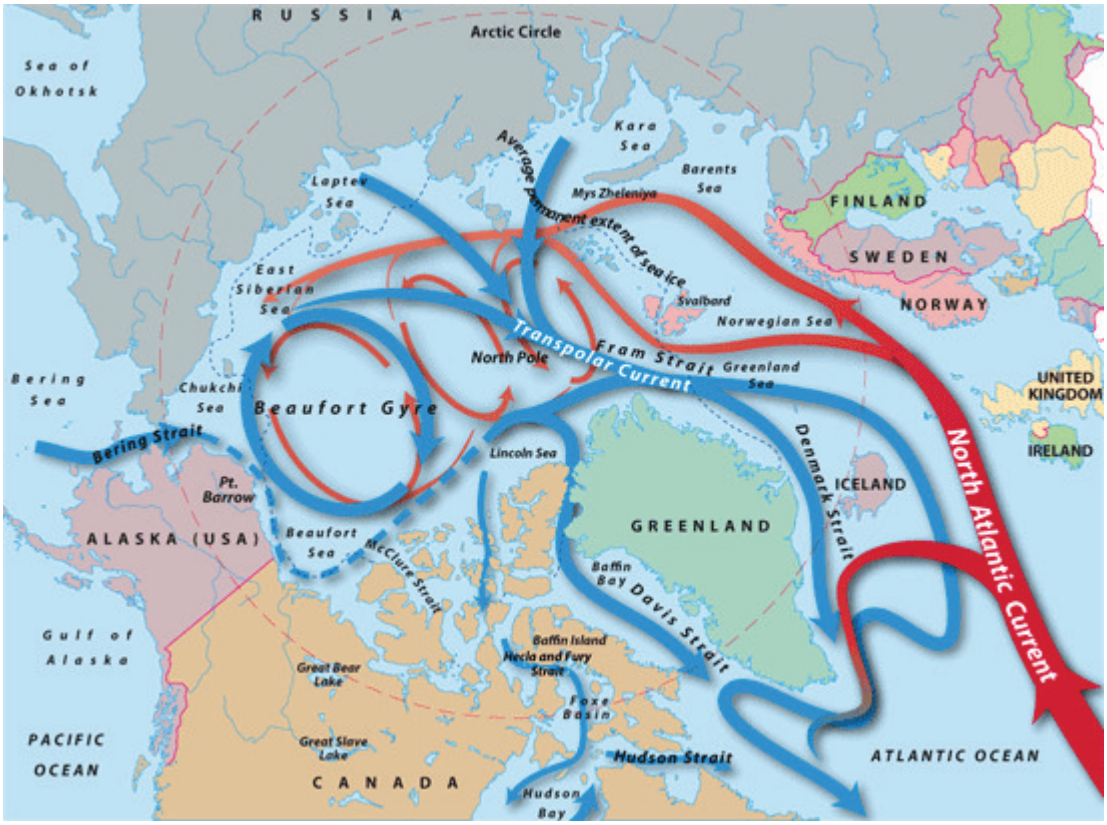

Figure 1.1: General Arctic Ocean circulation patterns. Blue lines highlight the Pacific-derived waters, and red lines follow the path of Atlantic-derived waters. *Image source: Woods Hole Oceanographic Institution, at http://www.whoi.edu/main/topic/arctic-ocean-circulation.*

tic change has been reflected in dramatic decreases in sea-ice thickness (*Kwok and Rothrock*, 2009) and summer sea-ice extent (*Stroeve et al.*, 2007, 2008), in the increase of atmospheric temperature (*Overland et al.*, 2008), oceanic heat content (*Polyakov et al.*, 2010; *Steele et al.*, 2008), and changes in the freshwater content and distribution (*Morison et al.*, 2006; *Rabe et al.*, 2011; *McPhee et al.*, 2009; *Morison et al.*, 2012). Changes in all these properties are of concern due to their possible linkages with global climate, for example, by controlling stratification changes in the sub-Arctic seas and

thereby modulating convection and the meridional overturning circulation (*Aagaard and Carmack*, 1989; *Serreze et al.*, 2006; *Hu et al.*, 2010).

Arctic Ocean warming has been attributed to atmospheric warming (*Johannessen et al.*, 2004), changes in sea-ice extent (*Perovich et al.*, 2007), and oceanic fluxes of heat from the Pacific and the Atlantic Oceans into the Arctic (*Schauer et al.*, 2004, 2008; *Woodgate et al.*, 2010; *Spielhagen et al.*, 2011; *Karcher et al.*, 2011).

The salinity contrast of Atlantic Water (e.g., 35 psu) and Pacific Waters (e.g., 32 psu) entering the Arctic is critical to controlling Arctic Ocean stratification, the stability of the Arctic halocline[1] and Arctic freshwater content and distribution. In the Arctic Ocean, changes in the salinity field, and therefore changes in freshwater content, determine the density field and consequently the stratification of the Arctic Ocean. Relative to the reference salinity of 34.8 (*Aagaard and Carmack*, 1989), the dominant sources of freshwater into the Arctic Ocean are river runoff (38%), followed by the oceanic inflow from the Pacific Ocean (30%) and net precipitation minus evaporation (24%) (*Serreze et al.*, 2006).

Arctic changes have been linked to the Arctic Ocean circulation and climate variability (*Morison et al.*, 2000, 2006). During the late 1980's and early 1990's, the Arctic Oscillation (AO)[2] (*Thompson and Wallace*, 1998) entered an extreme positive phase (see Figure 1.2). A positive AO implies anomalously low surface atmospheric pressure. During these years of positive AO, the spatial extent of the anticyclonic Beaufort High shrank, leading to a counterclockwise shift of the transpolar drift or zero vorticity line of sea ice motion (*Rigor et al.*, 2002), accompanied by a counterclockwise shift of the frontal line between Pacific and Atlantic waters in the central

[1]Commonly called cold halocline, is the layer of maximum salinity change in the water column with respect to depth. It is of fundamental climate interest because it insulates the ice and mixed layer from Atlantic water heat.

[2]AO is characterized by the leading mode of empirical orthogonal functions (EOF) of the monthly surface atmospheric pressure north of $\sim 20^\circ$ N.

basin (*Steele et al.*, 2004). This shift was consistent with a salinity increase in the upper ocean of the central Arctic (*Morison et al.*, 2000). The cold halocline also weakened and retreated counterclockwise (*Steele and Boyd*, 1998), enhancing melting of sea-ice due to the increased exposure with the warm Atlantic water. As the atmospheric circulation affects directly sea-ice motion, the wind field associated with the positive AO increased the export of multi-year ice through Fram Strait (*Rigor et al.*, 2002; *Rigor and Wallace*, 2004) (Figure 1.2).

During the early 2000s, the Arctic circulation relaxed back towards climatological conditions (e.g., prior to 1990s), as observed by a near-zero salinity anomaly in the upper ocean at the North Pole (*Morison et al.*, 2006). However, conditions reverted again in the late 2000s, to those of low salinity, as observed during high AO (*Morison et al.*, 2006, 2012). Thus, the Arctic continues to change at inter-annual and longer timescales. Evidence of this are the record minimum of the summer extent of sea-ice in 2007 (*Comiso et al.*, 2008), and the continued accumulation of freshwater in the Canada Basin (*Rabe et al.*, 2011; *Morison et al.*, 2012; *Giles et al.*, 2012; *McPhee*, 2008).

In order to understand the rapid changes in the Arctic system and their role in climate change, it is necessary to identify and monitor changes and patterns of the circulation of the Arctic Ocean. The available oceanographic observations in the Arctic are sparse in both space and time, making the task challenging. A new approach to tackle this challenge is the use of remote sensing observations of the time-varying ocean bottom pressure field, which reflect changes in mass concentration and distribution in the ocean. The NASA mission Gravity Recovery and Climate Experiment, GRACE, has provided such observations since March of 2002. The essence of this dissertation is therefore the study of the Arctic Ocean mass changes as indicators of changes in ocean circulation and freshwater distribution, based on

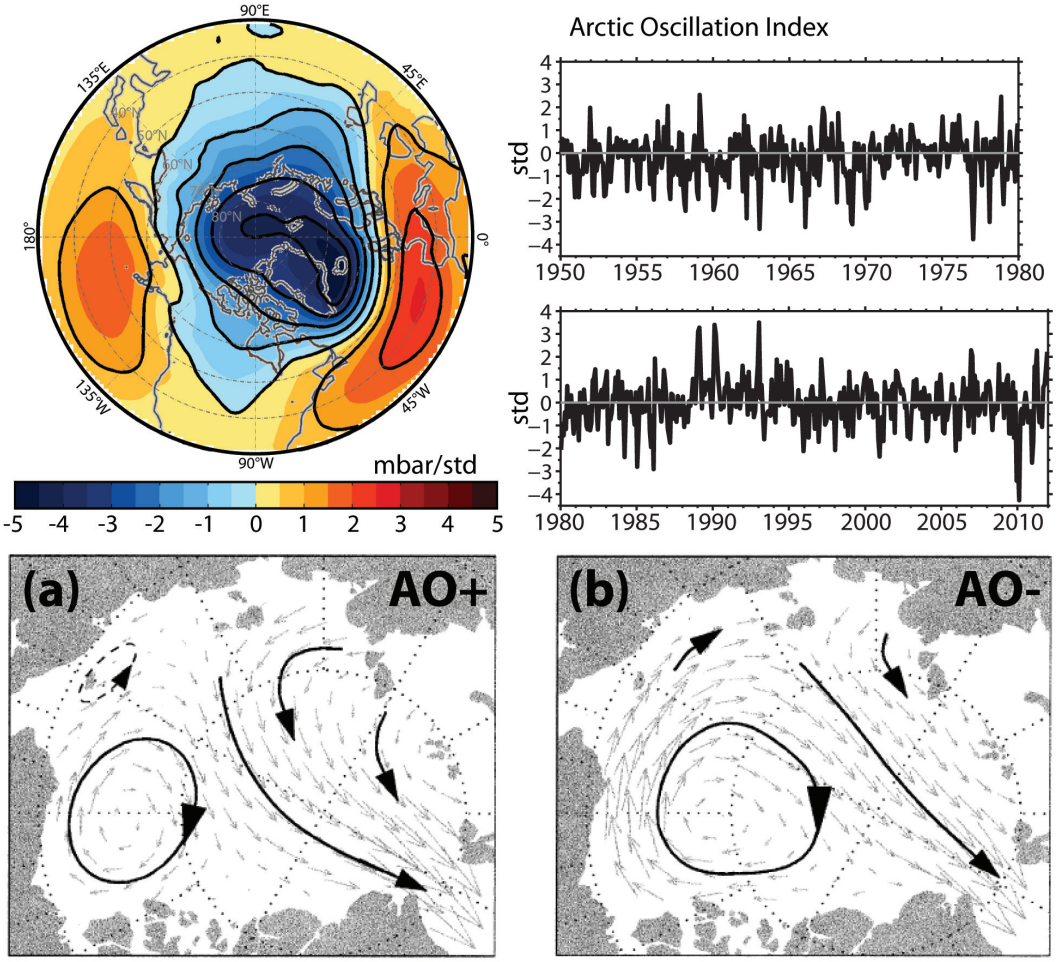

Figure 1.2: Top: the Arctic Oscillation (AO) pattern (left), generated by projecting the monthly anomalies of NCEP/NCAR sea level pressure (*Kalnay et al.*, 1996) from 1950 to 2011, upon the standardized AO Index (right). AO monthly index is obtained from the NOAA's Climate Prediction Center website http://www.cpc.ncep.noaa.gov/. Bottom: the circulation of sea-ice during (a) positive and (b) negative phases of AO from *Rigor et al.* (2002).

nearly a decade of GRACE observations. These measurements are complemented and validated with *in situ* bottom pressure data when available, and the unveiled forcing mechanisms are investigated using output from two ice-ocean models.

1.2 Objectives

The goal of this dissertation is to explain the physical processes that contribute to the temporal and spatial variability of the bottom pressure field of the Arctic Ocean and to use our understanding of these processes to explain changing patterns of Arctic Ocean circulation.

By analyzing observed and modeled ocean bottom pressure anomalies, this dissertation addresses the following questions:

- For a given time scale (e.g., sub-monthly, seasonal, inter-annual, etc.), what processes control the Arctic Ocean bottom pressure change?

- What is the Arctic Ocean circulation associated with each of these processes?

This dissertation builds on previous work published in *Peralta-Ferriz and Morison* (2010) and *Peralta-Ferriz et al.* (2011). These publications are included in Appendix A (Sub-monthly variations in Arctic Ocean mass) and Appendix B (Seasonal variations of Arctic Ocean mass). Additional new contributions related to these two publications have been included in their corresponding appendix and are referred to throughout this work where appropriate. Thus, this thesis provides an integrated and comprehensive view of our current understanding of Arctic ocean circulation as derived from mass changes and mass re-distribution at different timescales.

The dissertation is organized as follows: In Chapter two, the definition and relevance of ocean bottom pressure field to understand ocean circulation are presented, and the satellite mission GRACE is introduced. Chapter three describes the datasets and methods used. Results in Chapter four include the evaluation and validation of the solutions of GRACE that are used here, followed by the analysis of the patterns of variability of GRACE bottom pressure field focusing on monthly to inter-annual

timescales. Chapter five includes a summary of the patterns of the circulation revealed by the bottom pressure changes at different timescales, along with conclusions and some speculations on the impacts of recent mass changes to the future of the Arctic Ocean.

Chapter 2
BACKGROUND

2.1 Ocean bottom pressure

Ocean bottom pressure (OBP) is the sum of atmospheric and oceanic mass. Ocean mass may be approximated by integrating the hydrostatic relation from the bottom of the ocean to the top, as defined in Equation 2.1 (*Ponte*, 1999):

$$P_b = \rho_\circ g\eta + g\int_{-H}^{0} \rho dz + P_a \tag{2.1}$$

where

$$\eta = \eta' + \frac{1}{\rho_\circ g}(\overline{P_a} - P_a) \tag{2.2}$$

In Equations 2.1 and 2.2, P_b is the total pressure at the bottom; g is the gravitational acceleration; H is the total depth; ρ is the depth-dependent density and $\rho_\circ$ is a constant or reference ocean water density, typically taken as 1028 kg/m^3. P_a is the local surface atmospheric pressure and $\overline{P_a}$ is the spatially averaged surface pressure over the global oceans. η is the sea surface height (SSH) as measured by a tide gauge. Equation 2.2 shows that η includes the dynamic[1] part of the sea surface height, η', relative to the temporally averaged SSH or geoid, and the direct effect of the local atmospheric pressure loading, namely, inverted barometer response (IB), with a spatially averaged sea level pressure contribution.

Under the IB effect, the change of the local atmospheric or sea level pressure (SLP) is compensated by a change in sea surface height, for which the local variations in

[1]which is the part of the sea surface change that leads to horizontal pressure gradients.

SLP do not have an impact on ocean bottom pressure (OBP = P_b). One mbar in atmospheric pressure increase corresponds to one cm of SSH decrease. For regional to large scales and for time scales of $\sim$ 5 to 7 days and longer, the IB effect is a valid assumption in the Arctic Ocean according to altimetry-based observations (*Kwok et al.*, 2006) and numerical models (*Ponte et al.*, 1991; *Stepanov and Hughes*, 2006).

Consequently, by substituting Equation 2.2 in Equation 2.1, and rearranging terms, the OBP anomalies (indicated by prime) relative to the temporal mean or unperturbed field, may be expressed as:

$$P_b' = \rho_\circ g \eta' + g \int_{-H}^{0} \rho' dz + \overline{P_a'} \tag{2.3}$$

The averaged atmospheric pressure over the ocean, $\overline{P_a'}$ in Equation 2.3, is usually neglected in most modeling studies (*Ponte*, 1999). However, there are some cases in which this atmospheric contribution needs to be taken into account. One of these cases is when considering inter-basin mass exchanges with semi-enclosed basins (*Wunsch and Stammer*, 1997; *Peralta-Ferriz and Morison*, 2010), because it varies in time, and because where there is a gradient in the regional to global atmospheric pressure acting over a large oceanic region, the sea level may not be able to adjust completely. This was found to be the case of the study of the annual oscillation in Arctic Ocean mass (*Peralta-Ferriz and Morison*, 2010). Throughout this work however, the contribution of the atmospheric term $\overline{P_a'}$ will be neglected unless noted otherwise (e.g., for model - observation comparisons).

The first term of the right hand side in Equation 2.3 is the contribution to the bottom pressure change due to sea surface height variation. The second term represents the bottom pressure contribution due to the density variations of the water column. If two of these three terms are known, then a complete picture of the changes in the ocean circulation may be revealed. In this work, we will sometimes refer to the

pressure due to the vertically integrated density term as the steric pressure, defined as:

$$P'_{st} = g \int_{-H}^{0} \rho' dz \tag{2.4}$$

Furthermore, the steric pressure may be approximately related to Arctic Ocean freshwater content (FWC) relative to a reference salinity (e.g., 34.87 psu), using the following empirical relation (see *Morison et al.*, 2012):

$$FWC = -35.6 \frac{P'_{st}}{\rho_\circ g} \tag{2.5}$$

Reduced FWC will result in an increase in steric pressure, whereas increased FWC will result in decreasing the steric pressure.

Note that steric pressure is the negative of steric height anomaly, which results from the combination of the thermo-steric expansion and the halo-steric contraction of the water column. Following *Gill and Niiler* (1973):

$$\eta'_{steric} = -\frac{1}{\rho_\circ} \int_{-H}^{0} \rho' dz = -\frac{P'_{st}}{\rho_\circ g} \tag{2.6}$$

In the Arctic Ocean, due to the cold temperature of the Arctic Ocean, and strong stratification of the water column, density is dominated by salinity rather than temperature. Consequently, the thermosteric or temperature-induced SSH change is much smaller than the halosteric or salinity-induced SSH change. In many regions worldwide, these two components may have similar amplitudes and may also be of opposite sign (*Landerer et al.*, 2007a; *Antonov et al.*, 2002).

Throughout this work, OBP or mass variations will be referred to as its normalized form ($\frac{P'_b}{\rho_\circ g}$), and the units will be provided in equivalent water thickness. One mbar or one hPa unit pressure corresponds to one cm of equivalent water thickness.

2.2 Barotropic vs baroclinic contributions to OBP

In barotropic flow, the isobars (i.e., surfaces of equal pressure) are parallel to the isopycnals (i.e., surfaces of equal density) throughout the water column (*Gill and Niiler*, 1973) and consequently, the velocity is uniform with depth. It can be thought of as the component of the flow that results from the sea surface slope (Figure 2.1a).

In baroclinic flow, isopycnal surfaces intersect isobaric surfaces, and the velocity varies with depth. It can be thought of as the component of the flow that results from the density distribution of the fluid, which over time tends to adjust so that the baroclinic pressure gradient cancels the barotropic gradient at the bottom of the ocean, giving no flow at the bottom (Figure 2.1b).

Following Equation 2.3, and ignoring the atmospheric term $\overline{P'_a}$, OBP has two contributions: the steric pressure anomaly and the SSH anomaly. When the OBP change is predominantly dominated by the SSH anomaly (e.g., OBP = SSH), then the character of the ocean circulation is barotropic. When the steric pressure becomes important, the relationship between OBP and SSH breaks down, and the character of the ocean circulation is baroclinic.

The distinction between barotropic and baroclinic signals is essential for understanding current dynamics in the ocean. For a homogeneous body of water (i.e., density constant with depth), the flow will always be barotropic. For a stratified body of water, the flow may develop pressure gradients that are purely barotropic, purely baroclinic, or commonly a mix of both. The dominance of the barotropic contribution over the baroclinic contribution to OBP variations depends on depth, latitude, time scale and stratification (*Gill and Niiler*, 1973; *Vinogradova et al.*, 2007; *Bingham and Hughes*, 2008).

The modeling studies by *Vinogradova et al.* (2007, latitude limited to 80°N) and *Bingham and Hughes* (2008, with full Arctic Ocean) suggest that at annual and shorter

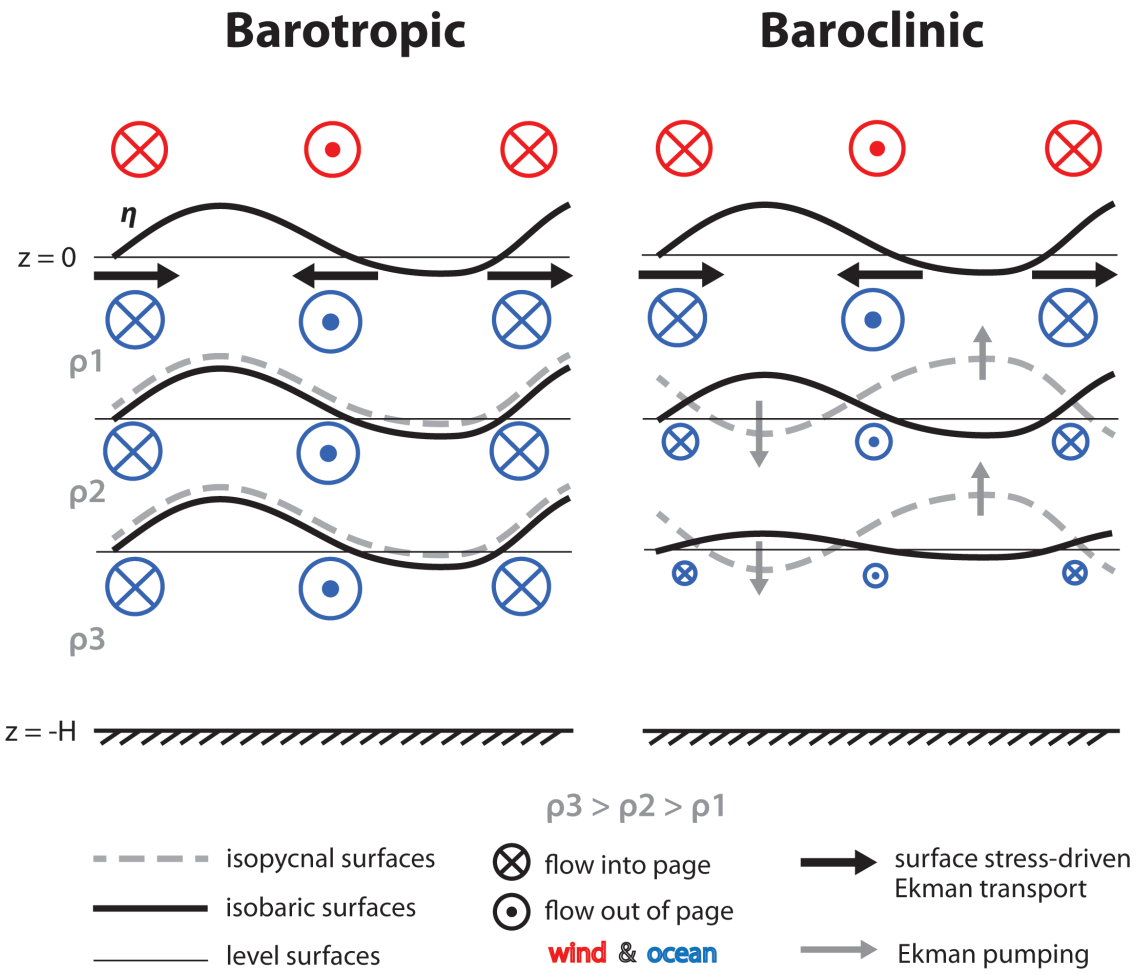

Figure 2.1: Pressure and density contours as a function of depth in (a) barotropic flow, where isobaric and isopycnal surfaces are parallel with each other and flow is invariant through depth, and in (b) baroclinic flow, where isobaric and isopycnal surfaces intersect each other and flow varies with depth.

timescales the Arctic Ocean is predominantly barotropic, whereas at inter-annual and longer timescales, the Arctic Ocean adjusts baroclinically. Only in the shallow regions of the Arctic shelves (e.g., <200 m deep), do the SSH fluctuations in the model of *Bingham and Hughes* (2008) remain coherent with OBP fluctuations at longer than

seasonal timescales (see Figure 2.2).

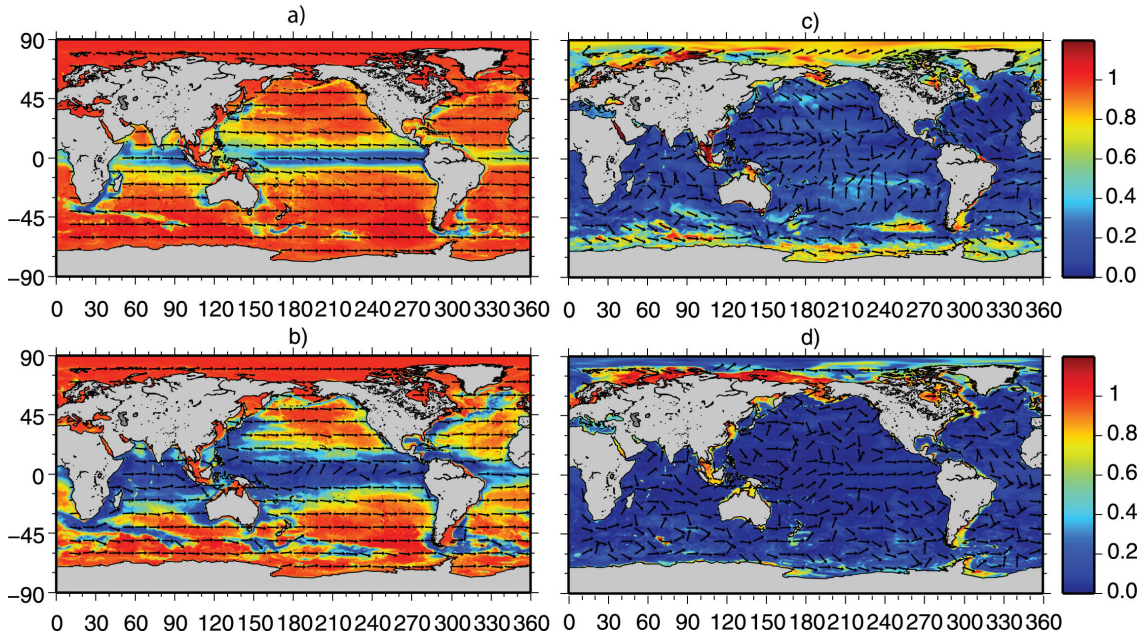

Figure 2.2: Contours show the admittance amplitude (where perfect correspondence is 1) between modeled SSH and OBP anomalies partitioned between (a) 10-20 cpd, (b) 20-60 cpd, (c) annual and (d) inter-annual frequency bands. Zero phase is indicated by an eastward pointing vector. Note that in the Arctic, at inter-annual timescales, OBP is coherent with SSH only in the shallow shelves. Image source: *Bingham and Hughes* (2008).

In order to understand which processes control the OBP changes, it is necessary to know whether observations support these modeling results. Recent advances towards this effort have been achieved by comparing OBP observations from GRACE and SSH observations from ICESat laser altimetry and *in situ*. *Kwok and Morison* (2011) compared observations of dynamic ocean topography, η', from ICESat with density-determined dynamic heights relative to 500 dbar, and found good agreement at multi-year timescales. *Morison et al.* (2012) compared GRACE OBP and ICESat SSH, and

in situ hydrography. Using this method, recent trends in distribution and origins of FWC change were quantified, and their associated ocean circulation patterns from 2005 to 2008 were revealed. These studies demonstrate that the ocean circulation is predominantly baroclinic in the Arctic basin (e.g., regions where ocean's depth exceeds 50 m): trends in SSH from 2005-2008 are compensated by the steric pressure field, and the resulting OBP change represented only a very small fraction of SSH variability. For the first time, a complete picture of freshwater variations and distribution in the Arctic Ocean was provided using remotely sensed observations (*Morison et al.*, 2012).

2.3 The Gravity Recovery and Climate Experiment: GRACE

NASA's satellite mission Gravity Recovery and Climate Experiment (GRACE) was launched in March 2002. The goal of GRACE is to measure the time-varying gravity field of the Earth. GRACE consists of twin satellites that fly in formation at $\sim$ 450 km above the Earth's surface and are separated by approximately 220 km. As the satellites orbit the Earth, areas of stronger gravity (i.e., areas of increased mass concentration) affect the leading satellite first and pull it away from the trailing one. As the satellites continue along their orbit, the trailing satellites experiences the area of stronger gravity and it then is pulled towards the leading satellite (Figure 2.3). Thus the distance between the satellites depends on the mass concentrations and re-distribution of mass in the Earth. The relative separation of the pair is continuously measured using a microwave ranging system (K-band radiometer). Accelerometers are used to measure the non-gravitational acceleration (e.g., due to atmospheric drag) of the system, and Satellite Global Positioning System (GPS) receivers are used to determine the exact position of the satellites as they orbit the Earth (*Tapley et al.*, 2004).

Over the ocean, changes in the time-varying gravitational field reflect temporal

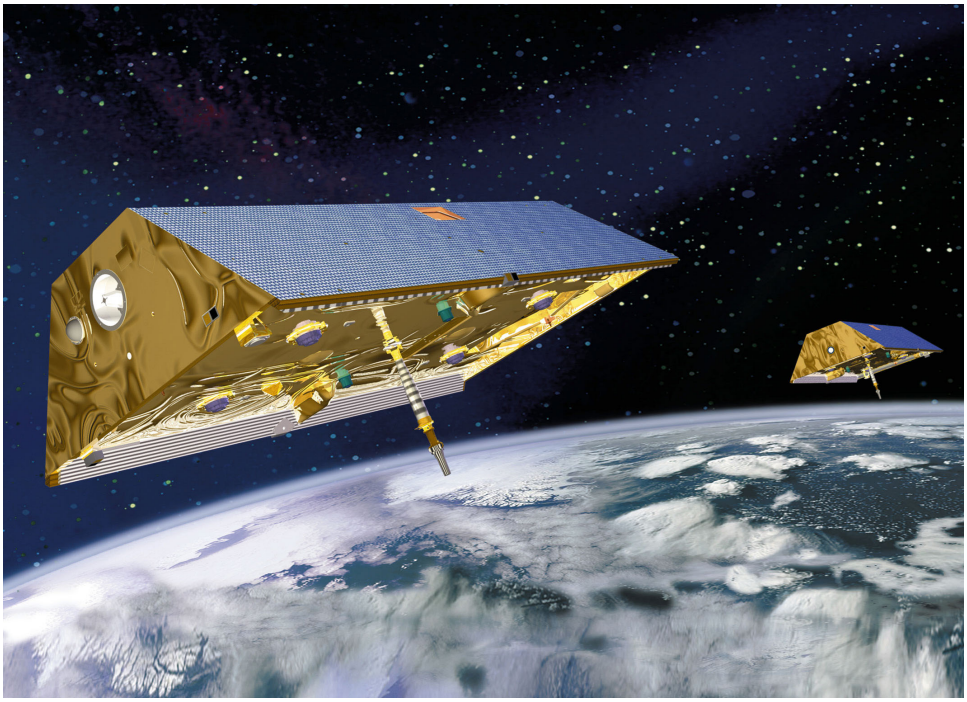

Figure 2.3: Squematic of NASA's twin satellites GRACE. Image from: http://grace.jpl.nasa.gov/.

variations of the ocean bottom pressure field. The conversion from gravitational field to ocean bottom pressure has been explained by *Wahr et al.* (1998). Of particular interest to the polar research field is the orbit of the GRACE satellites (i.e., 89° of inclination), which allows for essentially full coverage over the Arctic Ocean, and better temporal resolution for high-latitude regions, where mass distribution changes in the ocean, along with mass changes due to glacier melt and sea level rise are of major concern under climate change.

By measuring OBP changes, GRACE has become a powerful tool for investigating ocean dynamics that have been otherwise limited to sporadic locations or done with only short-term observations. OBP measurements can determine the abyssal

flow characteristics using the geostrophic relation (*Luther and Chave*, 1993). With simultaneous observations of OBP in different locations, the barotropic mass transport between the locations may be determined (*Morison*, 1991). Ocean mass transport may be used to study overturning flow variations (*Roussenov et al.*, 2008), mass exchange between ocean basins (*Chambers and Willis*, 2009; *Stepanov and Hughes*, 2006; *Hughes and Stepanov*, 2004), and freshwater changes in the ocean (*Morison et al.*, 2007, 2012). On a broader scale, changes in mass, and therefore changes in OBP, are directly related to water mass exchanges among the ocean, cryosphere, and hydrosphere (*Wahr et al.*, 1998).

Both the need for a ground-truth observation to validate GRACE in the Central Arctic, and the need for monitoring changes in Arctic Ocean circulation, justified the deployment of four Arctic Bottom Pressure Recorders (ABPRs) near the North Pole starting in the spring of 2005. These instruments were deployed as part of the North Pole Environmental Observatory (NPEO) program. Further details on the ABPRs are included in Chapter 3. The analysis of GRACE-derived Arctic OBP and the *in situ* measurements from the ABPRs forms the basis of the work described in this thesis.

2.3.1 GRACE for Arctic Ocean applications

Morison et al. (2007) first demonstrated the capabilities of GRACE to detect large-scale variations of mass distribution in the Arctic Ocean. GRACE data was evaluated using the first year of *in situ* OBP measurements from two ABPRs located near the North Pole. The datasets proved to be in excellent agreement with each other. GRACE comparisons with *in situ* observations in the Beaufort Sea and Fram Strait also showed good agreement (*Peralta-Ferriz and Morison*, 2010). *Morison et al.* (2007) showed that the difference between GRACE OBP and the pressure changes

due to density variations of the ocean as measured by hydrography of the upper 200 m, provides an estimate of the sea surface height variation that was consistent with changes in circulation patterns. These results inspired the work of *Morison et al.* (2012), which supports the idea that changes in Arctic freshwater content may reflect changes in the regimes of the Arctic Ocean circulation.

Previous studies suggested that the signal to noise ratio of GRACE OBP is largest at high latitudes (*Kanzow et al.*, 2005). Since GRACE flies over the Arctic more often (∼every 1.5 hours) than at lower latitudes, the potential to recover high frequency variations of OBP is larger, and therefore the tidal and sub-monthly aliasing effects on the monthly solutions may be significantly reduced (*Killett et al.*, 2011). Of particular relevance to high-frequency changes are the sub-monthly variations of Arctic Ocean mass, which are energetic during the winter, and significantly large relative to red noise and to the annual cycle of OBP, as revealed by a collection of pressure and tide gauges in the Arctic Ocean (*Peralta-Ferriz et al.*, 2011, Appendix A).

The origins of these sub-monthly variations −spatially coherent throughout the basin− were addressed in *Peralta-Ferriz et al.* (2011, see Appendix A). Briefly, the sub-monthly variations in OBP were detected in a 5-year record of bottom pressure at the North Pole, and were well reproduced by the Pan-Arctic Ice Ocean Modeling and Assimilation System, PIOMAS (*Zhang and Rothrock*, 2003). The Root-Mean-Squared (RMS) amplitude of these variations averaged throughout the basin is 3.3 cm. The character of these variations is not stationary, as revealed by the wavelet analysis shown in *Peralta-Ferriz et al.* (2011, Appendix A).

The sub-monthly mode of OBP variability was associated with episodic wind forcing over the nordic Seas, likely related to winter blocking events as described in *Rennert and Wallace* (2009). *Peralta-Ferriz et al.* (2011) suggested that the southerly winds over the Nordic Seas create a northward geostrophic slope current mainly

through Fram Strait, increasing the oceanic mass of the Arctic 1-2 days later, as shown in Fig. 3 of *Peralta-Ferriz et al.* (2011) in Appendix A. The modeled return flow out of the basin within the sub-monthly variation is consistent with the reversal of the wind patterns driving sea-ice out through Fram Strait (*Tsukernik et al.*, 2009). The flow reversal and its associated forcing (e.g., high SLP in Greenland and low SLP in Scandinavia) are illustrated in the composite maps of daily SLP, modeled SSH and modeled vertically integrated velocity field variations relative to the phase of modeled basin-averaged OBP (Figures A.4 and A.5).

The rapid response of this variation to the atmospheric forcing, along with the equivalent response of SSH and OBP, suggests that this mode of variability is of barotropic character, in agreement with *Vinogradova et al.* (2007) and *Bingham and Hughes* (2008). Detecting the sub-monthly oscillation is of fundamental interest to the GRACE-processing centers, because of the potential of aliasing of the strong sub-monthly signal into the monthly solutions of GRACE.

Another mode of variability in Arctic OBP clearly detectable in the GRACE solutions is the annual cycle of ocean mass, assessed in *Peralta-Ferriz and Morison* (2010, see Appendix B). This work suggests that the annual cycle of Arctic OBP variation, with a basin-averaged maximum during late summer to early fall, and a basin-averaged minimum during late winter to early spring, may be attributed primarily to the seasonally-varying river runoff discharging into the Arctic basin and, to a lesser extent, to the net precipitation minus evaporation (P-E), and to the sea level pressure difference inside and outside of the basin (see Appendix B). These results were in fair agreement with the modeling results of *Dobslaw and Thomas* (2007), where the annual OBP, of amplitude of 1 cm, was mainly attributed to runoff. The modeled OBP however, suggested a slightly earlier peak (early summer) relative to the GRACE-derived peak of maximum amplitude in summer to early fall. In

the work of *Peralta-Ferriz and Morison* (2010), a simple physical explanation for the phase discrepancy is given. *Peralta-Ferriz and Morison* (2010) suggest that the Arctic Ocean may be thought of as a rotating tank with a narrow channel connecting it to the world ocean. Assuming that meteoric (runoff + P-E) water pours in the middle of the tank with a seasonal cycle, and that the changes in sea surface height and hydrostatic pressure are geostrophically in balance, anticyclonic circulation through most of the water column would occur. The friction at the bottom would produce a boundary layer flow down the pressure gradient (e.g., out of the Arctic Ocean). The degree to which ocean mass can build up seasonally depends on the degree of leakage in the bottom boundary layer, which in turn depends on the bottom stress and background flow at the mouth of the channel. For an unrestricted leakage path, the maximum ocean mass would be nearly in phase with the input flow, while for a more restricted flow (possibly due to enhanced turbulence at the bottom owed to background currents or smaller scale processes), the phase of the maximum ocean mass would be delayed. The amplitude and phase of the annual variation of OBP resulting from this simple model are in good agreement with the amplitude and phase of the annual cycle of GRACE OBP (*Peralta-Ferriz and Morison*, 2010, Fig. 2 of Appendix B).

The analysis of the spatial re-distribution of Arctic mass at seasonal timescales is also included in Appendix B. This supplementary work addresses the seasonally varying bi-modal pattern of OBP variations between the East Siberian Sea and the Barents/Kara Seas. Spatial differences in the Arctic OBP seasonal change may be attributed to regional wind forcing, as suggested by the maximum covariance analysis performed on the residual GRACE[2] shown in Appendix B. During the winter to early spring, the northward component of the winds through the Nordic Seas associated with the spin-up of the westerly winds, forces the flow into the Barents and Kara Seas,

[2]defined as the total signal of GRACE at each grid point minus the basin-averaged OBP

and consequently increases the mass of this region. At the same time, anticyclonic wind patterns prevail in the Western Arctic, pulling SSH out of the East Siberian that converge into the Central Arctic, and consequently reduces the OBP in the East Siberian shelves. These dynamics are illustrated in Figure B.1.

2.4 GRACE in other relevant studies

There are several other studies in which observations of OBP by GRACE have been compared to *in situ* measurements in different regions of the world ocean.

Early releases of GRACE (first 1.5 year of data) showed large differences between GRACE and *in situ* OBP in the tropical northwest Atlantic, as reported by *Kanzow et al.* (2005). The authors attribute this difference to uncertainties in GRACE due to the errors in ocean models to produce high-frequency variations that are used to de-alias the GRACE monthly solutions, due to land contamination of the ocean signal in GRACE, and due to the several filtering steps in the GRACE processing.

Munekane (2007) compared three years of GRACE OBP with five *in situ* pressure sensors from the NOAA's tsunami gauges of the DART program[3], located in the northeast Pacific Ocean. The author found good correlations between the individual *in situ* data and the GRACE OBP at each location. When he compared the average OBP of the four most-closely clustered pressure gauges with the GRACE OBP at the center of the averaged region, the RMS-difference decreased to ~ 1.8 cm. Although the comparisons resulted in high correlations, the amplitude of the mass variations at individual locations were underestimated by GRACE, by nearly a factor of 2. The author argued that this could be due to the filtering of short spatial-scale oceanographic components in the GRACE-derived OBP. Interestingly, however, is to note that the GRACE-OBP at the North Pole does not underestimate the variations of OBP *in*

[3]Deep-ocean Assessment and Reporting of Tsunamis, available at: http://www.ndbc.noaa.gov/dart.shtml

situ, and yields high significant correlation with the ABPRs (R = 0.75, addressed in Chapter 4 of this dissertation). The excellent GRACE-ABPR agreement at the North Pole highlights the tendency of GRACE to generate more accurate measurements at high latitudes compared to lower latitudes, despite of the smoothing filters applied (*Morison et al.*, 2007).

In the western Pacific, over the Kuroshio Extension, an array of 46 pressure sensor -equipped inverted echo-sounders (PIES) measured OBP from May 2004 to June 2006, and were compared with GRACE (*Park et al.*, 2008). Results showed significant correlations between GRACE and *in situ* array-domain averaged OBP. The authors concluded that GRACE is capable of providing high-quality large-scale OBP data, with the seasonal cycle as the dominant variation. They also found that at the locations where the short-scale mesoscale OBP dominate the monthly averaged records of the *in situ* OBP, the point-wise comparison with GRACE yields low correlations.

Another study over the Crozet-Kerguelen region in the southern Indian Ocean was done by *Rietbroek et al.* (2006). This region is characterized by the presence of strong fronts, which correspond to a significant portion of the Antarctic Circumpolar Current transport in that region. The authors compared GRACE-derived OBP with two individual pressure gauges (Crozet and Kerguelen stations), with the average of both, and with the geostrophic flow associated with the sensors-derived pressure gradient. Generally correlations were significant, and the signal to noise ratio between GRACE and the difference of GRACE$-$*in situ* data was greater than one, except when comparing GRACE and *in situ* -derived vertically integrated flow. GRACE reproduced well the OBP variations at individual locations, but underestimated the resulting geostrophic flow, possibly due to the large smoothing of GRACE, or possibly due to greater sensitivity of GRACE to contamination by signals from the fronts.

Böning et al. (2008) developed a pattern-filtering method to obtain an improved

set of OBP data from GRACE. The optimized GRACE dataset yielded higher correlation coefficients with the point-wise *in situ* data from several locations around the world oceans. The method is based on identifying large-scale (∼1000-1500 km) coherent patterns of modeled OBP variability, to create a filter with a cut off radius of 20° of latitude equivalent distance around each grid point of GRACE solution. The resulting filter applied to the GRACE data generated a new set of OBP solutions where the mesoscale variability (e.g., Gulf Stream or Kuroshio Current) could be clearly identified, and land-contamination of the ocean signal was significantly reduced near the coastal regions worldwide.

Overall, comparisons between GRACE and *in situ* pressure data have shown mixed results. It is encouraging, however, that as the satellite record length has approached 10 years, optimized solutions and improved pre-processing of the data continue to emerge. The GRACE data used in this dissertation consists of newly optimized dataset to reduce land contamination from glacier melt into the ocean signals in the Arctic Ocean and Nordic Seas as developed by *Bonin and Chambers* (2012).

Chapter 3

DATA DESCRIPTION AND ANALYSIS TECHNIQUE

3.1 GRACE ocean bottom pressure

GRACE-Release 4 data from August 2002 to August 2011 are provided by the University of Texas, Center for Space Research (CSR) and the Jet Propulsion Laboratory (JPL)[1], and have been processed following *Chambers* (2006a,b). This processing includes a correction for the postglacial rebound using the model of *Paulson et al.* (2007), and a de-striping algorithm (*Chambers*, 2006a) to remove the north-south propagating errors of the gravity coefficients described by *Swenson and Wahr* (2006). The data is also filtered with a 300 or 500 km -radius Gaussian, and a spherical harmonic filter cutoff at degree 40. Monthly means of the Ocean Model for Circulation and Tides (OMCT) are added back to the GRACE solutions, to obtain the OBP variations. A special algorithm is also applied to minimize the leakage from land signals onto ocean signals. There are 4 missing monthly solutions out of the 109-month record used, due to technical issues with the GRACE satellites[2].

Despite applying a correction for the mass leakage from land into the ocean solutions (*Chambers*, 2006b), strong signals remain in the Arctic Ocean, particularly near the regions of recent significant glacial mass loss (e.g., around Greenland). A further step towards removing the land-contamination of the ocean mass change by the mass loss signals of Greenland and Svalbard has been performed as explained in *Bonin and Chambers* (2012). Briefly, this extra step consists of separating the

[1]available at ftp://podaac-ftp/jpl/nasa.gov/allData/tellus/L3/ocean_mass/netcdf/.

[2]more details may be found at http://grace.jpl.nasa.gov/.

land mass and ocean mass regions into several different basins, where each basin is assumed to have constant mass density. 16 basins are used across Greenland (eight in the coast, and eight in the interior), with 13 other land regions (including Iceland and Svalbard), and four ocean regions (defined by the auto-covariance of the OMCT time series). From the low-spatial resolution GRACE data, least squares estimation is used to solve for the high-resolution mass signal in each basin predicted to create that low-resolution signal. The 'forward model' solution over the Greenland basins are then smoothed with either a 300 or 500 km radius Gaussian filter, to estimate the land leakage from those areas into the ocean. This leakage estimate is removed from the original GRACE solutions, producing a leakage-removed mass signal.

Two GRACE post-processed solutions optimized by *Bonin and Chambers* (2012) are considered in this work: (a) De-striped (*Chambers*, 2006a), smoothed with a Gaussian filter of 300 km radius, and (b) Not de-striped, smoothed with a Gaussian filter of 500 km radius. The reasoning for including a solution without de-striping follows the hypothesis that the larger filter (500 km) may potentially eliminate the stripes without introducing any artificial effect due to non-linear de-striping algorithm applied to the fields (*Bonin and Chambers*, 2012). The solutions are evaluated and analyzed in Chapter 4.

3.2 In situ ocean bottom pressure at the North Pole

Ground-truth observations for GRACE validation and for independent measurements of ocean circulation change were taken at the North Pole with Arctic Bottom Pressure Recorders (ABPR). The ABPRs were developed in collaboration with the NOAA Tsunami early warning system engineering team (*Meinig et al.*, 2005). The ABPRs use Paroscientific Digiquartz 410K-101, 10,000 psi (68.94 MPa) pressure sensors with resolution of 0.25 mm and sensitivity better than 1 mm of water.

The ABPRs sample pressure and temperature every 15 seconds and store the data at 15 minute intervals. The instruments are equipped with an ATM-421 acoustic transducer and transmit the stored data to the surface using an internal Benthos ATM-880 acoustic modem (see Figure 3.1). The advantage of this system is that it allows for the collection of the pressure data approximately once a year, without disturbing the instrument and interrupting the pressure record and without the risk and logistical cost of retrieving the instrument through sea ice (Figure 3.2). Three out of the four units used were equipped with ORE 8242XS acoustically activated releases that can drop ballast weight for instrument recovery at end of battery life ($\sim$ 3 years, Figure 3.1).

Three precision ABPRs were deployed near the North Pole as part of the North Pole Environmental Observatory Program (NPEO)[3]. ABPR-1 and ABPR-3 were deployed in Spring 2005 and ABPR-4 was deployed in Spring 2006. ABPR-1 was deployed at 89° 15.26' N, 60° 21.58' E, in 4,301 m of water, and provided a total of 5 years of measurements of ocean bottom pressure, from Spring 2005 to Spring 2010. ABPR-3 was deployed near the base of the Lomonosov Ridge at 89° 14.85' N, 148° 7.54' E, in 4,192 m of water and provided 3 years of measurements, from Spring 2005 to Spring 2008. The distance of separation between ABPR-1 and ABPR-3 was 116 km. ABPR-4 was deployed very close to the North Pole at 89° 58.593' N, 178° 14.84' E, in 4,194 m of water, and provided one year of hourly measurements from Spring 2006 to Spring 2007.

A fourth ABPR, ABPR-5, based on an updated tsunami-warning system design, was deployed in Spring 2010 near the North Pole, at 89°, 58.708' N, 32° 55.433' W, in 4,197 m of water (Figure 3.3). A year later, in Spring 2011, the first year of ABPR-5

[3]Details on the NPEO program and the ABPR data are available at the program's website http://psc.apl.washington.edu/northpole/.

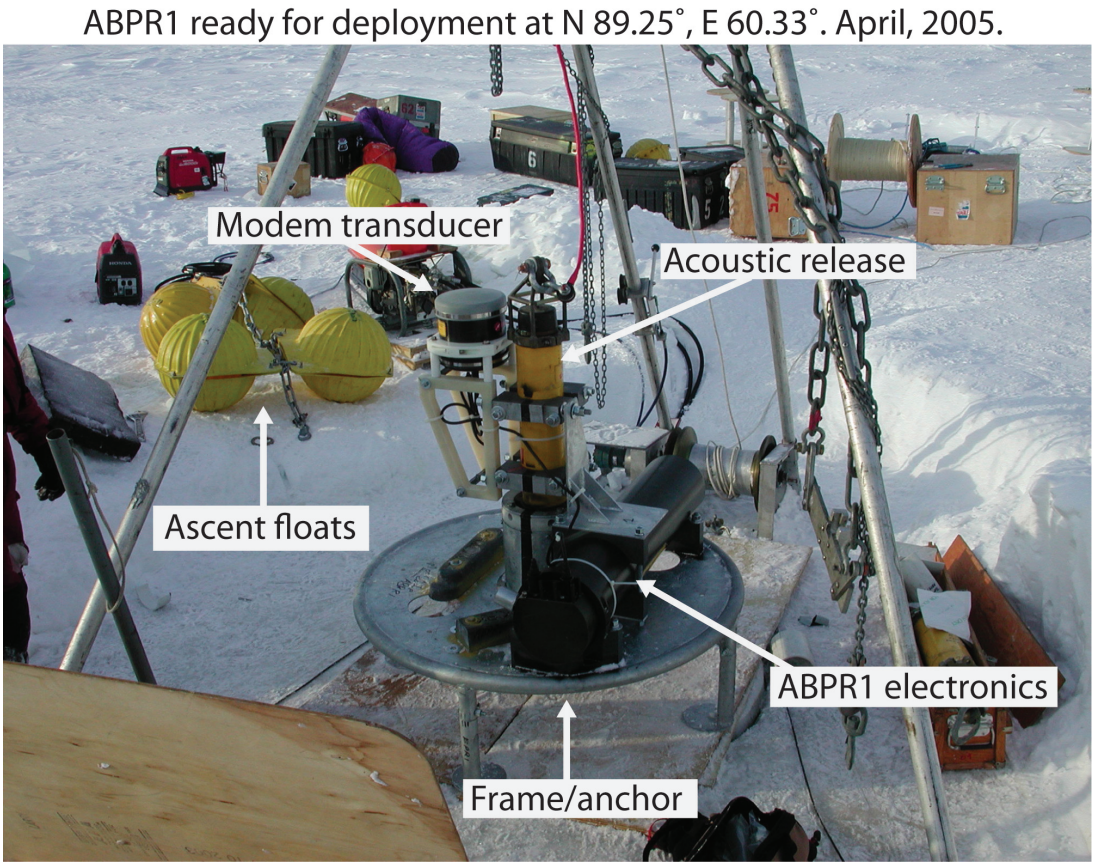

Figure 3.1: ABPR-1 ready for deployment in Spring 2005. Foto shows the major components of the ABPR system. Photo credit: J. Morison.

data were recovered. ABPR-5 is different from the previously deployed ABPRs in that it does not have a release and cannot be recovered. Similar to the other ABPRs, data are recovered through an acoustic modem, but at medium frequency. The life expectancy of the batteries in ABPR-5 is 5 years.

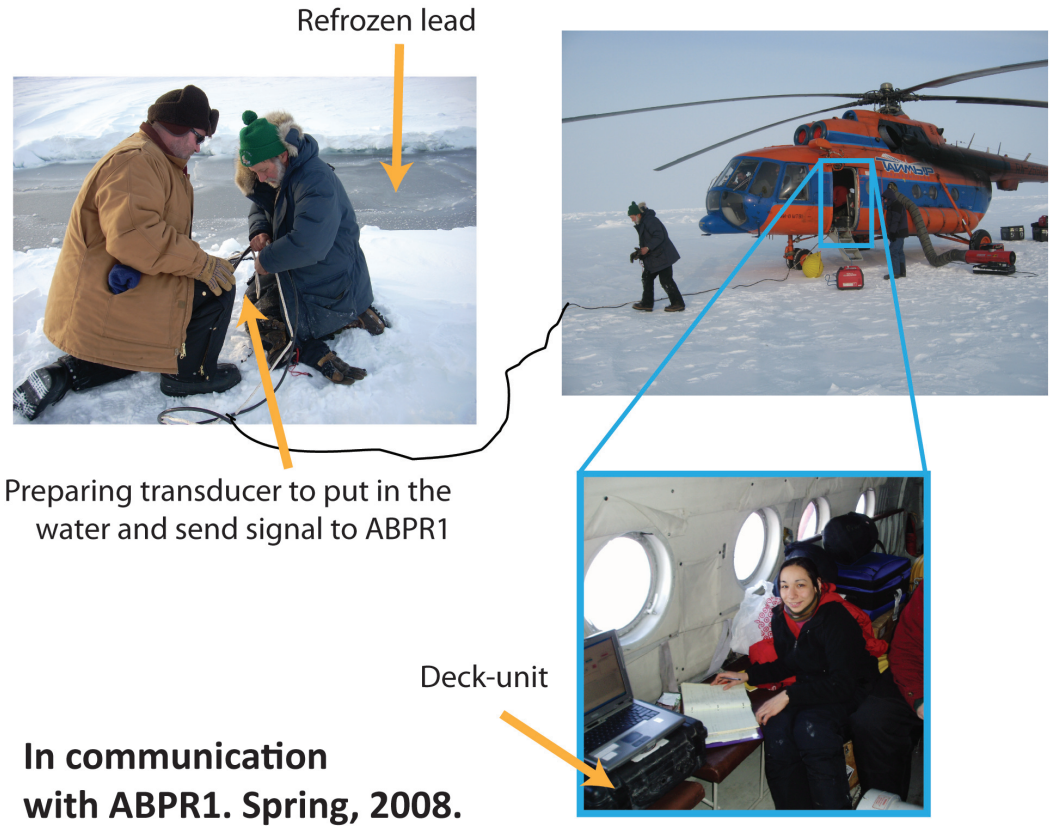

Figure 3.2: Collecting the data acoustically from ABPR1 in 2008. Photo credit: C. Peralta Ferriz.

3.2.1 Data quality control of ABPR-1: correction for instrumental drift and tidal constituents

Data from ABPR-1 was successfully collected for 5 years. ABPR-1 data, however, displayed an unrealistic $\sim$ 2 m/yr declining trend after the first year and a half of sampling (Figure 3.4). This drift was corrected by fitting an exponential function from December 14, 2006 to April 4, 2008, and a linear function fitted from April 26, 2008 until the end of the 5th year record, in April 11, 2010. The resulting drift

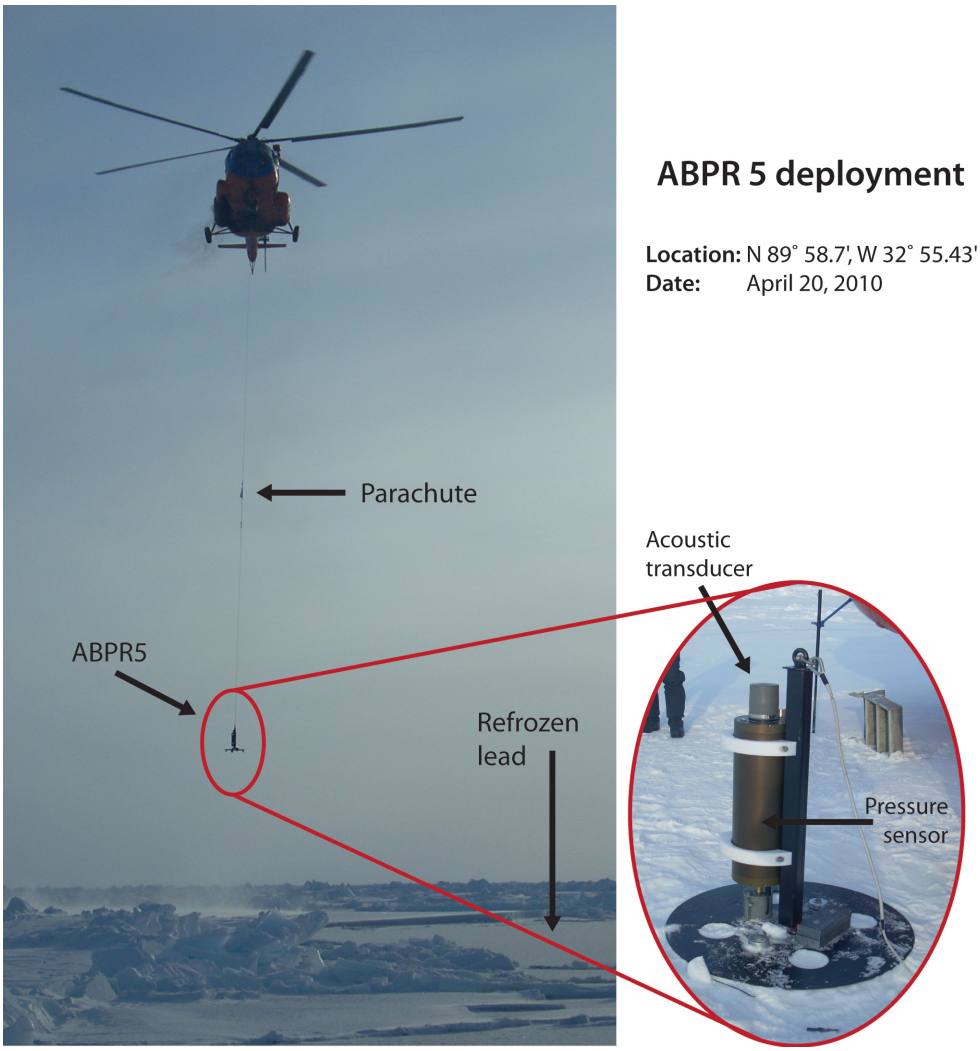

Figure 3.3: Deployment of ABPR-5 from helicopter. The ABPR-5 is lowered and left free-fall once crossing the surface of a re-frozen lead, with ice thickness of $\sim$ 10 cm. Photo credit: C. Peralta Ferriz.

(Figure 3.4b) was subtracted from the raw data, to yield Figure 3.4c. Note that during the recovery period in April of 2008 (color-separated in Figure 3.4a), the declining trend is interrupted for about 22 days (April 4 to 26, 2008), and no drift was removed

during this short period.

Once the total drift was removed, hourly averages were taken, and the tidal constituents were extracted from the signal, using the Matlab program *t_tide* (*Pawlowicz et al.*, 2002). The tidal signal is shown in Figure 3.4d. The tidal characteristics of ABPR1 are displayed in Appendix C. The constituent with the largest amplitude at the North Pole as revealed by ABPR-1 is the semi-diurnal M_2 tide (frequency = 0.0805 cph) with an amplitude of 6.3 cm, followed by the fortnightly tide M_f (0.00305 cph) with 3.2 cm, the K_1 tide (0.0417 cph) with 3.1 cm, and the S_2 tide (0.0833 cph) with 2.8 cm. Together with the OBP record of ABPR-3, ABPR-1 represents the first *in situ* measurements of OBP and tides of the Central Arctic. The M_2 and S_2 tides are in agreement with the amplitude of Arctic Ocean Tidal Inverse Model (*Padman and Erofeeva*, 2004), AOTIM[4], which predicts an M_2 tide of 5.9 cm and an S_2 tide of 3.1 cm. Aside from M_2 and S_2 tides, AOTIM underestimates the amplitudes of the observed tides (*Morison et al.*, 2007).

The residual OBP time series (raw−drift−tide−mean) was averaged in daily intervals, shown in Figure 3.4e. Since the drift was corrected with a low-order function, its removal from the data did not compromise the high-frequency variations in OBP. Also, monthly averages of the de-tided, de-drifted ABPR1 record are well correlated with the monthly OBP from GRACE at the North Pole (Figure 3.4f). Correlation coefficient between GRACE and ABPR1 is R = 0.75, significant above the 95% confidence level. The RMS error between GRACE (RMS = 3.87 cm) and ABPR1 (RMS = 3.41 cm) records is 2.6 cm.

---

[4]A barotropic inverse tidal model for the Arctic Ocean, available at http://www.esr.org/AOTIM/Arctic_Tides_2col.pdf

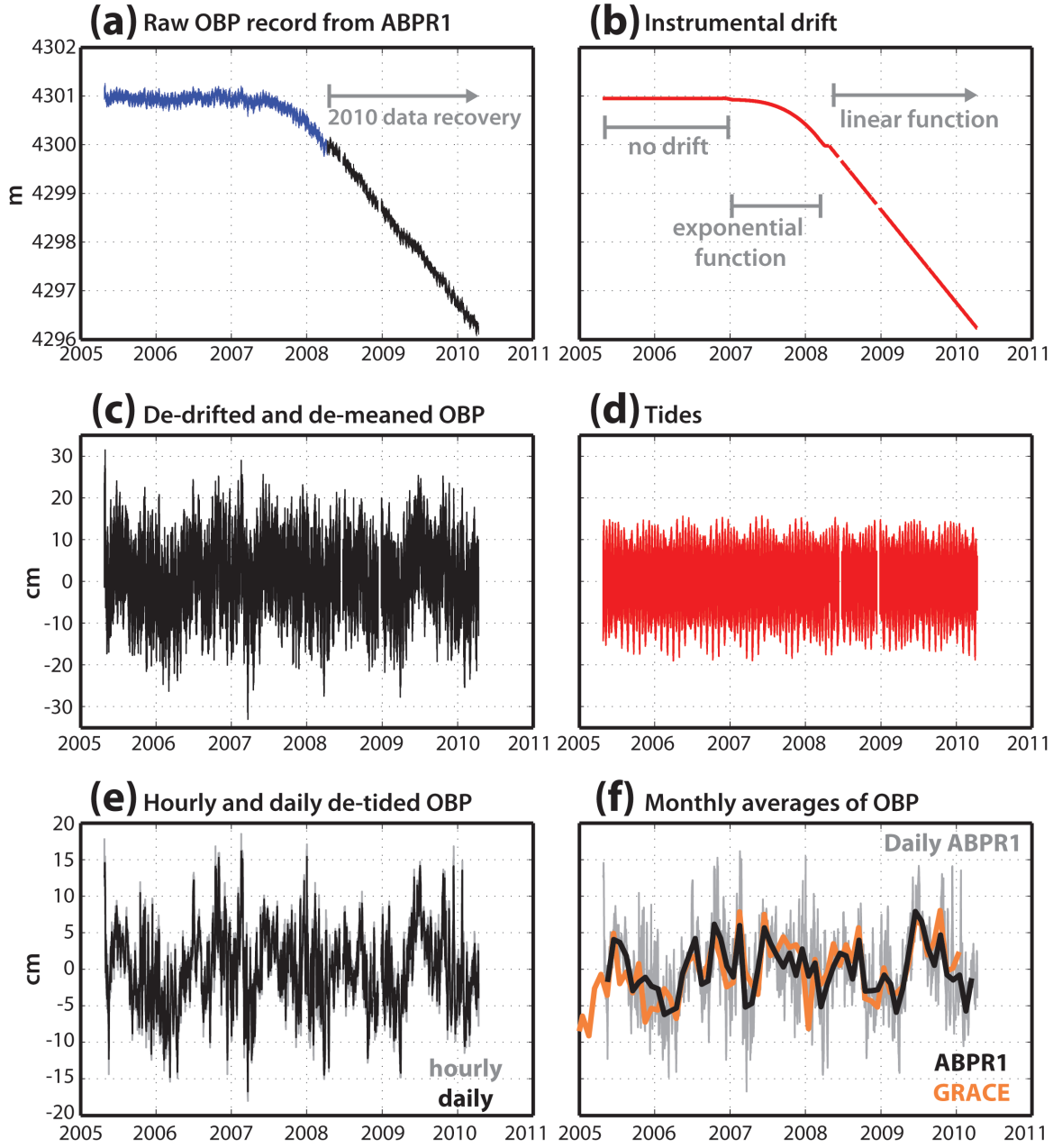

Figure 3.4: (a) Raw 5-year record of OBP from ABPR-1. (b) GRACE-CSR Rel. 4 at the ABPR-1 location (red), GRACE - monthly raw ABPR-1 (gray) and 4th order polynomial fit (black). (c) de-drifted hourly ABPR-1. (d) ABPR-1 tides. (e) De-tided, de-drifted ABPR-1 anomalies in hourly and daily averages. (f) Same as (e), but in monthly averages (gray) and same GRACE OBP (red) as in (b).

3.2.2 Data quality control of ABPR-3

ABPR-3 worked well for the first year (Figure 3.5). After that, the data displayed a similar unrealistic declining trend as the one observed in ABPR-1. The drift in ABPR-3 appeared half a year earlier than it did in ABPR-1. ABPR-3 data were corrected for this unexplained drift using the previously corrected ABPR-1. The correlation coefficient between the hourly records of ABPR-1 and ABPR-3 is R = 0.96, significant above the 95% confidence level, and the RMS difference between ABPR-1 and ABPR-3 is 1.63 cm, based on the first year and a half of the records, as reported in *Morison et al.* (2007), and 1.68 cm based on the three years. Once the drift in ABPR3 was removed, the record was de-tided as in ABPR-1. The tidal constituents from ABPR-3 are nearly identical to ABPR-1, and are also included in Appendix C.

3.2.3 Data quality control of ABPR-4

ABPR-4 worked one year, providing hourly-data only (Figure 3.6). The problem here was a modem malfunction at the end of the first data upload that drained the batteries. The collected data displayed a declining trend of $\sim$ 20 cm/yr. An initial increase in pressure during the first 50 days of the record was observed, perhaps due to the settling of the instrument (see Figure 3.6b). A smoother declining linear trend is observed later on the record. Part of this declining trend coincides with the period of seasonal drop in OBP. Regardless of the drift, the hourly record of ABPR-4 shows a high correlation (R = 0.97, significant above the 95% of confidence level) with ABPR-1 during the corresponding period (see Figure 3.6b). The tidal constituents from ABPR-4 are consistent with ABPR-1 and ABPR-3 (see Appendix C), and have been removed from the time series.

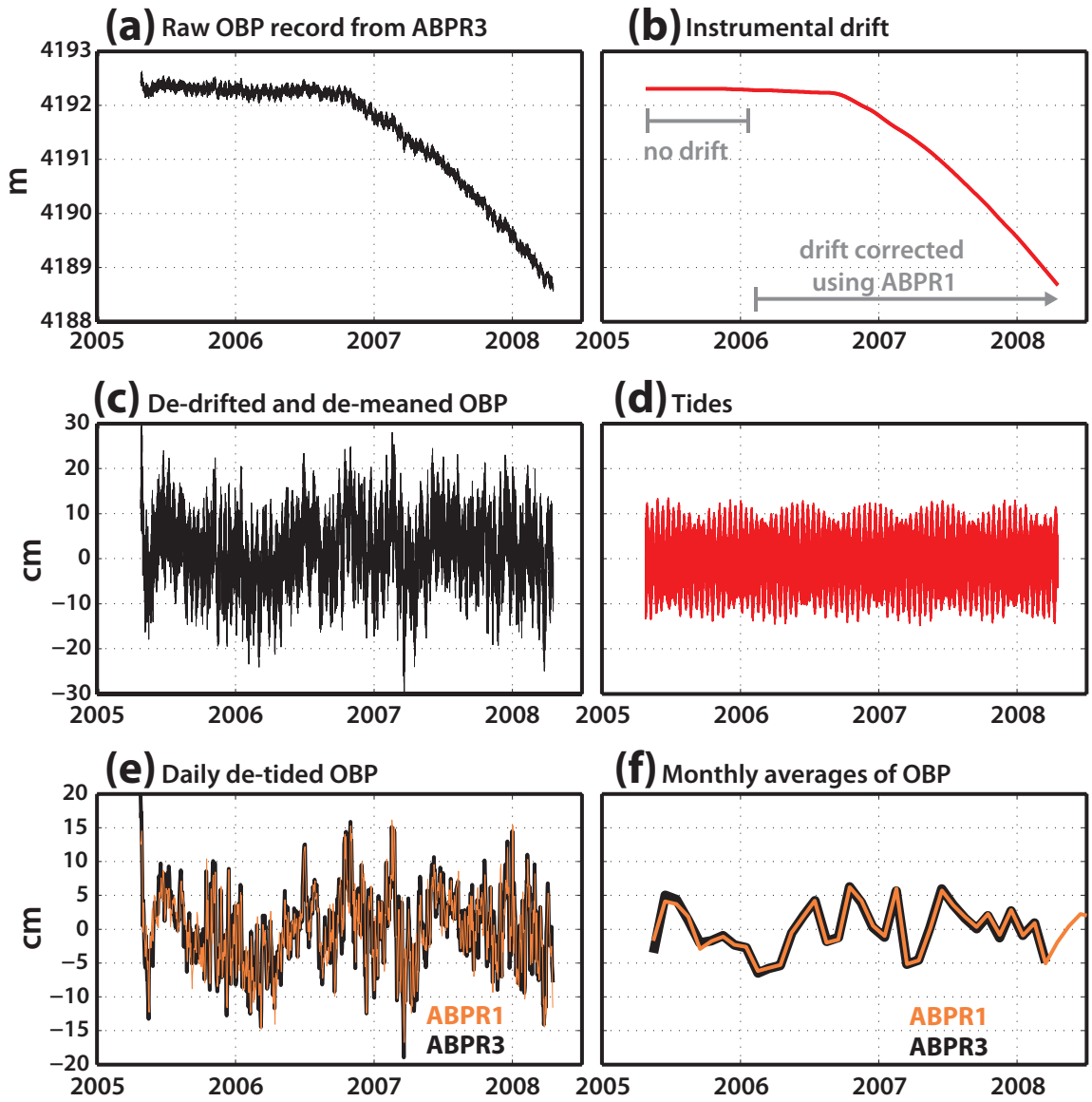

Figure 3.5: (a) Raw 3-year record of OBP from ABPR3. (b) de-drifted hourly ABPR3. (c) ABPR3 tides. (d) De-tided, de-meaned and de-drifted ABPR3 in hourly and daily averages

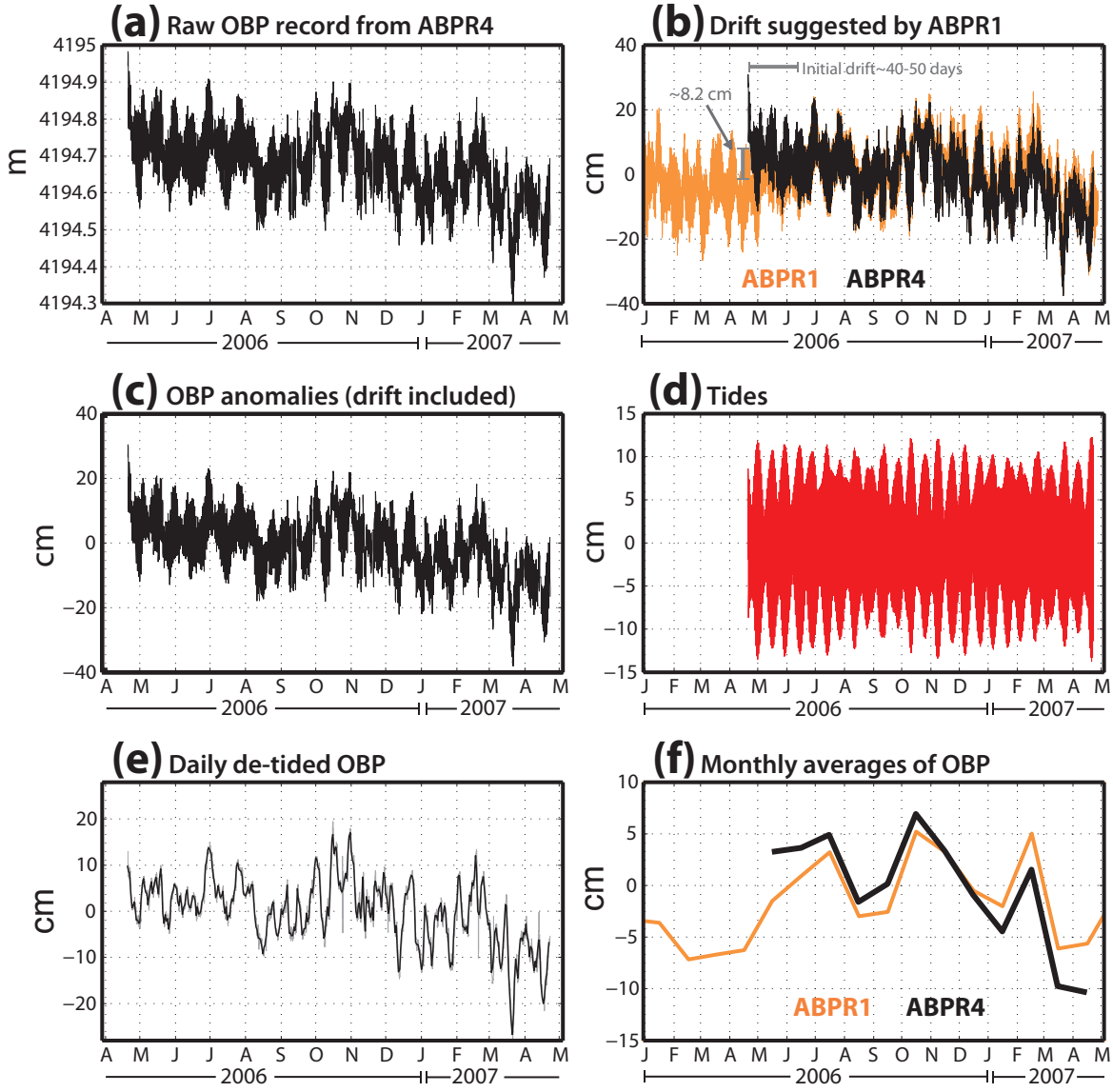

Figure 3.6: (a) Raw 1-year record of OBP from ABPR-4. (b) de-drifted hourly ABPR-4. (c) ABPR-4 tides. (d) De-tided and de-meaned ABPR-4 in hourly and daily averages

3.2.4 Data quality control of ABPR-5

As of today, the ABPR-5 continues to sample. The first year of ABPR5-OBP data displayed a drift of $\sim$ 26 cm/yr (Figure 3.7). The record was corrected for the drift using simply a linear trend fitted to the data. Then, the tides were removed similarly to the previous ABPRs, and the characteristics of the tidal constituents are included in Appendix C. As this dissertation is being written, a second year of ABPR-5 data has been collected. The new data shows no drift, and the drift problem is under investigation.

3.2.5 Six-year record of OBP at the North Pole

In order to get a representative record of OBP at North Pole, the first three years of daily ABPR-1 and ABPR-3 were averaged (de-tided, de-meaned and de-drifted), and ABPR-1 was used to complete the 5-year record. After the 5th year, ABPR-1 stopped working, likely due to exhausted batteries. None of the ABPRs 1, 3 and 4 were recovered and the origin of the instrumental drifts from ABPR-1 and ABPR-3 remain unclear. ABPR-5 was used to complete the 6th year of North Pole OBP record. Figure 3.8 shows the combined 6 years of ocean bottom pressure anomaly at the North Pole, and its comparison with GRACE-derived North Pole OBP. The 1-year long record of ABPR-5 was shifted to match the mean of GRACE OBP during the overlapping year.

3.3 Other Arctic pressure and tide gauges

In this dissertation, the ABPR data from the North Pole were complemented with other available records of OBP in the Arctic Ocean through different programs and institutions. Figure 3.9 shows a map of the location of all stations where available data from pressure and tide gauges are used in this work. The location of each *in*

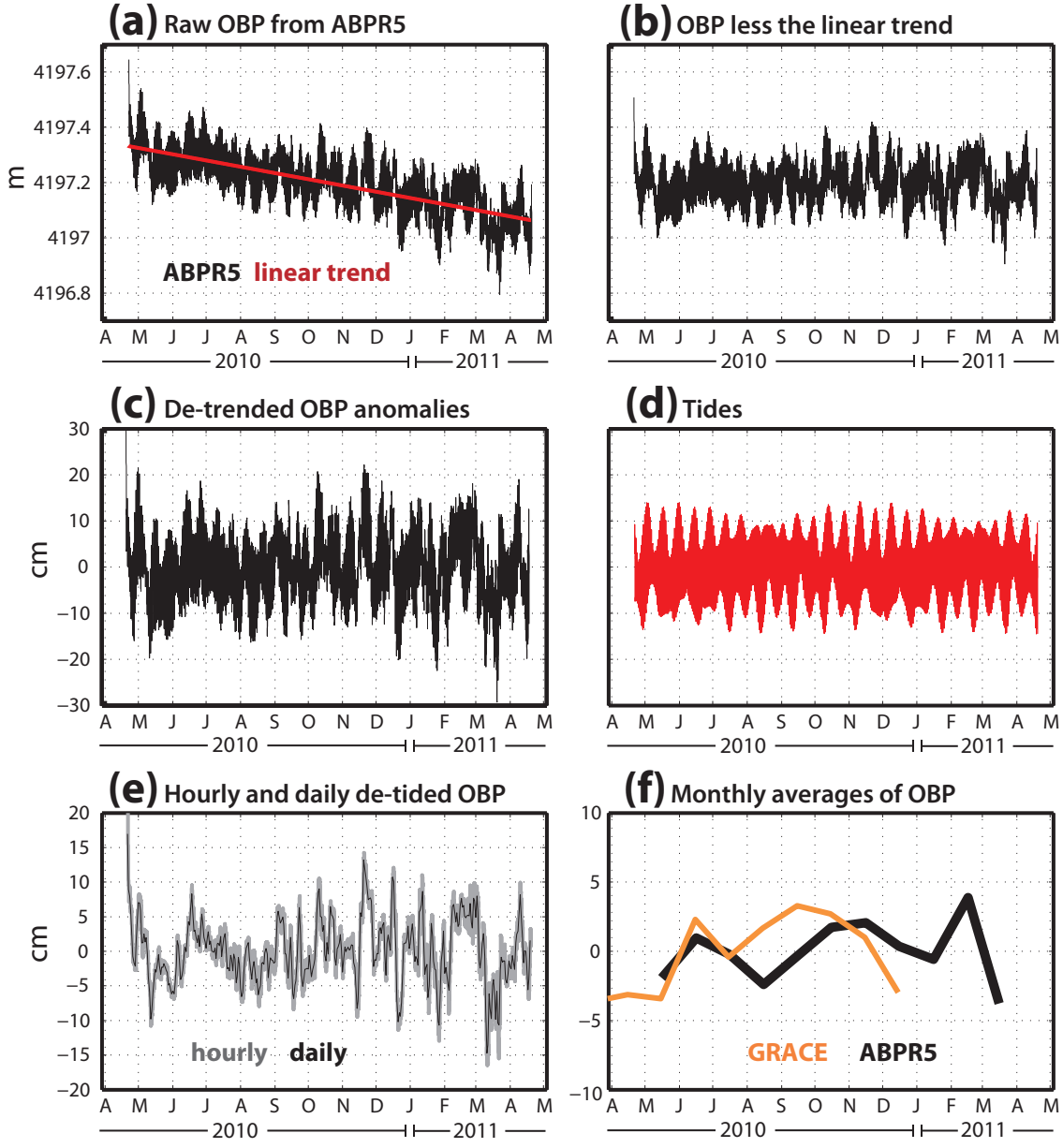

Figure 3.7: (a) Raw 1-year record of OBP from ABPR5. (b) De-drifted ABPR5, (c) ABPR5 tides. (e) De-tided, de-meaned and de-drifted ABPR5 in hourly and daily averages.

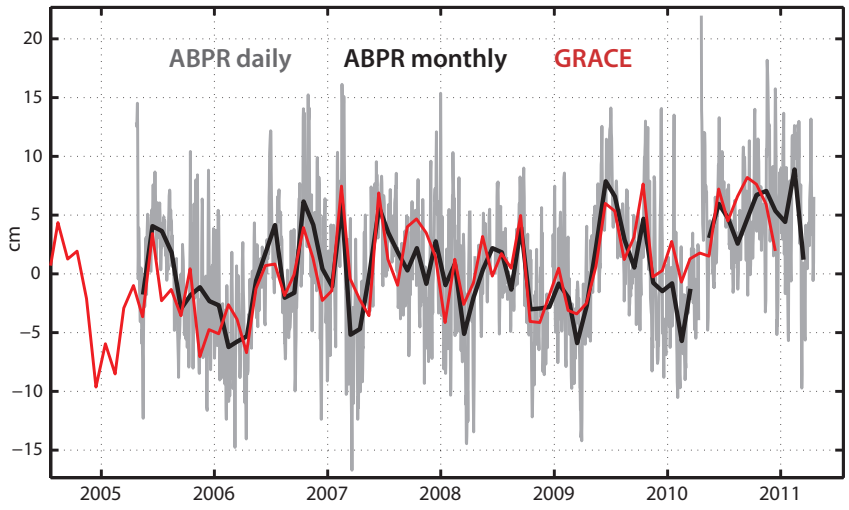

Figure 3.8: (a) De-tided, de-meaned and de-drifted 6-year record of ABPRs combined, hourly averaged. (b) Same as (a) but daily averaged, and (c) same as (b) but monthly averages (black) and GRACE at the North Pole (red).

situ record, length of the record, sampling frequency, record gaps and institution responsible for the data are summarized in Table 3.1.

In the Beaufort Sea, time series were used from three bottom pressure recorders (BPR) deployed by the Beaufort Gyre Exploration Project (BGEP)[5], at a) 75°N 0.449' N, 149° 58.66' W, b) 78° 1.49' N, 149° 49.203' W, and c) 76° 59.232' N, 139° 54.563' W, from August 2003 to August 2008. The BGEP OBP records are highly correlated with each other so these were averaged to obtain a single OBP record in the Beaufort Sea. BGEP BPRs are deployed yearly and thus continuity of the data is interrupted during recovery and re-deployment. In order to obtain continuous time series, the data gaps in individual BPRs are filled with averages from the overlapping records of the neighboring BPRs.

[5]http://www.whoi.edu/beaufortgyre/data_moorings.html/.

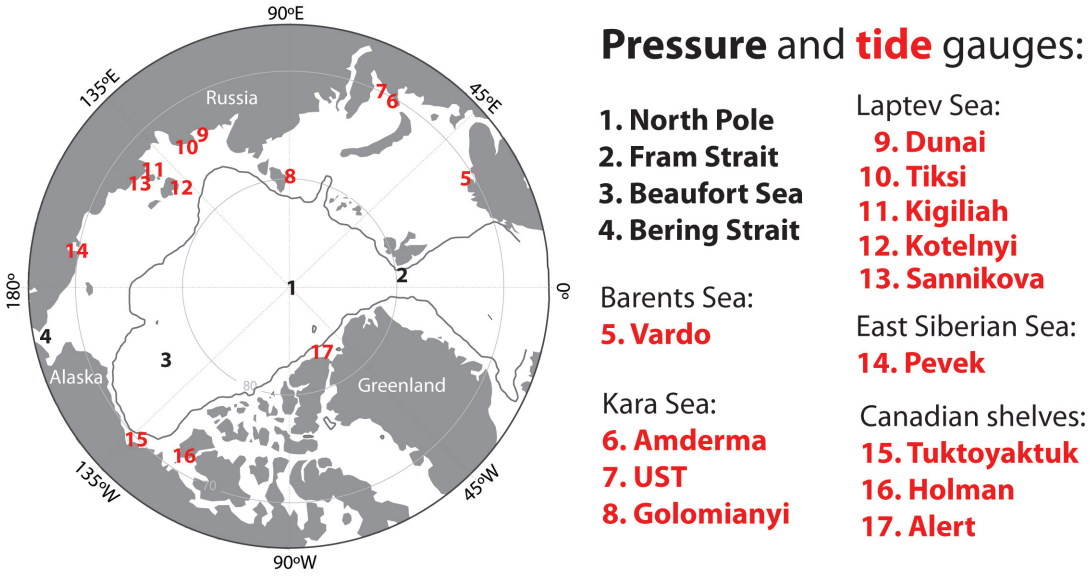

Figure 3.9: Map of the Arctic Ocean with the location of *in situ* tide (numbers in red) and pressure (numbers in black) gauges used in this dissertation. The gray solid line shows the 500-m isobath for reference. The source of each of the records and more information on the datasets are shown in Table 3.1.

In situ OBP records from the Bering Strait are provided by the Russian -American Long-term Census of the Arctic (RUSALCA)[6]. These records come from BPRs deployed at a) 65° 44.76' N, 168° 15.75' W and b) 65° 48.07' N, 168° 47.9' W, from September 2007 to 2009. These records were averaged to obtain a time series representative of Bering Strait.

OBP data in Fram Strait comes from Pressure Inverted Echo Sounders (PIES) deployed by the Alfred Wegener Institute at a) 78° 49.93' N, 5° 0.87' E, b) 78° 49.87' N, 2° 47.59' E and c) 78° 50.03' N, 8° 19.91' E, provided and post-processed by A. Beszczynska-Möller (personal communication, 2011). These data were averaged to give a time series of OBP representative of Fram Strait, from September 2003 to

[6]available at http://pcs.apl.washington.edu/HDL/BeringStrait.html.

Table 3.1: Stations of *in situ* pressure and tide gauges, location, length of record, sampling frequency, monthly record gaps, and source/institution responsible. The horizontal line separates pressure from tide gauge locations.

Station	**Location**	**Gauge**	**Temporal coverage**	**Sampling frequency**	**gaps (month)**	**Program/ Institution**
North Pole	89° 15.26' N, 60° 21.58' E	pressure	04/2005 - 04/2011	15 min	-	NPEO/UW
Beaufort Sea	76° 59.23' N, 139° 54.5' W	pressure	08/2003 - 08/2008	20 min	-	BGEP/WHOI
Fram Strait	78° 49.93' N, 5° 0.87' E	pressure	10/2003 - 12/2010	20 min	1	AWI
Bering Strait	65° 48.07' N, 168° 47.9' W	pressure	09/2007 - 09/2009	20 min	-	RUSALCA
Vardo	70° 19.8' N, 31° 6' E	tide	08/2002 - 12/2009	monthly	-	AARI/PSMSL
Dunai	73° 55.8' N, 124° 30' E	tide	08/2002 - 12/2009	monthly	2	AARI/PSMSL
Amderma	69° 45' N, 61° 42' E	tide	08/2002 - 12/2009	monthly	1	AARI/PSMSL
UST	69° 15' N, 64° 31.2' E	tide	08/2002 - 07/2009	monthly	11	AARI/PSMSL
Golomianyi	79° 33' N, 90° 37.2' E	tide	08/2002 - 07/2009	monthly	9	AARI/PSMSL
Kigiliah	73° 19.8' N, 139° 52.2' E	tide	08/2002 - 12/2009	monthly	1	AARI/PSMSL
Kotelnyi	76° N, 137° 52.2' E	tide	08/2002 - 12/2009	monthly	1	AARI/PSMSL
Pevek	69° 42' N, 170° 15' E	tide	08/2002 - 12/2009	monthly	1	AARI/PSMSL
Sannikova	74° 39.6' N, 138° 54' E	tide	09/2002 - 11/2009	monthly	3	AARI/PSMSL
Tiksi	71° 34.8' N, 128° 54' E	tide	08/2002 - 12/2009	monthly	-	AARI/PSMSL
Tuktoyaktuk	69° 25.81' N, 132° 59.4' W	tide	09/2003 - 12/2009	hourly	10	DFO, Canada
Holman	70° 44.21' N, 117° 45.53' W	tide	01/2003 - 04/2008	hourly	1	DFO, Canada
Alert	82° 29.51' N, 62° 19' W	tide	01/2003 - 07/2009	hourly	3	DFO, Canada

August 2010.

Tide gauge records are used from 3 locations on the Canadian Arctic Shelf, provided by the Department of Fisheries and Oceans (DFO), Canada[7]. Tide gauge locations are in Alert at 82° 29.51' N, 62° 19' W, from 2004 to 2007; Holman Station at 70° 44.21' N, 117° 45.5'W, from 2003 to 2008; and Tuktoyaktuk Station at 69° 26.4' N, 132° 59.4' W, from 2003 to 2008.

Over the European and Asian side of the Arctic, ten tide gauge records are used from the Arctic and Antarctic Research Institute in Russia (AARI), available through

[7]http://www.tides.gc.ca/english/Canada.shtml.

the UK National Oceanography Centre's program Permanent Service for Mean Sea Level (PSMSL)[8]. One station is on the Norwegian Arctic coast, in Vardo at 70° 19.8' N, 31° 6' E. The other stations used here span the Siberian coast, from the Kara to the Chukchi Seas. Their locations are shown in Table 3.1. These data are available only in monthly averages, for which tidal constituents are not extracted and presented here. These 10 tide gauges were selected based on their temporal coverage overlapping the OBP records of GRACE, from August 2002 to August 2011, and with less than 15% of missing months from the start to the end of each individual record.

Similar to the ABPRs, the high frequency tide and pressure gauge data were de-tided and averaged daily and monthly. All tide gauge data were corrected for the inverted-barometer effect to yield the dynamic portion of the SSH, using daily local sea level pressure (SLP) from NCEP/NCAR reanalysis (*Kalnay et al.*, 1996).

3.4 Atmospheric data

The atmospheric data used in this dissertation consists of zonal and meridional wind velocity fields at 925 hPa, and surface atmospheric pressure from the National Center for Environmental Prediction / National Center for Atmospheric Research (NCEP/NCAR) reanalysis (*Kalnay et al.*, 1996)[9]. Monthly averages from 2000 to 2011 are used.

Monthly values of the Arctic Oscillation Index are obtained from the NOAA's National Weather Service, Climate Prediction Center[10].

---

[8]available at http://www.psmsl.org/data/.

[9]Data was provided by the NOAA/OAR/ESRL PSD, Boulder, Colorado, USA, from their website at http://www.esrl.noaa.gov/psd/.

[10]available at http://www.cpc.ncep.noaa.gov/products/precip/CWlink/daily_ao_index/ao.shtml.

3.5 Bathymetry data

The bathymetry data used here is obtained from IBCAO Version 2.23 (*Jakobsson et al.*, 2008), at 100 km resolution[11].

3.6 Model output

3.6.1 PIOMAS

The Pan-Arctic Ice Ocean Modeling Assimilation System (PIOMAS) is a regional ice-ocean model with 30 vertical levels and spatial resolution better than 22 km (*Zhang and Rothrock*, 2003). The 'North Pole' of the model is located in northern Greenland, with the goal to maximize the resolution of flow exchange in the region of Fram Strait. PIOMAS is one-way nested to a global ocean model at 49° N, and is forced by the winds and surface atmospheric pressure from NCEP/NCAR reanalysis (*Kalnay et al.*, 1996). Monthly output of bottom pressure, sea surface height, temperature, salinity, ocean velocity u and v are obtained from January 2000 to December 2011. Daily bottom pressure and sea surface height output from PIOMAS are also used from 1949 to 2009.

3.6.2 ECCO2

The model Estimating the Circulation and Climate of the Ocean, Phase II: high resolution global-ocean and sea-ice data synthesis (ECCO2) is used to investigate the physics of the circulation in the Arctic, and for a second model confirmation to understand Arctic Ocean circulation change as observed by GRACE and the *in situ* data. ECCO2 was developed by the NASA Modeling, Analysis and Prediction (MAP) program. Synthesis data for ECCO2 are obtained from the global ocean and

[11]Gridded data is available at http://www.ibcao.org.

sea-ice configuration of the Massachusetts Institute of Technology general circulation model (MITgcm), and the available *in situ* and satellite data. The version of the model used in this dissertation is optimized by *Nguyen et al.* (2011). The optimized ECCO-2 version is forced with the Japanese 25-year Atmospheric Reanalysis Project (JRA-25). It has 50 vertical levels, and an average spatial horizontal resolution of 18 km. Monthly output of sea surface height, ocean bottom pressure, temperature and salinity fields are obtained from 2000-2009.

3.7 Methods

The primary goal of the research described in this dissertation is to understand the origin of ocean bottom pressure changes, and unveil dynamics of the ocean circulation associated with them. To do this, empirical orthogonal function (EOF) analysis is used to identify the primary modes of variability of the GRACE OBP field. EOF analysis -a widely used technique in climate studies-, transforms a space/time field into a set of vectors that are linear combinations of the original dataset. EOF decomposition is based on standard linear algebra techniques (e.g., singular value decomposition in this work).

The set of vectors that results from the EOF decomposition is usually truncated: the leading modes explain most of the variance of the original dataset. EOF analysis of any space/time field yields three products for each mode: (1) a scalar that determines the relative dominance of the mode in terms of the amount of variance of the field explained by that mode, (2) a principal component time series, and (3) a spatial pattern that varies in amplitude and polarity, depending on the corresponding PC time series. Regression maps of the leading modes are obtained by projecting the original dataset onto the PC time series of each mode, and the units are the same as the original dataset per standard deviation of the normalized PC time series.

In this dissertation, regression maps are not only used to identify EOF modes of variability, but also to unveil geophysical relationships between GRACE OBP, modeled OBP and SSH, and atmospheric data. Correlation coefficients are estimated between diverse fields to evaluate the performance of GRACE and models in representing *in situ* data.

Another statistical technique used in this dissertation is the estimate of the magnitude squared coherence between two time series (e.g., SSH and OBP), in order to measure the degree at which one variable explains the variability of the other variable as a function of frequency, and hence determine how barotropic or baroclinic the character of the ocean is through different timescales and in different regions of the Arctic.

Chapter 4

RESULTS

4.1 Evaluation of optimized GRACE solutions

Data from GRACE Release 4, post-processed as in *Chambers* (2006a) with the further step to remove land contamination of large ice-sheet mass loss on the ocean signals of GRACE by *Bonin and Chambers* (2012), consist of monthly data from August 2002 to August 2011. The two sets of GRACE solutions evaluated here are (1) GRACE-300: De-striped, smoothed with a Gaussian filter of radius 300 km, and (2) GRACE-500: Not de-striped, smoothed with a Gaussian filter of radius 500 km.

The most evident effect of the optimization to remove land contamination (*Bonin and Chambers*, 2012) is the elimination of the declining trend in OBP from 2002 to 2009 around South Greenland. This is illustrated in Figure 4.1 where the trends from 2002 to 2009 of both optimized GRACE solutions are compared to the trend obtained from previous available solutions (*Chambers*, 2006b). Away from the regions of leakage-optimization, GRACE-300 and the previous available solutions of GRACE (*Chambers*, 2006b, version dpc201012) remain consistent in structure, but the trends in mass change of GRACE-300 are slightly stronger.

4.1.1 Validation of GRACE and modeled OBP with observations in situ

GRACE-300 and GRACE-500 are validated with the available *in situ* monthly-averaged records from the stations shown in Figure 3.9. The monthly-averaged time series of modeled OBP and SSH from PIOMAS and ECCO-2 are also compared with the

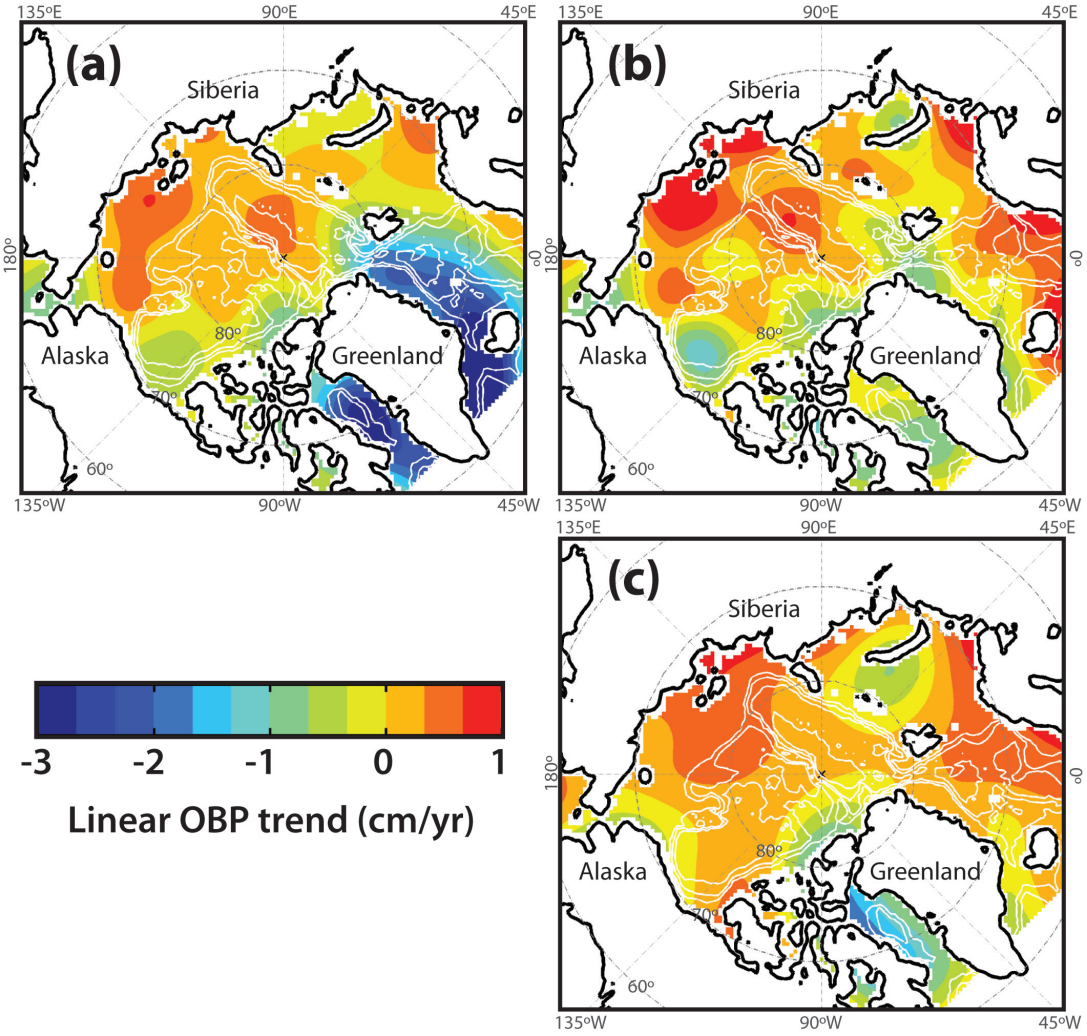

Figure 4.1: OBP trend (August 2002 to December 2009) using (a) GRACE-CSR Release 4, de-striped and smoothed with Gaussian filter of 300 km radius, processed by *Chambers* (2006a), (b) GRACE -CSR Rel. 4, de-striped and smoothed with 300 km -radius filter, optimized solution to reduce land-contamination by *Bonin and Chambers* (2012), and (c) same as (b), but non de-striped and using a 500 km -radius Gaussian filter. In all the panels, bathymetry is shown at 1000-m intervals.

monthly-averaged *in situ* records from the pressure and tide gauges, respectively. The resulting correlation coefficients and root-mean-squared error (RMSe) are included in Table 4.1.

Table 4.1: Correlation coefficient R and Root-Mean-Squared error (RMSe) between the monthly-averaged tide/pressure gauge records in the Arctic Ocean and GRACE, and between the *in situ* records and the model. All coefficients in bold face are significant above the 95% confidence level. RMSe units are cm. Modeled OBP is validated with *in situ* OBP data from pressure sensors (first four locations), and modeled SSH is validated with *in situ* data from tide gauges. OBP observations correspond to the four locations above the horizontal line. The other locations correspond to SSH observations.

No.	**Station**	**GRACE-Bonin300**		**GRACE-Bonin500**		**PIOMAS**		**ECCO-2**	
		R	**RMSe**	**R**	**RMSe**	**R**	**RMSe**	**R**	**RMSe**
1	**North Pole**	**0.76**	2.61	**0.85**	1.94	**0.58**	2.93	**0.46**	3.09
2	**Fram Strait**	**0.53**	3.07	0.27	3.82	**0.68**	2.17	**0.33**	2.95
3	**Beaufort Sea**	0.30	5.33	**0.46**	5.01	**0.69**	4.14	**0.49**	4.79
4	**Bering Strait**	**0.25**	9.46	**0.45**	8.13	**0.77**	6.56	**0.60**	7.09
5	**Vardo**	0.04	8.43	0.15	7.51	**0.73**	5.20	**0.82**	4.11
6	**Amderma**	-0.08	12.03	-0.18	12.34	**0.64**	8.40	**0.83**	6.75
7	**UST**	-0.28	11.95	-0.17	11.85	**0.46**	8.58	**0.60**	7.83
8	**Golomianyi**	0.18	6.14	**0.30**	5.80	**0.63**	4.80	**0.69**	4.45
9	**Dunai**	**0.48**	13.94	0.25	15.09	**0.53**	13.25	**0.42**	14.13
10	**Tiksi**	0.09	16.28	0.22	15.74	**0.43**	14.58	**0.31**	15.68
11	**Kigiliah**	**0.70**	9.09	**0.57**	10.19	**0.69**	8.56	**0.74**	8.06
12	**Kotelnyi**	**0.57**	8.68	**0.53**	9.11	**0.46**	9.36	**0.56**	8.70
13	**Sannikova**	**0.53**	11.35	**0.45**	12.04	**0.39**	12.20	**0.38**	12.23
14	**Pevek**	**0.77**	18.39	**0.56**	19.50	**0.65**	18.19	**0.66**	18.10
15	**Tuktoyaktuk**	**0.58**	12.77	**0.46**	13.47	**0.67**	10.76	**0.72**	10.89
16	**Holman**	-0.37	9.98	-0.04	7.68	**0.91**	3.09	**0.87**	4.72
17	**Alert**	**0.30**	4.39	**0.43**	4.07	**0.57**	3.73	**0.53**	4.05

In general, good correlations exist between OBP from GRACE and the *in situ* data, except with those records located in the Barents and Kara Seas (i.e., Vardo, Amderma, UST, Golomianyi). The highest correlations between GRACE-300 and *in situ* OBP records are at the North Pole and Pevek Station (East Siberian Sea), follow by those at Kigiliah Station (Laptev Sea). The modeled OBP and SSH from both ECCO2 and PIOMAS are significantly correlated with the *in situ* OBP and SSH records, respectively.

It would be expected that OBP and SSH variations are essentially the same in shallow regions, but this is not always the case. This is illustrated in Figure 4.2, where the time series of modeled OBP and SSH from ECCO2 and PIOMAS are compared with the *in situ* SSH from the tide gauge located in Amderma Station, in the Kara Sea at 69° 45' N, 61° 42' E. The difference between modeled OBP and modeled SSH is generally small, but the comparisons between modeled SSH and *in situ* tide-gauge records yield better correlations and lower RMS errors than the comparisons between modeled OBP and *in situ* tide-gauge records. One reason for the model OBP-SSH difference might be that the coastal Arctic tide-gauges are affected by the freshwater of the rivers discharging near them. The resulting freshwater input in very shallow water can yield strong fronts that might not be modeled well. This is also consistent with generally lower RMS errors between GRACE OBP and pressure gauges (e.g., North Pole, Beaufort Sea, Bering Strait, Fram Strait) than GRACE OBP with tide gauge records. Therefore, the model to *in situ* data comparison included in Table 4.1 is between modeled OBP and OBP records from pressure sensors, and between modeled SSH and SSH records from tide-gauges.

The time series comparisons between GRACE and modeled OBP and SSH with *in situ* records are shown here for 5 locations: North Pole (Figure 4.3), Fram Strait (Figure 4.4), one station in the Kara Sea (Figure 4.5), one station in the Laptev Sea,

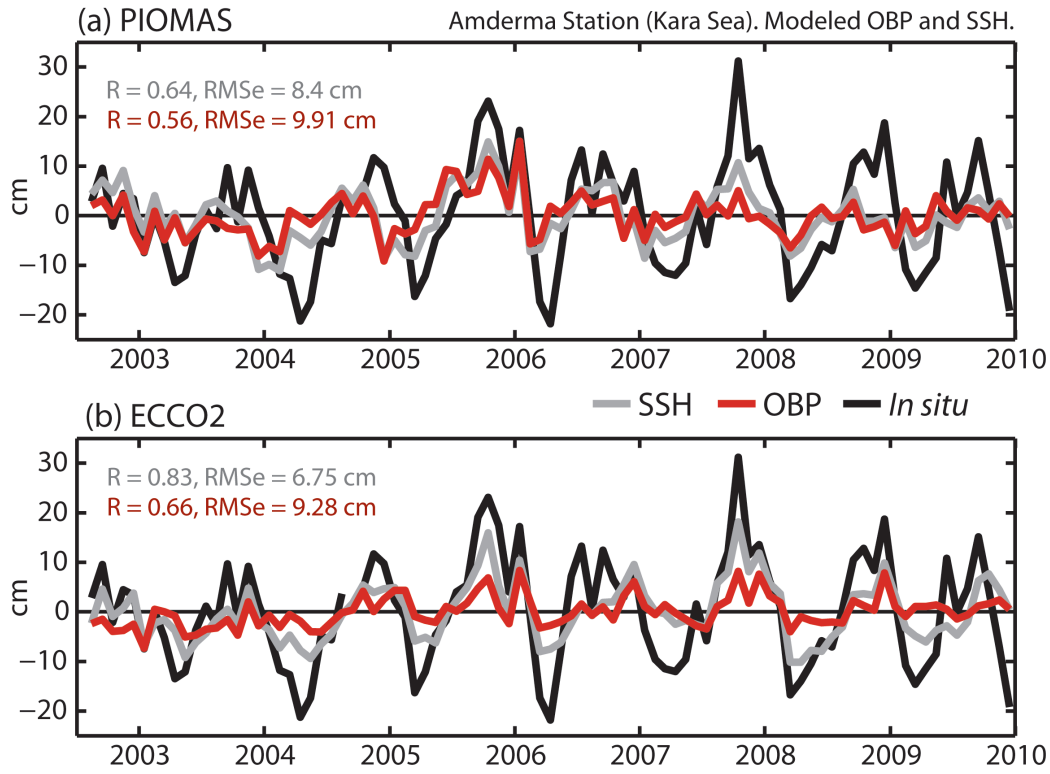

Figure 4.2: (a) Modeled OBP (red) and SSH (gray) from PIOMAS (August 2002 to December 2009) at Amderma Station (69° 45' N, 61° 42' E), compared with the *in situ* SSH data from the coastal tide-gauge (black). The correlation coefficient R and RMS error between the *in situ* data and each of the model timeseries are color-coded. The correlation coefficients shown are significant above the 95% confidence level. (b) Same as (a) but for the OBP and SSH from ECCO2.

near the border with the East Siberian Sea (Figure 4.6), and one in the Canadian Arctic shelf in Alert Station (Figure 4.7).

Table 4.2 is similar to Table 4.1, but the monthly-averaged time series of all sources have the seasonal mass variation removed. The seasonal variation was formed using the average of the available monthly means (e.g, means of January, February, March, etc.).

Table 4.2: Same as Table 4.1 but with the seasonal variation removed. RMSe units are cm.

No.	Station	GRACE-Bonin300		GRACE-Bonin500		PIOMAS		ECCO-2	
		R	RMSe	R	RMSe	R	RMSe	R	RMSe
1	**North Pole**	**0.70**	2.42	**0.79**	1.82	0.13	2.69	**0.56**	1.94
2	**Fram Strait**	**0.31**	2.47	-0.13	3.75	**0.64**	1.69	**0.38**	1.91
3	**Beaufort Sea**	**0.56**	2.98	0.16	4.19	**0.51**	3.06	0.39	3.27
4	**Bering Strait**	**0.48**	4.58	**0.55**	4.13	**0.42**	7.56	0.32	5.69
5	**Vardo**	0.25	4.32	**0.36**	4.02	**0.72**	2.83	**0.51**	3.88
6	**Amderma**	**0.33**	6.31	**0.47**	5.89	**0.44**	6.04	**0.73**	4.70
7	**UST**	**0.32**	7.09	**0.47**	6.63	0.26	7.63	**0.46**	6.69
8	**Golomianyi**	0.07	5.13	0.31	4.54	**0.53**	4.24	**0.59**	3.85
9	**Dunai**	**0.40**	12.10	0.23	12.78	**0.38**	12.12	0.29	12.55
10	**Tiksi**	0.22	12.61	0.29	12.34	**0.35**	12.13	**0.35**	12.15
11	**Kigiliah**	**0.49**	7.16	**0.47**	7.23	**0.61**	6.64	**0.67**	6.03
12	**Kotelnyi**	**0.45**	6.97	**0.41**	7.12	0.29	7.79	0.30	7.63
13	**Sannikova**	**0.38**	11.21	**0.37**	11.29	0.22	11.85	**0.28**	11.57
14	**Pevek**	**0.50**	9.08	**0.45**	9.17	**0.57**	9.03	**0.68**	7.46
15	**Tuktoyaktuk**	**0.52**	11.33	**0.46**	11.52	**0.74**	8.51	**0.86**	8.23
16	**Holman**	**0.48**	4.08	0.18	4.99	**0.81**	2.73	**0.70**	3.30
17	**Alert**	0.27	3.57	0.28	3.51	0.34	2.96	**0.56**	2.57

The discrepancy between GRACE-300, GRACE-500 and the *in situ* measurements in the Kara and Barents Seas may be explained by either one or both of the following hypothesis:

(1) GRACE estimates are not accurate, possibly due to contamination of the ocean signals by mass changes on land. Note that the GRACE solutions used here were optimized to reduce leakage from major glacial melt regions, i.e., Greenland, Iceland and Svalbard. However, the amplitude of the hydrologic signals from the terrestrial Arctic watersheds (e.g., Ob, Yenisey, Pechora, etc.) are also larger than

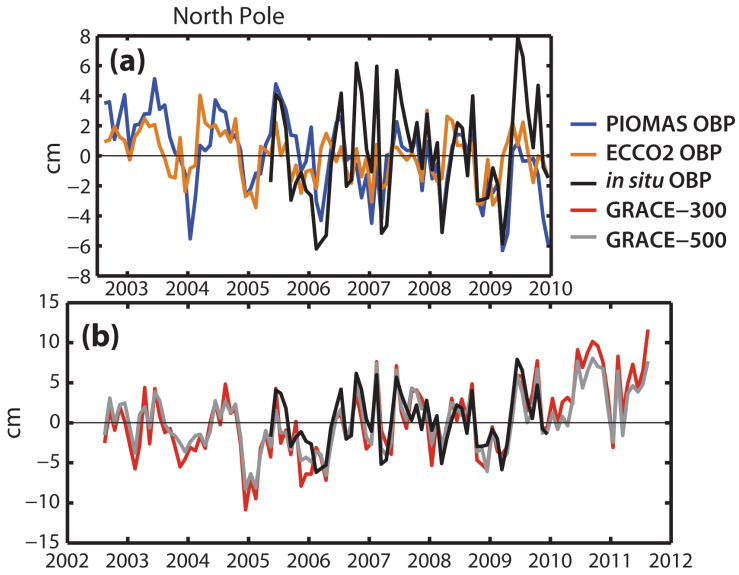

Figure 4.3: (a) Monthly-average time series of *in situ* (black), PIOMAS (blue) and ECCO-2 (orange) OBP at the North Pole. Pressure gauge location #1 in map of Fig. 3.9. (b) Time series of *in situ* (black), GRACE-300km (red) and GRACE-500km (gray) OBP at the North Pole.

the ocean gravity change, and thus may leak into the oceanic signals measured by GRACE. Supporting evidence of land-leakage from the Siberian Arctic watersheds is that the correlation between *in situ* data and GRACE-OBP data in the Kara and Barents Seas are lower when the seasonal variation is included than when it is removed (see Table 4.1 and Table 4.2). When the seasonal variation is removed, some of the correlation coefficients improve and in some locations are even above the significance level. Hence, the dominant seasonally varying land signal from the major Arctic watersheds may affect the ocean solutions.

To get a hint of this, GRACE water storage (in cm of water thickness) averaged over the watershed that discharges into the Kara Sea, and water storage averaged over the watershed of the Barents Sea (down to 60°N) have been compared with

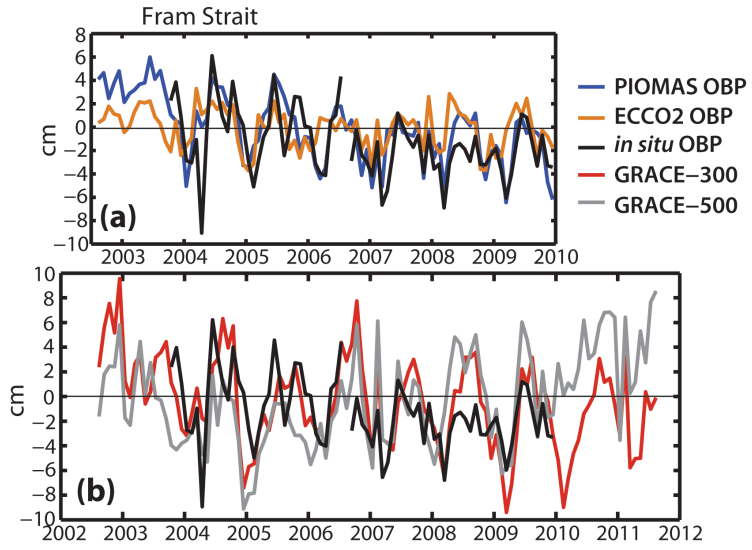

Figure 4.4: Same as in Figure 4.3, but in Fram Strait. Pressure gauge location #2 in map of Fig. 3.9.

the GRACE ocean mass change averaged over the Kara Sea and the Barents Sea, respectively (see Figure 4.8). The source of the GRACE water storage data used here is from S. Swenson and F. Landerer, version ssv201008 (*Landerer and Swenson*, 2012)[1], spanning from August 2002 to February 2012.

Figure 4.8 shows that there is a significant correlation between GRACE-derived OBP averaged over the (a) Kara Sea and (b) Barents Sea, with the GRACE-derived terrestrial water storage of the watershed that corresponds to each of these seas. The significant correlation at zero lag suggests that at least part of the oceanic signal from GRACE-300 and GRACE-500 may be due to leakage of land-based signal into the ocean solutions. Furthermore, the seasonal variation of Arctic OBP appears to have two components: the first one is a basin-averaged mass change that has been

[1]available at http://grace.jpl.nasa.gov

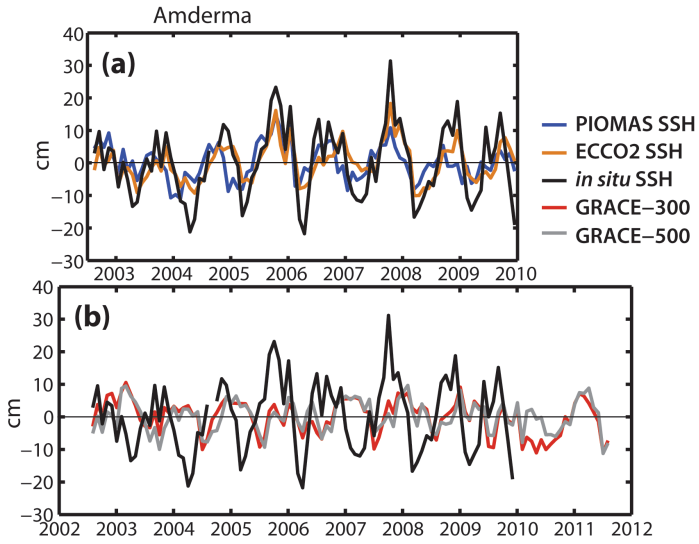

Figure 4.5: (a) Monthly-average time series of SSH from *in situ* tide gauge (black), PIOMAS (blue) and ECCO-2 (orange) in Amderma Station, in the Kara Sea, tide gauge location #6 in map of Fig. 3.9. (b) Time series of *in situ* SSH (black), GRACE-300km OBP (red) and GRACE-500km OBP (gray) in the same station.

attributed mainly to the river runoff (*Dobslaw and Thomas*, 2007; *Peralta-Ferriz and Morison*, 2010), which maximum peak is in the summer to early fall. The second component is a spatially varying mass re-distribution that may produce a mass signal in the Kara and Barents Seas of the same phase as the land signal due to forcing unrelated to land processes (e.g., wind forcing, see Appendix B). These dynamics are described in Appendix B, and briefly summarized in the next section.

(2) A second hypothesis for such discrepancy between GRACE and *in situ* data is that the steric contribution to OBP change might be large enough to break down the relationship between OBP and SSH in the Kara and Barents Seas, owing to stratification changes due to the input of runoff.

Can baroclinic adjustment produce disagreement between *in situ* tide-gauge data

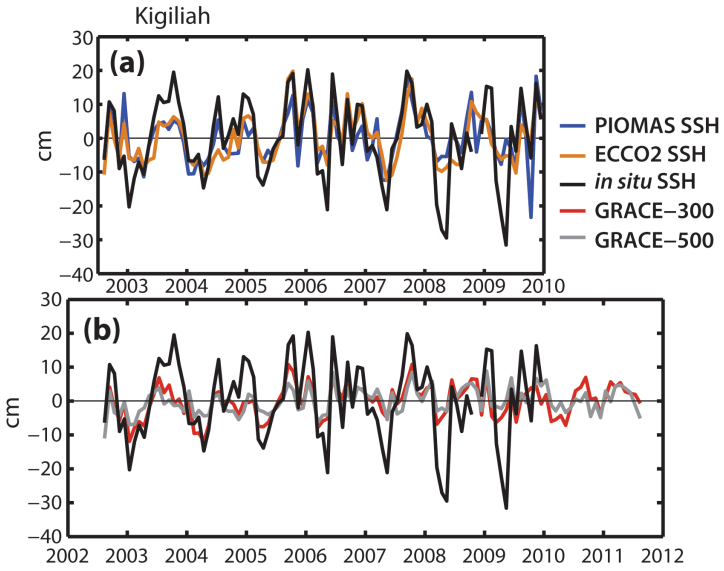

Figure 4.6: Same as in Figure 4.5, but for Station Kigiliah in the Laptev Sea. Tide gauge location #11 in map of Fig. 3.9.

and GRACE-OBP? There are a wide variety of tide gauges, and some of them do not use pressure gauges to measure the water level. In such cases, the *in situ* data from tide gauges in the Kara and Barents Seas only provide sea level observations (which have been corrected here for the inverted barometer response to yield the dynamic change in SSH). If the ocean is mainly barotropic, these *in situ* observations of SSH would reflect OBP as observed by GRACE, and would then prove useful to validate GRACE ocean bottom pressure estimates there. If however, the steric contribution is large, the relationship between *in situ* tide gauge data and GRACE OBP breaks down. If the baroclinic portion of the Kara and Barents Seas proved to be significant, however, it would be expected to affect the relationship between GRACE-OBP and SSH data at longer than seasonal timescales. Thus, for shorter timescales, GRACE would still be expected to detect changes similar to the tide-gauge derived water level

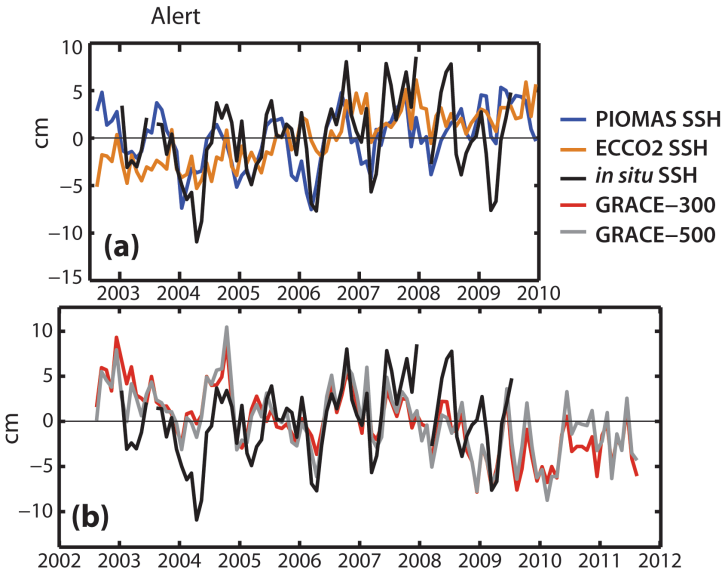

Figure 4.7: Same as in Figure 4.5 and 4.6, but for Station Alert in the Canadian Arctic shelf. Tide gauge location #17 in map of Fig. 3.9.

change, at least in the shallow parts of the shelves.

The barotropic vs baroclinic character of the Kara and Barents Seas will be assessed in a later section of this chapter, by using daily output of OBP and SSH from PIOMAS.

4.2 GRACE-model inter-comparison

In this work, the spatial and temporal variations of GRACE OBP are investigated, focusing on monthly to inter-annual timescales, but excluding the seasonal variation that was investigated by *Peralta-Ferriz and Morison* (2010, see Appendix B). As shown later, removing the seasonal signal clarifies the picture of variability at other timescales. The mean seasonal variation computed over the period from August 2002 to August 2011 for GRACE-300 OBP (shown in Figure 4.9), and for GRACE-500 (not

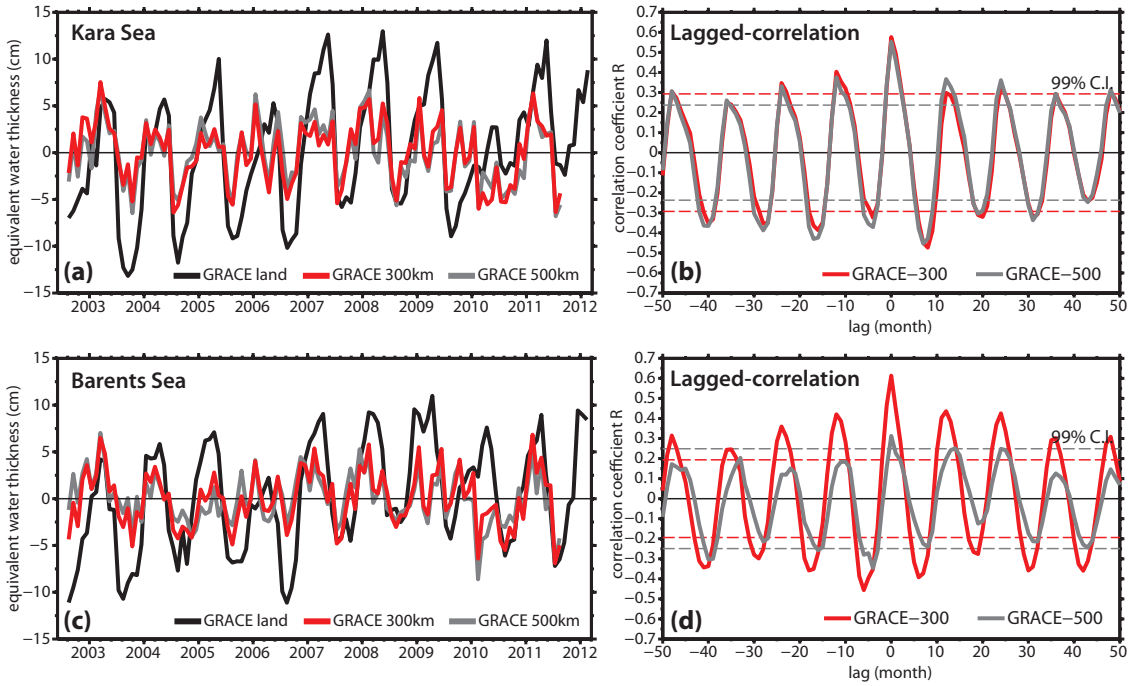

Figure 4.8: (a) Time series of GRACE-OBP averaged over the Kara Sea from GRACE-300 (red) and GRACE-500 (gray), compared to GRACE time series of water storage on land averaged over the Kara watershed from the coast, down to 60°N, and from 60°E to 105°E (black). The error (measurement and leakage from adjacent regions) is estimated as $\sim$ 4.26 cm in that region, following *Landerer and Swenson* (2012). (b) Lagged-correlation between OBP GRACE-300 (red) and OBP GRACE-500 (gray) with land signal (black line in (a)). Dashed lines are the 99% confidence level. (c) Same as (a) but for the Barents Sea, where the Barents watershed is delimited by the coast down to 60°N, and from 15°E to 58°E (black). The error for this region is estimated as 4.54 cm. (d) Same as (b), but for the Barents Sea watershed.

shown) has been removed from the monthly means of GRACE-300 and GRACE-500 datasets, respectively. The seasonal variation of GRACE-300 is consistent with the seasonal variation of GRACE-500 and similar to the seasonal variation of GRACE Release 4, using the 300-km filtered data shown in *Peralta-Ferriz and Morison* (2010).

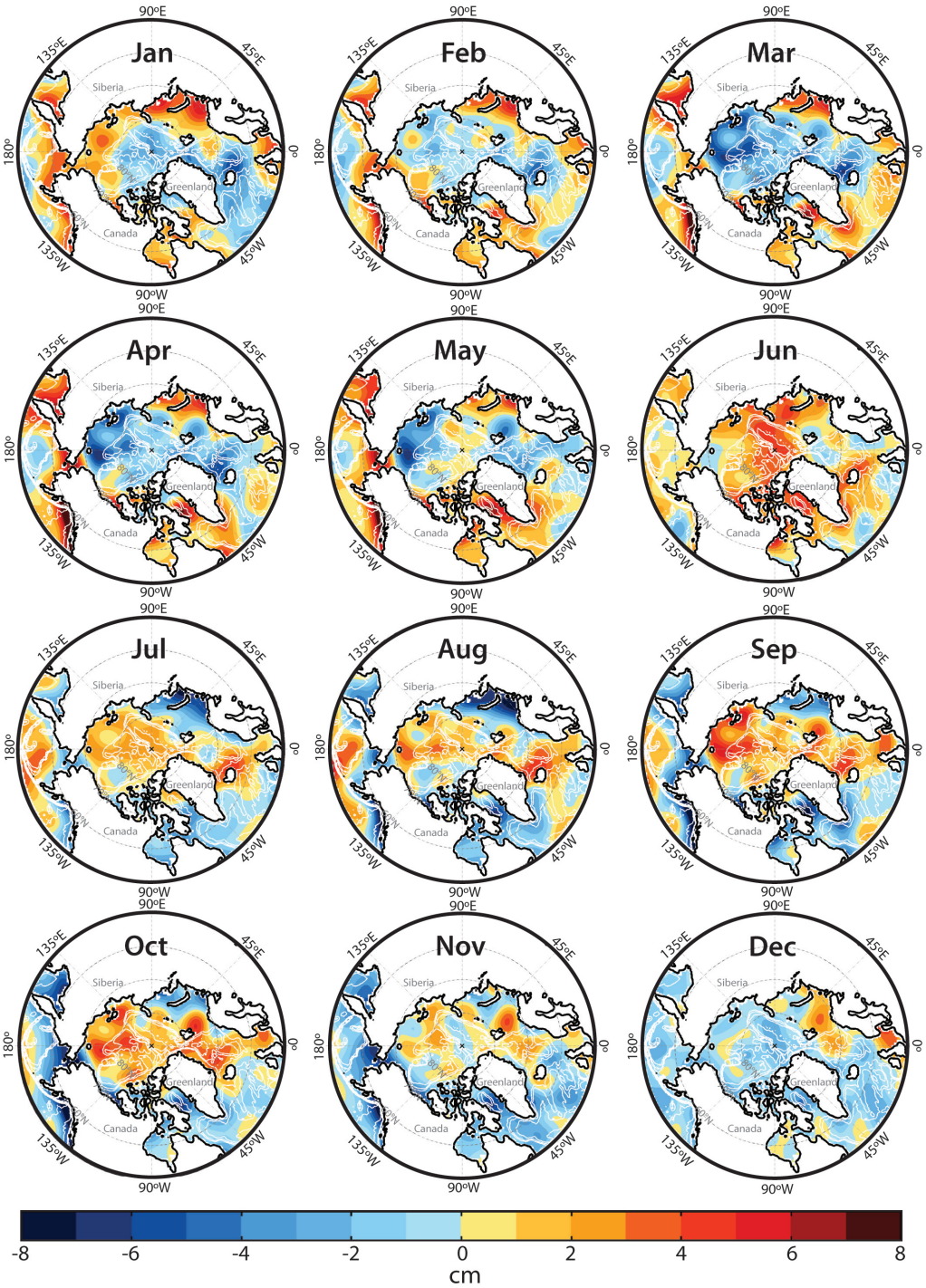

Figure 4.9: Monthly means of ocean bottom pressure from GRACE-300, processed as explained in the text.

Prior to inter-comparing GRACE OBP with the modeled OBP, the sea level pressure (SLP) averaged over the world oceans should be subtracted from the GRACE fields because this term is not included in the models ECCO2 and PIOMAS. This step was not performed in the study of the seasonal variations of OBP in the Arctic (*Peralta-Ferriz and Morison*, 2010). However, a comparison between the seasonal variation with and without this term suggests that the conclusions of *Peralta-Ferriz and Morison* (2010) are not substantially changed. Table 4.1 and Table 4.2 show that both models −ECCO2 and PIOMAS− are in good agreement with the observations from *in situ* records of OBP and SSH.

An additional step prior to comparing modeled OBP with GRACE consists of smoothing the modeled fields (OBP and SSH) with a Gaussian filter of 300 km radius[2]. Smoothing the fields with the Gaussian kernel decreases the rms variability of the PIOMAS-derived fields from $\sim$ 20 to 40%, but mainly near the coast of the Siberian shelves, particularly in the Chukchi and the East Siberian Sea, where the rms amplitude of the modeled and observed OBP and SSH anomalies are the largest (see Figure 4.10). The effects of the Gaussian-smoothing on the PIOMAS-derived SSH are also large along the South-Eastern coast of Greenland. The rms difference between smoothed and non-smoothed OBP and SSH from ECCO2 is slightly less than 1 cm over most of the Arctic Ocean. ECCO2 reproduces smaller rms variability in the Chukchi and East Siberian Seas than PIOMAS does. Overall, larger effects of the smoothing filter occur in regions of largest rms mass variability, e.g, East Siberian and Chukchi Seas. Thus, GRACE solutions are likely to underestimate by $20 - 40\%$ the OBP variations *in situ* in these shallow continental shelves, due to the smoothing filtering applied to the satellite data.

---

[2]Gaussian filter of the form $G(x,y) = \frac{1}{2\pi\sigma^2} e^{-\frac{x^2+y^2}{2\sigma^2}}$, where x and y are grid point positions, and σ is the standard deviation of the filter. Here $\sigma = 1$. The larger the σ is, the more smoothing or blur of the signal will be done.

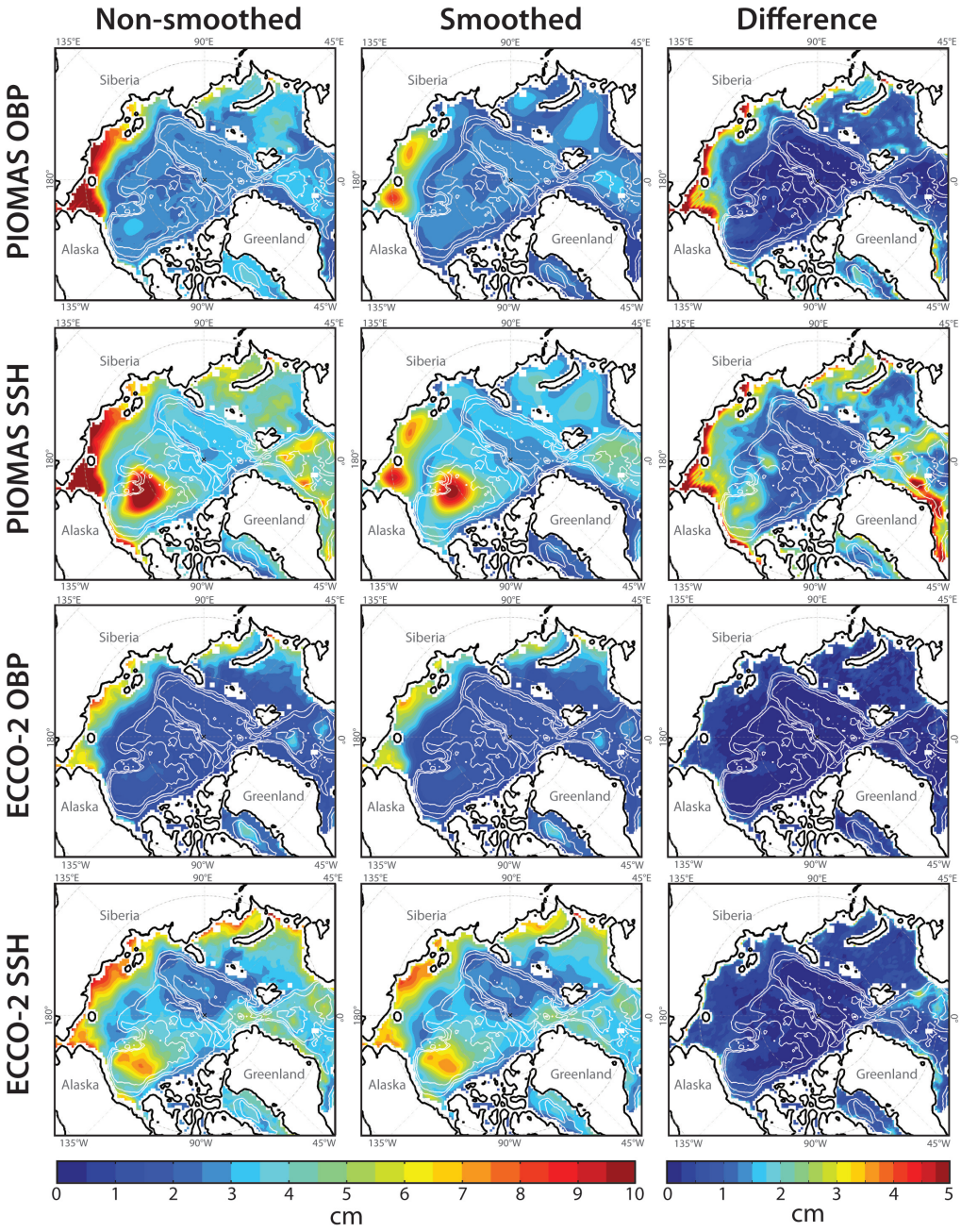

Figure 4.10: RMS variability of modeled OBP and SSH fields from Aug2002 to Dec2009 (with seasonal variation included) from PIOMAS (upper 2 rows) and from ECCO-2 (lower 2 rows) for the non-smoothed fields (left), smoothed with a Gaussian filter of 300 km radius (middle), and the RMS difference of the smoothed and non-smoothed field (right). White contours are the bathymetry, at 1000 m intervals.

The 300-km smoothed monthly OBP anomalies from PIOMAS and ECCO2 were then compared with GRACE-300 and with GRACE-500.

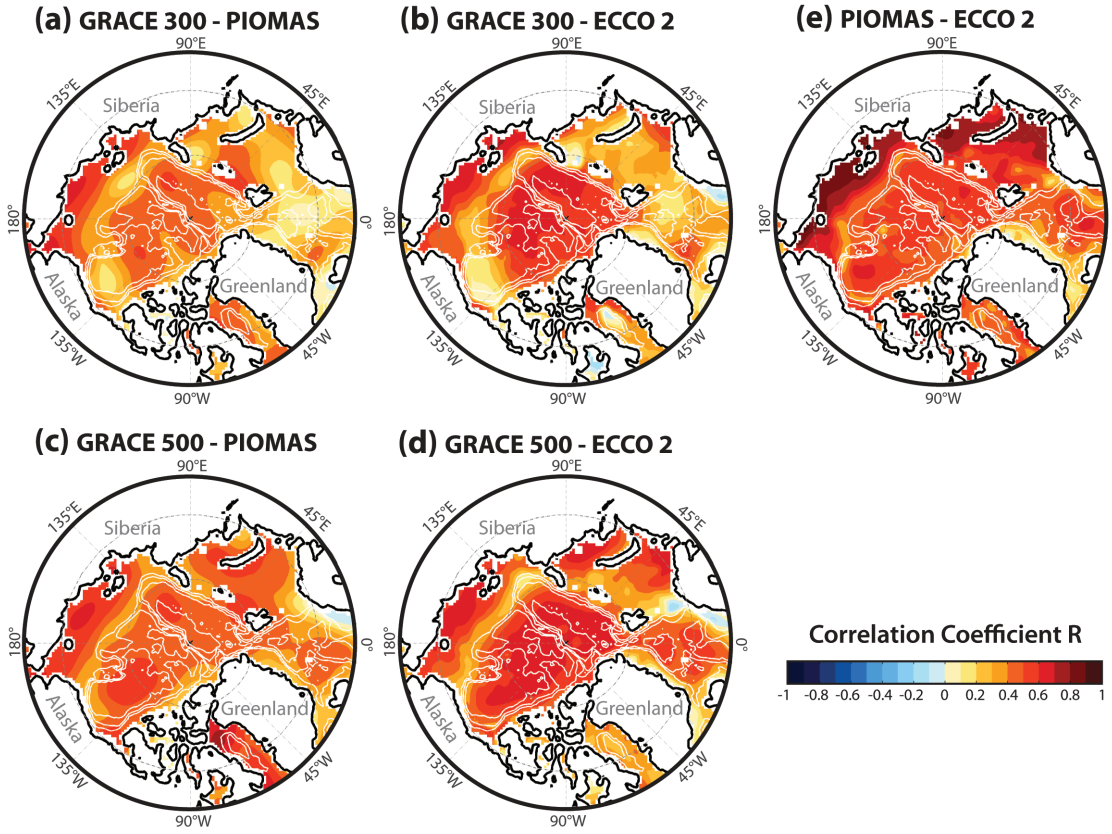

Figure 4.11: Correlation maps of GRACE-300 with equally smoothed (a) PIOMAS OBP and (b) ECCO-2 OBP, and GRACE-500 with (c) PIOMAS OBP and (d) ECCO-2 OBP. Correlation coefficient between PIOMAS OBP and ECCO-2 OBP is shown in (e). Correlations larger than 0.34 are significant above the 95% confidence level.

The GRACE-model inter-comparisons (Figure 4.11) are generally good, and greatly improved in most places, including the Kara and Barents Seas, compared to when the seasonal variation is included (not shown). This supports the hypothesis that the discrepancy between GRACE and *in situ* observations shown in a previous section,

might be due to leakage of the land mass signal into the GRACE solutions of the ocean seasonally, the seasonal time scale being that at which the hydrology signal is expected to have the largest change. The comparison between GRACE and the models is nearly identical, but in the Kara and Laptev seas, ECCO2 exhibits higher correlation with both GRACE-300 and GRACE-500 than PIOMAS does.

Low correlations between GRACE and the models are found along the Siberian shelf-breaks. The model to model correlation is generally significant and above 0.5, except also along the Siberian shelf-breaks. This might be a model problem commonly found in the shelf-break regions in the Arctic Ocean, associated with the advection of the Atlantic Water (e.g., *Holloway et al.*, 2007; *Hunke et al.*, 2008). When the seasonal variation from the models is removed, the model to model correlation is closer to 1 in all the Siberian shelves.

4.2.1 Modeling caveats affecting the representation of OBP field

In addition to the errors in simulating shelf-break dynamics, there are other potential sources of errors from the models that would affect the OBP field. Addressing the uncertainties of the models is beyond the scope of this dissertation, but three important sources of such model uncertainties are relevant:

- Volume-conserving instead of mass-conserving models

Like most of the ocean models, both PIOMAS and ECCO-2 use the Boussinesq approximation and conserve volume instead of mass. The main consequence of running a volume-conserving instead of a mass-conserving model is that the thermo-steric and halo-steric expansion and contraction of the water column (e.g., *Greatbatch*, 1994) are not accounted for by the model dynamics, even though these terms are included in the equation of state in the simulations. Thus, uncertainties may arise due to the inability to correctly represent the steric variations in sea surface height (i.e., Equation 2.6).

It is important to note, however, that apart from a globally uniform but time-varying correction applied to the models as suggested by *Greatbatch* (1994), the models do generally represent well steric SSH (assuming good grid resolution and forcing) (*Lombard et al.*, 2009). It follows that since this correction is spatially uniform, it does not lead to horizontal pressure gradients, and hence does not produce any dynamical effects on ocean motion. Consequently, the currents on the model are not affected by this correction. *Greatbatch* (1994) suggests that this correction needs to be included whenever *in situ* data is compared with model output of both OBP and SSH. This correction was applied in the ECCO-2 output of sea level (*A. Nguyen*, personal communication), and is therefore included in the computation of OBP. The correction was not applied to the PIOMAS output of sea level. This might be the reason why ECCO-2 generally shows slightly lower RMS difference with the *in situ* OBP and SSH data compared with PIOMAS (see Table 4.1 and Table 4.2). Overall, however, the correction is very small relative to the rms variability of observed SSH change in the Arctic (e.g., seasonal variation is $\sim$1 cm, *Mellor and Ezer*, 1995), and hence would not affect the interpretation of the mass distribution in this work.

Not only the correction to approach the Boussinesq solution to a non-Boussinesq result is small, but the fact that the models tend to represent the currents well regardless of not accounting for steric SSH, suggests that the models represent well the horizontal gradients in the density field, which through thermal wind relationship, would simulate well geostrophic currents (*Greatbatch*, 1994). Furthermore, based on *Bingham and Hughes* (2008), it would be expected that modeling errors regarding the representation of the steric sea level, would rather show up at multi-year to climate timescales. *Landerer et al.* (2009) used two models to simulated global ocean mass redistribution during the late 21st century, and showed that due to ocean's heat uptake from the atmosphere over time, and consequently thermal expansion in the

global ocean, the mass tends to increase in the shelves. The mass change is larger in the shelf regions (including the extensive Arctic Siberian shelves) relative to the global ocean, but the amount is still small (∼0.22 cm/yr over 100 years). In addition, altimetry-based SSH observations from yearly campaigns of ICESat (*Kwok and Morison*, 2011) are in good agreement with modeled SSH from both ECCO-2 and PIOMAS (not shown here). This suggests that despite of this source of uncertainty −corrected for or not−, the models reproduce well the SSH variations.

- Uncertainties in model estimates of freshwater fluxes: runoff

A common problem affecting ice-ocean models is that they do not simulate runoff-derived freshwater input into the Arctic. This is also the case for PIOMAS and ECCO-2. The models apply a correction to the salinity field by decreasing the salinity at most of the river mouths, but does not add volume of freshwater into the system. This is commonly known as virtual salt flux adjustment. In PIOMAS, this adjustment is based on monthly climatological values of runoff input into the ocean using values of runoff discharge from *Hibler and Bryan* (1987).

The salt flux adjustment to runoff in ECCO-2 is similar to that done in PIOMAS, except that ECCO-2 uses newer climatological values of monthly mean estuarine fluxes of freshwater, which are based on the Regional, Electronic, Hydrographic Data Net-work for the Arctic Region (R-ArcticNET) dataset (*Lammers et al.*, 2001). These values are further adjusted for underestimated freshwater fluxes by multiplying for a factor of 1.2 (*Nguyen et al.*, 2011). This adjustment helps the freshwater budget of the model to be closer to other estimates (e.g., *Serreze et al.*, 2006).

Aside of the use of climatological values to account for runoff in both ECCO-2 and PIOMAS −for which inter-annual variations of runoff and their effects cannot be resolved−, a common problem with ice ocean models in the Arctic Ocean is also the

insufficient communication between shallow shelf areas and the deep basins. A consequence of this is that the models tend to fail with properly dispersing the freshwater away from the coast.

- Uncertainties and biases in the atmospheric forcing re-analysis of the model

Two main differences between ECCO-2 and PIOMAS are the atmospheric forcing (JRA-25 and NCEP/NCAR reanalyses, respectively), and the representation of the surface fluxes. The uncertainty in precipitation is mainly due to insufficient observations in the Arctic. The estimate of the precipitation in the atmospheric forcing may present biases that affect the Arctic Ocean hydrography, as well as the flux exchanges between the Arctic and sub-Arctic Seas (*Gerdes et al.*, 2008). The sensitivity of other factors of the atmospheric re-analyses is an ongoing research topic. An additional challenge for identifying the sensitivity and uncertainties of most re-analysis datasets, including JRA-25 and NCEP/NCAR, is that these tend to perform better during specific seasons (e.g., *Holloway et al.*, 2007). The reason for such inconsistency remains unexplained.

Overall, consequences of all the aforementioned uncertainties in the model runs may be reflected only at the longer timescales of OBP and SSH variability, and thus, interpretation of the trends or multi-year circulation changes associated with the modeled OBP and SSH must be taken cautiously, as the origin of the trend in model outputs varies from model to model.

4.3 Spatial and temporal variations of Arctic OBP

In this section, the spatial and temporal variations of GRACE OBP are investigated using Empirical Orthogonal Function (EOF) analysis. First, the characteristics and the domain of the OBP field are described. Then the choice of GRACE-300 over

GRACE-500 for this analysis is discussed. Last, each of the leading significant modes and their associated physical processes and forcing mechanisms are explored.

The EOF analysis presented here was performed on the monthly record of GRACE-300 in the Arctic Ocean, from August 2002 to August 2011. The domain was delimited by the Bering Strait, Fram Strait and the Barents Sea path from South Svalbard to Norway along 15° E. The Canadian Archipelago channels were excluded. In order to focus on the month-to-month and inter-annual variations of Arctic OBP (of $\sim$ 4-year period), the seasonal signal shown in Figure 4.9 was removed. The 9-year linear trend of the data has been shown to be small (Figure 4.1) and was also removed from the datasets prior to the EOF decomposition. Thus, it is important to keep in mind that these modes of variability are anomalies relative to the overall mean field, long term trend, and seasonal variability. The multi-year variations within the 9-year record will be addressed in a later section.

The results of the EOF analysis performed on GRACE-500 (not shown) are nearly identical to the EOF patterns obtained from GRACE-300. This suggests that the modes of variability are robust, and that the potential effects due to de-striping the solutions of GRACE-300 appear not to affect the EOF analysis. Since the GRACE-300 correlations with *in situ* data are overall similar to the GRACE-500 correlations (see Table 4.2), and GRACE-300 has slightly higher spatial resolution, GRACE-300 was selected over GRACE-500 dataset to investigate the physical mechanisms that may be associated with the modes of OBP variability.

The EOF decomposition of the GRACE-300 -derived ocean bottom pressure field reveals three significant modes (see Figure 4.12), and these are well separated according to the criterion of *North et al.* (1982). The first mode explains 49% of the total variance and reveals a basin-coherent variation in mass. The second mode explains 19% of the variance and is characterized by a dipole of mass between the Siberian

continental shelves and the Central Arctic Ocean. The third mode explains 9% of the variance and shows a dipole of mass change between the eastern (i.e., Barents and Kara Seas) and the western (i.e., East Siberian and Chukchi Seas) Arctic shelves (Figure 4.13).

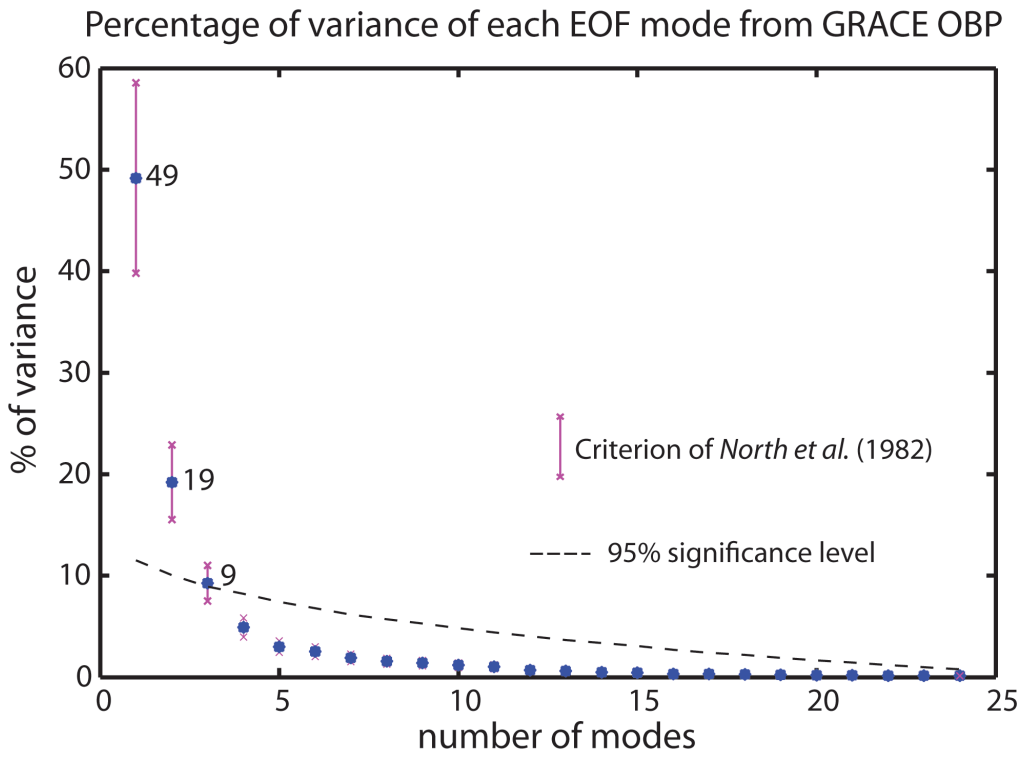

Figure 4.12: Percentage of variance explained by the resulting EOF modes using singular value decomposition. Blue dots locate each mode. Pink error bars are the confidence intervals for modal separation, estimated as in *North et al.* (1982). The black dashed line corresponds to the 95% level of confidence, estimated with a monte-carlo simulation on random data.

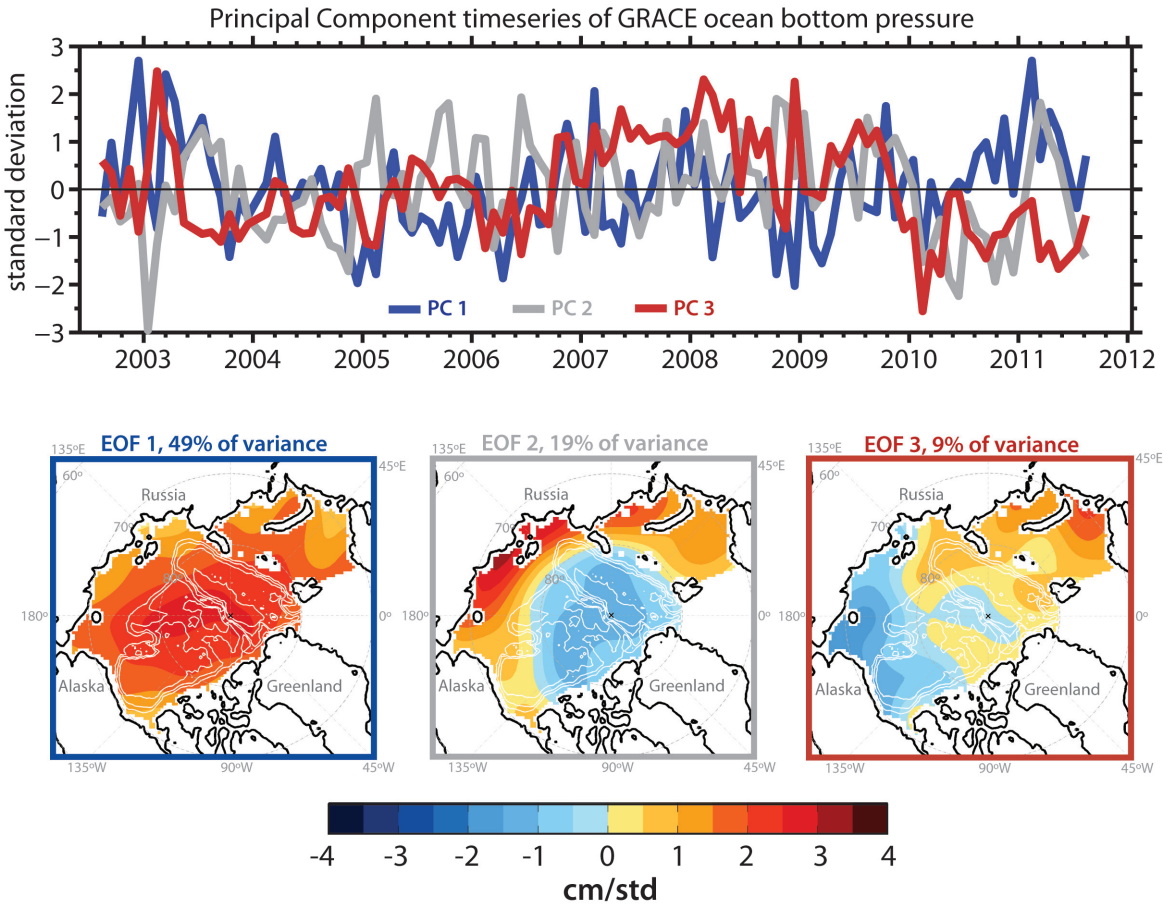

Figure 4.13: On the top are the principal component (PC) time series of the leading EOF modes of GRACE-300 OBP with the mean seasonal variation and the long term trend removed. On the bottom are the regression maps of each of the modes projected on their corresponding PC time series.

4.3.1 Mode 1: a basin-wide Arctic mass oscillation

EOF 1 reveals a basin-coherent mass change, with stronger center of action in the Central basin (Figure 4.15, top). The cross-correlation of PC1 and the *in situ* OBP at the North Pole (R = 0.67, significant above 95% C.I.) is shown in Figure 4.14. For consistency with GRACE-PC1, the seasonal variation of the *in situ* OBP at the North

Pole has also been removed. The cross-correlation supports our sense that GRACE is capturing real signals of mass change in the Arctic Ocean.

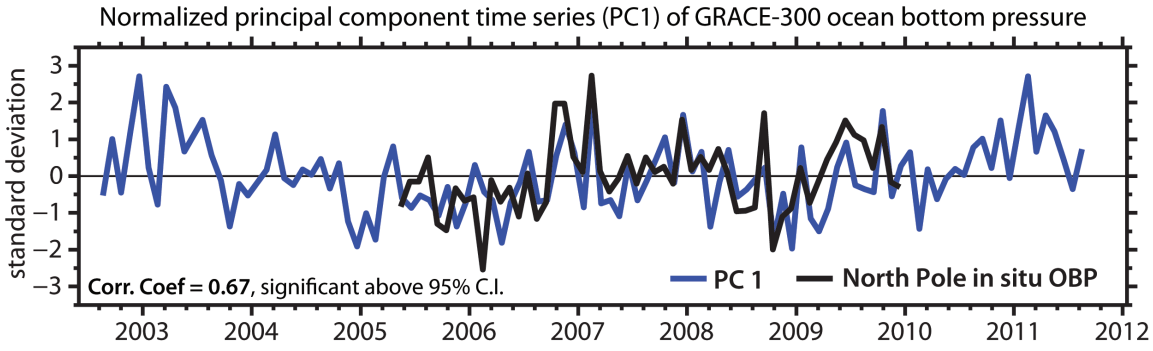

Figure 4.14: Normalized principal component time series of mode 1 (PC1) in blue, and the normalized *in situ* OBP record from the North Pole in black, with cross-validation (R=0.67).

The atmospheric forcing associated with this mass change is investigated by using monthly averages of the NCEP/NCAR sea level pressure (SLP) and surface winds at 925 hPa, north of 30°N, from August 2002 to August 2011. For consistency with GRACE, the seasonal variation and the long term trend have been removed from the SLP and wind fields. The non-seasonal SLP and wind fields were then projected on the principal component time series of the mode 1 (PC1). The resulting regression maps (Figure 4.15) suggest that the Arctic OBP change of this mode is not forced locally, and is strongly related to large-scale changes in atmospheric circulation over the North Atlantic and Nordic Seas, likely associated with the strengthening of the westerly winds over the North Atlantic. The SLP pattern consists of a high pressure anomaly over Scandinavia, and a low pressure anomaly over the North Atlantic centered around 50°N (Figure 4.15, upper right). The wind anomaly associated with PC1 (Figure 4.15, upper left) is consistent with the SLP pattern and shows predominantly southeasterly

winds aligned from Scotland to Iceland and a strong northward component through the Nordic Seas into the Arctic. Additional forcing into the Arctic basin is shown on the Pacific Ocean side, characterized by a prevailing northward component of the winds through Bering Strait.

We can learn about the variations in seasonal behavior by examining the PC time series for their characteristics during cold months (DJFMA) and warm months (JJAS). The mean seasonal variation has been removed from all the fields prior to the EOF analysis. Thus, the regression maps that result from projecting the OBP or SSH fields upon the PC time series for the specific months highlight the modal variability relative to the total mean and annual variation of the fields. This separation also reveals whether a particular mode tends to be dominated by winter or summer dynamics, or if the processes are persistent throughout the year.

The regression maps of the SLP and wind fields, projected upon GRACE-PC1 during winter-only months (DJFMA) and summer-only months (JJAS) suggests that the atmospheric forcing associated with mode 1 is predominantly a winter mode (Figure 4.15). The SLP and wind anomaly fields have a very weak relationship with GRACE-mode 1 during the summer (Figure 4.15, bottom).

The wind pattern associated with the EOF mode 1 is consistent with enhancement of northward transport through Fram and Bering straits, likely through a geostrophically enhanced slope current. These are driven by high-pressure cells over Scandinavia and to a weaker extent Alaska.

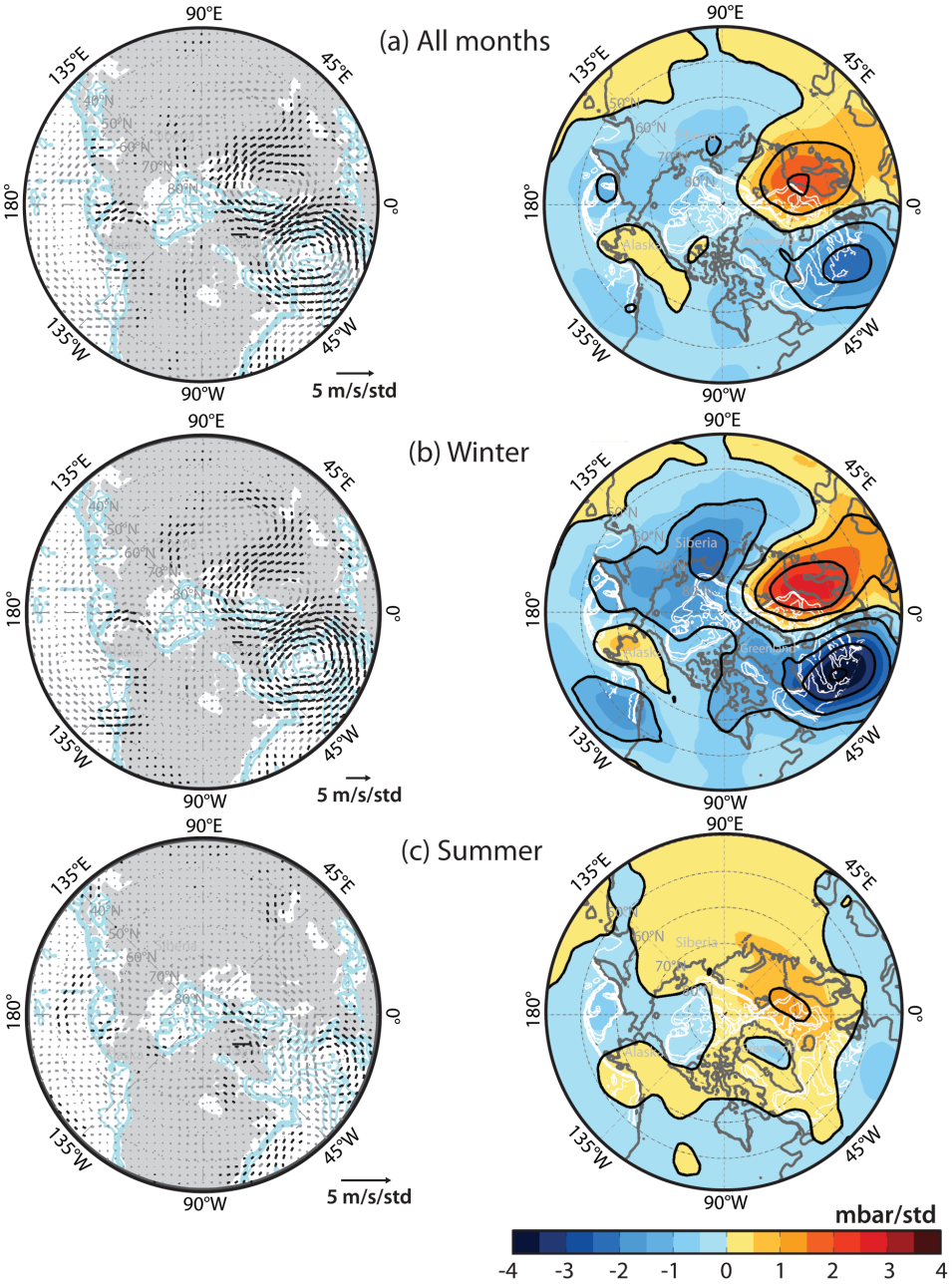

Figure 4.15: (a) Regression maps of NCEP/NCAR 925 hPa winds (left) and SLP (right) projected on GRACE-PC1. Gray arrows show all wind patterns and black arrows are significant above 95% C.I. Blue and white contours are the bathymetry with 1000-m isobath intervals. Black contour lines are the SLP in 1 mbar/std intervals. (b) Same as (a) but during winter months only (DJFMA). (c) Same as (a) and (b), but for the summer months (JJAS).

The pattern of EOF 1 is a broad time scale phenomenon similar to the sub-monthly wintertime variation described by *Peralta-Ferriz et al.* (2011, see their figure 3, also shown in Appendix A). It is also similar to the basin-coherent mode of variability in Arctic OBP identified by *Hughes and Stepanov* (2004), for sub-annual timescales (i.e., their monthly data were high-pass filtered with a cutoff of 9 months). The atmospheric pattern most highly correlated with the Arctic OBP variations of *Hughes and Stepanov* (2004) also reveal a high SLP in Scandinavia, but with no associated low SLP at mid-latitudes. Thus, it could be argued that the main forcing mechanism that increases the Arctic mass is due to the northward component of the wind that results from the high SLP anomaly near Scandinavia, likely through a slope current, and to a lesser extent, due to the direct effect of the meridional pressure gradient of Figure 4.15 (top). This SLP pattern could create northward Sverdrup transport associated with the strong positive atmospheric vorticity produced by the low SLP centered in the North Atlantic $\sim$ 50°N. This forcing might be related to the one described by *Morison* (1991), who associated the seasonal variability of the West Spitsbergen current with positive anomaly of wind stress curl.

If mass converged in the Arctic, a corresponding drop of mass at mid-latitudes might be expected in order to conserve total ocean mass. The regression map of the GRACE OBP field in the northern hemisphere (north of $30°N$) projected upon the PC1 time series illustrates this process (Figure 4.16). In this figure, increasing PC1 is reflected by the Arctic OBP basin-wide, and a drop of mass in the North Atlantic and North Pacific. These signals of decreasing mass are of low amplitude, but expand over an area wider than the Arctic Ocean. Figure 4.16 also shows that the projection for all months is dominated by the GRACE pattern during the winter. The ocean mass response, together with the identified atmospheric forcing, shows that the energy in this mode is only significant during the winter.

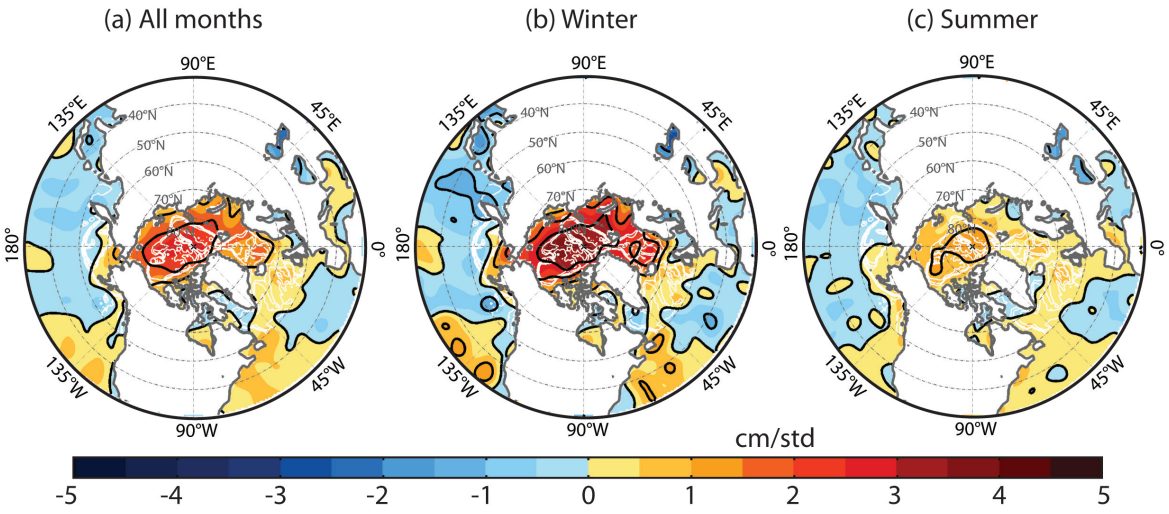

Figure 4.16: GRACE-300 OBP above 30° N regressed upon GRACE PC1 for all (left), winter (middle) and summer (right) months. White contours are bathymetry with 1000-m isobath intervals.

The OBP and SSH from the ECCO2 and PIOMAS models are used to investigate the ocean processes in the Arctic Basin associated with this mode. To do this, the modeled OBP and SSH fields, with their corresponding seasonal variation and long term trend removed, were projected on the time series PC1. Since the modeling output ends in December 2009, the regression maps of modeled OBP and SSH, and the corresponding wind field in the same figures, are projected on the PC1 from August 2002 to December 2009 only. Generally, however, these regression maps are in good agreement with the regression maps that span through August 2011 of Figure 4.15. The regression maps of PIOMAS-derived OBP and SSH are shown in Figure 4.17, and the regression maps of ECCO2-derived OBP and SSH are shown in Figure 4.18. The contributions of summer and winter on the total OBP and SSH change are also included in these figures.

PIOMAS and ECCO-2 -derived OBP changes are in agreement with each other

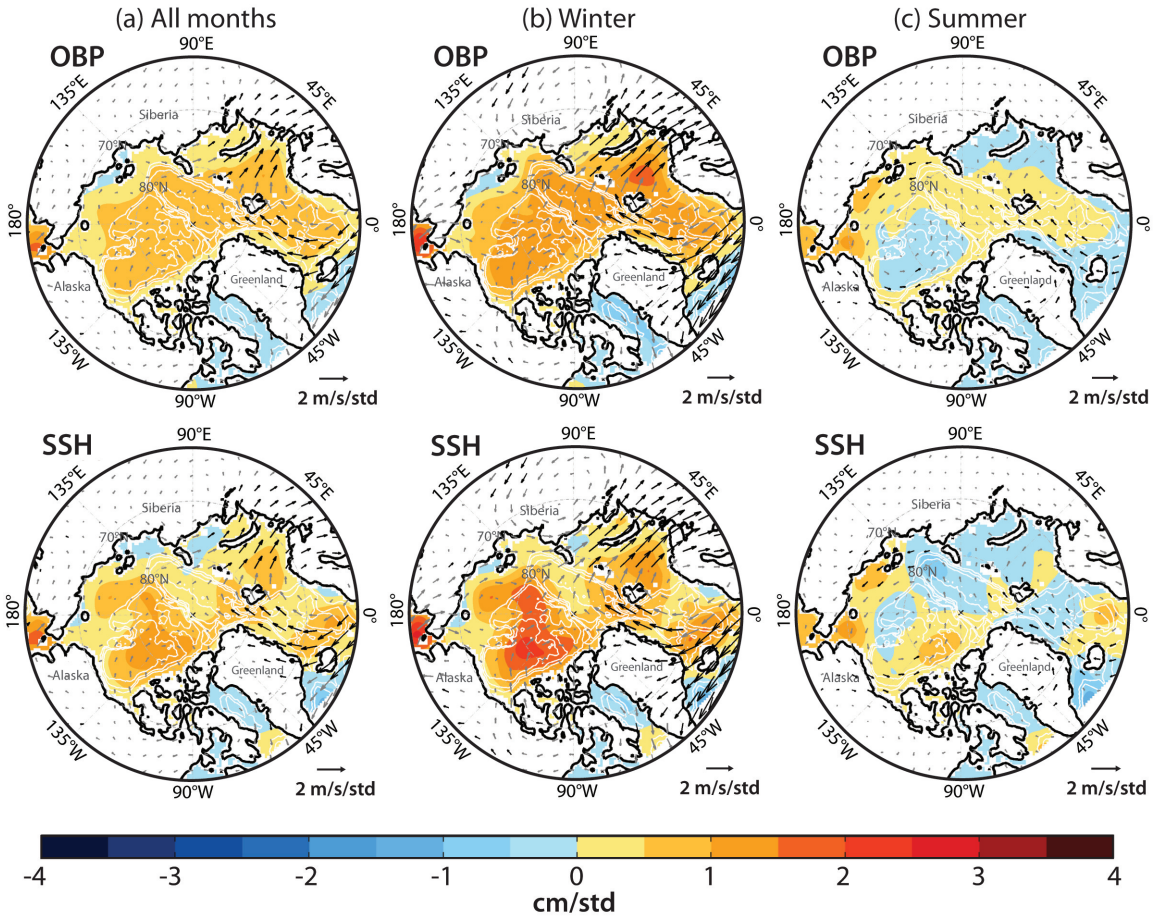

Figure 4.17: Non-seasonal and detrended PIOMAS-modeled OBP (top), SSH (bottom), and 925 hPa NCEP/NCAR winds projected on PC1 for all months (left), during the cold months (middle) and during the warm months (right), from August 2002 to December 2009. Black arrows highlight the wind patterns that are significant above the 95% confidence level. White line contours show the bathymetry with 1000-m isobath intervals

and with GRACE: The models show an increase in OBP basin-wide during positive PC1 when all months are included, with a relatively weaker response near the coast of the Siberian shelves. The model OBP and SSH responses are consistent with GRACE in which the observed basin-wide OBP change associated with mode 1 is dominated

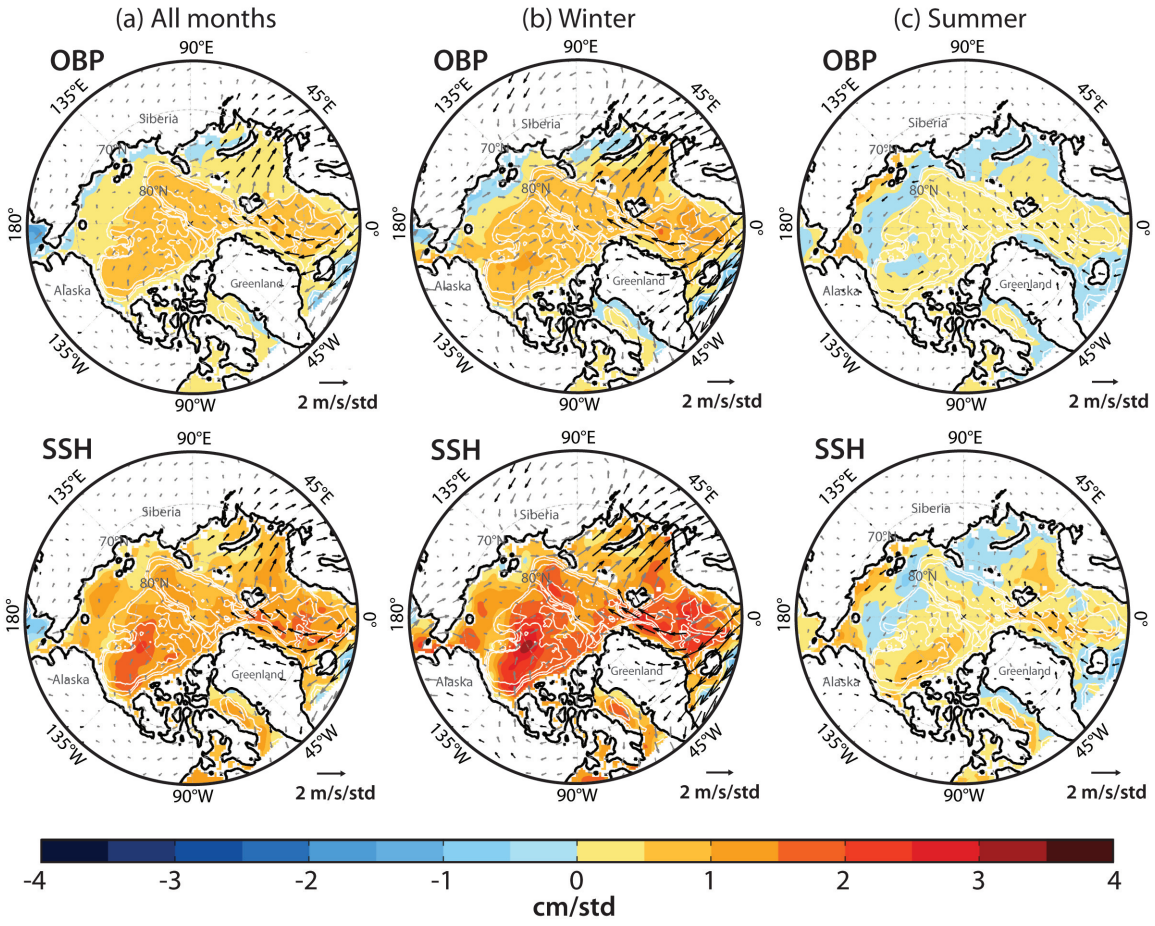

Figure 4.18: Non-seasonal and detrended ECCO2-modeled OBP (top), SSH (bottom), and 925 hPa NCEP/NCAR winds projected on PC1 for all months (left), during the cold months (middle) and during the warm months (right), from August 2002 to December 2009. Black arrows highlight the wind patterns that are significant above the 95% confidence level. White line contours show the bathymetry with 1000-m isobath intervals

by winter dynamics. For most of the Arctic Ocean during the winter, the modeled SSH increase is partially compensated through baroclinic adjustment in the Canada Basin, suggesting that this mode is of baroclinic character in the basin (deep regions), and predominantly barotropic elsewhere.

The wind forcing of the modeled OBP and SSH changes associated with mode 1 (Figure 4.17 and Figure 4.18) are similar to the observed mode 1 forcing (Figure 4.15). During the winter months, over the Nordic Seas, the strongest winds associated with PC1 are characterized by southerly winds through Fram Strait.

During the summer months, the winds are weakly associated with PC1. They show, however, cyclonic circulation along the Siberian shelves, which likely increases the coastal SSH through surface Ekman transport. This pattern of the atmospheric circulation may explain why during the summers, the modeled OBP and SSH tend to pile water up into the Arctic western shelves. Summer months observe weak downwelling-favorable winds in the southern Beaufort Sea.

Overall, GRACE mode 1 is a winter-dominated basin-coherent mass increase in the Arctic forced by high-pressure over Scandinavia and the Nordic Seas that in its positive phase forces northward winds and a geostrophic slope current through Fram Strait, and to a lesser extent, by the SLP gradient (high in Alaska and low over Russia) that generate northward winds and a geostrophic slope current through Bering Strait. The models are in agreement with GRACE, and are also consistent with each other in the basin-OBP increase.

4.3.2 Mode 2: Mass change on the Siberian shelves

The second mode of OBP variability in its positive phase consists of increasing mass along the Siberian Shelves, and decreasing mass in the Central Arctic (Figure 4.13). The spatial pattern of this mode is similar to that of the positive Arctic Oscillation (AO) (*Thompson and Wallace*, 1998), and the AO index is significantly correlated with the PC2 time series of GRACE OBP (Figure 4.19). The positive phase of the AO is characterized by an anomalously low surface atmospheric pressure centered in the Nordic Seas and eastern longitudes of the Central Arctic Ocean (see Figure 1.2). This

pattern enhances a general cyclonic atmospheric circulation, which tends to offset the Beaufort High, and advance more saline Atlantic Water further into the Arctic Ocean (*Morison et al.*, 2000, 2012).

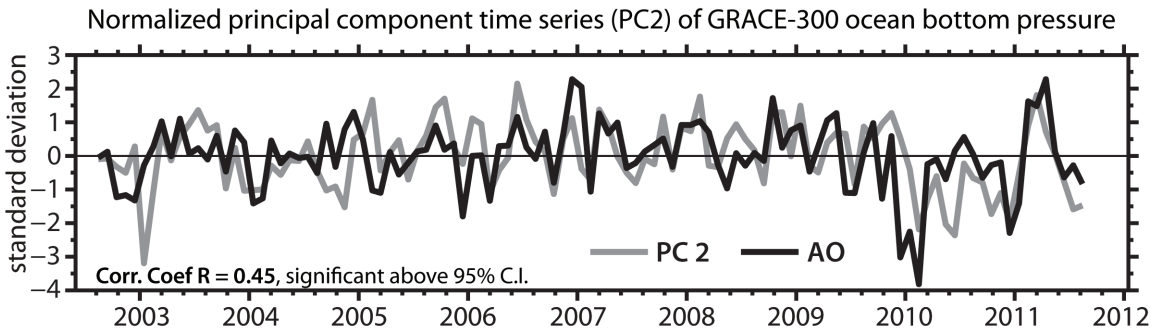

Figure 4.19: Normalized time series PC2 (gray) and Arctic Oscillation index (black).

Similar to mode 1, the atmospheric forcing associated with the mode 2 is investigated by projecting the SLP and wind anomaly fields on the PC2 (Figure 4.20). The resulting regression maps are consistent with anomalously low SLP, which resembles the pattern of the positive phase of the AO index (e.g., Figure 1.2). The regression map of the wind field projected on PC2 suggests that the mass change in the Siberian shelves of GRACE mode 2 is due to surface Ekman transport: the alongshore cyclonic winds along the Siberian shelves pile the water up to the right from the Barents Sea eastward to the Chukchi Sea, which in turn forces an eastward along-coast flow similar to that which modifies the trajectory of Eurasian runoff at multi-year timescales (*Morison et al.*, 2012).

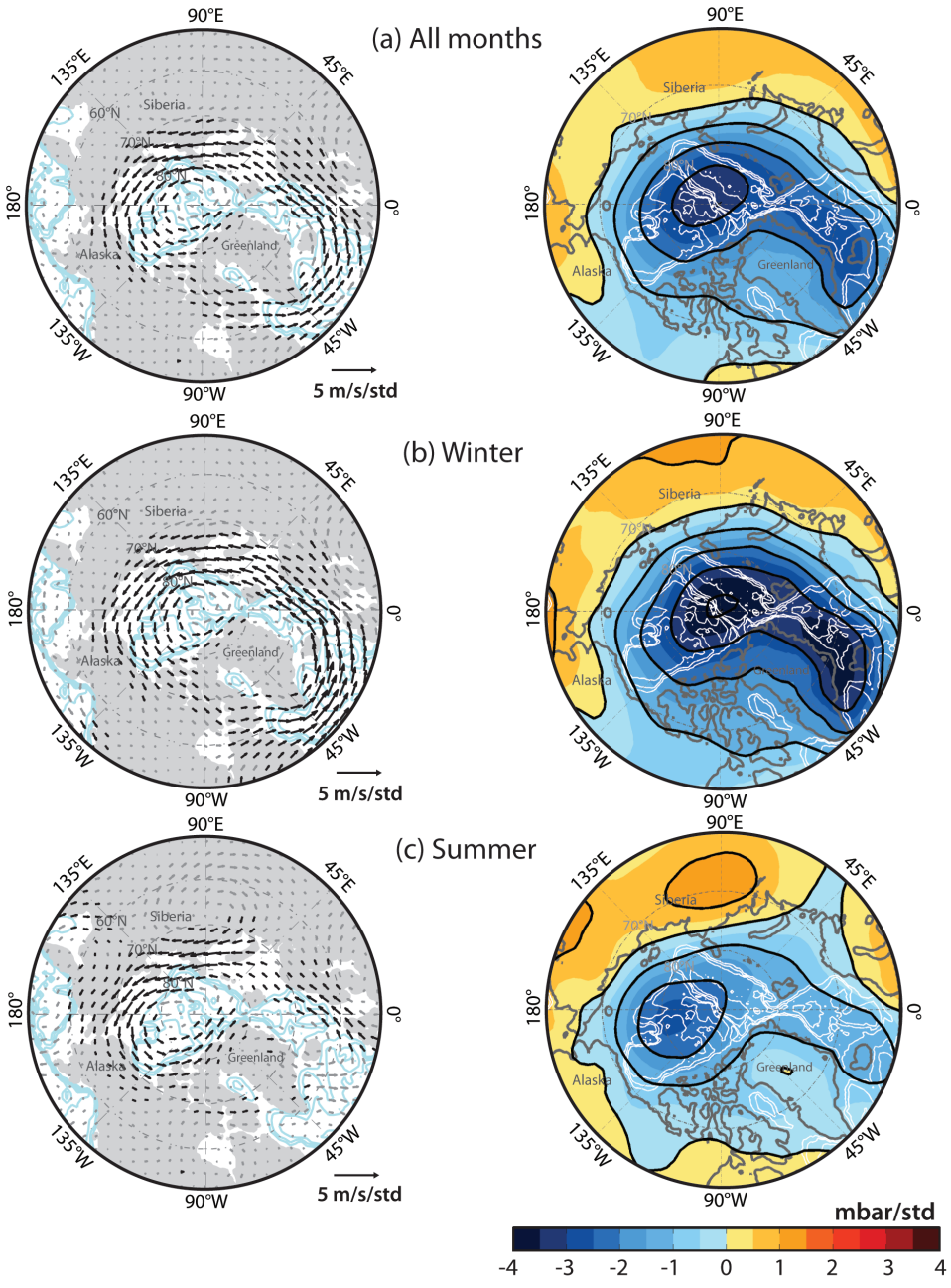

Figure 4.20: (a) Regression maps of NCEP/NCAR 925 hPa winds (left) and SLP (right) projected on GRACE-PC2. Gray arrows show all wind patterns and black arrows are significant above 95% C.I. Blue and white contours are the bathymetry with 1000-m isobath intervals. Black contour lines are the SLP in 1 mbar/std intervals. (b) Same as (a) but during winter months only (DJFMA). (c) Same as (a) and (b), but for the summer months (JJAS).

Figure 4.20 shows that the atmospheric circulation associated with PC2 is important throughout the year. Over the Western Arctic, the SLP and wind patterns are nearly identical during the summer and the winter. During the summer months, however, the SLP and wind pattern is weaker in the region near the Nordic Seas and in the Barents Sea. In addition to the difference in strength, the center of action of the SLP pattern during the summer is shifted towards the Western Central Arctic (e.g., over the Makarov Basin), compared to the SLP in the winter that has a double center of action, one near the North Pole in the Eurasian Basin and the other in the Western Nordic Seas.

The atmospheric circulation associated with GRACE mode 2, suggests that the corresponding ocean response follows surface Ekman dynamics. The modeled OBP and SSH are used to further explore this idea. The regression maps between modeled OBP and SSH, projected on PC2 reveal an increase in OBP that is equivalent to the increase in SSH, along all the Siberian shelves from the Barents to the Chukchi Seas. Both models reveal the SSH and OBP increase in the Siberian shelves under positive PC2, which resembles the pattern of the EOF 2 in Figure 4.13. Note that this GRACE-model agreement occurs regardless of the low correlation obtained between GRACE and *in situ* data in the Kara and Barents Sea (Table 4.2), and between GRACE and each of the models (Figure 4.11), suggesting that even if the GRACE solutions of OBP in the Kara and Barents seas were contaminated with leakage from land, GRACE is still observing real signals of ocean mass change there.

The weaker GRACE mode 2 during the summer is also captured by the models (Figures 4.21 and 4.22). The modeled SSH change in the Barents and Kara Seas is smaller during the summer, compared to the SSH change in the same region during the winter. However, a strong correspondence between cold and warm months prevails in the Chukchi and East Siberian Seas, suggesting that in these region, the atmospheric

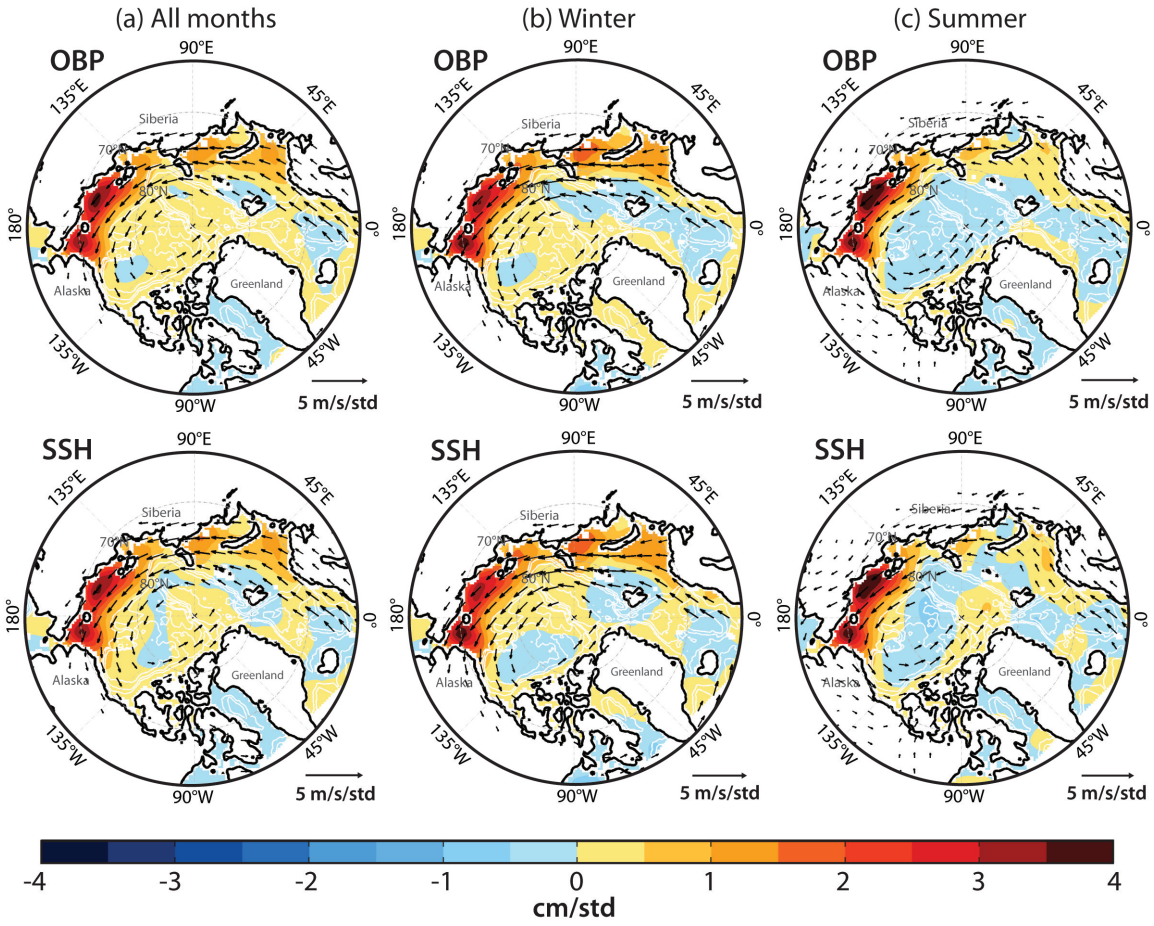

Figure 4.21: Non-seasonal and detrended PIOMAS-modeled OBP (top), SSH (bottom), and 925 hPa NCEP/NCAR winds projected on PC2 for all months (left), during the cold months (middle) and during the warm months (right), from August 2002 to December 2009. Black arrows highlight the wind patterns that are significant above the 95% confidence level. White line contours show the bathymetry with 1000-m isobath intervals

forcing associated with PC2 is nearly equally important throughout the year. A closer look to the ocean response from ECCO2 during the summer months (Figure 4.22) may indicate that the SSH and OBP change in the Chukchi and East Siberian Seas are slightly larger in the summer than in the winter, regardless of the similar strength

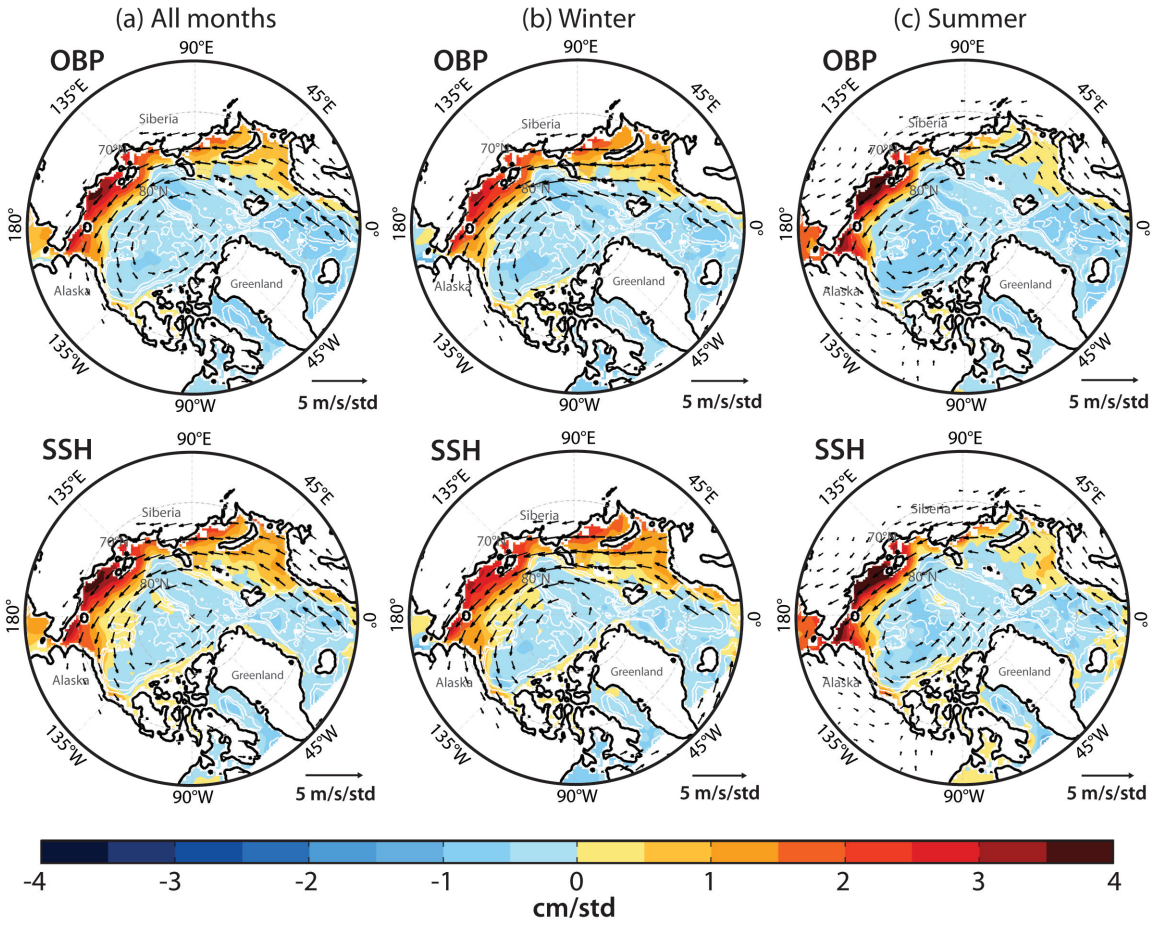

Figure 4.22: Non-seasonal and detrended ECCO2-modeled OBP (top), SSH (bottom), and 925 hPa NCEP/NCAR winds projected on PC2 for all months (left), during the cold months (middle) and during the warm months (right), from August 2002 to December 2009. Black arrows highlight the wind patterns that are significant above the 95% confidence level. White line contours show the bathymetry with 1000-m isobath intervals

of the winds there between the seasons. It could be speculated that the lack of sea-ice during the summer allows a stronger response to the atmospheric forcing there. Note that no significant change in OBP or SSH −associated with PC 2− occurs in the Central basin.

Furthermore, the change in OBP is of the same amplitude as the change in SSH for the respective models, regardless of the season. This correspondence suggests that the ocean response associated with this mode is essentially of barotropic character (i.e., SSH response = OBP response).

4.3.3 Mode 3: Mass change dipole eastern vs western Eurasian Arctic shelves

The EOF mode 3 (Figure 4.13) reveals a sea-saw of mass change between the 'Western' Arctic (i.e., Beaufort, Chukchi, and East Siberian seas) and the 'Eastern' Arctic shelves (i.e., Kara and Barents Seas). This mode explains 9% of the total variance of the GRACE field. In contrast with PC1 and PC2, the principal component time series of the mode 3 (PC3) contains a distinct low-frequency variation (Figure 4.23).

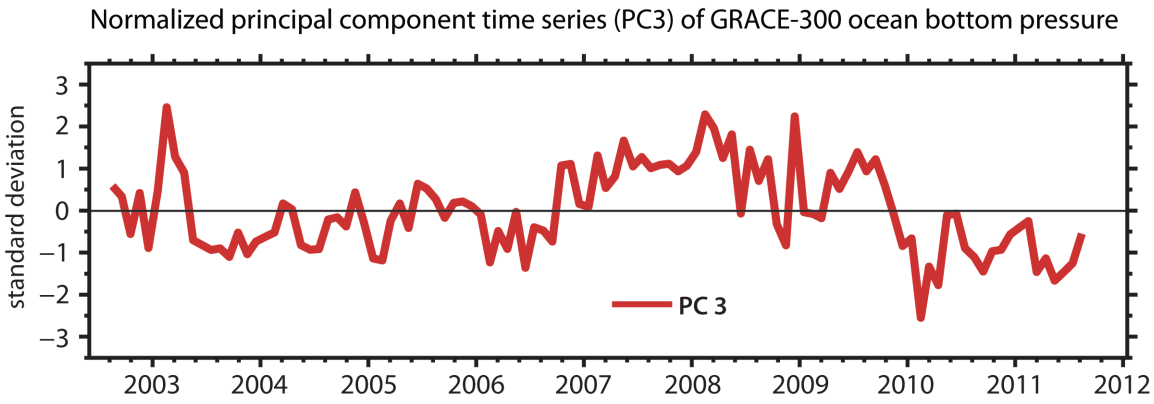

Figure 4.23: Normalized principal component time series of the EOF mode 3 (PC3) from the non-seasonal detrended GRACE-300 dataset.

The SLP and wind anomaly fields regressed on PC3 are shown in Figure 4.24. Generally, mode 3 is associated with the strengthening of the anticyclonic Beaufort Gyre, which is consistent with anomalously high SLP. The increase in SLP in the Beaufort Sea is accompanied by a weaker but low SLP in the 'Eastern' Arctic.

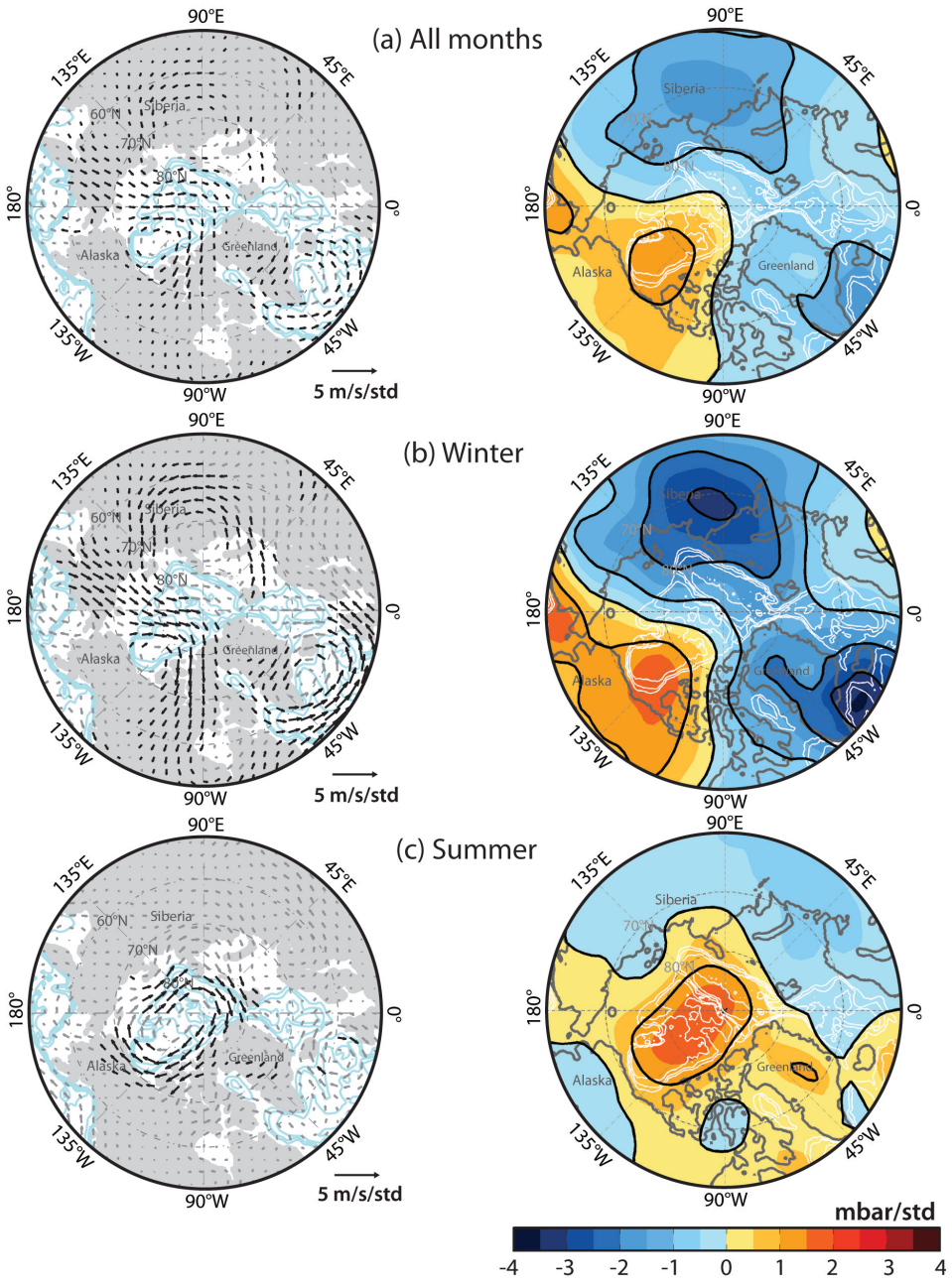

Figure 4.24: (a) Regression maps of winds (left) and SLP (right) projected on GRACE-PC3. Gray arrows show all wind pattern and black arrows highlight the winds that are significant above 95% C.I. Blue and white contours are the bathymetry with 1000-m isobath intervals. Black contour lines are the SLP in 1 mbar/std intervals. (b) Same as (a) but during winter months only (DJFMA). (c) Same as (a) and (b), but for the summer months (JJAS).

In contrast with the spatial patterns of SLP and wind field associated with PC1 and PC2, the spatial patterns associated with PC3 are very different during the winter and the summer (Figure 4.24, middle and bottom panels). This could be due to low stability of EOF patterns of higher order modes. While mode 3 proved significant, it only explains 9% of the variance, so interpretation of this pattern should be done conservatively.

The origin of the dipole in atmospheric pattern comes from the winter months, when a strong negative anomaly in SLP over the 'Eastern' Arctic is associated with PC3. During the summer months, the atmospheric pattern associated with PC3 is characterized by a larger scale anticyclonic circulation, which encompasses all the 'Western' Arctic. This pattern contributes to the high SLP centered in the Beaufort Sea, but offsets the anomalously low SLP in 'Eastern' Arctic (see Figure 4.24).

The relationship between winds and modeled fields of OBP and SSH, with PC3 is, like the atmospheric patterns, different during winter months and summer months (Figure 4.24).

During the winter, The projections of the modeled OBP and SSH on PC3 (Figures 4.25 and 4.26) reveal a wind pattern offshore from the East Siberian Sea that becomes anticyclonic over the Beaufort Sea. This wind pattern appears to be associated with increased SSH in the Canada and Makarov basins, along with reduced OBP and SSH from the Chukchi and East Siberian Seas. Thus, surface Ekman convergence over the Beaufort Sea pulls water off the coast of the East Siberian and Chukchi Seas. Additionally, non-geostrophic mechanisms may play a significant role to vector the water away from the coast of the East Siberian Sea, nearly in the direction of the wind. This is not surprising given that these shelves are on average very shallow (e.g, $<$50 m).

Because PC3 has a rather low-frequency variation, baroclinic adjustment in the

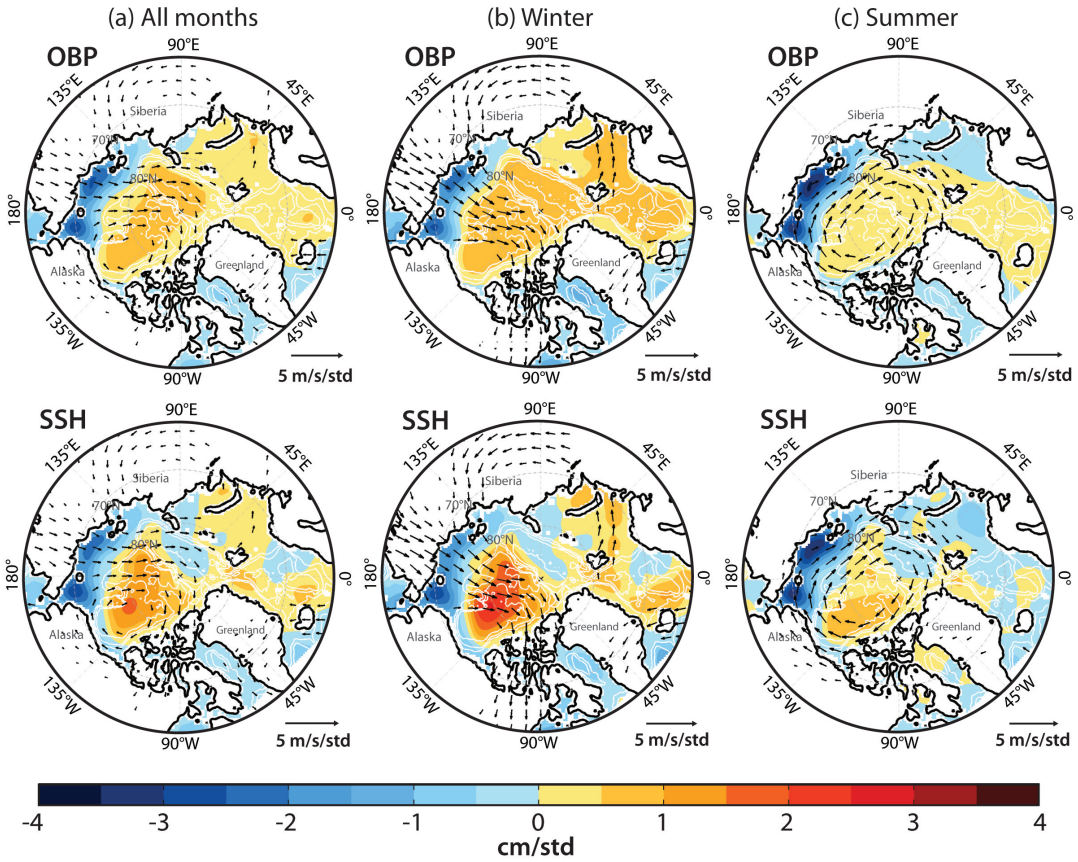

Figure 4.25: Non-seasonal and detrended PIOMAS-modeled OBP (top), SSH (bottom), and NCEP/NCAR winds projected on PC3 for all months (left), during the cold months (middle) and during the warm months (right), from August 2002 to December 2009. Black arrows highlight the wind patterns that are significant above the 95% of confidence level. White line contours show the bathymetry with 1000-m isobath intervals

deep basin may occur. Baroclinic adjustment is likely the reason why the models reflect a change in OBP (i.e., $\sim 0.5-1$ cm/std) weaker than the change in SSH (i.e., $\sim 2.5-3$ cm/std) in the Canada and Makarov basins (see Figures 4.25 and 4.26), supporting the results of *Vinogradova et al.* (2007), *Bingham and Hughes* (2008) and *Morison et al.* (2012). In contrast, the modeled OBP and SSH changes are of

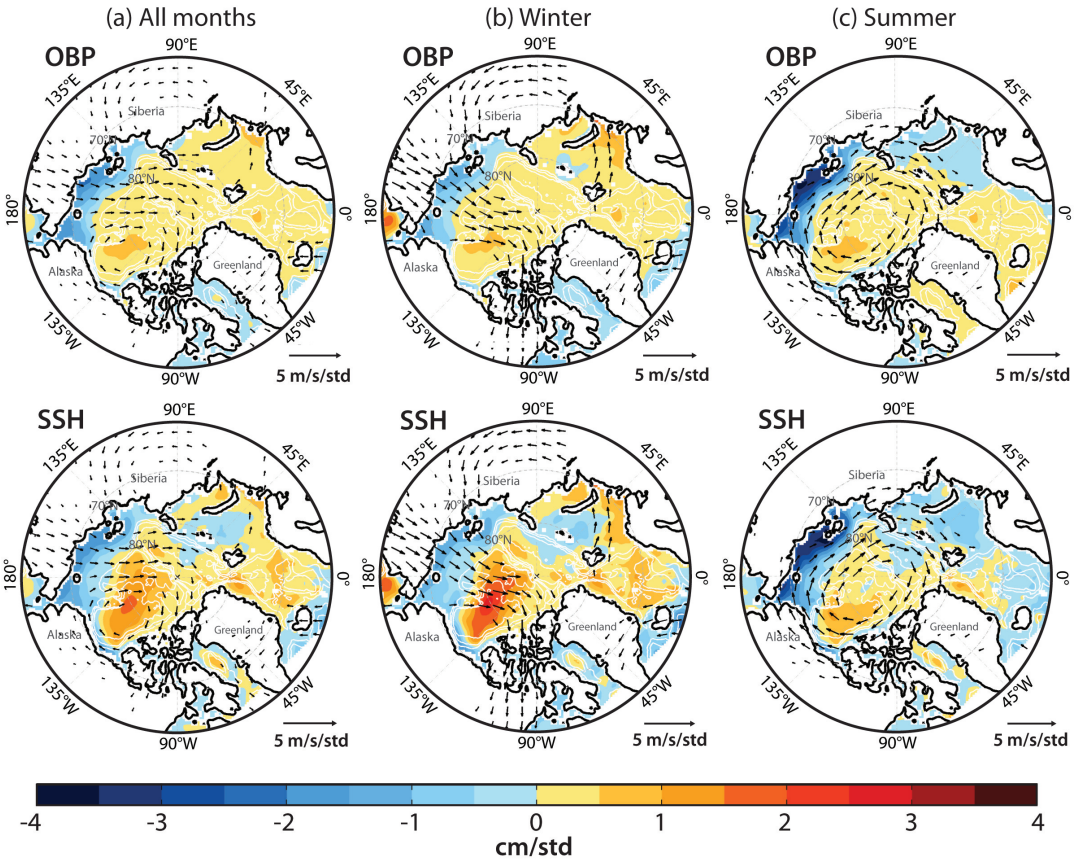

Figure 4.26: Non-seasonal and detrended ECCO2-modeled OBP (top), SSH (bottom), and NCEP/NCAR winds projected on PC3 for all months (left), during the cold months (middle) and during the warm months (right), from August 2002 to December 2009. Black arrows highlight the wind patterns that are significant above the 95% of confidence level. White line contours show the bathymetry with 1000-m isobath intervals

comparable magnitude in the shelves (Figures 4.25 and 4.26). This result also confirms the modeling results of *Bingham and Hughes* (2008), that for shallow depths (e.g., 'Western' Arctic shelves), the ocean response tends to be more barotropic.

Also, during the winter, southwesterly winds from the Nordic Seas tend to blow into the Barents Seas, associated with a slight increase in OBP and SSH in both

Barents and Kara Seas. Thus, the observed OBP increase of GRACE-mode 3 over the Kara and Barents Seas (Figure 4.13) reveals also a predominantly barotropic behavior. According to the models, the OBP and SSH increase in the Kara and Barents Seas is only a wintertime process.

During the summer, the winds that are most highly correlated with the warm months of PC3 observe an anticyclonic pattern that encompasses all the basins. These winds are upwelling-favorable along the Chukchi, East Siberian and Laptev seas, converging water into the Canada Basin through surface Ekman transport. The corresponding modeled ocean response is anomalously low SSH and OBP in the Siberian Shelves, and high SSH and OBP in the central basin but of smaller amplitude. Possibly the modeled SSH and OBP drop in the East Siberian and Chukchi seas might be stronger during the summer due to the lack of summer sea-ice there, which would likely reduce the momentum exchange between the ocean and the atmosphere.

PC3 is on average low (-1 std) from mid 2003 to mid 2006 (Figure 4.23), and becomes on average $\sim$ 1 std high from late 2006 to late 2009. PC3 changes polarity again from the beginning of 2010 until the end of the record in August 2011. This later period is not captured by the models, because the model output used here only includes results through 2009.

Figure 4.23, along with Figures 4.25 and 4.26, suggest that during times of positive PC3 (2007 through 2009), the Beaufort Gyre strengthens due to prevailing anticyclonic winds over the Canada Sea for all months, consistent with modeled SSH increase in the Canada and Makarov basins.

4.3.4 Atmospheric vorticity associated with the modes of variability

Mode 3 suggests a direct relationship between the ocean mass distribution within the basin, and the cyclonic/anticyclonic character of the wind field over the Arctic

Ocean. This is the reason why in this section, the atmospheric vorticity associated with the leading EOF modes is explored. The relationship between the vorticity of the wind field and the mass distribution is critical to the distribution of freshwater in the Arctic. The vorticity of the atmospheric forcing, estimated here as the curl of the wind field anomaly, is defined as:

$$\bigtriangledown \times \mathbf{u}\,|\mathbf{u}| = (\frac{\partial(v\,|\mathbf{u}|)}{\partial x} - \frac{\partial(u\,|\mathbf{u}|)}{\partial y})\hat{z} \tag{4.1}$$

where $|\mathbf{u}| = \sqrt{(u^2 + v^2)}$ and u and v are the zonal and meridional wind velocity at 925 hPa from NCEP/NCAR reanalysis (*Kalnay et al.*, 1996).

Positive vorticity or curl of the wind enhances surface Ekman divergence and decreases SSH. Negative vorticity or curl of the wind implies Ekman convergence and increases SSH. The resulting change in OBP will depend on the level of baroclinic adjustment in the water column through Ekman pumping. Note that the variations of the wind curl (Equation 4.1) are taken here as an approximation to the variations in the curl of the wind stress, which is what directly affects Ekman pumping. Wind stress is a function of the wind velocity and the drag coefficient, which in turn depends on the wind velocity and the roughness of the surface of the ice or open ocean (e.g. *Thorndike and Colony*, 1982). The reasoning for estimating the curl of the wind field instead of the wind stress is to avoid introducing uncertainties due to changes in ice thickness that affect ice roughness and remain difficult to determine accurately.

The temporal mean (from 2002 to 2011) and seasonal variation of the curl of the wind were removed for consistency with the other fields used in this study. Figure 4.27 shows the regression maps of the curl of the wind field anomaly projected on the PC1, PC2 and PC3 time series from the EOF analysis. The curl of the wind field anomaly that is most highly associated with PC1 shows negative vorticity in the Bering Strait and the Nordic Seas. The curl of the wind field associated with PC2

shows nearly basin-scale positive vorticity, consistent with the cyclonic wind pattern that corresponds to the pattern of positive AO. The curl of the wind associated with PC3 shows negative atmospheric vorticity in the Canada Basin that extends all the way to the Lomonosov Ridge and into the Amundsen Basin. In contrast, significant centers of positive vorticity are shown in the Barents Sea and in the 'Eastern' Siberian shelves and shelf break. The atmospheric vorticity pattern associated with PC3 captures the winter-dipole of atmospheric forcing in the basin, prevailing during the winter months.

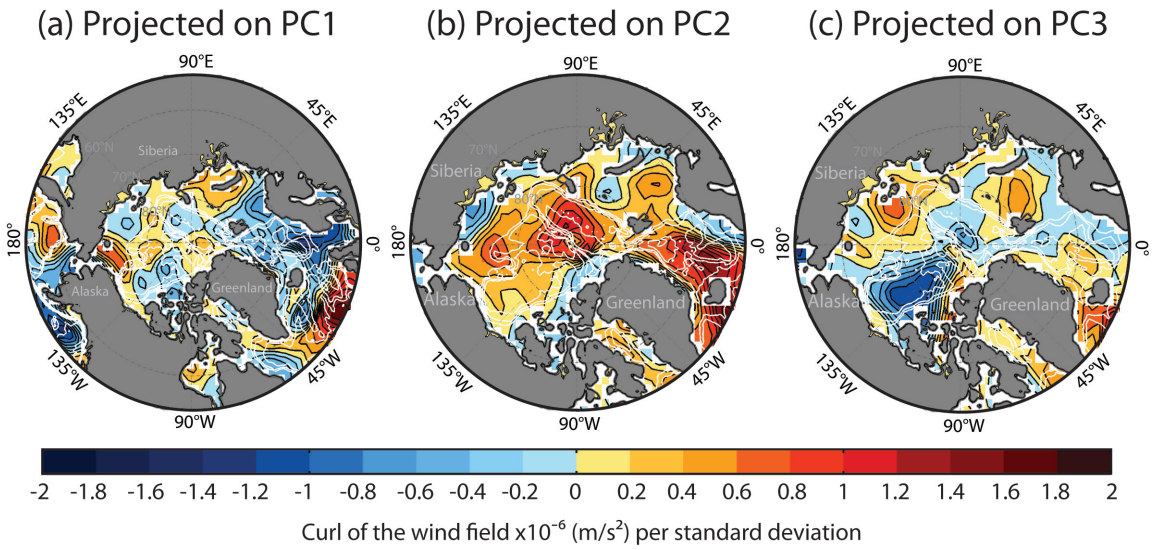

Figure 4.27: Curl of the wind field projected on GRACE PC1 (a), PC2 (b) and PC3 (c). White line contours show the bathymetry with 1000-m isobath intervals. Black contours are isolines of wind curl in 2x10^{-7} m/s^2 intervals.

4.4 Inter-annual mass changes before and after the year of minimum summer sea-ice extent, 2007

The results in the previous section show how changes in the atmospheric circulation drive changes in OBP and mass re-distribution in the Arctic, mainly on a month-

to-month basis (e.g., PC1 and PC2). In this section, inter-annual variations of OBP from 2002 to 2011 as driven by the atmosphere are investigated. In particular, the year 2007, which marked the record low in sea-ice extent at least since 1979[3], is taken as hypotetical turning point for changes in the dynamics of the Arctic Ocean. It has been shown in previous studies that month-to-month and year-to-year shifts in wind patterns over the Arctic Ocean have a strong effect in both determining and pre-conditioning the summer sea-ice extent (*Rigor et al.*, 2002; *Rigor and Wallace*, 2004; *Ogi and Wallace*, 2007, 2012). These changes in the wind field also affect the ocean circulation and the spatial distribution of freshwater in the basin (*Morison et al.*, 2006; *Rabe et al.*, 2011; *Morison et al.*, 2012; *Giles et al.*, 2012). Therefore, it might be expected that the reduction in ice-cover can strengthen the ocean-response to atmospheric forcing.

In order to investigate this, the atmospheric conditions prevailing prior to 2007 are compared to those prevailing from 2007 to August 2011. The difference between the wind anomaly averaged from 2007 through 2011 minus the wind anomaly averaged from 2002 through 2006 is shown in Figure 4.28, along with the difference in the curl of the wind field between the same periods. The differences were taken for the summer months (JJAS), winter months (DJFMA) and for all months. Note that the seasonal variation has been removed from the fields, for which the comparisons between summer and winter months also reflect year-to-year variations.

The summer wind pattern shows a tendency towards increasingly anticyclonic circulation with negative curl of the wind field over most of the Arctic basin. This atmospheric pattern resembles the difference of the wind anomaly averaged from 2007-2011 minus the average from 1979 to 2006 of *Ogi and Wallace* (2012, their Figure 5). The anticyclonic tendency of the winds during the most recent years has contributed

[3]which is when the satellite observations began.

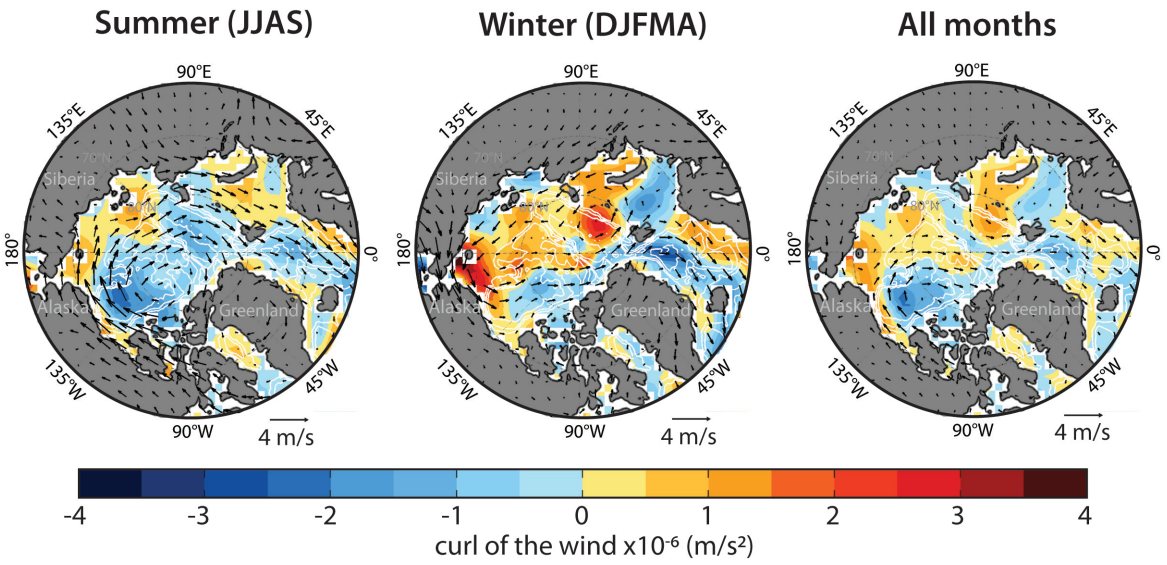

Figure 4.28: The change in curl of the wind field (color contours) and wind field (vectors) difference for JJAS (a), DJFMA (b) and all months (c): the change is the 5-year average from 2007 to 2011 minus the average from 2002 through 2006. White line contours show the bathymetry with 1000-m isobath intervals. The total mean and seasonal variability have been removed from all fields.

to the record lows in recent September sea ice extent (*Rigor and Wallace*, 2004; *Kwok and Rothrock*, 2009; *Ogi and Wallace*, 2012).

Does the increase in anticyclonic winds during the summer affect the ocean bottom pressure field? The differences in the modeled OBP and SSH, along with GRACE-OBP averaged from 2007 to 2009, minus the average from 2002 to 2006 (Figure 4.29) suggest it does. During the summer months, GRACE-OBP shows a basin-wide increase in mass that extends through the Nordic Seas. This increase has been accompanied by a mass loss in the Barents and Kara seas, and a mass loss in the Chukchi and East Siberian seas. Both ECCO2 and PIOMAS detect the observed summertime OBP decrease along the Eastern Siberian and Chukchi seas, revealed by a drop in

both SSH and OBP there (Figure 4.29, left panels). The atmospheric to ocean bottom pressure link appears to follow surface Ekman dynamics: Negative wind curl in the central Arctic basin and the Nordic Seas enhances mass convergence (positive SSH anomaly), while positive wind curl enhances surface divergence, and hence reduces the SSH. Over the Barents and Kara Seas, OBP has been generally low, but not as low as the modeled OBP and SSH suggest over the Chukchi and East Siberian seas. Furthermore, it is possible that the decrease of mass north of Ellesmere Island might be associated with land-contamination of the Canadian Archipelago region, which was not taken into account by the optimization technique of the GRACE solutions presented here (*Bonin and Chambers*, 2012).

In contrast, the tendency of the wind and wind curl for the winter months is toward more cyclonic conditions and positive vorticity in the Eurasian basin, Kara and Chukchi Seas (Figure 4.28). Tendency toward negative vorticity and relatively more anticyclonic winds are constrained to the eastern Canada basin and the Lincoln Sea north of Ellesmere Island and Greenland. GRACE-OBP during the winters tends to slightly increase, particularly in the eastern Laptev Sea and western East Siberian Sea ($\sim 3-4$ cm). The westerly winds along the siberian shelves, associated with positive wind vorticity likely enhances surface Ekman transport toward the Laptev, East Siberian and Chukchi Seas, where GRACE-OBP has tended to increase (Figure 4.29, right panels). However, the models show a basin-scale tendency toward decreasing OBP during the winter months (~ -2 cm), with a slight tendency to increasing OBP in the East Siberian and Laptev Seas of ~ 2 cm, half the magnitude of the GRACE-OBP increase there. ECCO2-OBP shows a winter-tendency to increase in all the Siberian shelves, including the Barents and Kara Seas. PIOMAS shows negligible change of OBP during winter months.

Winter OBP from ECCO2 has generally decreased at basin-scale, except near the

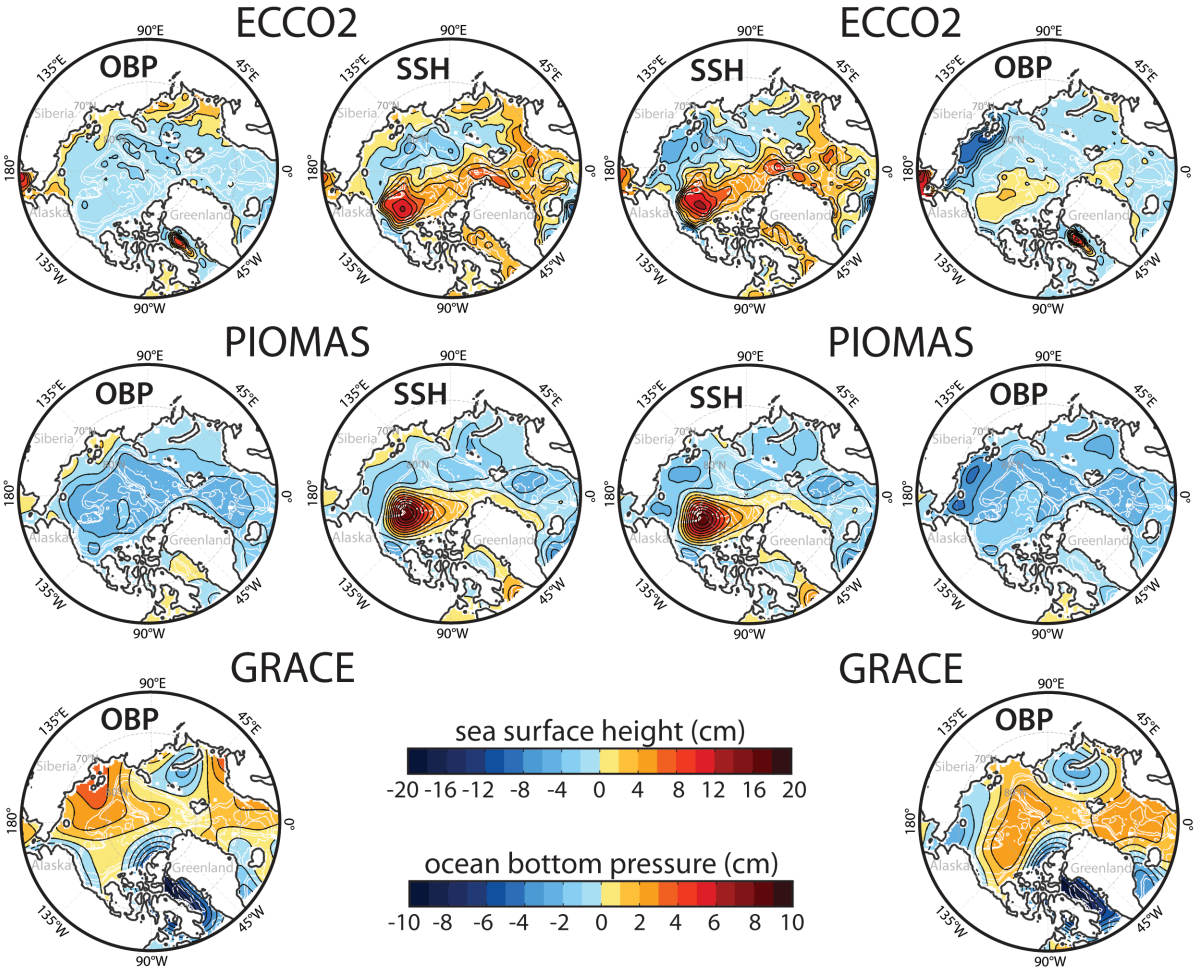

Figure 4.29: Left panels show the average of OBP and SSH from 2007-2009 minus the average from 2002-2006 for the summer months, from ECCO2 (top), PIOMAS (middle) and GRACE (bottom). Right panels are the same as left panels, but for the winter months. White line contours show the bathymetry with 1000-m isobath intervals. Note that OBP and SSH have different scales. Black line contours show the isolines at 1-cm intervals for OBP and 2-cm intervals for SSH.

coast of the Chukchi, East Siberian and Laptev Seas, where the OBP increase follows the SSH increase there. During the winters, steric pressure appears to compensate

the large SSH change in the Beaufort Sea, which is reflected in the small change in OBP in that region. The OBP change is positive in GRACE-OBP ($\sim 2-3$ cm), but is not a center of strong change, and is much smaller than the SSH increase revealed by the models and also observed by ICESat altimetry (*Morison et al.*, 2012). The tendency of GRACE-OBP during the winters in the East Siberian Sea and Laptev Sea shelves is toward increasing mass, also revealed by ECCO2.

Both PIOMAS and ECCO2 indicate that the SSH over the Canada Basin has been increasing in the recent years (2007-2009), relative to the 2002-2006 average ($\sim 8-14$ cm, see Figure 4.29). This tendency to high SSH is consistent with the negative vorticity of the winds prevailing during the most-recent summers. Modeled OBP from ECCO2 suggests a slight increase in the Beaufort Sea during the summer, but the amplitude is very small (~ 1 cm) compared to the modeled SSH there (~ 10 cm).

Overall, since 2007, for all months, the atmospheric vorticity has been more negative and the winds more anticyclonic in the Canada Basin, while to a lesser degree more positive elsewhere in the Arctic Ocean (Figure 4.28). The GRACE-OBP and modeled OBP and SSH changes from pre-2007 to post-2007 for all months is shown in Figure 4.30. GRACE-OBP change from pre-2007 to post-2007 for all months appears to be dominated by the changes during the winter (compare to Figure 4.29). ECCO2-derived OBP changes for all months in the Kara and Barents seas are also dominated by winter processes, but in the Chukchi and East Siberian seas the OBP changes are dominated by processes during the summer months (compare ECCO2 OBP of Figure 4.29 to Figure 4.30). PIOMAS-derived OBP exhibits a declining mass change basin-wide that essentially prevails during the summer and winter.

Inter-annual changes in OBP and SSH of the East Siberian and Laptev seas might be associated with changes in regional hydrography, which is strongly affected by

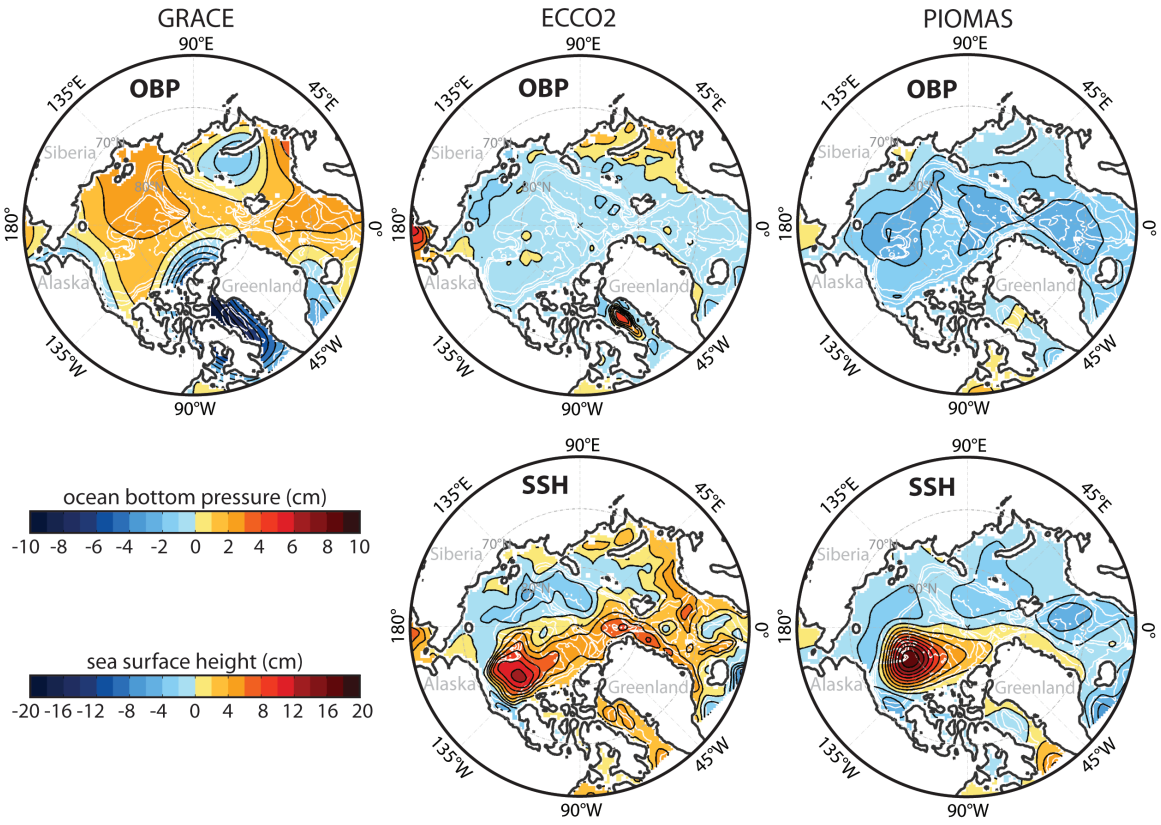

Figure 4.30: Upper panels show the difference of OBP averaged from 2007 to 2009 minus the average from 2002 to 2006, from GRACE (left), ECCO2 (middle) and PIOMAS (right). Lower panels are the same as in the upper panels, but for the modeled SSH from ECCO (middle) and PIOMAS (right). White line contours show the bathymetry with 1000-m isobath intervals. Note that OBP and SSH have different scales. Black line contours show the isolines at 1-cm intervals for OBP and 2-cm intervals for SSH.

inter-annual variations in the polarity of the atmospheric vorticity over the Laptev and East Siberian seas (*Dmitrenko et al.*, 2008a). The study of *Dmitrenko et al.* (2008a) showed that when the atmospheric vorticity on the shelves is negative (i.e., anticyclonic atmospheric circulation), the wind is predominantly northward (offshore)

over the Laptev Sea, and westward over the East Siberian Sea. The associated salinity anomaly resulted in loss of freshwater from the shelves to the Central Arctic Ocean mainly via Laptev Sea. In contrast, when the atmospheric vorticity on the shelves is positive (i.e., cyclonic), the wind is predominantly eastward along the Laptev and East Siberian seas. The resulting salinity anomaly is negative, i.e., more freshwater tends to remain on the Laptev and East Siberian sea shelves.

During the summer, *Dmitrenko et al.* (2008b) showed that this atmospheric-ocean relationship has a near-decadal character, whereas during the winter, the relationship tended to weaken due to predominantly negative atmospheric vorticity (i.e., anticyclonic wind) that was more steady during the period of the study, spanning from 1963 to 1993 (*Dmitrenko et al.*, 2008b, their Figure 3).

Thus, for the period of this study (2002-2011), the tendency of the winds to be more cyclonic, eastward alongshore winds (Figure 4.28) during the winter, might contribute to change the trajectory of the riverine freshwater eastward along the Eastern Siberian shelves, to finally enter the Makarov and Canada basins. This could explain the observed increased freshwater content in the Canada Basin during the late 2000s (*Rabe et al.*, 2011; *Morison et al.*, 2012; *Giles et al.*, 2012). These dynamics support the study of *Morison et al.* (2012), which indicates that the recent freshwater content increase is predominantly of Eurasian river origins.

GRACE-OBP has been increasing in the East Siberian and Laptev seas ($\sim$ 2.5 cm/yr), whereas modeled-OBP has decreased in the same region (~ -1 cm/yr). The reason for all these model - GRACE OBP discrepancies at multi-year timescales remains unclear. However, as *Morison et al.* (2012) indicated, multi-year OBP changes are small relative to the changes of SSH. Hence, the steric pressure change strongly resembles minus the SSH change. This is illustrated in Figure 4.31, where the steric pressure (OBP-SSH) from the models averaged from 2007-2009 minus the 2002-2006

average (i.e., equivalent to $\sim 5-7$ m FWC increase in the Canada Basin, which represents a FWC trend of 1.5 to 1.75 m/yr), resembles the 2005-2008 trend in steric pressure (i.e., equivalent to $\sim 1.5-2$ m/yr FWC increase there) from ICESat altimetry and GRACE (*Morison et al.*, 2012, their Fig. 2b).

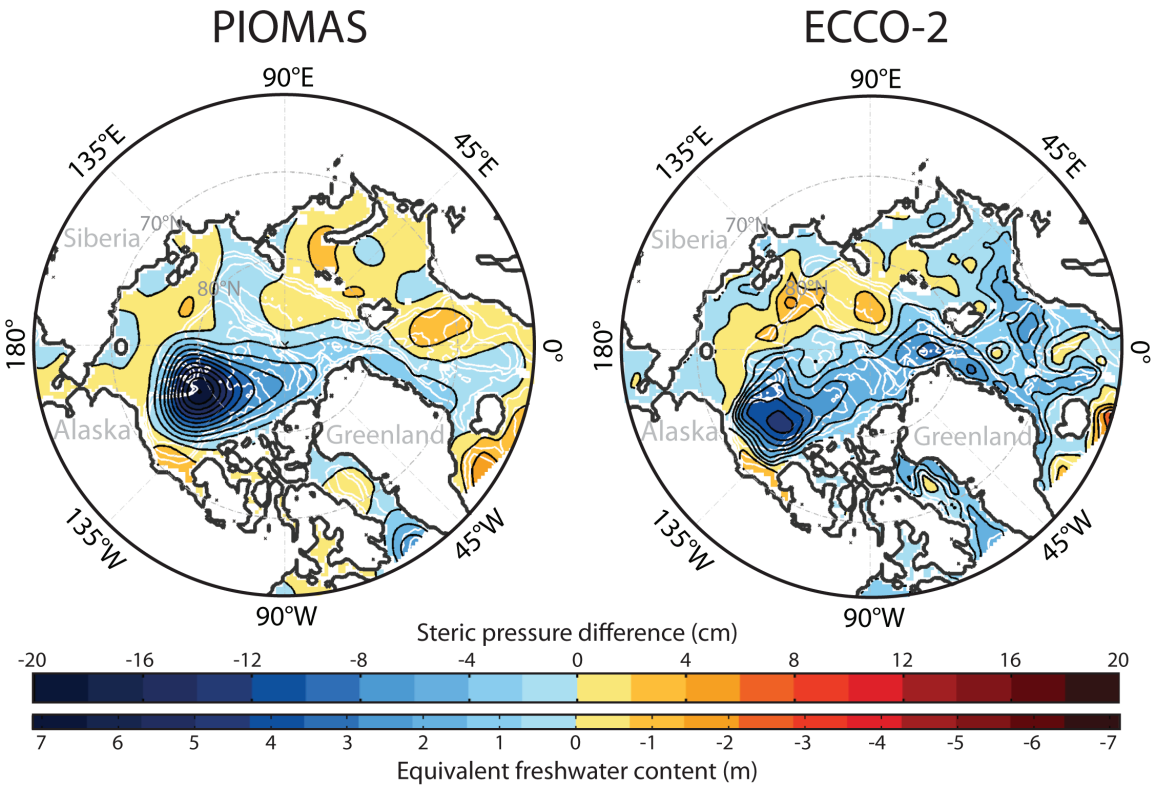

Figure 4.31: Steric pressure (OBP-SSH) difference: average from 2007 to 2009 minus the average from 2002 to 2006, from PIOMAS (left) and ECCO-2 (right). White line contours show the bathymetry with 1000-m isobath intervals. Black line contours show the isolines at 2-cm intervals.The second scale represents the estimated freshwater content change using Equation 2.5.

The dipole vorticity pattern of Figure 4.31 showing low steric pressure in the Canada Basin, and weaker but positive steric pressure tongue along the Eurasian

Basin and southern region of the Makarov Basin, is similar to the pattern of satellite-derived steric pressure trend from 2005-2008 discussed in *Morison et al.* (2012). The positive steric pressure tends to offset the freshwater accumulation in the Canada Basin, to produce a small net change in the freshwater content of the entire Arctic Ocean. The model tendency towards negative steric pressure in the Canada basin is consistent with their satellite analysis. The positive steric pressure tendency is larger in *Morison et al.* (2012) because GRACE OBP change is small but slightly larger than the modeled OBP change.

4.5 Assessing the barotropic vs baroclinic character of the Siberian Arctic shelves

The ocean response to atmospheric forcing as revealed by GRACE in the previous section suggests overall, that the Chukchi, East Siberian and Laptev Seas have a predominantly barotropic behavior (i.e., OBP variations essentially resemble the SSH variations). It was also shown that the variability in the Kara and Barents Seas associated with the AO pattern has a predominantly barotropic character, even if the responses are separated in cold months versus warm months. It still remains to explain, however, the other sources of variability of OBP in the Kara and Barents Seas, which are arguably related to the discrepancy between the observations of OBP from GRACE and the *in situ* observations of SSH in that region. In order to investigate this, the freshwater sources in these regions are examined.

The largest contribution of freshwater input to the Arctic Ocean from runoff comes from the six largest Eurasian Rivers (Severnaya Dvina, Pechora, Ob, Yenisey, Lena and Kolyma) and two North American rivers (Mackenzie and Yukon) (Figure 4.32). The river discharge to the Arctic Ocean from the Eurasian rivers has increased since 1936, with the most significant positive trend (12 km^3/yr) from 1987-2009 (*Shiklomanov and Lammers*, 2009). The Yenisey (largest of the Arctic rivers), Ob (third

largest) and Pechora rivers discharge into the Kara Sea, and the Severnaya Dvina discharges into the Barents Sea.

Thus the Kara Sea is the region through which the largest runoff discharge into the Arctic Ocean occurs (see Figure 4.32), and hence a region with a large source of freshwater. In this strongly stratified region of the Arctic Ocean, forcing at the surface of the Kara Sea would result in SSH variations that may compensate baroclinically down through the water column. If baroclinic adjustment occurs, then the difference between the GRACE OBP and the modeled and observed SSH in the Barents and Kara Seas may be larger there. In addition, large amounts of freshwater may change the salinity from the surface to the bottom. In this case, likely in the very shallow areas, SSH changes due to steric changes could be large and reduce the correspondence between OBP and SSH there.

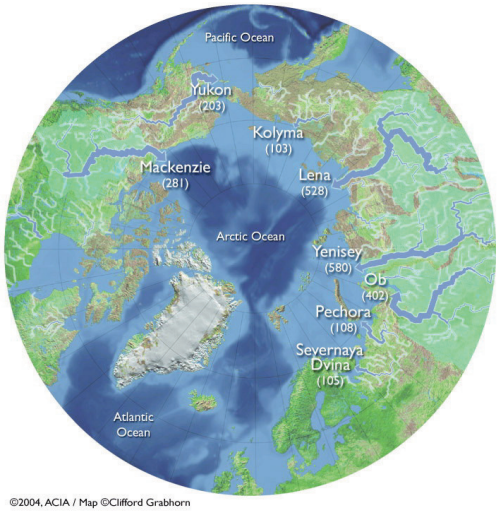

Figure 4.32: Map of the largest rivers draining into the Arctic Ocean. The width of the arrows represent the volume discharge, and the numbers correspond to the averaged volume in km^3/yr. Photo source: Arctic Climate Impact Assessment Report (*ACIA*, 2006).

In addition to the strong stratification, the bathymetry of the Barents and Kara Seas is complex compared to the uniformly shallow Laptev, East Siberian and Chukchi Sea shelves (see Figure 4.33). A sense of the effects of the bathymetry on the OBP change in the different shelves are examined here by calculating the magnitude squared coherence between the PIOMAS-derived daily OBP and SSH, for shallow (< 50 m) and for deep (> 50 m) parts of the Siberian shelves. The magnitude squared coherence (MSC) is defined as:

$$C_{xy}(\omega) = \frac{|P_{xy}(\omega)|^2}{P_{xx}(\omega)P_{yy}(\omega)} \tag{4.2}$$

In Equation 4.2, P_{xy} is the cross-spectral density function between OBP and SSH, P_{xx} is the auto-spectrum or power spectrum density function of OBP, P_{yy} is the auto-spectrum of SSH and ω is the frequency. Thus, MSC provides a measure of the correspondence between OBP and SSH as a function of frequency, similar to the admittance estimate of *Vinogradova et al.* (2007) and *Bingham and Hughes* (2008). A coherence value C_{xy} equal to one corresponds to a predominantly barotropic character of the ocean, whereas a coherence value of zero corresponds to a predominantly baroclinic character (Figure 4.34).

Ten years of daily output of PIOMAS OBP and SSH have been used to produce Figure 4.34. The shelves were separated in four main regions: Chukchi Sea, East Siberian and Laptev seas, Kara Sea and Barents Sea. The MSC values between OBP and SSH at each grid point were averaged for each of the shelves, and also averaged within the shallower and deeper bathymetry.

Figure 4.34 shows high MSC values in all the shelves from daily to periods of $\sim$100 days, for all depths. Model OBP and SSH in the Chukchi Sea are essentially coherent at all timescales, for all depths, suggesting that the stratification does not contribute to the mass change there, in the model. The SSH and OBP in the East Siberian and

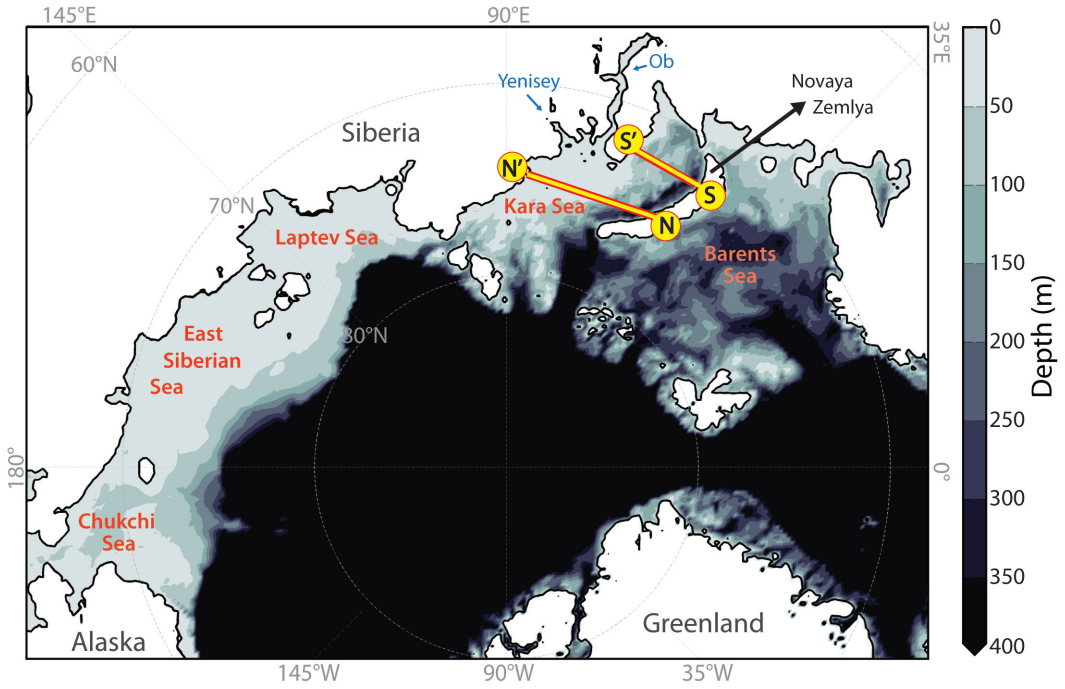

Figure 4.33: On the top is the IBCAO bathymetry of the Siberian shelves, from 0 to 400 m deep. Red lines denote the Southern (S - S', along 72°N) and Northern (N - N', along 75°N) transects across the Kara Sea.

Laptev seas combined show significant MSC values even at inter-annual timescales (at least above the 95% confidence interval). The MSC in the regions shallower than 50 m of the East Siberian and Laptev seas are not as high as the MSC found in the Chukchi Sea. This could be due to a steric contribution to OBP originating from the runoff discharge into the East Siberian and Laptev coastal regions, which is generally much larger than the runoff input into the Chukchi Sea. The MSC of the East Siberian and Laptev seas drops in the locations where bathymetry is deeper than 50 m. This might not be surprising, given that at the 50 m threshold, the ocean is affected by complex dynamics of the continental slope.

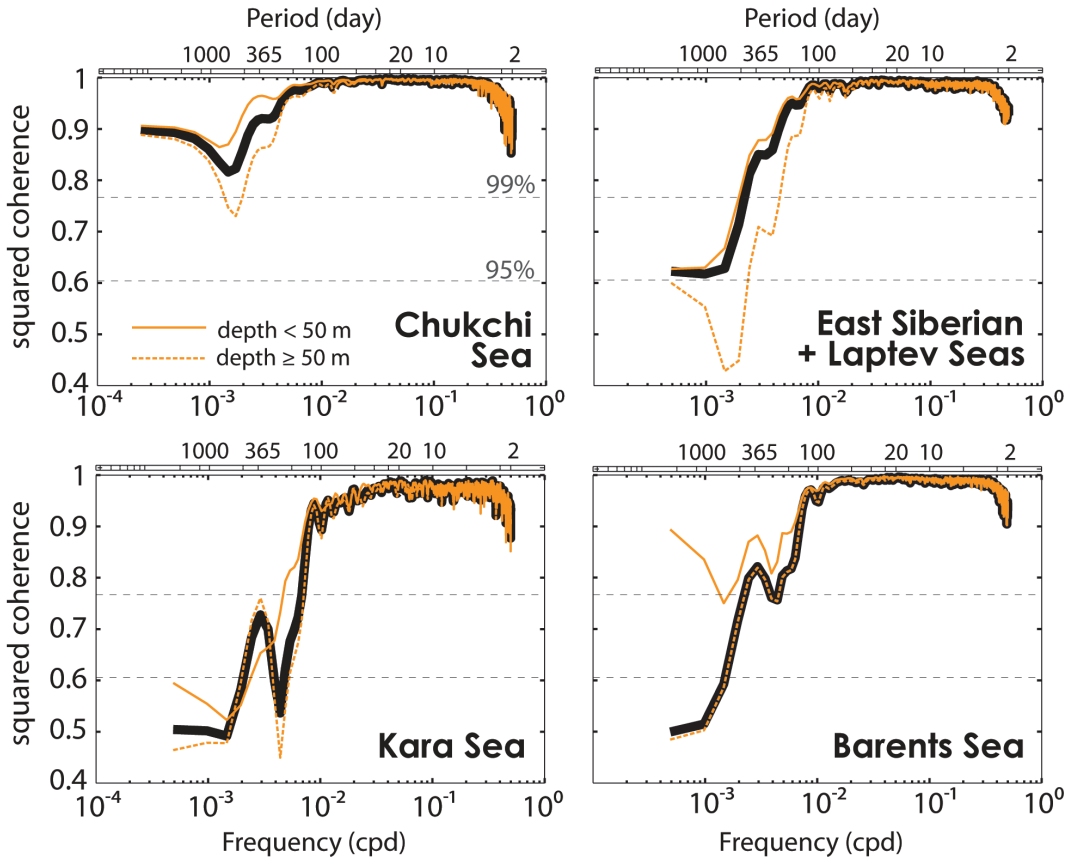

Figure 4.34: Magnitude squared coherence (MSC) between daily output of OBP and SSH from PIOMAS model, averaged over different Siberian Arctic continental shelves. Total MSC is shown in black thick lines. Solid yellow lines indicate the MSC averaged over the grid points with depths shallower than 50 m, and dashed orange lines show the MSC values averaged within grid points of over 50 m deep for each of the shelves. 95% and 99% significant levels are shown in thin black dashed lines.

In the Barents Sea, the relationship between OBP and SSH follows a more straightforward behavior: For those locations where depth exceeds 50 m, the MSC is low (e.g., baroclinic adjustment plays a significant role in affecting OBP), whereas in the locations shallower than 50 m, the character of the ocean is predominantly barotropic

at all timescales. Since most of the Barents Sea grid points are over 50 m deep (Fig. 4.33), the total MSC for all points in the Barents Sea are nearly identical to the MSC estimated in the other locations over 50 m deep. This explains why GRACE and the tide-gauge in Vardo Station (Norwegian coast of Barents Sea) disagree: Only limited areas of the Barents Sea are shallow enough and hence, barotropic enough to produce OBP changes consistent with SSH changes: The footprint of GRACE over the Barents Sea captures most of the OBP change in the area where baroclinic adjustment offsets the OBP change at longer than seasonal timescales.

It remains to explain the origins of the steric contribution to OBP in the Kara Sea, which in turn, may explain the discrepancy between GRACE data and the tide-gauge records of SSH. Figure 4.34 shows that the MSC in the Kara Sea drops below significant levels very rapidly beyond 100 day periods, and remains low, except for the annual period, which is the timescale where MSC shows a high value, significant above 95% confidence level. The fast roll-off of the MSC in the Kara Sea constrained between the frequency range of $\sim 1/100$ to $\sim 1/300$ cycles per day (cpd), is not observed in the other Siberian shelves. This behavior might be due to the massive amounts of runoff discharge in that area, which would alter the density of the water column from top to bottom, and hence increase the steric contribution to OBP variations there. It is important to know, however, that PIOMAS adjusts the salinity field at the mouth of each river discharging into the Arctic Ocean, based on climatological values of runoff. Thus, multi-year variations of freshwater changes in runoff are not modelled, but the ocean dynamics of the inter-action of meteoric freshwater due to surface forcing may still be recovered.

Correspondence between OBP and SSH in the Kara Sea at the annual period is likely due to the annual variation of the winds during the winter and early spring, which forces the ocean to enter from Nordic Seas into the Barents and Kara seas due

to surface Ekman transport (e.g., Figure B.1 in Appendix B).

At longer than annual timescales, MSC in the Kara Sea drops again to small coherence values in both areas of shallower and deeper than 50 m. In the deep regions, baroclinic adjustment may explain the small MSC, but in the shallow regions, the steric change through the water column due to runoff might explain the small MSC value obtained there.

To get a sense of the causes of baroclinic character of the Kara Sea for timescales longer than $\sim$ 100 days, two vertical transects across the Kara Sea are examined using monthly values of PIOMAS-derived salinity anomaly from January 2000 to 2011. The transects are shown in Figure 4.33. The southern transect follows the latitude line of 72°N, and the northern transect follows the latitude line of 75°N. These were chosen based on their location relative to the largest river mouths in the area, namely Ob and Yenisey. The southern cross-section is presumably not directly impacted by these rivers, whereas the northern cross-section extends passed the river's mouth. The seasonal variation of the salinity fields was removed for each section, and the residual fields were low-pass filtered with a cutoff frequency of 1/4 cycle per month (cpm) or 1/120 cpd. This is because, as shown in Figure 4.34, any frequency higher than $\sim$ 1/120 days exhibits a predominantly barotropic character in the Kara Sea.

The RMS variability of the salinity field of each transect in the Kara Sea is shown in Figure 4.35, along with the RMS of SSH and OBP. The steric pressure was calculated as the difference between OBP anomalies minus SSH anomalies. Similar to OBP and SSH, the steric pressure was low-pass filtered, and the seasonal variation was removed. Figure 4.35 shows that the zonal-RMS variability of the steric pressure anomalies (dashed-lines) is consistent with the salinity variability through the water column (e.g., along both transects, the dashed-line follows the RMS change of the salinity through the water column). This suggests that in the Kara Sea, as in the rest

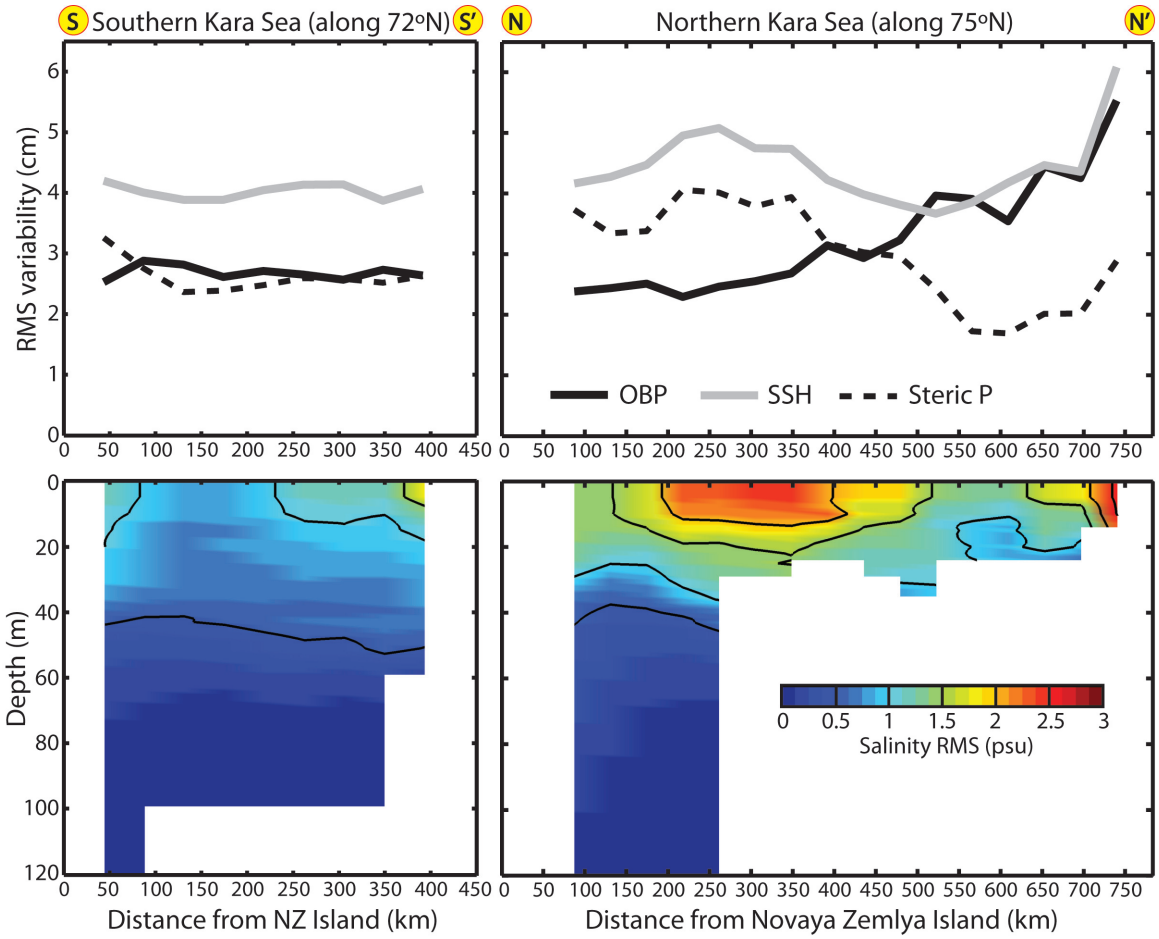

Figure 4.35: Upper panels show the RMS variability of modeled OBP (black line), modeled SSH (gray line) and modeled Steric pressure (inferred from the difference OBP-SSH, dashed line) in the southern −along 72°N− (left) and northern −along 75°N− (right) transects of the Kara Sea, from January 2000 to December 2011. The seasonal variation of each field was removed, and the records were low-pass filtered with a cut-off frequency of 1/4 cpm. Lower panels show the RMS variability of the salinity anomaly for the sections corresponding to the upper panels. Black contours are the RMS values at 0.5 psu intervals.

of the Arctic Ocean, the density variations through the water column are strongly driven by the salinity fluctuations.

SSH variability in the southern transect is $\sim$ 4 cm (Figure 4.35, gray line on the upper left), whereas the RMS variability of OBP is $\sim$ 2.7 cm (same figure, black line). This suggests that the steric pressure has a significant contribution that offsets the OBP response to SSH change. Even though this transect is not located directly by the river mouths, the depth of the cross-section is minimum $\sim$ 100 m, which is deep enough to get baroclinic adjustment through the water column, as revealed by the results for the deeper than 50 m region in the Barents Sea (e.g., Figure 4.34).

The western-most part of the northern cross-section is deeper than 120 m. This, again, allows for baroclinic adjustment to occur. This is likely the process that offsets the OBP response to SSH change. RMS variability of OBP there is in average $\sim$ 2.3 cm, whereas the RMS of SSH is $\sim$ 4.5 cm. This is consistent with a large RMS variability of the steric pressure, which in the western side averages $\sim$ 3.75 cm.

Moving eastward along the northern transect, a strong RMS variation of salinity is observed (e.g., between 200 to 400 km east from Novaya Zemlya Island, Figure 4.35, right panels). This increased RMS signal encompasses an area deeper than 120 m to the west, and an area of $\sim$ 25 m deep to the east. The RMS salinity signal of the shallow area spans nearly from top to bottom, and lower OBP RMS relative to SSH and steric pressure RMS suggest that a strong freshening there (which coincides with the longitudes of the Ob runoff) must offset the SSH change there, producing little OBP variation.

Further east through the shallow part of the transect, the OBP RMS variability tends to increase and to follow the SSH RMS variability, while the steric pressure RMS begins to drop. This suggests that the ocean there exhibits a more barotropic behavior. The eastern-most side of the northern transect, by the western coast of the main land in Siberia, is again affected by a strong RMS signal of salinity. This must be due to the Yenisey river, which discharges nearby south from there. OBP

variability there is almost as large as SSH ($\sim 5.5-6$ cm) variability. The steric part, although smaller, appears to also play a role in the OBP change there.

In summary, the complex bathymetry and large freshwater input from runoff into the Kara Sea make of this region an interesting mix of physical processes contributing to OBP change through different timescales. PIOMAS suggests that there is an inter-play between two mechanisms: the first one is through baroclinic adjustment of the SSH change in the regions deeper than ~ 50 m, which is generally in the southern part of the Kara Sea and the western side along the Novaya Zemlya Island. This process may take place from a few months and up to inter-annual timescales. The second one is the steric pressure change in the regions shallower than ~ 50 m, responding to the freshwater input from the rivers. Large additions of freshwater may decrease the hydrostatic pressure as freshening occurs throughout the water column, which could offset the OBP variations relative to the SSH change. In some of these very shallow regions of the Kara Sea, however, the OBP tends to follow SSH changes (i.e., barotropic character dominates). Thus, this inter-play between different ocean responses complicate the picture of the physical processes in the Kara Sea. Further investigation is encouraged and required to fully understand the contributions of the OBP variations in the Kara Sea, and get a better sense of how these affect the large-scale mass distribution of the Arctic Ocean, particularly at inter-annual timescales.

Chapter 5

SUMMARY AND CONCLUSIONS

In this dissertation, changes and distribution in the Arctic Ocean bottom pressure field have been used to identify ocean circulation patterns and their associated forcing. To do this, the causes of the OBP variations were examined at different timescales. This approach was taken in spirit of previous modeling findings revealing that OBP variability is dominated by SSH variability (i.e., the ocean is predominantly barotropic) in high latitudes and at annual and shorter timescales (*Vinogradova et al.*, 2007). In the Arctic Ocean, these modeling studies revealed that on the shelves (e.g., areas shallower than $\sim$ 200 m) the SSH variability dominates the OBP variations at all timescales (*Bingham and Hughes*, 2008).

Using available *in situ* observations of OBP and SSH, along with GRACE-derived OBP, it was possible to reproduce an observational perspective of the work of *Vinogradova et al.* (2007) and *Bingham and Hughes* (2008), and demonstrate that for different regions and timescales, consistency and disagreement between the aforementioned model results and observations may occur. Both model-observation similarities and differences addressed in this work have provided insights in the dynamics of the Arctic Ocean and have allowed for the generation of new questions and hypothesis for future investigation.

In this final chapter, these results are summarized, the associated ocean circulation dynamics are discussed, and finally, some speculations towards the future of the Arctic and suggested future work are presented.

5.1 Timescales of Arctic OBP variations

Throughout this work, it has been possible to dissect the Arctic Ocean bottom pressure field into its major components of the energy spectrum. Significant non-tidal energy in the Arctic OBP field has been identified at sub-monthly (*Peralta-Ferriz et al.*, 2011), seasonal (*Peralta-Ferriz and Morison*, 2010), intra-seasonal, inter-annual and multi-year timescales (*Morison et al.*, 2007, 2012). The analysis of the OBP changes at these diverse timescales reveal interesting changes of the circulation that have been previously unexplained or even unknown, providing an important contribution to our current understanding of the circulation of the Arctic Ocean.

5.1.1 Sub-monthly variability

The 5-year record of *in situ* OBP changes from the ABPRs allows for the identification of wintertime, non-tidal sub-monthly oscillations in OBP. *In situ* records from available pressure sensors and tide gauges in the Arctic Ocean reveal that these oscillations in OBP are coherent throughout the basin. This mode of variability in OBP is associated with the zonal surface atmospheric pressure gradient (i.e., high over Scandinavia and low over Greenland), which resembles an atmospheric pattern referred to as winter atmospheric blocking events (*Rennert and Wallace*, 2009). The SLP gradient produces a northward slope current in the ocean. This northward ocean flow increases the flow into the Arctic Ocean through Fram Strait, and to a lesser extent, through the Barents Sea Opening. These changes in OBP are controlled by the SSH changes, which suggests a predominantly barotropic character of the ocean at these timescales, everywhere in the basin.

At the time of this study (*Peralta-Ferriz et al.*, 2011), and as this dissertation is written, GRACE solutions at higher temporal resolution than monthly are being generated. Outside of the Arctic, GRACE has been shown to be capable of observing

sub-monthly mass changes at global scales (*Bonin and Chambers*, 2011; *Quinn and Ponte*, 2012). Once these solutions are generated and available for the Arctic Ocean, it would be valuable to see if the sub-monthly non-tidal Arctic mass variation can be captured by GRACE.

5.1.2 Seasonal variability

At seasonal timescales, the variability of the Arctic OBP is studied using GRACE. GRACE reveals two major spatial patterns of OBP: The first one is a basin-scale variation −analyzed in terms of the basin-averaged annual cycle of OBP−, with a maximum OBP amplitude of ~ 2.5 cm during late summer to early fall. The second pattern exhibits a sea-saw oscillation of mass between the East Siberian Sea and the Kara/Barents seas region.

Both modeling results (*Dobslaw and Thomas*, 2007) and observations (*Peralta-Ferriz and Morison*, 2010) showed that the annual oscillation of the basin-averaged OBP change is mainly attributed to runoff. *Peralta-Ferriz and Morison* (2010) complemented this work by developing a simple analytical model, and found that in addition to the effects of runoff, the net P-E and the SLP variation play a minor but significant role on the annual cycle of Arctic OBP (see Appendix B). This case study proved to be one example in which the atmospheric pressure is not fully compensated via inverted barometer effect, likely due to the enclosed nature of the Arctic Ocean that constrains the adjustment to SLP over the entire Arctic Ocean.

The spatial variability of the Arctic Ocean at seasonal timescales consists of high OBP anomaly in the Kara and Barents seas during late winter to early spring, and low OBP anomaly in the East Siberian Sea. The sign of the anomalies reverses during late summer to early fall, i.e., anomalously high OBP is observed in the East Siberian Sea while low OBP anomaly is observed in the Kara and Barents seas. In

Appendix B of this dissertation, it is suggested that these changes may be attributed to the seasonal character of the regional wind forcing: the winter westerlies spin-up enhances northward flow into the Barents Seas that increases the mass in the Barents and Kara seas through surface Ekman transport. In addition, during the fall, strong winds tend to flow eastward along the East Siberian Sea, increasing the mass via surface Ekman transport. These dynamics were identified using maximum covariance analysis between GRACE OBP and NCEP/NCAR surface winds.

5.1.3 Month-to-month, non-seasonal variability

The non-seasonal, month-to-month variations in OBP were identified using EOF analysis on 9-years of monthly GRACE data, from 2002 to 2011. Together, the three leading modes of variability explain nearly 80% of the GRACE-OBP total variance.

The first mode (50% of the variance) corresponds to a basin-coherent change in OBP that is also observed in the monthly averages of *in situ* record at the North Pole. Forced by northward winds over the Nordic Seas and to a lesser extent over Bering Strait, this mode is energetic during the winter, and weak during the summer. The basin-coherent mass increase appears to respond to increased flow mainly through Fram Strait by a northward slope current: the northward component of the wind would set up a surface slope to the east, which would in turn enhance a northward geostrophic flow into the Arctic Ocean.

The second mode, explaining 20% of the variance, shows an OBP increase in the Siberian shelves, and a OBP decrease in the Central Arctic. This mode is attributed to the phases of the Arctic Oscillation (AO). In several other studies, many changes in the Arctic have been related or attributed to different strengths of the AO (*Thompson and Wallace*, 1998). Here, the AO effects on the mass distribution in the basin have been isolated for the first time in a monthly basis within nearly a decade-worth

of observations with full coverage of the Arctic Ocean. A positive AO pattern is characterized by anomalously low SLP, and is associated with strong cyclonic winds along the Siberian shelves that increase the mass toward the East on the shelves through surface Ekman dynamics. The ocean models used here obey such dynamics, and are consistent with GRACE. The SSH change from the models is fully captured by the OBP change, suggesting that the ocean response to AO in the shelves is of barotropic character. A secondary flow alongshore and eastward, via slope current, may emerge out of the mass pile-up onto the Siberian shelves. This slope current would be an effective way to direct riverine water into the 'Western sector' of the Arctic Ocean (*Morison et al.*, 2012).

The third mode explains 10% of the variance, and is characterized by a dipole of mass change with opposing centers of action in the Chukchi and East Siberian seas, versus Barents and Kara seas. This mode may be attributed to a strengthening of the antiyclonic Beaufort Gyre. The spin-up of the anticyclonic wind pulls water away from the Chukchi and East Siberian shelves, consequently decreasing the OBP in the shelves. During the winter, alongshore westerly winds over the Barents Seas appear to increase the OBP in the Barents and Kara seas via surface Ekman transport. The barotropic character that corresponds to this mode is consistent with the modeling results of *Bingham and Hughes* (2008)

5.1.4 Inter-annual to multi-year variability

The third mode of OBP variability from GRACE may be also thought of as an inter-annual type of variation in Arctic OBP. For instance, warm months of the mode 3 reflect the multi-year trend in OBP. Although little of the total variance of GRACE-OBP is explained by this mode (9%), it reveals a pattern of the OBP field that might be associated with the accumulation of freshwater in the Canada Basin due

to Ekman transport convergence (*Morison et al.*, 2012; *Giles et al.*, 2012). Summer and wintertime forcing of this mode of variability are related to the atmospheric vorticity during each season. The resulting winds may affect the extent to which Eurasian runoff can be advected eastward along the Siberian shelves and shelve-breaks, or directed towards central basin by surface Ekman dynamics, as suggested by *Dmitrenko et al.* (2008b) and *Morison et al.* (2012).

Multi-year changes in mass distribution have been analyzed here by assuming a turning point for significant changes in the Arctic environment. This turning point was the year 2007, in which the Arctic Ocean experienced its record low in summer sea-ice extent, and significant thinning (*Kwok and Rothrock*, 2009). These effects may have lead to enhanced ocean warming, increased mixing, and increased air-sea interactions, as suggested by *Steele et al.* (2008) and *Rainville and Woodgate* (2009). Furthermore, the Arctic observed in 2007 a new record high in Eurasian river discharge, which was 10% higher than the previous record in 2002 (*Shiklomanov and Lammers*, 2009).

Averages of the observed OBP, NCEP/NCAR winds and SLP, and modeled OBP and SSH between 2007-2009, minus the averages of 2002-2006 showed that the summers have tended toward more anticyclonic atmospheric circulation, in agreement with *Ogi and Wallace* (2012). This atmospheric circulation has tended to reduce GRACE OBP and modeled OBP and SSH in the western Siberian shelves. Aside of the rest of the Arctic OBP, the summer OBP decrease in the Chukchi and East Siberian seas is captured by both PIOMAS and ECCO-2.

OBP during the winter has tended to increase mass, mostly in the East Siberian and Laptev seas. The models detect this increase in coastal OBP, but underestimate the change. The atmospheric circulation change in wintertime has shown a bi-pole pattern that in the Siberian shelves is of positive vorticity, and of negative

vorticity in the Beaufort Sea. Associated with this winter atmospheric forcing, the Siberian shelves have experienced GRACE-derived OBP increase. The OBP increase in the East Siberian and Laptev Seas is detected (and slightly underestimated) by the models, but the OBP increase in the Barents Sea is only detected by ECCO2. The associated process might be related to a barotropic response in Ekman transport, given that the modeled OBP and SSH changes are consistent with each other.

Morison et al. (2012) find that the multi-year changes in OBP are very small compared to the changes in SSH, particularly in the Canada basin. This hold true in the analysis of this dissertation for both GRACE and modeled OBP changes. The small OBP change may be attributed to baroclinic adjustment through the water column. The results of *Morison et al.* (2012) were done for February and March values. Using the models in this work, and including all monthly anomalies of OBP and SSH (as supposed to only the Feb-Mar campaigns of ICESat), it is found that the steric pressure change, and hence, the estimate of the freshwater content difference of the 2007-2009 average minus the 2004-2006 average, is equally important throughout the year. The estimate of steric pressure change from the models is consistent with the remote sensing -based results of *Morison et al.* (2012) and *Giles et al.* (2012), showing that the Canada Basin has freshened. In addition to this freshening, *Morison et al.* (2012) suggested that a tongue-shape increase in the salinity has occurred in the Eurasian basin and along the southern Makarov basin, and towards the East Siberian Sea, which led to the transport trajectory of Eurasian runoff eastward to the Canada Basin. This tongue was found here in the model-based estimate of freshwater content via OBP-SSH, but the increase of salinity there was somewhat weaker (by a factor of 2) than the observed by *Morison et al.* (2012). This could be due to the way the river input is implemented in the models (i.e., climatologically-based, and virtually adjusting the simulated salinity field near the river mouths).

In the shallow continental shelves of the Arctic, the comparisons between OBP-SSH yield mixed results. The magnitude square coherence (MSC) estimated from 10-years of daily OBP and SSH solutions of the model PIOMAS for each of the different Siberian shelves (Chukchi Sea, East Siberian and Laptev Seas, Kara Sea and Barents Sea), indicated that modeled OBP and SSH are highly coherent (i.e., the ocean is barotropic) at high frequencies (2-100 day periods). Chukchi Sea remains coherent at all timescales for all depths (max. depth there is ~ 60 m). The SSH and OBP in the East Siberian Sea and Laptev Sea are coherent at all timescales, but for the areas with depths ≥ 50 m, the MSC begins to roll-off, suggesting that the steric pressure (OBP-SSH) may begin to play a role at longer than seasonal timescales for the deeper regions. These regions, however, are very close to the shelf-break, where diverse dynamics may break-down the OBP-SSH relationship that remains high over the relatively smoother bathymetry of these seas.

The Kara and Barents seas exhibit complex bathymetry, and in many areas is ≥ 50 m. In the shallower regions of the Barents Sea, the relation between modeled OBP and modeled SSH is predominantly barotropic at all timescales. In the regions deeper than 50 m, the modeled OBP and SSH breaks-down due to baroclinic adjustment of the water column to SSH changes.

The Kara Sea presents another interesting mechanism that might explain the lack of relationship between modeled OBP and SSH, and may partially explain the difference between GRACE OBP and *in situ* data there: Two of the largest Eurasian rivers that discharge into the Arctic Ocean −Ob and Yenisey−, are located there. The runoff induces very large steric pressure variations that may, in shallow regions, compensate for the SSH change, and consequently breaking down the OBP-SSH relation. This appears to occur at timescales between 100-300 day periods, and again at longer than annual timescales, according to two vertical sections of the salinity field,

OBP and SSH analyzed from PIOMAS.

In summary, at inter-annual timescales, in Arctic regions $\geq$ 50 m deep, the SSH-OBP correspondence is small, and the ocean circulation is predominantly baroclinic. This includes most of the Barents Sea, and parts of the Kara Sea. This result is in contrast with *Bingham and Hughes* (2008), who found that the Barents and Kara seas were barotropic at longer than seasonal timescales. In the central basins, observations from *Morison et al.* (2007) and *Morison et al.* (2012) are consistent with the model results of *Bingham and Hughes* (2008). In the shallow regions, $\leq$ 50 m (i.e., Chukchi, East Siberian, Laptev and Kara seas), our results indicate that the ocean is predominantly barotropic, except in the Kara Sea, where large amounts of freshwater alter the steric pressure, which at times may break-down the SSH-OBP relationship. Thus, the barotropic character of the shallow Siberian shelves is in agreement with *Bingham and Hughes* (2008), except in the Kara Sea.

5.2 The role of the models to understand Arctic Ocean circulation

Throughout this work, it has been demonstrated that the models play a significant role in our understanding the dynamics of the Arctic Ocean. Both PIOMAS and ECCO-2 are capable of capturing the observed Arctic OBP anomalies at most timescales, and the modeled SSH has provided means for describing the physical mechanisms associated with the observed and modeled OBP changes.

Generally for short periods (e.g., daily) and up to inter-seasonal timescales, the models capture the large-scale circulation very well. At inter-annual to multi-year timescales, the model to observation inter-comparison presents a few discrepancies that might be related to the way the models simulate the freshwater fluxes into and out of the Arctic Ocean, due to runoff and other model response to reanalyses (e.g., *Jahn et al.*, 2012). The fact that the multi-year change in modeled SSH resembles

well the trend in SSH from satellite altimetry suggests that the errors of the model to reproduce the steric effects on sea level change are not a significant cause of the discrepancy between GRACE and modeled OBP.

It is important to note that the multi-year OBP difference in the deep basins is essentially negligible compared to the absolute OBP there, and falls within the uncertainty of the modeled time-varying OBP field. Hence, apart from the shallow shelves, its difference with GRACE-OBP may be ignored, since it is negligible relative to the SSH variations there.

5.3 Perspective and speculations for the future Arctic Ocean

Perhaps one of the major difficulties in separating the causes of OBP change in the Arctic Ocean by timescales, is the long de-correlation timescale of the large scale atmospheric circulation, along with the strong seasonality variations of the signal. This is reflected in common atmospheric forcing patterns that have been identified as the controlling mechanisms of OBP change at certain timescales. For instance, during the winter, storm systems over the Nordic Seas and Bering Strait increase in both frequency and intensity. This increased activity in the atmospheric field during the cold months results in increased inflow to the Arctic Ocean through Fram Strait and the Barents Sea Opening. The effects of the wintertime are thus not only observed at annual timescales, but from monthly timescales.

The pace of the Arctic change demands for the implementation and programs to create observing systems for monitoring variations in its atmosphere, terrestrial discharge, sea-ice and ocean. The satellite mission GRACE has proved to be an invaluable tool in the identification of mass changes, their accumulation, depletion and distribution on Earth (see *Chambers and Schröter* (2011) for a general overview on ocean findings), but very few studies have focused on the mass changes and distribu-

tion patterns in the Arctic Ocean. It is thus crucial to take advantage of the essentially full coverage of GRACE, and of upcoming gravitational and altimetry missions over the Arctic Ocean. The identification of month-to-month and inter-annual variations in OBP using EOFs clearly proves the capabilities of the satellite system to observe mass distribution in the Arctic Ocean. This dissertation justifies the need to maintain a long-term monitoring system of the Arctic Ocean like GRACE, complemented by high-frequency *in situ* observations to validate and improve post-processing methods of the remote sensing techniques.

Based on the results from this dissertation, at the timescales and the places where the Arctic Ocean is barotropic (all timescales in the coastal siberian shelves, up to seasonal timescales in the Barents Seas, and shorter than 100 days and seasonal timescales in the Kara Sea), GRACE OBP may be used to identify SSH variations. Analogously, satellite altimetry with polar orbit (e.g, Cryosat, or formerly ICESat) may be used to identify changes in the circulation that is dominated by barotropic motion. In those locations where the ocean circulation is predominantly barotropic through all timescales (i.e., Chukchi, East Siberian and Laptev seas), a longer record of GRACE would be fundamental to study the trend in SSH that has been reported by *Proshutinsky et al.* (2009) using available tide gauges, but the sparseness of the data in space and time have made this difficult to investigate.

The combination of altimetry and gravity measurements has offered a new technological resource to monitor circulation of the ocean at global and regional scales (*Chambers and Schröter*, 2011; *Morison et al.*, 2012; *Quinn and Ponte*, 2012). In the Arctic Ocean, this combination has yielded for the first time a complete picture of the changes in steric pressure, which yielded an estimate of the freshwater content and distribution in the Arctic Ocean. Thus, both types of measurements should be maintained as long as possible, if we are to understand changes in the Arctic system

and their potential effects on climate.

The ocean dynamics in the Kara Sea are of fundamental interest to the distribution and accumulation of freshwater content in the Arctic Ocean. Understanding these dynamics would allow to identify the effects of an increasing runoff input into the basin as the climate continues to warm. Evidence of increased discharge into the Arctic has been documented by *Shiklomanov and Lammers* (2009). It may be that increased runoff would continue to alter the SSH-OBP relation there, and this could begin to be observed also in the Laptev Sea within the next few years. Furthermore, as most of the freshwater content increase in the Canada basin is of Eurasian rivers origin (*Morison et al.*, 2012), close attention should be paid to monitoring the changes in the Eurasian runoff discharge into the Arctic.

5.4 Suggested future work

The research presented in this dissertation lays the path for future work with understanding Arctic Ocean circulation using OBP measurements.

The solutions of GRACE may also be further improved to remove terrestrial leakage into the ocean solutions, particularly in the Barents, Kara and Laptev seas, and north of Ellesmere Island. One suggestion is to apply the same method as for the Northern Greenland Sea and Svalbard, as performed by *Bonin and Chambers* (2012) for the analysis presented in this dissertation, or possibly applying the smoothing technique by *Böning et al.* (2008). Removing any leakage contamination from the GRACE solutions in the Kara Sea would not only greatly improve the correspondence between GRACE-derived OBP and *in situ* measurements where barotropic processes dominate this field (e.g., response of OBP and SSH to AO), but would also allow to quantify the steric contribution to the OBP field that are not fully accounted for by the models. For instance, the runoff contribution in both models is only of

climatologic origin, and net flow is not added into the ocean domain, but the salinity is adjusted in the regions near the river mouths. With the recent increase in Eurasian runoff, the OBP-SSH relationship would be expected to break-down even more.

Certainly the ideal solution to closely monitor the changes in ocean mass and the clear interpretation of OBP responding to SSH, would call for the long-term deployment of *in situ* bottom pressure sensors in different regions. The Kara Sea (e.g., deep western side, shallow in the middle, and shallow by the river mouths) would be one of the best seas to do so, to provide ground-truth validation of GRACE, and identify the freshwater input effects on the OBP field at different timescales, and how these changes may affect or be reflected in the circulation of the Arctic. The deployment of pressure sensors near the coastal regions of large glacier mass loss like Greenland would provide a complete validation of the leakage-removal technique implemented by *Bonin and Chambers* (2012), for the solutions of GRACE used in this dissertation.

BIBLIOGRAPHY

Aagaard, K., and E. Carmack (1989), The role of sea ice and other fresh water in the Arctic circulation., *J. of Geophys. Res.*, *94*, 14,485–14,498.

Aagaard, K., and R. A. Woodgate (2001), Some thoughts on the freezing and melting of sea ice and their effects on the ocean, *Ocean modelling*, *3*, 127–135.

ACIA (2006), Arctic climate impact assessment - scientific report, *Tech. rep.*, Cambridge University Press.

Antonov, J. I., S. Levitus, and T. P. Boyer (2002), Steric sea level variations during 1957−1994: Importance of salinity, *J. Geophys. Res.*, *107*(C12), 8013, doi: 10.1029/2001JC000964.

Bingham, R. J., and C. W. Hughes (2008), The relationship between sea-level and bottom pressure variability in an eddy permitting ocean model, *Geophys. Res. Lett.*, *35*, L03602.

Bonin, J. A., and D. P. Chambers (2011), Evaluation of high-frequency oceanographic signal in GRACE data: Implications for de-aliasing, *Geophys. Res. Lett.*, *38*, L17608, doi:10.1029/2011GL048881.

Bonin, J. A., and D. P. Chambers (2012), Uncertainty Estimates of GRACE Forward Modeling Technique over Greenland using a Simulation, *Submitted to Geophys. J. International*.

Böning, C., R. Timmermann, A. Macrander, and J. Schröter (2008), A pattern-filtering method for the determination of ocean bottom pressure anomalies from GRACE solutions, *Geophys. Res. Lett.*, *35*, L18611, doi:10.1029/2008GL034974.

Bretherton, C. S., C. Smith, and J. M. Wallace (1992), An Intercomparison of Methods for Finding Coupled Patterns in Climate Data, *J. Climate*, *5*, 541–560.

Chambers, D. P. (2006a), Observing seasonal steric sea level variations with GRACE and satellite altimetry, *J. of Geophys. Res.*, *111*, C03010.

Chambers, D. P. (2006b), Evaluation of new GRACE time-variable gravity data over the ocean, *Geophys. Res. Lett.*, *33*, L17603, doi:10.1029/2006GL027296.

Chambers, D. P., and J. Schröter (2011), Measuring ocean mass variability from satellite gravimetry, *J. of Geodynamics*, *52*, 333–343.

Chambers, D. P., and J. K. Willis (2009), Low-frequency exchange of mass between ocean basins, *J. Geophys. Res.*, *114*, C11008, doi:10.1029/2009JC005518.

Comiso, J. C., C. L. Parkinson, R. Gersten, and L. Stock (2008), Accelerated decline in the Arctic sea ice cover, *Geophys. Res. Lett.*, *35*, L01703, doi:10.1029/2007GL031972.

Dmitrenko, I. A., S. A. Kirillov, and L. B. Tremblay (2008a), The long-term and interannual variability of summer fresh water storage over the eastern Siberian shelf: Implication for climatic change, *Journal of Geophys. Research*, *113*, C03007, doi:10.1029/2007JC004304.

Dmitrenko, I. A., S. A. Kirillov, L. B. Tremblay, D. Bauch, and M. Makhotin (2008b), Effects of atmospheric vorticity on the seasonal hydrographic cycle over the eastern Siberian shelf, *Geophys. Res. Letters*, *35*, L03619, doi:10.1029/2007GL032739.

Dobslaw, H., and M. Thomas (2007), Impact of river run-off on global ocean mass redistribution, *Geophys. J. Int.*, *168*(2), 127–132, doi:10.1111/j.1365-246X.2006.03247.x.

Environmental Working Group (1997), Joint US-Russian Winter Atlas of the Arctic Ocean [cd-rom], Natl. Snow and Ice Data Cent., Boulder, Colorado.

Fukumori, I., D. Menemenlis, and T. Lee (2007), A Near-Uniform Basin-Wide Sea Level Fluctuation of the Mediterranean Sea, *J. of Phys. Oceanogr.*, *37*, 338–358.

Gerdes, R., M. Karcher, C. Köberle, and K. Fieg (2008), Simulating the Long-term variability of liquid freshwater export from the Arctic Ocean, in *Arctic–Subarctic Ocean Fluxes*, edited by R. R. Dickson, J. Meincke, and P. Rhines, pp. 405–425, Springer.

Giles, K. A., S. W. Laxon, A. L. Ridout, D. J. Wingham, and S. Bacon (2012), Westerm Arctic Ocean freshwater storage increases by wind-driven spin-up of the Beaufort Gyre, *Nature Geoscience*, *5*, 194–197, doi:10.1038/ngeo1379.

Gill, A. E. (1982), *Atmosphere-Ocean Dynamics*, 662 pp., Academic Press, New York.

Gill, A. E., and P. Niiler (1973), The theory of seasonal variability in the ocean, *Deep Sea Res.*, *20*(2), 141–177.

Grabs, W. E., F. Portmann, and T. de Couet (2000), Discharge observation networks in Arctic regions: Computation of the river runoff into the Arctic Ocean, its seasonality and variability, in *The Freshwater Budget of the Arctic Ocean*, edited by E. L. L. et al., pp. 249–267, Kluwer-Academic.

Greatbatch, R. J. (1994), A note on the representation of steric sea level in models

that conserve volume rather than mass, *Journal of Geophys. Research*, *99*(C6), 12,767–12,771.

Grinsted, A. J., C. Moore, and S. Jevrejeva (2004), Application of the cross wavelet transform and wavelet coherence to geophysical time series, *Nonlinear Processes in Geophysics*, *11*, 561–566.

Hanzlick, D. J. (1983), The West Spitsbergen Current: Transport, forcing and variability, Ph.D. thesis, University of Washington.

Hibler, W. D., and K. Bryan (1987), A diagnostic ice-ocean model, *J. Phys. Oceanogr.*, *7*, 987–1015.

Holloway, G., F. Dupont, E. Golubeva, S. Häkkinen, E. Hunke, M. Jin, M. Karcher, F. Kauker, M. Maltrud, M. A. M. Maqueda, W. Maslowski, G. Platov, D. Stark, M. Steele, T. Suzuki, J. Wang, and J. Zhang (2007), Water properties and circulation in Arctic Ocean models, *J. of Geophys. Res.*, *112*, C04S03, doi: 10.1029/2006JC003642.

Hu, A., G. A. Meehl, B. L. Otto-Bliesner, C. Waelbroeck, W. Han, M.-F. Loutre, K. Lambeck, J. X. Mitrovica, and N. Rosenbloom (2010), Influence of Bering Strait flow and North Atlantic circulation on glacial sea-level changes, *Nature geoscience*, *3*, 118–121.

Huang, R. X. (1993), Real freshwater flux as a natural boundary condition for the salinity balance and thermohaline circulation forced by evaporation and precipitation, *J. Phys. Oceanogr.*, *23*(11), 2428–2446.

Hughes, C. W., and V. N. Stepanov (2004), Ocean dynamics associated with rapid J_2 fluctuations: Importance of circumpolar modes and identification of a coherent Arctic mode, *J. of Geophys. Res.*, *109*, C06002.

Hunke, E. C., M. Maltrud, and M. Hecht (2008), On the grid dependence of lateral mixing parameterizations for global ocean simulations, *Ocean Modelling*, *20*, 115–133, doi:10.1016/j.ocemod.2007.06.010.

Ingvaldsen, R. B., L. Asplin, and H. Loeng (2004), Velocity field of the western entrance to the Barents Sea, *J. Geophys. Res.*, *109*, C03021.

Isachsen, P. E., J. H. LaCasce, C. Mauritzen, and S. Häkkinen (2003), Wind-driven variability of the large-scale recirculating flow in the Nordic Seas and Arctic Ocean, *J. of Phys. Oceanogr.*, *33*, 2534–2550.

Jahn, A., Y. Aksenov, B. A. de Cuevas, L. de Steur, S. Häkkinen, E. Hansen, C. Herbaut, M.-N. Houssais, M. Karcher, F. Kauker, C. Lique, A. Nguyen, P. Pemberton, D. Worthen, and J. Zhang (2012), Arctic Ocean freshwater: How robust are model simulations?, *Journal of Geophysical Research*, *117*, C00D16, doi: 10.1029/2012JC007907.

Jakobsson, M., R. Macnab, L. Mayer, R. Anderson, M. Edwards, J. Hatzky, H.-W. Schenke, and P. Johnson (2008), An improved bathymetric portrayal of the Arctic Ocean: Implications for ocean modeling and geological, geophysical and oceanographic analyses, *Geophysical Research Letters*, *35*, L07602, doi: 10.1029/2008GL033520.

Johannessen, O. M., L. Bengtsson, M. W. Miles, S. I. Kuzmina, V. A. Semenov, G. V. Alekseev, A. P. Nagurnyi, V. F. Zakharov, L. P. Bobylev, L. H. Pettersson, K. Hasselmann, and H. P. Cattle (2004), Arctic climate change: observed and modeled temperature and sea-ice variability, *Tellus*, *56*, 328–341.

Kalnay, E., M. Kanamitsu, R. Kistler, W. Collins, D. Deaven, L. Gandin, M. Iredell, S. Saha, G. White, J. Woollen, Y. Zhu, M. Chelliah, W. Ebisuzaki, W. Hig-

gins, J. Janowiak, K. C. Mo, C. Ropelewski, J. Wang, A. Leetmaa, R. Reynolds, R. Jenne, and D. Joseph (1996), The NCEPNCAR 40-year reanalysis project, *Bull. Am. Meteorol. Soc.*, *77*(3), 437–471.

Kanzow, T., F. Flechtner, A. Chave, R. Schmidt, P. Schwintzer, and U. Send (2005), Seasonal variation of ocean bottom pressure from Gravity Recovery and Climate Experiment (GRACE): Local validation and global patterns, *J. Geophys. Res.*, *110*, C09001, doi:10.1029/2004JC002772.

Karcher, M., A. Beszczynska-Möller, F. Kauker, R. Gerdes, S. Heyen, B. Rudels, and U. Schauer (2011), Arctic Ocean warming and its consequences for the Denmark Strait overflow, *J. Geophys. Res.*, *116*, C02037, doi:10.1029/2010JC006265.

Killett, B., J. Wahr, S. Desai, D. Yuan, and M. Watkins (2011), Arctic Ocean tides from GRACE satellite accelerations, *J. Geophys. Res.*, *116*, C11005, doi: 10.1029/2011JC007111.

Kwok, R., and J. Morison (2011), Dynamic topography of the ice-covered Arctic Ocean from ICESat, *Geophys. Res. Lett.*, *38*, L02501, doi:10.1029/2010GL046063.

Kwok, R., and D. A. Rothrock (2009), Decline in Arctic sea ice thickness from submarine and ICESat records: 1958 - 2008, *Geophys. Res. Lett.*, *36*, L15501, doi: 10.1029/2009GL039035.

Kwok, R., G. F. Cunningham, H. J. Zwally, and D. Yi (2006), ICESat over arctic sea ice: Interpretation of altimetric and reflectivity profiles, *J. Geophys. Res.*, *111*, C06006, doi:10.1029/2005JC003175.

Lammers, R. B., A. I. Shiklomanov, C. J. Vorosmarty, B. Fekete, and B. J. Peterson (2001), Assessment of contemporary Arctic river runoff based on observational discharge records, *J. Geophys. Res.*, *106*(D4), 3321–3334, doi:10.1029/2000JD900444.

Landerer, F. W., and S. C. Swenson (2012), Accuracy of scaled GRACE terrestrial water storage estimates, *Water Resources Research*, *48*, W04531, doi: 10.1029/2011WR011453.

Landerer, F. W., J. H. Jungclaus, and J. Marotzke (2007a), Regional dynamic and steric sea level change in response to the IPCC-A1B scenario, *J. Phys. Oceanogr.*, *37*(2), 296–312.

Landerer, F. W., J. H. Jungclaus, and J. Marotzke (2007b), Ocean bottom pressure changes lead to a decreasing length-of-day in a warming climate, *Geophys. Res. Lett.*, *34*, L06307, doi:10.1029/2006GL029106.

Landerer, F. W., J. H. Jungclaus, and J. Marotzke (2009), Long-term polar motion excited by ocean thermal expansion, *Geophys. Res. Letters*, *36*, L17603, doi: 10.1029/2009GL039692.

Loeng, H. (1991), Features of the physical oceanographic conditions of the Barents Sea, *National Institute Polar Research Memoirs*, *10*, 5–18, doi:10.1111/j.1751-8369.1991.tb00630.x.

Loeng, H., V. Ozhigin, and B. A. dlandsvik (1997), Water fluxes through the Barents Sea, *ICES J. of Marine Science*, *54*, 310–317.

Lombard, A., G. Garric, and T. Penduff (2009), Regional patterns of observed sea level change: insights from a 1/4° global ocean/sea-ice hindcast, *Ocean Dynamics*, *59*, 433–449, doi:10.1007/s10236-008-0161-6.

Luther, D., and A. Chave (1993), Observing integrating variables in the ocean, *Proceedings 7th Aha Huliko'a Hawaiian Winter Workshop on Statistical Methods in Physical Oceanography*, pp. 103–128.

McPhee, M. (2008), Turbulent Ocean Boundary Layer Exchange Processes, in *Air-Ice-Ocean Interaction*, Springer, New York.

McPhee, M. G., A. Proshutinsky, J. H. Morison, M. Steele, and M. B. Alkire (2009), Rapid change in freshwater content of the Arctic Ocean, *Geophys. Res. Letters*, *36*, L10602, doi:10.1029/2009GL037525.

Meinig, C., S. E. Stalin, A. I. Nakamura, and H. B. Milburn (2005), Real-Time Deep-Ocean Tsunami Measuring, Monitoring, and Reporting System: The NOAA DART II Description and Disclosure, http://www.ndbc.noaa.gov/dart/dart_ii_description_6_4_05.pdf.

Melling, H. (2000), Exchanges of freshwater through the shallow straits of the North American Arctic, in *The freshwater budget of the Arctic Ocean*, pp. 479–502, Kluwer Academic.

Melling, H., T. A. Agnew, K. K. Falkner, D. A. Greenberg, C. M. Lee, A. Münchow, B. Petrie, S. J. Prinsenberg, R. M. Samelson, and R. A. Woodgate (2008), Freshwater fluxes via Pacific and Arctic outflows across the Canadian Polar shelf, in *Arctic–Subarctic Ocean Fluxes*, edited by R. R. Dickson, J. Meincke, and P. Rhines, pp. 193–247, Springer.

Mellor, G. L., and T. Ezer (1995), Sea level variations induced by heating and cooling: An evaluation of the Boussinesq approximation in ocean models, *Journal of Geophys. Res.*, *100*(C10), 20,565–20,577.

Morison, J. (1991), Seasonal variations in the West Spitsbergen Current estimated from bottom pressure measurements, *J. Geophys. Res.*, *96*(C10), 18,381–18,395.

Morison, J., K. Aagaard, and M. Steele (2000), Recent environmental changes in the Arctic: A review, *Arctic*, *53*(4), 359–371.

Morison, J., M. Steele, T. Kikuchi, K. Falkner, and W. Smethie (2006), Relaxation of central Arctic Ocean hydrography to pre-1990s climatology, *Geophys. Res. Lett.*, *33*, L17604.

Morison, J., J. Wahr, R. Kwok, and C. Peralta-Ferriz (2007), Recent trends in Arctic Ocean mass distribution revealed by GRACE, *Geophys. Res. Lett.*, *34*, L07602, doi:10.1029/2006GL029016.

Morison, J., R. Kwok, C. Peralta-Ferriz, M. Alkire, I. Rigor, R. Andersen, and M. Steele (2012), Changing Arctic Ocean Freshwater Pathways Measured with ICESat and GRACE, *Nature*, pp. 66–70.

Morison, J. H., M. Steele, and R. Andersen (1998), Hydrography of the upper Arctic Ocean measured from the nuclear submarine USS Pargo, *Deep Sea Res. Part I*, *45*, 15–38.

Münchow, A., K. K. Falkner, and H. Melling (2007), Spatial continuity of measured seawater and tracer fluxes through Nares Strait, a dynamically wide channel bordering the Canadian Archipelago, *J. of Marine Research*, *65*, 759–788.

Munekane, H. (2007), Ocean mass variations from GRACE and tsunami gauges, *J. of Marine Research*, *112*, B07403, doi:10.1029/2006JB004618.

Neumann, G., and W. J. P. jr. (1966), *Principles of Physical Oceanography*, Prentice-Hall, Englewood Cliffs, N. J.

Nguyen, A. T., D. Menemenlis, and R. Kwok (2011), Arctic ice-ocean simulation with optimized model parameters: Approach and assessment, *J. Geophys. Res.*, *116*.

North, G. R., T. L. Bell, and R. F. Cahalan (1982), Sampling Errors in the Estimation of Empirical Orthogonal Functions, *Mon. Weather Rev.*, *110*(7), 699–706.

Nøst, O. A., and P. E. Isachsen (2003), The large-scale time-mean ocean circulation in the Nordic Seas and Arctic Ocean estimated from simplified dynamics., *J. of Marine Res.*, *61*, 175–210.

Ogi, M., and J. M. Wallace (2007), Summer minimum Arctic sea ice extent and the associated summer atmospheric circulation, *Geophys. Res. Lett.*, *34*, L12705, doi:10.1029/2007GL029897.

Ogi, M., and J. M. Wallace (2012), The role of summer surface wind anomalies in the summer Arctic sea ice extent in 2010 and 2011, *Geophys. Res. Lett.*, *39*, L09704, doi:10.1029/2012GL051330.

Onogi, K., J. Tsutsui, H. Koide, M. Sakamoto, S. Kobayashi, H. Hatsushika, T. Matsumoto, N. Yamazaki, K. Takahashi, S. Kadokura, K. Wada, K. Kato, R. Oyama, T. Ose, N. Mannoji, and R. Taira (2007), The JRA-25 Reanalysis., *J. Meteorol. Soc. Jpn.*, *85*(3), 369–432, doi:10.2151/jmsj.85.369.

Overland, J. E., M. Wang, and S. Salo (2008), The recent Arctic warm period, *Tellus*, *60*(4), 589–597, doi:10.1111/j.1600-0870.2008.00327.x.

Padman, L., and S. Erofeeva (2004), A barotropic inverse tidal model for the Arctic Ocean, *Geophys. Res. Lett.*, *31*, L02303, doi:10.1029/2003GL019003.

Park, J. H., D. R. Watts, K. A. Donohue, and S. R. Jayne (2008), A comparison of in situ bottom pressure array measurements with GRACE estimates in the Kuroshio Extension, *Geophys. Res. Lett.*, *35*, L17601, doi:10.1029/2008GL034778.

Paulson, A., S. Zhong, and J. Wahr (2007), Inference of mantle viscosity from GRACE and relative sea level data, *Geophys. J. Int.*, *171*, 497–508, doi:10.1111/j.1365-246X.2007.03556.x.

Pawlowicz, R., B. Beardsley, and S. Lentz (2002), Classical tidal harmonic analysis including error estimates in MATLAB using t_tide, *Comput. Geosci.*, *28*, 929–937.

Peralta-Ferriz, C., and J. Morison (2010), Understanding the annual cycle of the Arctic Ocean bottom pressure, *Geophys. Res. Lett.*, *37*, L10603, doi: 10.1029/2010GL042827.

Peralta-Ferriz, C., J. Morison, J. M. Wallace, and J. Zhang (2011), A basin-coherent mode of sub-monthly variability in Arctic Ocean bottom, *Geophys. Res. Lett.*, *38*, L14606, doi:10.1029/2011GL048142.

Perovich, D. K., B. Light, H. Eicken, K. F. Jones, K. Runciman, and S. V. Nghiem (2007), Increasing solar heating of the Arctic Ocean and adjacent seas, 1979-2005: Attribution and role in the ice-albedo feedback, *Geophys. Res. Lett.*, *34*, L19505, doi:10.1029/2007GL031480.

Polyakov, I. V., L. A. Timokhov, V. A. Alexeev, S. Bacon, I. A. Dmitrenko, L. Fortier, I. E. Frolov, J.-C. Gascard, E. Hansen, V. V. Ivanov, S. Laxon, C. Mauritzen, D. Perovich, K. Shimada, H. L. Simmons, V. T. Sokolov, M. Steele, and J. Toole (2010), Arctic Ocean Warming Contributes to Reduced Polar Ice Cap, *Phys. Oceanogr.*, *40*, 2743–2756.

Ponte, R. M. (1999), A preliminary model study of the large-scale seasonal cycle in bottom pressure over the global ocean, *J. Geophys. Res.*, *104*(C1), 1289–1300.

Ponte, R. M., D. A. Salstein, and R. D. Rosen (1991), Sea level response to pressure forcing in a barotropic numerical model, *J. Phys. Oceanogr.*, *21*, 1043–1057.

Ponte, R. M., K. J. Quinn, C. Wunsch, and P. Heimbach (2007), A comparison of model and GRACE estimates of the large-scale seasonal cycle in ocean bottom pressure, *Geophys. Res. Lett.*, *34*(L09603).

Prinsenberg, S. J., and J. Hamilton (2005), Observing and interpreting the seasonal variability of the oceanographic fluxes passing through Lancaster Sound of the Canadian Arctic Archipelago, *Atmosphere-Ocean*, *43*(1), 1–22.

Program, W. C. R. (1998), Report of the ACSYS workshop on status and directions for the Arctic runoff data base., arctic climate system study, report, Geneva Switzerland.

Proshutinsky, A. R., R. Krishfield, M.-L. Timmermans, J. Toole, E. Carmack, F. McLaughlin, W. J. Williams, S. Zimmermann, M. Itoh, and K. Shimada (2009), Beaufort Gyre freshwater reservoir: State and variability from observations, *J. Geophys. Res.*, *114*, C00A10.

Quinn, K. J., and R. M. Ponte (2012), High frequency barotropic ocean variability observed by grace and satellite altimetry, *Geophys. Res. Lett*, *39*, L07603, doi: 10.1029/2012GL051301.

Rabe, B., M. Karcher, U. Schauer, J. M. Toole, R. A. Krishfield, S. Pisarev, F. Kauker, R. Gerdes, and T. Kikuchi (2011), An assessment of Arctic Ocean freshwater content changes from the 1990s to the 2006-2008 period, *Deep-Sea Research Part I: Oceanographic Research Papers*, *58*(2), 173–185.

Rainville, L., and R. A. Woodgate (2009), Observations of internal wave generation in the seasonally ice-free Arctic, *Geophys. Res. Lett*, *36*, L23604, doi: 10.1029/2009GL041291.

Rennert, K. J., and J. M. Wallace (2009), Cross-Frequency Coupling, Skewness, and Blocking in the Northern Hemisphere Winter Circulation, *J. of Climate*, *22*(21), 5650–5666.

Rietbroek, R., P. LeGrand, B. Wouters, J.-M. Lemoine, G. Ramillien, and C. W. Hughes (2006), Comparison of in situ bottom pressure data with GRACE gravimetry in the Crozet-Kerguelen region, *Geophys. Res. Lett.*, *33*, L21601, doi: 10.1029/2006GL027452.

Rigor, I. G. (2005), Interdecadal Variations in Arctic Sea ice, Ph.D. thesis, Dept. of Atmospheric Sciences.

Rigor, I. G., and J. M. Wallace (2004), Variations in the age of Arctic sea-ice and summer sea-ice extent, *Geophys. Res. Lett.*, *31*(L09401).

Rigor, I. G., J. M. Wallace, and R. L. Colony (2002), Response of Sea Ice to the Arctic Oscillation, *J. of Climate*, *15*, 2648–2663.

Roach, A. T., K. Aagaard, C. H. Pease, S. A. Salo, T. Weingartner, V. Pavlov, and M. Kulakov (1995), Direct measurements of transport and water properties through Bering Strait, *J. Geophys. Res.*, *100*, 18,443–18,457.

Roussenov, V. M., R. G. Williams, C. W. Hughes, and R. J. Bingham (2008), Boundary wave communication of bottom pressure and overturning changes for the North Atlantic, *J. Geophys. Res.*, *113*, C08042.

Rudels, B., H. J. Friedrich, and D. Quadfasel (1999), The Arctic Circumpolar Boundary Current, *Deep Sea Research Part II: Topical Studies in Oceanography*, *46*(6-7), 1023 – 1062, doi:10.1016/S0967-0645(99)00015-6.

Saloranta, T. M., and H. Svendsen (2001), Across the Arctic front west of Spitsbergen: High resolution CTD sections from 1998 - 2000, *Polar Res.*, *20*(2), 177–184.

Schauer, U., E. Fahrbach, S. Osterhus, and G. Rohardt (2004), Arctic warming

through the Fram Strait: Oceanic heat transport from 3 years of measurements, *J. Geophys. Res.*, *109*, C06026, doi:10.1029/2003JC001823.

Schauer, U., A. Beszczynska-Möller, W. Walczowski, E. Fahrbach, J. Piechura, and E. Hansen (2008), Variation of measured heat flow through the Fram Strait between 1997 and 2006., in *Arctic-Subarctic Ocean Fluxes*, edited by R. R. Dickson, J. Meincke, and P. Rhines, pp. 385–404, Springer.

Serreze, M. C., A. P. Barrett, A. G. Slater, R. A. Woodgate, K. Aagaard, R. B. Lammers, M. Steele, R. Moritz, M. Meredith, and C. M. Lee (2006), The large-scale freshwater cycle of the Arctic, *J. Geophys. Res.*, *111*, C11010, doi:10.1029/2005JC003424.

Shiklomanov, A. I., and R. B. Lammers (2009), Record Russian river discharge in 2007 and the limits of analysis., *Environ. Res. Lett.*, *4*(4), 045015, doi:10.1088/1748-9326/4/4/045015.

Spielhagen, R. F., K. Werner, S. A. S. rensen, K. Zamelczyk, E. Kandiano, G. Budeus, K. Husum, T. M. Marchitto, and M. Hald (2011), Enhanced Modern Heat Transfer to the Arctic by Warm Atlantic Water, *Science*, *331*(6016), 450–453.

Steele, M., and T. Boyd (1998), Retreat of the cold halocline layer in the Arctic Ocean, *J. Geophys. Res.*, *103*(C5), 10,419–10,435, doi:10.1029/98JC00580.

Steele, M., J. Morison, and T. Curtin (1995), Halocline water formation in the Barents Sea, *J. Geophys. Res.*, *100*, 881–894, doi:10.1029/94JC02310.

Steele, M., J. Morison, W. Ermold, I. Rigor, M. Ortmeyer, , and K. Shimada (2004), Circulation of summer Pacific halocline water in the Arctic Ocean, *J. Geophys. Res.*, *109*, C02027, doi:10.1029/2003JC002009.

Steele, M., W. Ermold, and J. Zhang (2008), Arctic Ocean surface warming trends over the past 100 years, *Geophys. Res. Lett.*, *35*, L02614, doi: 10.1029/2007GL031651.

Stepanov, V. N., and C. W. Hughes (2006), Propagation of signals in basin-scale ocean bottom pressure from a barotropic model, *J. Geophys. Res.*, *111*, C12002, doi:10.1029/2005JC003450.

Stroeve, J., M. M. Holland, W. Meier, T. Scambos, and M. Serreze (2007), Arctic sea ice decline: Faster than forecast, *Geophys. Res. Lett.*, *34*, L09501, doi: 10.1029/2007GL029703.

Stroeve, J., A. Frei, J. McCreight, and D. Ghatak (2008), Arctic sea-ice variability revisited, *Annals of Glaciology*, *48*, 71–81.

Su, F., J. C. Adam, L. C. Bowling, and D. P. Lettenmaier (2005), Streamflow simulations of the terrestrial Arctic domain, *J. Geophys. Res.*, *110*, C08112, doi: 10.1029/2004JD005518.

Swenson, S. C., and J. Wahr (2006), Post-processing removal of correlated errors in GRACE data, *Geophys. Res. Letters*, *33*, L08402, doi:10.1029/2004GL019920.

Tapley, B. D., S. Bettadpur, M. Watkins, and C. Reigber (2004), The gravity recovery and climate experiment: Mission overview and early results, *Geophys. Res. Lett.*, *31*, L09607, doi:10.1029/2004GL019920.

Teigen, S. H., F. Nilsen, and B. Gjevik (2010), Barotropic instability in the West Spitsbergen Current, *J. Geophys. Res.*, *115*, C07016.

Thompson, D. W., and J. M. Wallace (1998), The Arctic Oscillation signature in the

winter-time geopotential height and temperature fields, *Geophys. Res. Lett.*, *25*, 1297 – 1300.

Thorndike, A. S., and R. Colony (1982), Sea Ice Motion in Response to Geostrophic Winds, *J. Geophys. Res.*, *87*(C8), 5845 – 5852, doi:10.1029/JC087iC08p05845.

Torrence, C., and G. P. Compo (1998), A practical guide to wavelet analysis, *Bull. of Am. Meteor. Soc.*, *79*, 61–78.

Tsukernik, M., C. Deser, M. Alexander, and R. Tomas (2009), Atmospheric forcing of Fram Strait sea ice export: A closer look., *Climate Dyn.*, doi:10.1007/s00382-009-0647-z.

Vinogradova, N. T., R. M. Ponte, and D. Stammer (2007), Relation between sea level and bottom pressure and the vertical dependence of oceanic variability, *Geophys. Res. Lett.*, *34*, L03608, doi:10.1029/2006GL028588.

Wadley, M. R., and G. R. Bigg (2002), Impact of flow through the Canadian Archipelago and Bering Strait on the North Atlantic and Arctic circulation: An ocean modelling study, *Q. J. R. Meteorol. Soc.*, *128*, 2187–2203.

Wahr, J. M., M. Molenaar, and F. O. Bryan (1998), Time variability of the Earth's gravity field: Hydrological and oceanic effect and their possible detection using GRACE, *J. Geophys. Res.*, *103*, 30,205 – 30,229.

Wassmann, P., C. M. Duarte, S. Agusti, and M. K. Sejr (2010), Footprints of climate change in the Arctic marine ecosystem, *Global Change Biology*, *17*(2), 1,235–1,249.

Woodgate, R. A., and K. Aagaard (2005), Revising the Bering Strait freshwater flux into the Arctic Ocean., *Geophys. Res. Lett.*, *32*, L02602, doi:10.1029/2004GL021747.

Woodgate, R. A., K. Aagaard, and T. J. Weingartner (2006), Interannual changes in the Bering Strait fluxes of volume, heat and freshwater between 1991 and 2004., *Geophysical Research Letters*, *33*, L15609, doi:10.1029/2006GL026931.

Woodgate, R. A., T. Weingartner, and R. Lindsay (2010), The 2007 Bering Strait oceanic heat flux and anomalous Arctic sea-ice retreat, *Geophys. Res. Lett.*, *37*, L01602, doi:10.1029/2009GL041621.

Wunsch, C., and D. Stammer (1997), Atmospheric loading and the oceanic 'inverted barometer' effect, *Reviews of Geophysics*, *31*(1), 79–107.

Zhang, J., and D. A. Rothrock (2003), Modeling global sea ice with a thickness and enthalpy distribution model in generalized curvilinear coordinates, *Mon. Weather Rev.*, *131*, 845–861.

Appendix A

SUB-MONTHLY VARIABILITY IN ARCTIC OCEAN BOTTOM PRESSURE

PUBLISHED IN: Peralta-Ferriz, C., J. H. Morison, J. M. Wallace, J. Zhang (2011), A basin-coherent mode of sub-monthly variability in Arctic Ocean bottom pressure, Geophys. Res. Lett., 38, L14606, doi:10.1029/2011GL048142.

A basin-coherent mode of sub-monthly variability in Arctic Ocean bottom pressure

Cecilia Peralta-Ferriz,[1] James H. Morison,[1] John M. Wallace,[2] and Jinlun Zhang[1]

Received 16 May 2011; revised 9 June 2011; accepted 10 June 2011; published 22 July 2011.

[1] A sub-monthly mode of non-tidal variability of ocean bottom pressure (OBP) is observed in a 5-year record of deep-sea bottom pressure at the North Pole. OBP records from other regions in the Arctic show that the North Pole non-tidal mass fluctuation is part of a non-propagating basin-coherent variation that is well represented by the ice-ocean model PIOMAS, with a basin-averaged winter-only RMS of 3.3 cm. Wavelet analysis of the modeled OBP shows that the basin-averaged mass variations are non-stationary and only significant during the winter. The basin-averaged OBP is strongly related to the meridional wind component over the Nordic Seas. The ocean response is consistent with episodic wind forcing driving a northward geostrophic slope current. The mass transport anomaly associated with the mode is significant relative to the annual net mean flow. **Citation:** Peralta-Ferriz, C., J. H. Morison, J. M. Wallace, and J. Zhang (2011), A basin-coherent mode of sub-monthly variability in Arctic Ocean bottom pressure, *Geophys. Res. Lett.*, *38*, L14606, doi:10.1029/2011GL048142.

1. Introduction

[2] Mass fluxes into and out of the Arctic Ocean are fundamental to the distribution of heat and freshwater. Changes in these are of major concern due to their possible linkages with global climate, for example, by controlling stratification in the sub-Arctic seas and thereby modulating convection and the meridional overturning circulation. Direct measurements of the fluxes are challenged by spatial and temporal variability. In this paper we explore a heretofore-unknown sub-monthly mode of Arctic Ocean variability recorded by *in situ* ocean bottom pressure (OBP) measurements. We examine its effects on the circulation and the mass fluxes into and out of the Arctic basin using output from an ice-ocean model. The analysis of sub-monthly variations in Arctic Ocean mass and mass flux is feasible in part due to advances in ice-ocean modeling and also because we now have deep sea *in situ* observations of OBP that represent an integral measurement inherently less sensitive to high frequency noise than direct flux measurements.

[3] The first hints of the sub-monthly variations in Arctic OBP actually came from pairs of deep-sea pressure gauges monitoring the West Spitsbergen Current [*Morison*, 1991]. These showed OBP variations with a 19-day period, but the spatial extent and significance of the variations were unknown. Now we have sufficient observations and model results to show that sub-monthly variations in Arctic Ocean mass are significant compared to the mean fluxes into the basin, and to understand the associated circulation patterns.

2. Observations and Model Output

[4] Our observations come from pressure and tide gauges across the Arctic Ocean, shown in Figure 1. In conjunction with the North Pole Environmental Observatory program we deployed two Arctic bottom pressure recorders (ABPR) near the North Pole, ABPR1 at 89° 15.26′ N, 60° 21.58′ E, and ABPR3 at 89° 14.85′ N, 148° 7.54′ E [*Morison et al.*, 2007]. ABPR1 recorded five full continuous years, from Spring 2005 to Spring 2010, and ABPR3 worked continuously for 3 years. Long-term drift errors in the later part of ABPR records were removed using monthly OBP observations from the Gravity Recovery and Climate Experiment, without compromising the high-frequency variations in OBP. The resulting de-trended records of the two ABPRs are highly correlated (R = 0.99). We averaged the first three years of data of both ABPR records (available at http://psc.apl.washington.edu/northpole/) to form a single record representative of the North Pole, and used ABPR1 data collected in April 2010 to complete the 5-year record.

[5] We also use time series from bottom pressure recorders (BPR) deployed by the Beaufort Gyre Exploration Project, BGEP, at a) 75° 0.449′N, 149° 58.660′W, b) 78° 1.49′N, 149° 49.203′W, and c) 76° 59.232′N, 139° 54.563′W (http://www.whoi.edu/beaufortgyre/data_moorings.html/), from August 2003 to August 2008. The BGEP OBP records are highly correlated with each other so we average them to obtain a single OBP record in the Beaufort Sea. OBP data from Pressure Inverted Echo Sounders deployed by the Alfred Wegener Institute at a) 78°49.93′N, 005°00.87′E, b) 78°49.87′N, 002°47.59′E and c) 78°50.03′N, 008°19.91′E (A. Beszczynska-Möller, personal communication, 2007), were averaged to give a time series of OBP representative of Fram Strait, from September 2003 to August 2006.

[6] Tide gauge records are used from 2 locations on the Canadian Arctic Shelf, in Alert at 82° 29.51′ N, 62° 19′ W, from 2004 to 2007, and Holman at 70° 44.21′ N, 117° 45.5′W, from 2003 to 2008 (http://www.meds-sdmm.dfo-mpo.gc.ca/isdm-gdsi/twl-mne/inventory-inventaire/index-eng.htm). These were corrected for the inverted-barometer effect to yield bottom pressure, using local sea level pressure (SLP) from NCEP/NCAR reanalysis [*Kalnay et al.*, 1996]. For the analysis of large-scale atmospheric patterns driving the ocean mass variations, we use daily SLP and winds at 925 hPa from the NCEP/NCAR reanalysis, from January 2000 to December 2009, north of 30°N.

[1]Polar Science Center, Applied Physics Laboratory, University of Washington, Seattle, Washington, USA.
[2]Department of Atmospheric Sciences, University of Washington, Seattle, Washington, USA.

0094-8276/11/2011GL048142

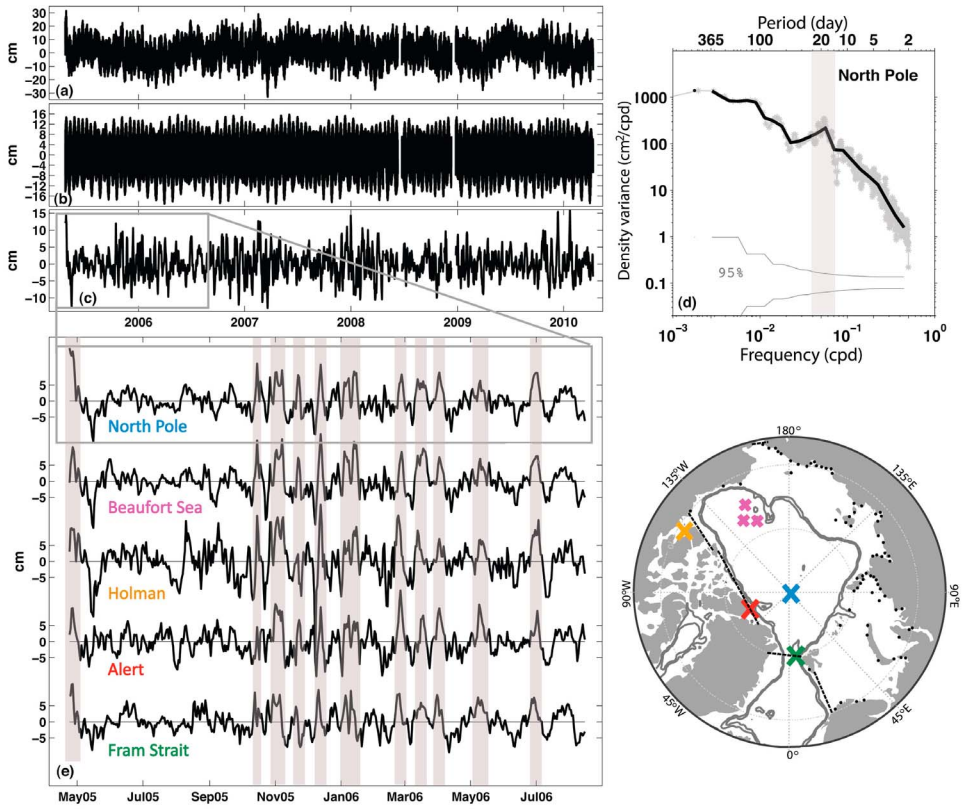

Figure 1. (a) De-trended, hourly ocean bottom pressure anomalies at the North Pole. (b) Tide signal extracted from Figure 1a. (c) North Pole daily non-tidal high-pass filtered OBP anomalies. (d) Power spectrum of the North Pole non-tidal OBP record (gray dots), smoothed spectrum (black) and the 95% confidence interval (thin gray). Shaded line highlights the 15–30 day period range. (e) Daily non-tidal high-pass filtered OBP records from Spring 2005 to Summer 2006 in five regions, color-coded in the map. Shaded lines highlight the coherence of OBP variations among regions. The map shows the regions of the OBP records, and the black dashed-lines delimit the area of the basin-averaged OBP from the model. Black dots in the map show the approximate location of the tide gauges of *Hughes and Stepanov* [2004], and gray lines show the 500 and 1000 m isobaths.

[7] All OBP records are de-tided using the Matlab program t_tide [*Pawlowicz et al.*, 2002], and averaged daily. To emphasize the sub-monthly variations, the de-tided OBP data are high-pass filtered with a 90-day cutoff period. We give OBP in cm of water equivalent.

[8] In addition to *in situ* observations, we analyze the daily output of OBP, SSH and depth-dependant horizontal velocity from the Pan-Arctic Ice Ocean Modeling Assimilation System, PIOMAS [*Zhang and Rothrock*, 2003]. PIOMAS is a regional baroclinic ice-ocean model with 30 vertical levels and maximum spatial resolution of ~20 km. PIOMAS is one-way nested to a global ocean model at 49°N, and is forced by the winds and surface atmospheric pressure from NCEP/NCAR reanalysis data. The model does not include tides, and assumes a perfect inverted barometer effect.

3. Ocean Bottom Pressure Variability

[9] Our five-year hourly time series of OBP at the North Pole (Figure 1) represents the longest OBP record in the central Arctic. The high-pass filtered data reveals winter amplification of OBP variations (Figure 1). The RMS variance of the high-pass filtered, de-tided record is 4 cm, and the winter-only RMS is 4.6 cm. The power spectrum of the unfiltered OBP record at the North Pole shows a spectral peak around 0.05 cycles per day (cpd, ~20 days, Figure 1). Although its statistical significance is not far above the noise level, it resembles the OBP variations in the West Spitsbergen Current reported by *Morison* [1991].

[10] All the OBP records used here overlap from April 2005 to August 2006. Similar to the records from the North Pole, we high-pass filter each time series and compare the OBP anomalies among regions. All records in the 5 regions are highly correlated with each other (at better than the 95% confidence level, R = 0.58 to 0.9, Table S1 in the auxiliary material) with no lag, except for the record from Fram Strait, which leads all the others by 1 day.[1]

[11] Large-scale coherent variations of OBP in the Arctic Ocean have been previously identified using modeling results [*Hughes and Stepanov*, 2004]. These agreed with tide gauge records from shallow regions of the Arctic, but most of the observations were from the Russian and Scandinavian continental shelves (Figure 1). Hence, the full spatial extent of the mass oscillation was not confirmed.

[1] Auxiliary materials are available in the HTML. doi:10.1029/2011GL048142.

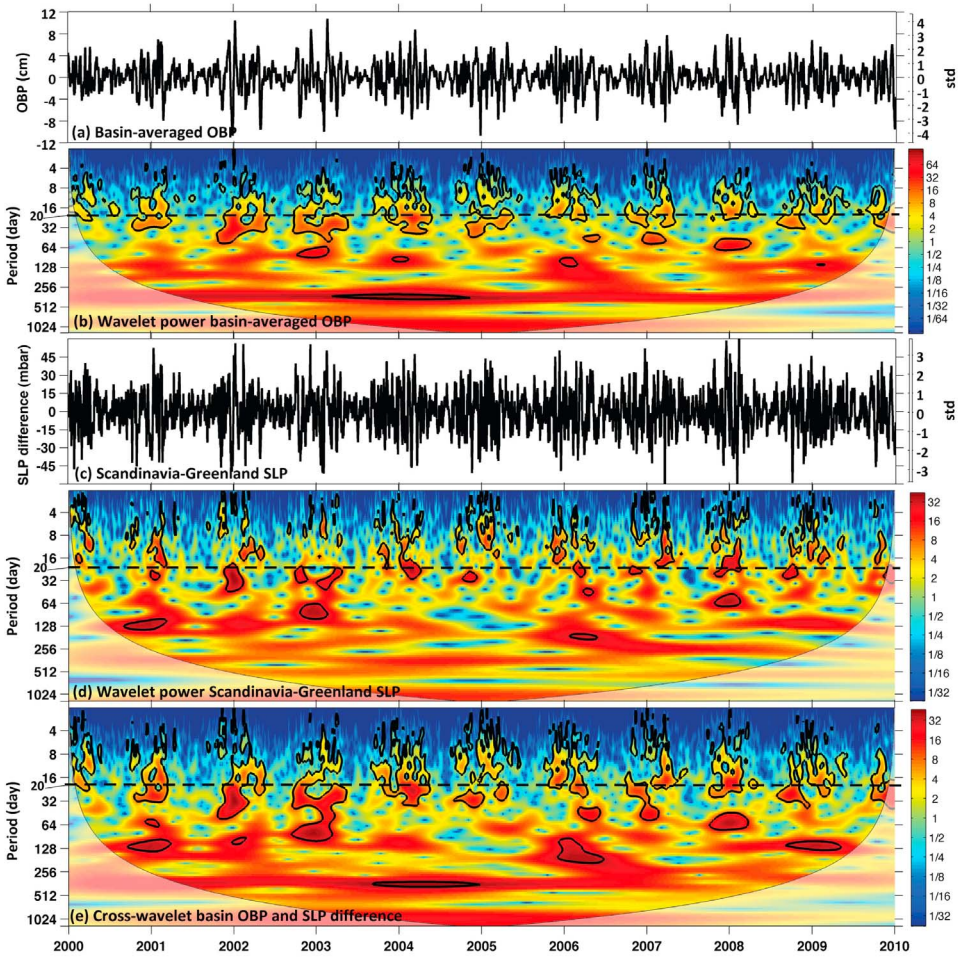

Figure 2. (a) Time series of daily non-tidal high-pass filtered basin-averaged OBP from the model. (b) Normalized wavelet power of the unfiltered time series of basin-averaged OBP. Black contour is the 95% confidence level, and the faint area is the cone of influence. Dashed black line shows the 20-day period for reference. (c) Same as Figure 2a but for the SLP gradient. (d) Same as Figure 2b but for the SLP gradient. (e) Cross wavelet transform between basin-averaged OBP and SLP gradient.

Also, the OBP records of *Hughes and Stepanov* [2004] were analyzed in monthly averages, for which a sub-monthly oscillation could have not been detected and may have been aliased into the monthly values. Our pressure record compilation suggests that the sub-monthly oscillation is indeed a basin-wide mode of OBP variability, with coherent anomalies in both the shallow Western and deep Central Arctic Ocean, at zero lag.

[12] The non-tidal high-pass filtered observations of OBP variations are well represented by the filtered OBP from PIOMAS at all five regions. Although the model tends to underestimate the observed amplitudes, all model-*in situ* correlation coefficients are above R = 0.53 and are significant at better than the 95% confidence level (Table S1 in the auxiliary material). Therefore, we average the daily PIOMAS OBP output from 2000 to 2009 over the Arctic basin, delimited by Fram Strait, the Barents Sea entrance path, the Bering Strait and the northern passages into the Canadian Archipelago (CA). The ocean mass within the CA is not included in the average (see map in Figure 1).

[13] The high-pass filtered basin-averaged OBP from the model captures the observed winter amplification of OBP (Figure 2a). The RMS variance of the high-pass filtered basin-averaged OBP is 2.6 cm, and the winter-only RMS variance is 3.3 cm.

[14] Year to year variations in the observed OBP suggests that the signal is non-stationary. To test this, we perform a wavelet analysis on the unfiltered basin-averaged OBP. We use a Morlet mother wavelet, and a Monte Carlo simulation to extract the significance of the wavelet power, tested against red noise [*Grinsted et al.*, 2004; *Torrence and Compo*, 1998]. The wavelet power spectrum of the basin-averaged OBP is shown in Figure 2b. The sub-monthly peaks are only significant during the winters and typical periods for individual years range from 15 to 30 days.

4. Atmospheric Forcing

[15] A regression map of the SLP and wind field at 925 hPa, projected on the modeled standardized basin-averaged OBP of Figure 2a (Figure 3) shows that the basin-averaged OBP is highly correlated with the sea level atmospheric pressure gradient between Scandinavia and Greenland and southerly winds in the Nordic Seas. To

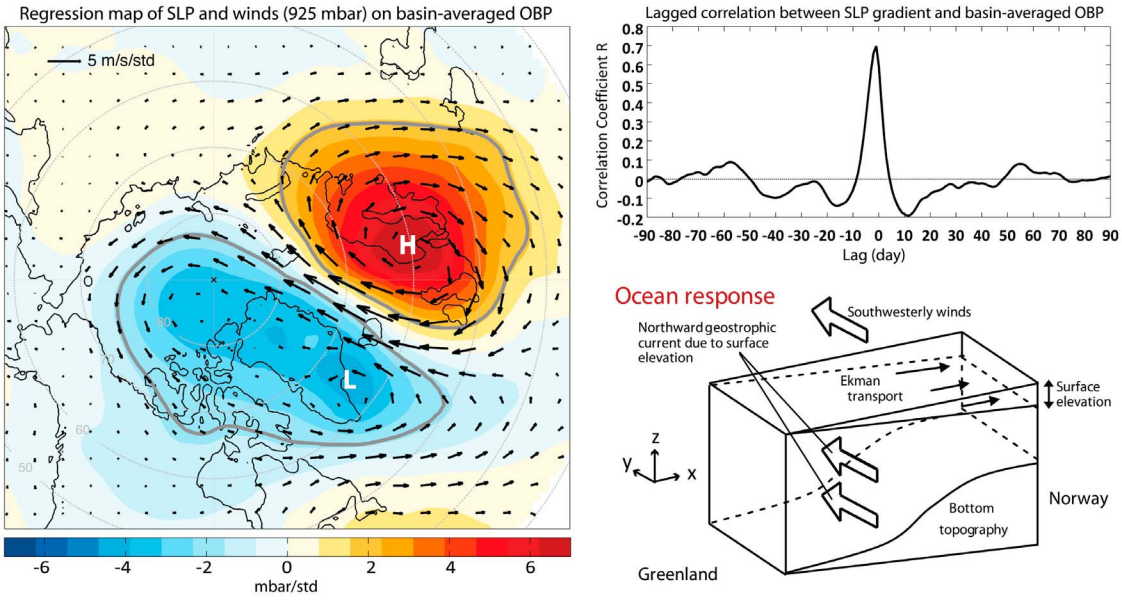

Figure 3. (left) Map shows the NCEP/NCAR SLP (color contours) and winds at 925 mbar (vectors) regressed on the normalized basin-averaged OBP of Figure 2; the gray line is the 95% confidence level of the correlation between SLP gradient and basin-averaged OBP. (top right) The cross-correlation between SLP gradient and basin-averaged OBP. Maximum correlation is 0.7 with the OBP lagging SLP by 2 days. (bottom right) The hypothetical ocean response to SLP through a wind-driven slope current.

characterize the SLP gradient, we select the locations with the largest positive and negative correlation coefficients between SLP and basin-averaged OBP (Figure 3). We refer to the difference in SLP between these two locations as the SLP gradient time series (Figure 2c). The maximum correlation with the daily basin-averaged OBP is with SLP gradient leading OBP by 2 days (Figure 3). The atmospheric pattern associated with the basin OBP variation is consistent with a wind-driven slope current through the Nordic Seas, as illustrated in Figure 3.

[16] The time series and the wavelet power of the SLP gradient are shown in Figures 2c and 2d. The SLP gradient, consistent with the basin-averaged OBP, shows the winter increase in energy (Figure S1 in the auxiliary material), and the strongest energy of the SLP gradient is concentrated within the 5–30 day period range. The cross-wavelet power between SLP gradient and basin-averaged OBP (Figure 2e) indicates that both time series share the high-energy episodes, and their common power is largest at the sub-monthly scale (~15–30 day periods), with lags ranging from near 0° to ~30°. The regression map (Figure 3) and the wavelet results suggest that the wintertime variations in basin OBP are forced by the atmospheric circulation. The sea level pressure regression pattern shown in Figure 3 strongly resembles the leading empirical orthogonal function of 6–30 day bandpass filtered 500-hPa height over the Atlantic sector [*Rennert and Wallace*, 2009, Figure 2]. The prevalence of this pattern is attributable to the episodic occurrence of blocking events.

[17] Additional atmospheric forcing enhances the mass entering the basin through the Bering Strait, as suggested by the regression maps of SLP projected onto modeled OBP at individual locations in the basin closer to the Bering Strait pathway (Figure S1 in the auxiliary material). However, there is no correlation between basin-averaged OBP and SLP near the Bering Strait (Figure 3).

5. Ocean Circulation and Mass Exchange Associated With the Sub-monthly Mode

[18] Ocean circulation changes at sub-monthly timescales are barotropic [*Vinogradova et al.*, 2007; *Bingham and Hughes*, 2008], and for which we use depth-integrated only velocity fields from PIOMAS. Composite maps of the PIOMAS model anomalies of SSH and depth-integrated velocity field (mSv per unit length = 10^3 m^2s^{-1}), reveal the ocean circulation at times of maximum and minimum basin-averaged OBP and the state 3 and 6 days before and after the maximum basin-averaged OBP (Figure 4). The composites for maximum and minimum average OBP are based on the dates when OBP anomaly exceeds 1.5 standard deviations, which occurs only during winter (n = 42 dates over the 10 years analyzed, Figure 2a). We then generate the composites of the flow through Bering Strait, Fram Strait, Barents Sea path and the CA, to the Arctic Ocean, and the total net volume flow into the basin (Table S2 in the auxiliary material).

[19] The SLP pattern observed in association with enhanced southwesterly winds (i.e., high over Scandinavia and low over Greenland) is first discernible six days prior to maximum average OBP. The resultant SSH gradient yields the aforementioned slope current into the Arctic Ocean (Figure 3). This sets up gyre circulation patterns, cyclonic at maximum average OBP and anticyclonic at minimum OBP in the Eurasian Basin, with counter-rotating patterns in the Nordic Seas (Figure 4).

[20] During the maximum and minimum basin-averaged OBP, there is minimum mass exchange between Arctic and

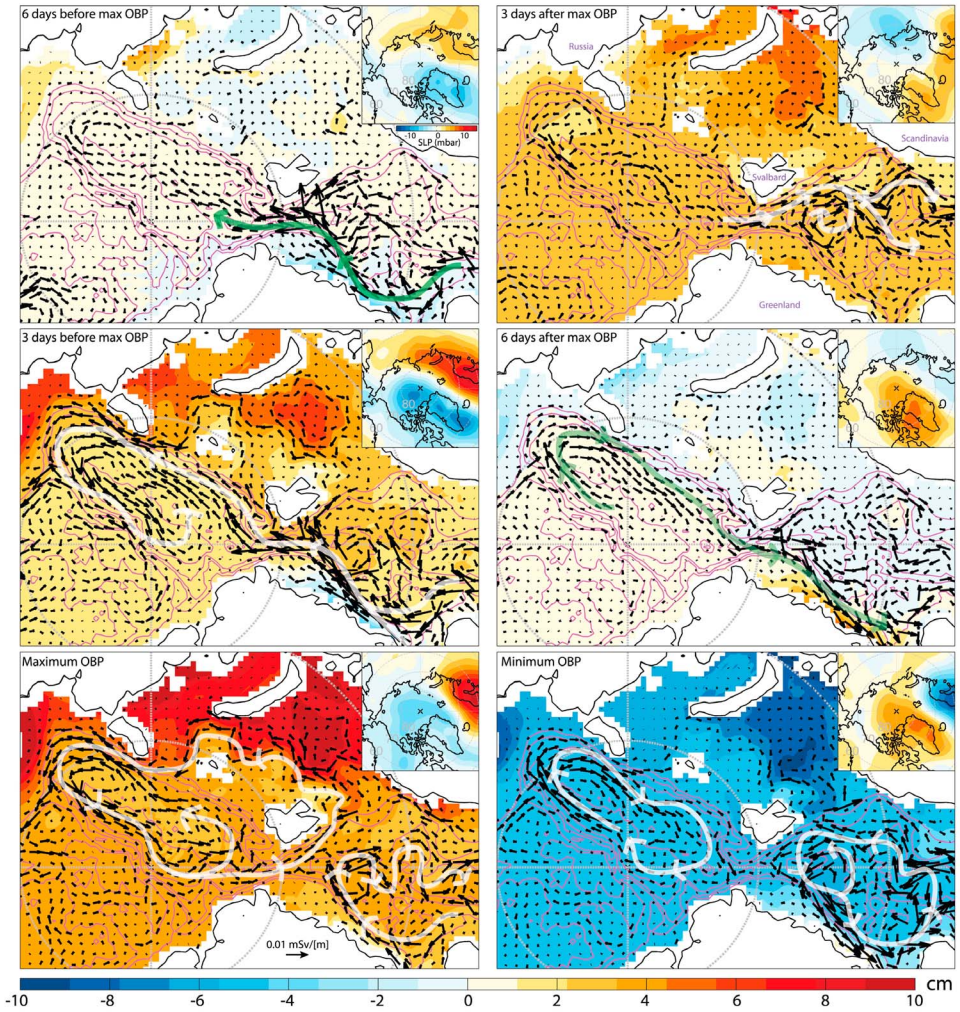

Figure 4. Composite maps of the anomalies of high-pass filtered sea surface height (color contours) and depth-integrated velocity (vectors) from 10 years of daily model output (2000–2009), for when the basin-averaged OBP is (top left) 6 days before maximum, (middle left) 3 days before maximum, (bottom left) at maximum, (top right) 3 days after maximum, (middle right) 6 days after maximum, and (bottom right) at minimum. Composite maps of SLP anomaly are shown inside the panels for each corresponding phase of basin-averaged OBP. Bathymetry is shown in magenta, with 1000 m interval contours. Faint green and white arrows emphasize the general patterns of the circulation associated with the winter sub-monthly mode of variability.

Nordic Seas. The largest net volume inflow towards the Arctic basin through Bering and Fram Straits, CA and Barents Sea paths is between 1.51 and 1.37 Sv (6 to 3 days before maximum, respectively). Most of the mass transport is through Fram Strait, followed by the Barents Sea path. The composite daily progression of net flow into the basin, integrated over time relative to the maximum OBP (not shown), divided by the area of the Arctic Ocean, represents an increase of a basin-averaged OBP of ~3.5 cm. This mass increase is consistent with the wintertime RMS value of OBP from PIOMAS to within 10% error. The largest net volume transport exiting the basin is between 1.25 and 1.11 Sv (3 to 6 days after maximum OBP, respectively).

[21] The circulation associated with the sub-monthly mode largely follows the topography (Figure 4). Topographic steering of the flow in the Nordic Seas and Arctic Ocean has long been recognized [e.g., *Isachsen et al.*, 2003; *Nøst and Isachsen*, 2003], but sub-monthly variations have been unknown. The temporal mean of the vertically integrated velocity from PIOMAS (not shown) consists of cyclonic circulation in the Nordic Seas and the Eurasian Basin, northward flow into the basin through the east side of Fram Strait, and flow southward from the basin through the west side of Fram Strait, in agreement with previous modeling results and observations [e.g., *Nøst and Isachsen*, 2003]. *Isachsen et al.* [2003] showed that the flow variability in the Nordic Seas and Arctic Ocean is well represented by a barotropic model, and the flow follows the bathymetry. The opposing vortices revealed by PIOMAS (Figure 4) at maximum and minimum basin OBP show the vertically-integrated flow anomaly, and represent a measure of the strengthening and weakening of the climatological-mean field at the sub-monthly timescales, owing to the atmospheric forcing in the Fram Strait region.

[22] Although the spectral peak in OBP at around 20 days (Figure 1) is at the uncertainty level, the variance-preserving spectrum (Figure S2 in the auxiliary material) depicts a strong concentration of energy between 15 and 30 days. Modeling results and the comparison with SLP gradient spectra suggest that this is due to a broader peak in the spectra of atmospheric forcing and a frequency limitation in the ocean response. *Isachsen et al.*'s [2003] model assumes that mass divergence in the surface Ekman layer is balanced by convergence in the bottom Ekman layer, and based on observed wind stress in the Nordic Seas ($\tau = 0.1$ Nm^{-1}) and typical values of depth $H = 3000$ m, density $\rho = 1000$ kgm^{-1}, and ocean currents $u \sim 10$ cm/s, the associated spin-down timescale of the response to surface forcing ($T \propto H\rho u/\tau$) is about 30 days (see *Isachsen et al.* [2003] for model details). Following their analysis, the depth-integrated currents from PIOMAS, which are of order 1 cm/s, yield a decay timescale of ~3 days, which corresponds to a period of 2π*3 days ~18 to 22 days. This suggests that the ocean response will be limited at shorter periods.

[23] The variance-preserving spectra of SLP gradient and basin-averaged OBP (Figure S2 in the auxiliary material) show similar peaks around 1/18 cpd, but at higher frequencies the spectra of SLP gradient show less roll-off with frequency, and the frequency response function (ratio of OBP and SLP gradient Fourier transforms, Figure S3 in the auxiliary material) rolls off at greater than the inverse of frequency squared above ~1/15 cpd. The circulation decay timescale from *Isachsen et al.* [2003] and the low-pass filter character of the OBP/SLP frequency response function, all suggest that the ocean is unable to respond to the SLP gradient above a cutoff frequency around 1/18 to 1/15 cpd. Combined with the increase with frequency in variance preserving spectral density of the forcing (SLP gradient) below ~1/15 cpd, the ocean response cutoff produces a more peaked response in ocean mass than is shown by the forcing (Figure S2 in the auxiliary material).

[24] The 2-day lag between the SLP gradient and the basin OBP (Figure 3) is also consistent with the ocean spin-down time taken from *Isachsen et al.* [2003] and by itself suggests the importance of inertial effects. If the variation in ocean mass represented the filling of a vessel balanced by basin pressure forced leakage paths, we would expect OBP in the basin to rise and fall in phase with the forcing (wind-driven slope current should follow SLP gradient within $1/f$) so as to balance leakage against inflow. Alternatively if leakage were negligible, the ocean mass would represent only the integral of the periodic forced inflow and OBP would lag the forcing by 90° (e.g., 4 to 7 -day lag for a 15 to 30 day period). The 2-day lag suggests a situation between these two extremes with impedance of the leakage paths by friction and inertial effects. Similar wind-driven effects on basin-scale mass variations through a narrow strait have been documented in the Mediterranean Sea (e.g., through the Strait of Gibraltar) [*Fukumori et al.*, 2007].

6. Summary and Speculation

[25] Wavelet analysis indicates that the wind forcing and ocean response are episodic, significant during wintertime, and vary from year to year in strength and predominant period. The sub-monthly Arctic mass variations are due to wind-driven slope currents forced by zonal SLP gradient and southwesterly winds. The PIOMAS wind-forced mass fluxes into and out of the Arctic Ocean are large enough to produce the observed sub-monthly mass variations and associated barotropic topographically controlled circulation patterns, and the timescales and frequency response is consistent with the theory of *Isachsen et al.* [2003].

[26] The sub-monthly mass variations are large and their associated longer-term effects may be important. The wind events that cause them conceivably have associated net effects on the mass transport into the Arctic Ocean, and sub-monthly variations must clearly impact the attempts to observe Fram Strait mass transport. We also speculate that if temperature fluctuations prove to be correlated with the changes in mass flux at sub-monthly timescales, the mass transport variations could result in a long-term change in Arctic Ocean heat content [e.g., *Schauer et al.*, 2004].

[27] **Acknowledgments.** This work was supported by NASA grant NNX08AH62G. We thank the Beaufort Gyre Exploration Project (BGEP), the Alfred Wegener Institute (AWI), and Fisheries and Oceans, Canada, for the data provided for this work. We also thank two anonymous reviewers for their helpful comments and suggestions that largely improved this paper.

[28] The Editor thanks two anonymous reviewers for their assistance in evaluating this paper.

References

Bingham, R. J., and C. W. Hughes (2008), The relationship between sea-level and bottom pressure variability in an eddy permitting ocean model, *Geophys. Res. Lett.*, *35*, L03602, doi:10.1029/2007GL032662.

Fukumori, I., D. Menemenlis, and T. Lee (2007), A near-uniform basin-wide sea level fluctuation of the Mediterranean Sea, *J. Phys. Oceanogr.*, *37*, 338–358, doi:10.1175/JPO3016.1.

Grinsted, A., J. C. Moore, and S. Jevrejeva (2004), Application of the cross wavelet transform and wavelet coherence to geophysical time series, *Nonlinear Processes Geophys.*, *11*, 561–566, doi:10.5194/npg-11-561-2004.

Hughes, C. W., and V. N. Stepanov (2004), Ocean dynamics associated with rapid J2 fluctuations: Importance of circumpolar modes and identification of a coherent Arctic mode, *J. Geophys. Res.*, *109*, C06002, doi:10.1029/2003JC002176.

Isachsen, P. E., J. H. LaCasce, C. Mauritzen, and S. Hakkinen (2003), Wind-driven variability of the large-scale recirculating flow in the Nordic Seas and Arctic Ocean, *J. Phys. Oceanogr.*, *33*, 2534–2550, doi:10.1175/1520-0485(2003)033<2534:WVOTLR>2.0.CO;2.

Kalnay, E., R. Kanamitsu, and R. Kistler (1996), The NCEP/NCAR 40-year reanalysis project, *Bull. Am. Meteorol. Soc.*, *77*, 437–471, doi:10.1175/1520-0477(1996)077<0437:TNYRP>2.0.CO;2.

Morison, J. (1991), Seasonal variations in the West Spitsbergen Current estimated from bottom pressure measurements, *J. Geophys. Res.*, *96*(C10), 18,381–18,395, doi:10.1029/91JC01916.

Morison, J., J. Wahr, R. Kwok, and C. Peralta-Ferriz (2007), Recent trends in Arctic Ocean mass distribution revealed by GRACE, *Geophys. Res. Lett.*, *34*, L07602, doi:10.1029/2006GL029016.

Nøst, O. A., and P. E. Isachsen (2003), The large-scale time-mean ocean circulation in the Nordic Seas and Arctic Ocean estimated from simplified dynamics, *J. Mar. Res.*, *61*, 175–210, doi:10.1357/002224003322005069.

Pawlowicz, R., B. Beardsley, and S. Lentz (2002), Classical tidal harmonic analysis including error estimates in MATLAB using T_TIDE, *Comput. Geosci.*, *28*, 929–937, doi:10.1016/S0098-3004(02)00013-4.

Rennert, K. J., and J. M. Wallace (2009), Cross-frequency coupling, skewness, and blocking in the Northern Hemisphere winter circulation, *J. Clim.*, *22*(21), 5650–5666, doi:10.1175/2009JCLI2669.1.

Schauer, U., E. Fahrbach, S. Osterhus, and G. Rohardt (2004), Arctic warming through the Fram Strait: Oceanic heat transport from 3 years of measurements, *J. Geophys. Res.*, *109*, C06026, doi:10.1029/2003JC001823.

Torrence, C., and G. P. Compo (1998), A practical guide to wavelet analysis, *Bull. Am. Meteorol. Soc.*, *79*, 61–78, doi:10.1175/1520-0477(1998)079<0061:APGTWA>2.0.CO;2.

Vinogradova, N. T., R. M. Ponte, and D. Stammer (2007), Relation between sea level and bottom pressure and the vertical dependence of oceanic variability, *Geophys. Res. Lett.*, *34*, L03608, doi:10.1029/2006GL028588.

Zhang, J., and D. A. Rothrock (2003), Modeling global sea ice with a thickness and enthalpy distribution model in generalized curvilinear coordinates, *Mon. Weather Rev.*, *131*(5), 845–861, doi:10.1175/1520-0493(2003)131<0845:MGSIWA>2.0.CO;2.

J. H. Morison, C. Peralta-Ferriz, and J. Zhang, Polar Science Center, Applied Physics Laboratory, University of Washington, 1013 NE 40th St., Seattle, WA 98105-6698, USA. (ferriz@u.washington.edu)

J. M. Wallace, Department of Atmospheric Sciences, University of Washington, Box 354235, Seattle, WA 98195-4235, USA.

A.1 Supplementary information of peer-reviewed work

The supplementary information corresponding to *Peralta-Ferriz et al.* (2011) contains two tables and three figures:

Table A.1 includes the correlation coefficients among all the regions from where the pressure records are analyzed, and also the correlation coefficient between observations and the model at these different regions.

Table A.1: (a) Correlation coefficient between the ocean bottom pressure records in the Arctic Ocean for unfiltered (upper segment) and high-pass filtered (cutoff = 90 days, lower segment). All coefficients are significant above the 95% confidence level. (b) Correlation coefficient between OBP records and the modeled output at each location for unfiltered time series and for high-pass filtered time series.

	(a) Correlation coefficient R among OBP records					**(b) *In situ* and model correlation R**	
	Fram Strait	**North Pole**	**Alert**	**Beaufort Sea**	**Holman**	**filtered**	**unfiltered**
Fram Strait	-	0.81	0.72	0.78	0.61	0.60	0.56
North Pole	0.84	-	0.68	0.86	0.71	0.68	0.55
Alert	0.66	0.67	-	0.72	0.69	0.58	0.53
Beaufort Sea	0.77	0.90	0.65	-	0.72	0.72	0.61
Holman	0.58	0.67	0.59	0.65	-	0.68	0.62

Table A.2 shows the net volume flow into the basin through the four exit paths of the Arctic Ocean, by the area limits of the basin-averaged OBP.

Figure A.1 compares in both time and frequency the atmospheric forcing (SLP gradient) with the modeled ocean response (basin-averaged OBP). This figure highlights the common winter energy variance between 1/30 and 1/15 cycles per day (cpd) shared by these time series.

Figure A.2 shows that in addition to the atmospheric forcing over the Nordic Seas on the Arctic Ocean described in the article, atmospheric forcing through the Bering

Table A.2: Oceanic volume transport (Sv, 1 Sv = $10^6 m^3/s$) through different paths of the Arctic Ocean associated with the sub-monthly mode of variability of OBP, for each stage shown in Figure 4 of *Peralta-Ferriz et al.* (2011). Positive values denote flow into the basin. Number in parenthesis is the interpolated flow relative to the time where peak maximum OBP corresponds to total net zero flow, (i.e., 12 hours earlier than the model daily averages). Total is the sum of Bering Strait, Fram Strait, Barents Sea, and Canadian Archipelago.

Arctic Ocean pathway	**6 days before max OBP**	**3 days before max OBP**	**Maximum OBP**	**3 days after max OBP**	**6 days after max OBP**	**Minimum OBP**
Bering Strait	0.11 (0.10)	-0.02 (0.01)	-0.13 (-0.13)	-0.14 (-0.14)	0.05 (0.04)	0.05 (0.05)
Fram Strait	1.07 (0.97)	1.25 (1.01)	-0.45 (0.07)	-0.83 (-0.83)	-0.92 (-0.81)	-0.29 (-0.41)
Barents Sea	0.42 (0.52)	0.31 (0.26)	0.25 (0.21)	-0.23 (-0.12)	-0.28 (-0.34)	0.36 (0.18)
Canadian Arch.	-0.09 (-0.05)	-0.16 (-0.14)	-0.17 (-0.18)	-0.05 (-0.07)	0.04 (0.03)	0.22 (0.17)
TOTAL	**1.51 (1.53)**	**1.37 (1.15)**	**-0.49 (-0.03)**	**-1.25 (-1.17)**	**-1.11 (-1.07)**	**0.34 (-0.01)**

Strait also enhances the mass entering the Arctic basin.

Figure A.3 shows the frequency response function or transfer function of the SLP gradient and the basin-averaged OBP to demonstrate that there is no resonance between the atmospheric forcing and the ocean response, but there is a cutoff frequency at which the ocean response rolls-off, suggesting that the ocean acts as a filter at frequencies higher than $\sim 1/15$ cpd.

A.2 Daily SLP, SSH and transport within the sub-monthly OBP mode

Composite maps of the daily progressions of SLP, SSH and vertically integrated velocity field for a full near $\sim$ 20-day cycle before maximum OBP and after maximum OBP are shown in Figure A.4 and in Figure A.5, respectively.

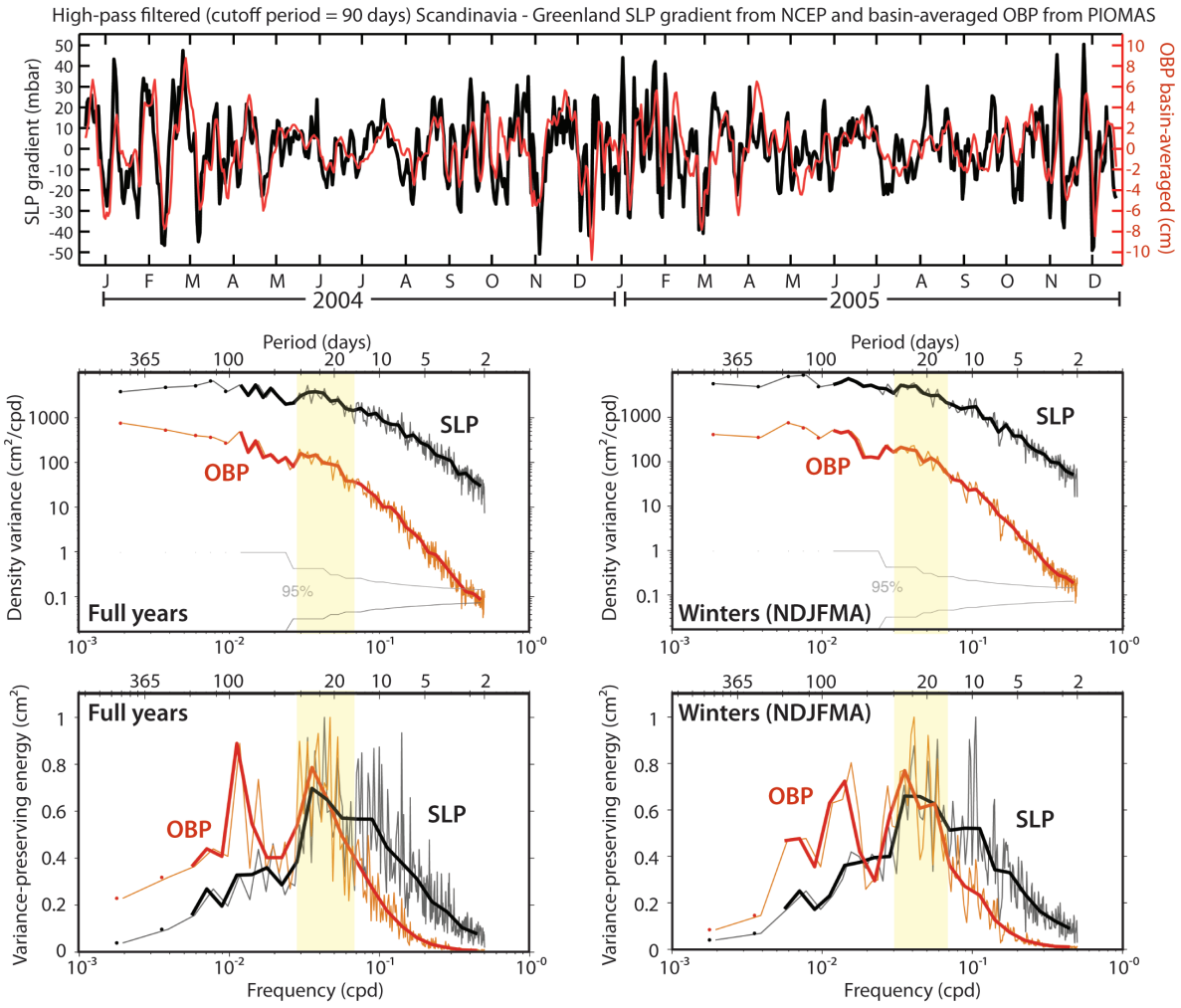

Figure A.1: On the top, 2 years of high-pass filtered SLP gradient (black) and basin-averaged OBP (red). Middle panels show the power spectra of unfiltered time series (10 years, 2000 to 2009), full year (left) and winter-only (right). The lower panels show the variance-preserving energy for the spectrum of the full year (left) and winter-only (right). Shaded bars highlight the range of frequencies between 1/30 to 1/15 cpd.

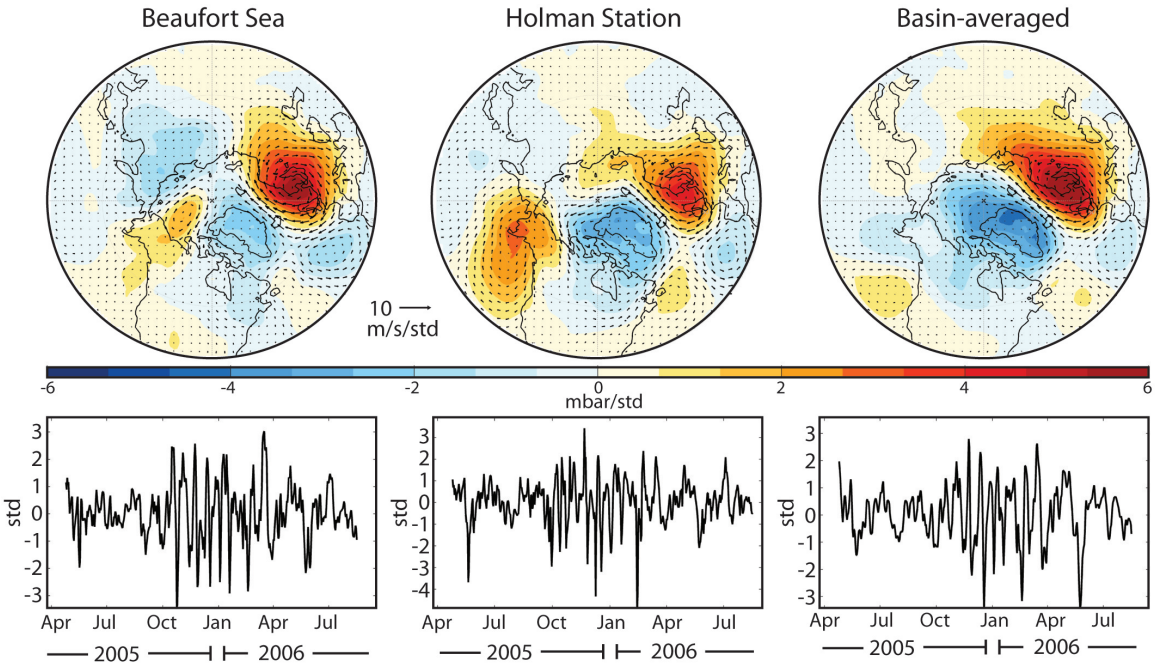

Figure A.2: On the top are shown the regression maps of high-pass filtered (cutoff period = 90 days) SLP anomaly field projected on 1.5 years of modeled OBP from Beaufort Sea (left), Holman Station (middle) and basin-averaged OBP (right). The gray crosses show the location of the model grid-point, and the area of the average is in gray lines. On the bottom are the normalized high-pass filtered OBP time series associated with the regression maps. Note the winter amplification of the OBP variation.

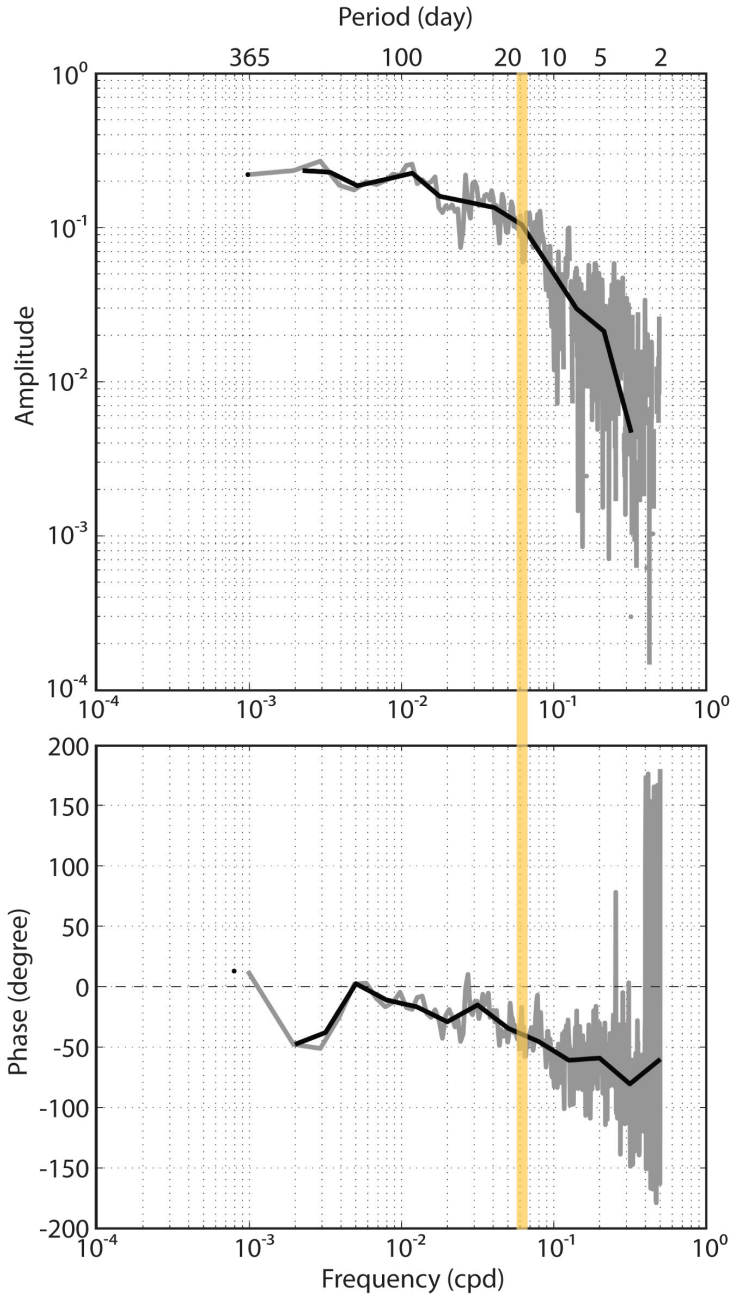

Figure A.3: Transfer function estimate of the relation between the SLP gradient (forcing) and the basin-averaged OBP (response), amplitude (top) and phase (bottom). Yellow line highlights the cutoff frequency ($\sim$ 1/15 cpd) after which the response function begins to roll-off

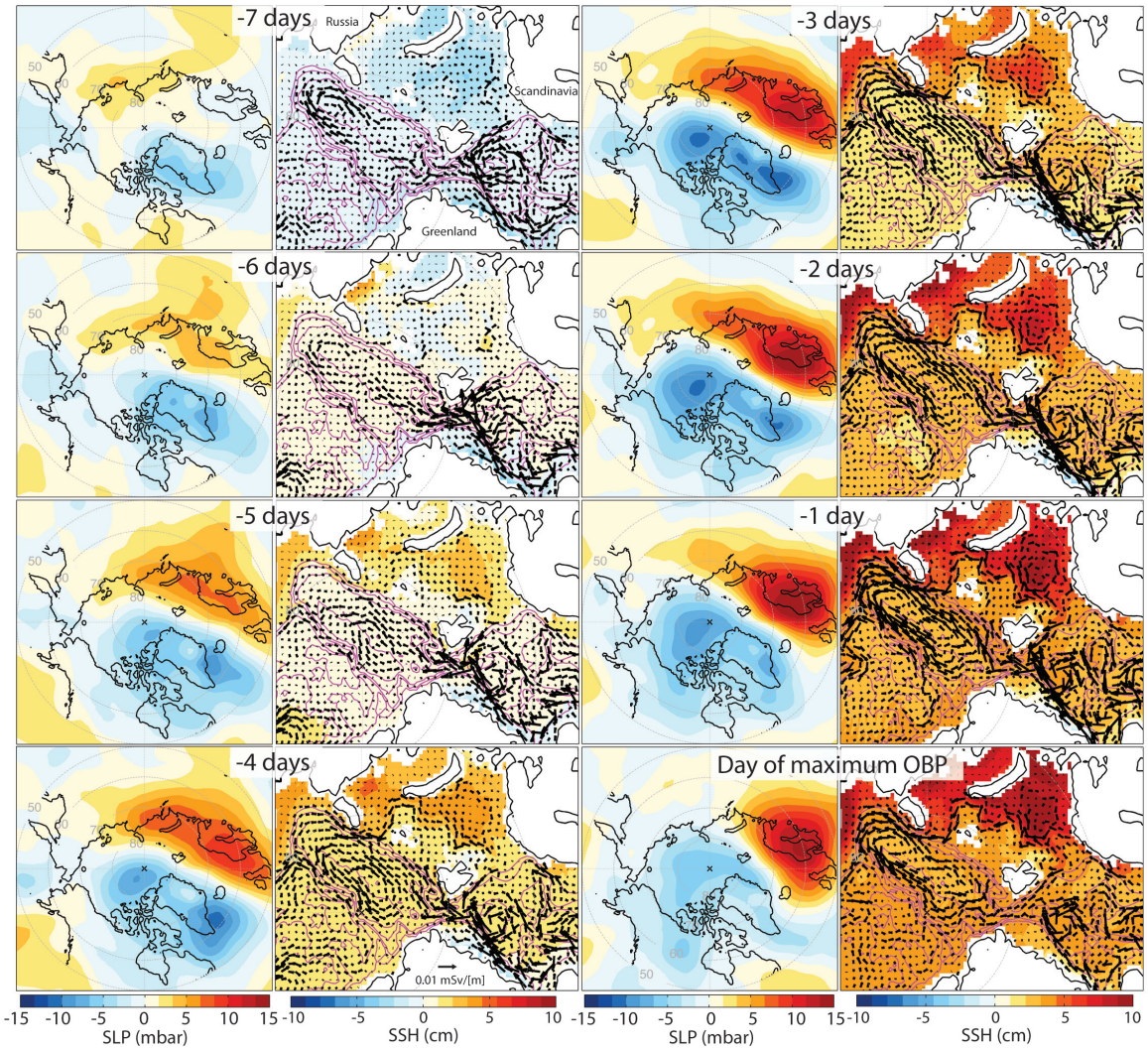

Figure A.4: (a) and (c) Composite maps of the daily progression of high-pass filtered SLP before the maximum basin-averaged OBP from the model. (b) and (d) are the respective composite maps of daily progression of high-pass filtered sea surface height (color contours) and depth-integrated velocity (vectors) from 10 years of daily model output (2000-2009). Bathymetry is shown in magenta, with 1000 m interval contours.

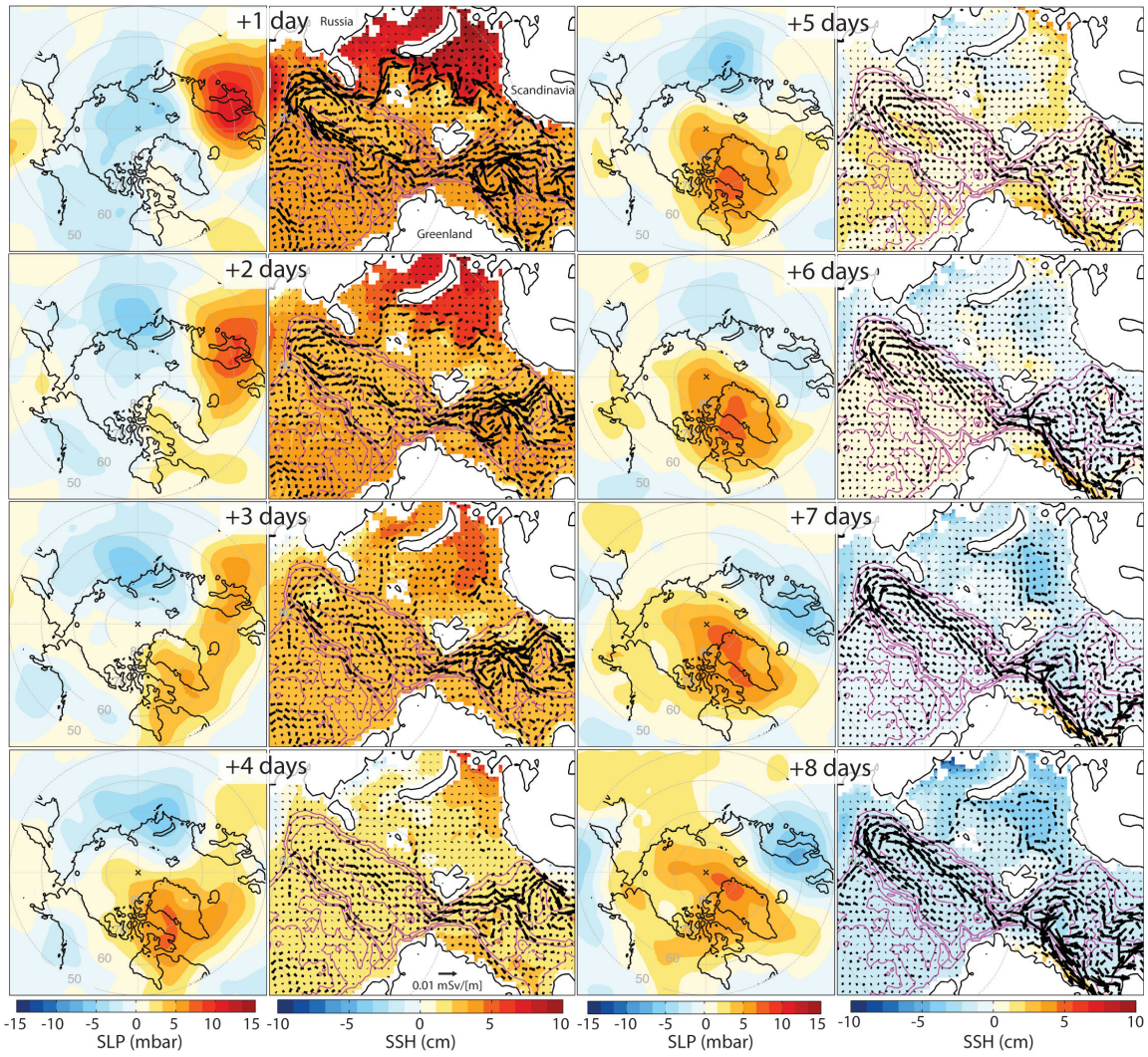

Figure A.5: Same as in Figure A.4, but the daily progression is after the modeled basin-averaged OBP has been reached. The SLP pattern observed from 5 days to 8 days after basin OBP max is consistent with the SLP pattern that forces sea-ice export through Fram Strait at sub-monthly timescales, as described by *Tsukernik et al.* (2009).

Appendix B

SEASONAL VARIABILITY OF ARCTIC OCEAN BOTTOM PRESSURE

PUBLICATION: Peralta-Ferriz, C. and J. Morison (2010), Understanding the annual cycle of the Arctic Ocean bottom pressure, Geophys. Res. Letters, 37, L10603, doi:10.1029/2010GL042827.

GEOPHYSICAL RESEARCH LETTERS, VOL. 37, L10603, doi:10.1029/2010GL042827, 2010

Understanding the annual cycle of the Arctic Ocean bottom pressure

Cecilia Peralta-Ferriz[1] and James Morison[1]

Received 7 February 2010; revised 8 April 2010; accepted 21 April 2010; published 22 May 2010.

[1] Ocean bottom pressure (OBP) observations in the Arctic from *in situ* pressure recorders and the Gravity Recovery and Climate Experiment (GRACE) satellite mission, averaged over the basin, reveal annual oscillations of about 2 cm. The maximum occurs in late summer to early fall and the minimum in late winter to early spring. We derive a simple model of OBP response to runoff and precipitation minus evaporation (P-E) that agrees in phase with the observations and is 10% larger. **Citation:** Peralta-Ferriz, C., and J. Morison (2010), Understanding the annual cycle of the Arctic Ocean bottom pressure, *Geophys. Res. Lett.*, *37*, L10603, doi:10.1029/2010GL042827.

1. Introduction

[2] Seasonal variation is a dominant signal in Ocean Bottom Pressure (OBP) measured with *in situ* pressure gauges in the Arctic Ocean. The seasonal variations of the Arctic OBP have appeared in early releases of OBP measurements by the Gravity Recovery and Climate Experiment (GRACE) [*Ponte et al.*, 2007; *Morison et al.*, 2007] since 2002, and in numerical simulations [*Dobslaw and Thomas*, 2007].

[3] According to *Ponte et al.* [2007] GRACE release 2 from the Jet Propulsion Laboratory, and GRACE release 3 from Geo Forschungs Zentrum Potsdam, reveal a global average 1-cm water equivalent annual cycle in OBP with a maximum in the summer. Their GRACE results for the Arctic suggest a larger amplitude (2–3 cm) and a later peak (October). They suggest that the seasonal variation of the world ocean average OBP is the result of seasonality in Northern Hemisphere runoff and world ocean average atmospheric pressure.

[4] *Dobslaw and Thomas* [2007] show that the seasonal cycle in the Arctic OBP, averaging 1 cm peak to peak over the basin, is due to the seasonal cycle of runoff. Their modeled basin-averaged OBP is a little less than half the magnitude of the mass variation observed by GRACE, and the maximum simulated OBP is in July, earlier than the main peak observed by GRACE [*Ponte et al.*, 2007]. In addition, the simulations indicate that the seasonal OBP change is mainly barotropic, in agreement with general modeling results [*Vinogradova et al.*, 2007; *Gill and Niiler*, 1973].

[5] Runoff is the dominant meteoric water input to the Arctic Ocean (61%), followed by net precipitation minus evaporation (P-E, 39%), both with significant seasonal variations [*Serreze et al.*, 2006]. The ocean inflows to and outflows from the Arctic Ocean show seasonal fluctuation [e.g., *Woodgate and Aagaard*, 2005; *Schauer et al.*, 2004], but models without runoff driven only by wind do not show the seasonal mass change [*Dobslaw and Thomas*, 2007; *Zhang and Rothrock*, 2003]. This is likely because any pressure buildup in the Arctic Ocean due to ocean inflow acts to reduce the inflow or create a compensating outflow. In contrast, runoff and P-E are independent of ocean pressure. We might expect the addition of runoff mass to the Arctic Ocean to quickly propagate away to the rest of the world ocean at the barotropic wave speed. The model results by *Dobslaw and Thomas* [2007] show that runoff is retained in the Arctic Basin at seasonal time-scales, long enough to achieve a geostrophically balanced circulation. The observations indicate a lag in the OBP disturbance of about 2 months relative to the *Dobslaw and Thomas* [2007] model result.

[6] Here we provide a simple explanation for the observed annual cycle of the Arctic OBP by exploring Arctic Ocean GRACE and *in situ* OBP data, and deriving a simple physical model for the ocean response to runoff, P-E and atmospheric pressure.

2. Data

[7] We use GRACE monthly fields from the University of Texas Center for Space Research release 4 (CSR4), from August 2002 to May 2008 (http://grace.jpl.nasa.gov/data/mass/). The post-processing of the GRACE (CSR4) to obtain the time varying OBP from spherical harmonic gravity coefficients is explained by *Chambers* [2006a, 2006b]. The values represent anomalies relative to the mean from January 2003 to December 2006. We use data filtered [*Chambers*, 2006a, 2006b] with a Gaussian smoother with a 300 km half-amplitude radius. GRACE Arctic OBP is validated with measurements from two Arctic Bottom Pressure Recorders (ABPR) near the North Pole (89° 15.26′N, 60° 21.58′E and 89° 14.85′N, 148° 7.54′E), that report pressure every 15 minutes from April 2005 to April 2008. The data from the two ABPRs are well correlated with each other and agree well with GRACE [*Morison et al.*, 2007]. We also average well correlated OBP time series from three bottom pressure recorders (BPR) deployed annually by the Beaufort Gyre Exploration Project at a) 75° 0.449′N, 149° 58.660′W, b) 78° 1.49′N, 149° 49.203′W, and c) 76° 59.232′N, 139° 54.563′W, [http://www.whoi.edu/beaufortgyre/data_moorings.html] from August 2003 to August 2007. OBP data from Pressure Inverted Echo Sounders, September 2003 to August 2006 (A. Beszczynska-Möller, personal communication, 2007), were averaged to give a time-series of OBP in Fram Strait. The *in situ* pressure records were de-tided using the

[1]Polar Science Center, Applied Physics Laboratory, University of Washington, Seattle, Washington, USA.

0094-8276/10/2010GL042827

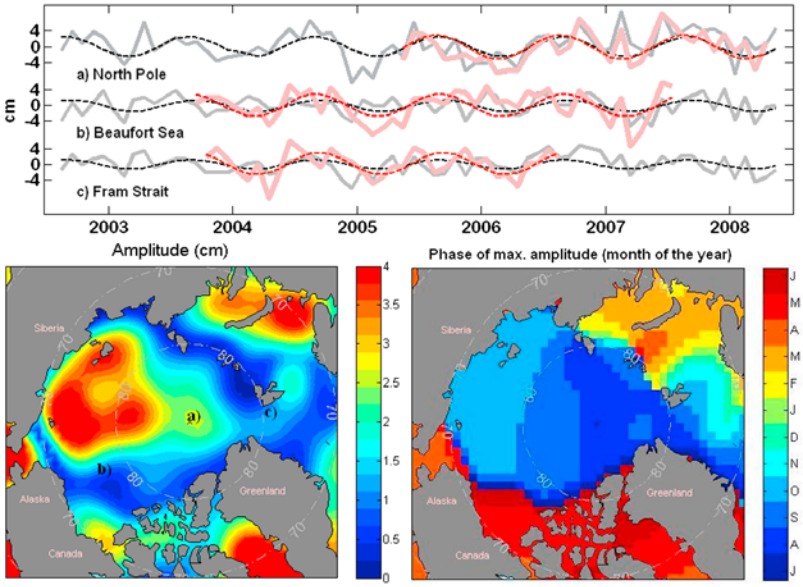

Figure 1. (top) Time-series of monthly averages of *in situ* (shaded red) OBP anomaly, and their respective annual harmonic fit (dashed red) at the North Pole, Beaufort Sea and Fram Strait (letter coded in the map on the bottom left). GRACE OBP at each location is shown in grey, and the annual cycle in dashed black lines. All the time-series have a long term linear trend removed. (bottom left) Amplitude and (bottom right) phase of the GRACE OBP annual fit.

T_TIDE MATLAB analysis program of *Pawlowicz et al.* [2002], and averaged to the same 30-day bins as GRACE.

[8] We use monthly averages of atmospheric sea level pressure (SLP) from the NCEP/NCAR reanalysis [*Kalnay et al.*, 1996] (http://dss.ucar.edu/pub/reanalysis/). Like GRACE, the SLP anomalies are estimated relative to the average from Jan. 2003 to Dec. 2006.

[9] We use runoff data from the Arctic-Regional, Integrated Hydrological monitoring System (Arctic-RIMS) provided by the Water Systems Analysis Group (http://rims.unh.edu/) and from the Regional, Electronic and Hydrographic Data Network for the Arctic Region (R-Arctic Net, http://www.r-arcticnet.sr.unh.edu/v3.0/). Total runoff is dominated by the gauged runoff of the major rivers: Yenisey, Ob, Pechora, Kolyma, Lena, Severnaya Dvina and Mackenzie. Smaller gauged rivers add 12% to this amount. *Dobslaw and Thomas* [2007] assumed that ungauged runoff accounted for 22% of the total. We assume that the ungauged part amounts 30% of the total runoff [*World Climate Research Program*, 1998], in agreement with hydrologic model results [*Su et al.*, 2005]. Consequently, we take total runoff as 1.6 times the contribution of the 7 major rivers. We use climatology data of precipitation minus evaporation (P-E) from ERA-40 [*Serreze et al.*, 2006].

3. Seasonal Cycle

[10] GRACE and *in situ* OBP measurements from the North Pole, Beaufort Gyre and Fram Strait show good agreement and a common seasonal signal (Figure 1, top), indicative of variation in the Arctic OBP at basin-wide scale in Central Arctic. The fit of an annual harmonic to the GRACE OBP time-series of the Arctic Ocean (Figure 1, bottom) shows the maximum OBP occurring in August–October in the Central Arctic. The maximum OBP in the Barents and Kara Seas is in early spring. The amplitude of the basin-averaged GRACE OBP annual cycle is 2 cm peak to peak, about twice the amplitude of the *Dobslaw and Thomas* [2007] model, but consistent with *Ponte et al.* [2007], with the phase of maximum amplitude in September. The annual harmonic fit to the basin-averaged OBP explains 15% of the variance of the OBP signal. This indicates the OBP is highly variable at shorter than seasonal time scales. In more localized regions, the amount of variance explained by an annual fit to the GRACE observations of OBP reaches about 50% in the East Siberian Sea, 60% in the Barents Sea and 25% at the North Pole.

4. Simple Model of Seasonal OBP Variation

[11] Possibly the simplest model of the Arctic Ocean is a rotating tank with a narrow channel connecting it to the world ocean. As meteoric water pours into the middle of the tank in a seasonal cycle, the changes in sea surface height and hydrostatic pressure are geostrophically balanced, producing anticyclonic flow through most of the water column. There is an ageostrophic radial flow only in the bottom boundary layer where the flow turns down pressure gradient. For most of the tank where there is no channel, there is a helical secondary flow outward at the bottom and inward at the surface, but at the channel opening, ocean mass is able to leak out radially in the bottom boundary layer, decreasing water volume in the tank.

[12] For a meteoric input (runoff + P-E) with a mean annual component and seasonal variation, the annual mean input would result in a surface displacement in the tank sufficient to drive equivalent leakage through the bottom boundary layer in the channel. The degree to which ocean mass can build up seasonally depends on the degree of leakage in the bottom boundary layer, which in turn depends on the bottom stress at the mouth of the channel. If the leakage path were unrestricted, the seasonal buildup in

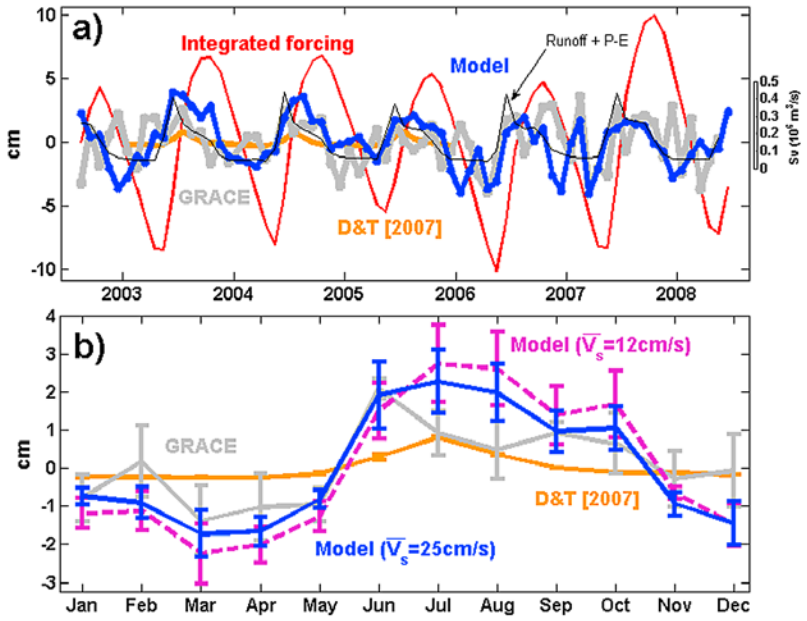

Figure 2. (a) GRACE OBP averaged over the Arctic (gray); monthly basin-averaged OBP derived from the model (blue); time-integral of the forcing over the basin minus a linear trend (red); the basin-averaged modeled OBP from *Dobslaw and Thomas* [2007] (orange); and forcing of the model (runoff + P-E) as thin black line along with its own scale on the right. (b) Monthly means (centered in day 15) of OBP from GRACE (gray), our model with enhanced mixing (blue), model without enhanced mixing (dashed magenta) and *Dobslaw and Thomas* [2007] (orange). Vertical bars are the standard error of the modeled and observed OBP.

ocean mass would be small and in phase with the input. Actually, the Arctic Ocean seasonal OBP variation is nearly in phase with and half the amplitude of the time-integral of the seasonal variation in meteoric forcing (Figure 2a). This suggests that the leakage of meteoric input from the Arctic Ocean is restricted but not completely.

[13] The conceptual model for temporal change in Arctic Ocean mass can be expressed as

$$A\frac{dh}{dt} = F(t) - \frac{L}{\rho f}\tau_b^x(t) \tag{1}$$

where A is the area of the Arctic Ocean (9×10^{12} m^2); h is the ocean surface displacement and F is the volume input (runoff plus P-E); t is time. The second term on the right represents the leakage, given by the Ekman transport in the bottom boundary layer, where τ_b^x is the bottom shear stress in the zonal direction [*Gill*, 1982]. L is the width of the channel where the flow exits the basin, ρ is the average density of the sea water (1025 kg/m^3), f is the Coriolis parameter. Bottom stress can be expressed in terms of the geostrophic velocity away from the boundary [*Gill*, 1982]:

$$\tau_b^x(t) = \rho C_d V_s^2 \cos(\alpha) \tag{2}$$

Here, C_d is the bottom drag coefficient, and α is the turning angle of the flow within the bottom boundary layer.

[14] In the model, the resulting ocean mass change h can be thought of as sea surface height (SSH) change in this barotropic model. OBP variations are the sum of the SLP changes and the variations of the ocean mass. Therefore, the basin-averaged SLP added to the ocean response h from the model gives the modeled OBP. $V_s = (g/f)(\Delta h/\Delta y)$ is the scaled geostrophic velocity in terms of the pressure difference ($\Delta h = h + P_a - P_{bo}$) inside and outside the basin over a distance Δy, where P_a is the basin-averaged SLP variation and P_{bo} is the averaged OBP variation outside, given by the global ocean mean of OBP [*Ponte et al.*, 2007]. L, taken as 2×10^6 m, represents the approximate width of the exit path from the Arctic Ocean at Fram Strait, across the Barents Sea shelf edge to the Norwegian Sea, and a contribution for the Canadian Archipelago. We take $\Delta y = 0.25 \times 10^6$ m as a representative distance through Fram Strait and across the gateway to the Barents Sea.

[15] Assuming that no other physics at the bottom boundary occur besides the seasonal response to meteoric water and SLP, and using reasonable values of C_d, the amplitude of the modeled OBP is in phase with but larger than the observed. This suggests that insufficient leakage is occurring in the bottom boundary layer, likely because the background non-seasonal velocity associated with the mean wind driven circulation and other factors is ignored. This background velocity is much larger than the seasonal variation due to runoff, so ignoring it results in erroneously low levels of bottom boundary layer turbulence. Enhanced turbulence thickens the boundary layer and increases the seasonally varying Ekman transport at the bottom. In order to account for the effect of steady background currents, we assume the velocity is the sum of the seasonally varying part and a mean part, $\overline{V}_s$, dominated by an ambient background velocity, V_{amb}, and linearize equation (1):

$$A\frac{dh}{dt} = F(t) - \frac{LC_d}{f}\overline{V}_s^2\cos(\alpha) - \frac{2LC_d}{f}\cos(\alpha)\overline{V}_s\frac{g}{f}\frac{[h'(t) + P_a'(t) - P_{bo}'(t)]}{\Delta y} \tag{3}$$

where $\overline{V}_s = V_{amb} + (g/f)([\overline{h} + \overline{P}_a - \overline{P}_{bo}]/\Delta y)$. Bars indicate the time-independent average and primes indicate pertur-

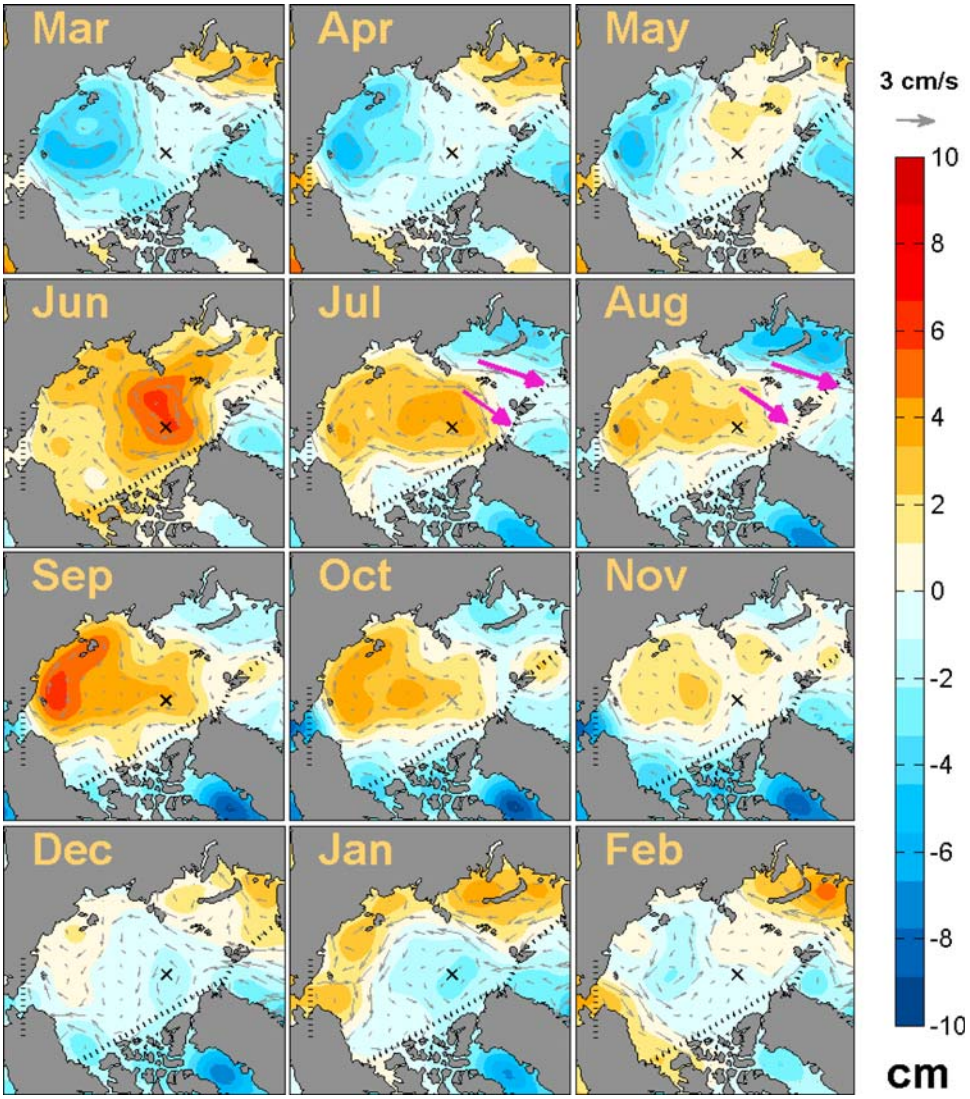

Figure 3. Color contours show the monthly means of GRACE OBP; the gray arrows show the geostrophic velocity due to OBP gradient; black dotted lines show the boundary of the area that accounts for the basin-averaged OBP. The magenta arrows emphasize the geostrophic-leak out of the basin.

bation. The right hand side of equation (3) includes time-independent and time-varying terms. The perturbation part of equation (3) (last term of the right hand side) gives the seasonally varying response. Background velocity estimates in the Fram Strait, Barents shelf-break gateway region range from 5 cm/s [*Schauer et al.*, 2004] to 25 cm/s [*Hanzlick*, 1983; F. Nilsen, personal communication, 2009]. For this study, we start by assuming a background velocity of 12 cm/s, much larger than the runoff–induced seasonal variation.

[16] We estimate a value for C_d and α using the Rossby similarity drag law [*McPhee*, 2008] applied to the benthic boundary layer. With this universal relation and assuming stable and near neutral stratification, the relation of surface stress to velocity outside the boundary layer is dependent on the boundary layer surface roughness scale, z_o. For the abyssal benthic layer (i.e., generally flat, relatively smooth surface), z_o is ~1 cm (M. McPhee, personal communication, 2009); for much rougher underside of sea-ice, z_o ~ 3 cm is typical [*McPhee*, 2008]. We would expect the roughness length scale in the Fram Strait–Barents shelf-break region to lie between these values. Here we use $z_o = 2$ cm. According to the Rossby similarity, C_d is weakly dependant on velocity. For 12 cm/s and $z_o = 2$ cm, C_d is 4.3×10^{-3} and α is 18.8°.

5. Model Results

[17] We spin up the model for 10 years using repeated monthly means of the meteoric forcing from 2002–2008. A steady state is reached within one year, with a mean SSH increase of ~0.35 m (i.e., $\Delta\overline{h}$). After a year, the time-varying response is dominated by the seasonal variations. With $\overline{V}_s$ = 12 cm/s, the simulated seasonal variation of amplitude ~2.3 cm is in general agreement in phase and slightly larger than the monthly values of the basin-averaged observed OBP (Figure 2b). The amplitude of the modeled OBP variations is reduced by a factor of about 2 relative to the simple time-integral of the seasonal meteoric input. As with *Dobslaw and Thomas* [2007], our model response is dominated by runoff,

with a smaller contribution of P-E. The maximum model response without atmospheric pressure forcing, P_a, is slightly larger (~8%) than with P_a, and advanced in phase by a couple of months relative to the phase of the observed OBP.

[18] The RMS-difference between GRACE and our modeled OBP is ~1.2 cm (Figure 2b), with the maximum differences in the months of July and August. The RMS difference is in part due to OBP variations at shorter than seasonal time scales (e.g., 19 days [*Morison*, 1991]) that are not related to the runoff and pressure forcing used in the model.

[19] The RMS-difference associated with seasonal cycle can be partly reduced by additional enhancement of mixing to increase the leakage. We illustrate this by assuming a larger value of $\overline{V}_s$, 25 cm/s ($C_d = 3.7 \times 10^{-3}$ and $\alpha = 17.5°$). One rationale for such an enhancement is that it would represent mixing produced by the higher frequency or smaller scale processes such as tides, eddies, internal waves and winter time convection on the shelves [e.g., *Saloranta and Svendsen*, 2001; *Teigen et al.*, 2010]. The enhancement reduces the RMS difference from observed OBP to 0.85 cm (Figure 2b).

[20] However, as shown by comparison of the monthly mean values, even with enhanced mixing, the model response is consistently higher than the observed OBP in July and August (Figure 2b). The observed OBP drops slightly after the increase in June that coincides with the peak in annual runoff. We do not think this is due to semi-annual or 161-day (K2 tidal alias) errors in GRACE because harmonic fits at these periods to the observed OBP (semi-annual ~ 0.3 cm and 161-day ~ 0.05 cm) are much smaller and explain less variance (1.7% and 0.04%) than the annual fit (amplitude ~1 cm, 15% of variance). We think the difference is likely due to leakage during July and August that represents departure of the Arctic Ocean from the one-dimensional rotating tank analogy. This is illustrated by spatial distribution of the monthly means of observed OBP (Figure 3). May shows a positive OBP anomaly spreading from the Kara Sea, a region of numerous large rivers, out toward the North Pole. This develops in June to the largest positive monthly OBP anomaly as a basin-wide closed cell of anticyclonic circulation analogous to our idealized model. During July and August the closed nature of the cell breaks down and appears to interact with the Fram Strait-Barents Sea geography to possibly direct at least a fraction of the geostrophic flow out of the Arctic Ocean. The break down of the cell may occur because ageostrophic leakage first increases mass in the Barents Sea. Alternatively, Ekman pumping due to summer time northeasterly winds may shift ocean mass to form the OBP dipole between the Central Arctic (high pressure) and the Barents Sea (low pressure). Diversion of a small fraction of the total geostrophic flow due to the dipole could eliminate the July–August model-observed OBP difference, accounting for 30% of the RMS difference between the model and observed OBP. In September and October, the flow appears more nearly closed by a center of high OBP that develops at the exit path.

6. Conclusion

[21] The idealized rotating tank model driven by runoff, and to a lesser degree by seasonal variation of P-E and atmospheric pressure, shows reasonable agreement with observed seasonal variation in Arctic Ocean average bottom pressure. To achieve the best agreement, it is necessary to maximize leakage by non-geostrophic Ekman transport in the bottom boundary layer of the exit channel by enhancing turbulence and hence bottom stress for a given OBP anomaly. We believe the enhanced turbulence is largely explained and well parameterized by a background current, larger than the seasonally varying current, which represents observed mean currents in the exit regions. Additional enhancement is also justified for short time-scale processes that increase turbulence. The model OBP response to runoff alone peaks in early to mid summer near the time of peak runoff, but tails off more slowly than runoff. The added effect of average atmospheric pressure variation helps to reduce the model peak response and shift the peak toward the end of summer in agreement with observations. The analogy between the Arctic Ocean and the idealized model appears to break down in July–August as the observed OBP drops toward Fram Strait and the anticyclonic OBP cell spreads toward Svalbard to possibly vector a portion of geostrophic flow out of the Basin. This geostrophic flux would reduce actual OBP relative to the idealized model with only ageostrophic bottom boundary layer leakage.

[22] **Acknowledgments.** We thank John Wahr and Ron Kwok for their help and anonymous reviewers for their helpful comments. This work was supported by NSF grant OPP-0326109 and NASA grant NNX08AH62G.

References

Chambers, D. P. (2006a), Observing seasonal steric sea level variations with GRACE and satellite altimetry, *J. Geophys. Res.*, *111*, C03010, doi:10.1029/2005JC002914.

Chambers, D. P. (2006b), Evaluation of new GRACE time-variable gravity data over the ocean, *Geophys. Res. Lett.*, *33*, L17603, doi:10.1029/2006GL027296.

Dobslaw, H., and M. Thomas (2007), Impact of river run-off on global ocean mass redistribution, *Geophys. J. Int.*, *168*(2), 527–532, doi:10.1111.j.1365-246X.2006.03247.x.

Gill, A. E. (1982), *Atmosphere-Ocean Dynamics*, 662 pp., Academic, New York.

Gill, A. E., and P. Niiler (1973), The theory of seasonal variability in the ocean, *Deep Sea Res.*, *20*, 141–177.

Hanzlick, D. J. (1983), The West Spitsbergen Current: Transport, forcing and variability, Ph.D. dissertation, 127 pp., Uni. of Wash., Seattle.

Kalnay, E., et al. (1996), The NCEP/NCAR 40-year reanalysis project, *Bull. Am. Meteorol. Soc.*, *77*, 437–471, doi:10.1175/1520-0477(1996)077<0437:TNYRP>2.0.CO;2.

McPhee, M. (2008), *Air-Ice-Ocean Interaction: Turbulent Ocean Boundary Layer Exchange Processes*, 215 pp., Springer, New York.

Morison, J. (1991), Seasonal variations in the West Spitsbergen Current estimated from bottom pressure measurements, *J. Geophys. Res.*, *96*(C10), 18,381–18,395, doi:10.1029/91JC01916.

Morison, J., J. Wahr, R. Kwok, and C. Peralta-Ferriz (2007), Recent trends in Arctic Ocean mass distribution revealed by GRACE, *Geophys. Res. Lett.*, *34*, L07602, doi:10.1029/2006GL029016.

Pawlowicz, R., B. Beardsley, and S. Lentz (2002), Classical tidal harmonic analysis including error estimates in MATLAB using T_TIDE, *Comput. Geosci.*, *28*, 929–937, doi:10.1016/S0098-3004(02)00013-4.

Ponte, R. M., K. J. Quinn, C. Wunsch, and P. Heimbach (2007), A comparison of model and GRACE estimates of the large-scale seasonal cycle in ocean bottom pressure, *Geophys. Res. Lett.*, *34*, L09603, doi:10.1029/2007GL029599.

Saloranta, T. M., and H. Svendsen (2001), Across the Arctic front west of Spitsbergen: High resolution CTD sections from 1998–2000, *Polar Res.*, *20*(2), 177–184, doi:10.1111/j.1751-8369.2001.tb00054.x.

Schauer, U., E. Fahrbach, S. Osterhus, and G. Rohardt (2004), Arctic warming through the Fram Strait: Oceanic heat transport from 3 years of measurements, *J. Geophys. Res.*, *109*, C06026, doi:10.1029/2003JC001823.

Serreze, M. C., A. P. Barrett, A. G. Slater, R. A. Woodgate, K. Aagaard, R. B. Lammers, M. Steele, R. Moritz, M. Meredith, and C. M. Lee

(2006), The large-scale freshwater cycle of the Arctic, *J. Geophys. Res.*, *111*, C11010, doi:10.1029/2005JC003424.

Su, F., J. C. Adam, L. C. Bowling, and D. P. Lettenmaier (2005), Streamflow simulations of the terrestrial Arctic domain, *J. Geophys. Res.*, *110*, D08112, doi:10.1029/2004JD005518.

Teigen, S. H., F. Nilsen, and B. Gjevik (2010), Barotropic instability in the West Spitsbergen Current, *J. Geophys. Res.*, doi:10.1029/2009JC005996, in press.

Vinogradova, N., R. M. Ponte, and D. Stammer (2007), Relation between sea level and bottom pressure and the vertical dependence of oceanic variability, *Geophys. Res. Lett.*, *34*, L03608, doi:10.1029/2006GL028588.

Woodgate, R. A., and K. Aagaard (2005), Revising the Bering Strait freshwater flux into the Arctic Ocean, *Geophys. Res. Lett.*, *32*, L02602, doi:10.1029/2004GL021747.

World Climate Research Program (1998), Report of the ACSYS workshop on status and directions for the Arctic runoff data base. Arctic climate system study, report, Geneva Switzerland.

Zhang, J., and D. A. Rothrock (2003), Modeling global sea ice with a thickness and enthalpy distribution model in generalized curvilinear coordinates, *Mon. Weather Rev.*, *131*, 845–861.

J. Morison and C. Peralta-Ferriz, Polar Science Center, Applied Physics Laboratory, University of Washington, 1013 NE 40th St., Seattle, WA 98105, USA. (morison@apl.washington.edu; ferriz@u.washington.edu)

B.1 Supplemental information of seasonal variability in Arctic OBP

B.1.1 Regional effect of geostrophic winds

While the annual cycle of the basin-averaged Arctic Ocean mass variations (which is consistent with PC/EOF 1, Fig. B.1a.1) may be attributed to the response to meteoric input, the regional mass redistribution appears to be controlled by wind forcing. This idea is explored here by using the singular value decomposition approach to Maximum Covariance Analysis (MCA) (*Bretherton et al.*, 1992; *Rigor*, 2005). The goal of MCA analysis is to identify the primary modes of covariability between two datasets. Here, the two fields are the wind field at 925hPa from NCEP/NCAR reanalysis (*Kalnay et al.*, 1996) and the ocean bottom pressure field from GRACE used in (*Peralta-Ferriz and Morison*, 2010), for the period August 2002 to May 2008. While in EOF the leading modes account for the maximal fraction of variance in a single dataset, in MCA the leading modes account for the maximal fraction of the squared covariance between the time series in a pair of datasets.

For each mode, MCA yields two expansion coefficient time series (one for each dataset) and two spatial patterns (one for each field). These paired maps represent the patterns of variability in one dataset that are most highly correlated with a mode of the second dataset. The regression maps are estimated by projecting the original datasets on the standardized time series, in the units of the original datasets per standard deviation of the corresponding EC time series.

Before performing MCA, the GRACE EOF1 (Fig. B.1) is removed from the field because it is well correlated with annual cycle of the basin-averaged OBP, which is what *Peralta-Ferriz and Morison* (2010) considered is the meteoric response.

The first 2 modes of co-variability between wind and OBP are then extracted from the residual GRACE field (original−EOF 1), both of which resemble the centers of

action of EOF mode 2 (see see-saw pattern in Figure B.1a.2) that are dominated by the annual oscillation. Here, only one of the pair of EC time series is shown: EC1 from the wind field, and EC2 from the OBP field. The spatial patterns correspond to both fields projected on the selected EC1 (Fig. B.1b.1) and EC2 (Fig. B.1b.2).

MCA modes 1 and 2 together explain more than 85% of the total covariance squared (mode1 = 50% and mode2 = 38%). These modes are not well separated (*North et al.*, 1982), likely because they both correspond to the annual oscillation, but the spatial fields MCA 1 and MCA 2, orthogonal to each other, are also consistent with the regions of maximum amplitude and phase of the annual harmonic fitted to the original GRACE field (*Peralta-Ferriz and Morison*, 2010, see Fig. 1).

The regression map MCA1 has a center of action in the Chukchi and East Siberian Seas, where the annually decreasing mass during the winter to early spring, is associated with predominantly easterly alongshore winds. The regression map MCA 2 has a center of action in the Barents and Kara Seas. This map shows that the annually increasing mass there is most highly correlated with regional southwesterly or cyclonic winds, with a maximum in the winter to early spring.

These wind-OBP relationships suggest that the seasonal relationship between regional OBP and winds in both regions of the Arctic shelves is mainly due to surface Ekman transport. This response is highlighted by the thick arrows in Fig. B.1. During the winter and early spring, cyclonic winds in the Norwegian Sea drive mass towards the coast into the Barents and Kara Seas, whereas during late summer to early fall, easterly winds along the siberian shelves −primarily in the Chukchi and East Siberian Seas− act to pile water into these shelves (which is analogous to the winter-early forcing/response of opposite sign shown in the regression map MCA1).

The monthly means of the OBP field is consistent with the mass re-distribution obtained from MCA (*Peralta-Ferriz and Morison*, 2010, see Fig. 3).

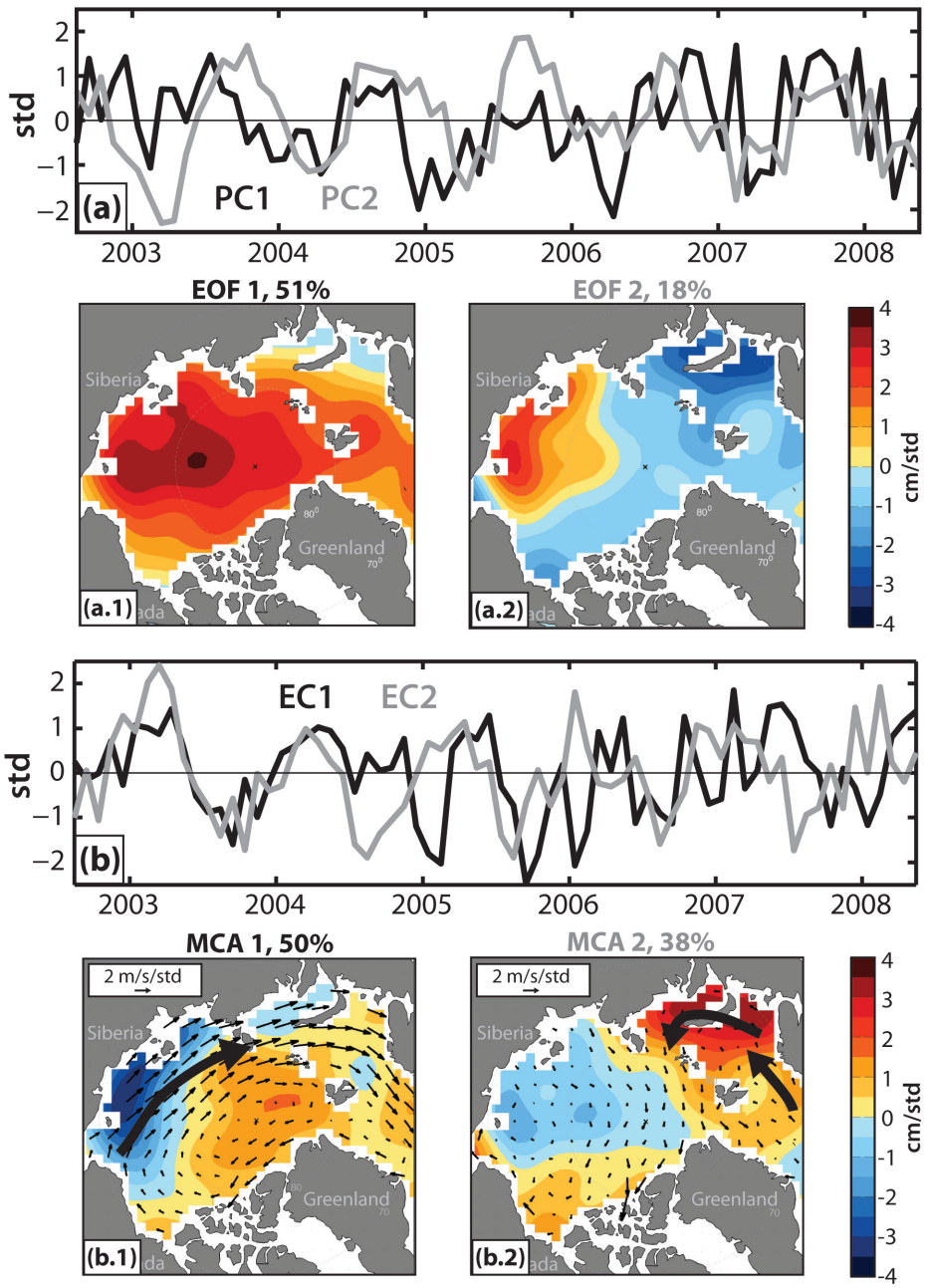

Figure B.1: (a) Normalized principal component (PC) time series of GRACE OBP modes 1 (black) and 2 (gray), and their associated regression maps of the first (a.1) and second (a.2) EOF modes. (b) Normalized expansion coefficient (EC) time series of MCA mode 1 of the wind field (black) and mode 2 of the GRACE OBP field (gray). The regression maps are estimated from projecting both field on the standardized EC 1 of the wind field (b.1) and from projecting both original fields onto the standardized EC 2 of GRACE OBP (b.2).

Appendix C

TIDAL ANALYSIS OF ABPRS NEAR THE NORTH POLE

C.1 ABPR1

North Pole pressure gauge ABPR1. Location: 89° 15.26' N, 60° 21.58' E. Tidal analysis for 5 continuous years (2005 - 2010) of ABPR1 (tidal amplitude and phase, with 95% confidence intervals), with two missing days (NaNs) is shown in Table C.1. The tidal analysis is based on matlab program of *Pawlowicz et al.* (2002).

Location of ABPR1: 89° 15.26' N, 60° 21.58' E. Amplitude units are cm.

All constituents are used to de-tide the pressure record, except SA and SSA, which pertain to real oceanographic signal of annual and semiannual cycles.

Number of standard constituents used: 68. Points used: 42581 of 43532. Percent of var residual after lsqfit/var original: 36.17%. Percent of var residual after synthesis/var original: 41.24%.

Date of analysis: 13-May-2010.

Number of observations = 43532. Number of good observations = 42581. Record length (days) = 1813.83.

Start time: 24-Apr-2005 04:00:00, rayleigh criterion = 1.0.

Greenwich phase computed with nodal corrections applied to amplitude and phase relative to center time.

x0= 0.0458, x trend= 3.41. var(x)= 77.2042 var(xp)= 47.4329 var(xres)= 31.8404.

Percent var predicted/var original= 61.4%.

Table C.1: Tidal constituents, amplitude, amplitude error, phase, phase error, signal to noise ratio (snr) for ABPR 1. Units of frequency are cycles per hour, and units of amplitude are cm. The signal to noise ratio is snr.

tide	frequency	amplitude	amp err	phase	pha err	snr	tide	frequency	amplitude	amp err	phase	pha err	snr
SA	0.0001141	3.6541	0.921	207.61	17.15	16	**H1**	0.0803973	0.2571	0.022	233.89	5.18	130
SSA	0.0002282	2.2002	0.882	171.58	24.01	6.2	**M2**	0.0805114	6.4738	0.026	60.40	0.22	63000
MSM	0.0013098	0.9819	0.866	193.64	53.82	1.3	**H2**	0.0806255	0.3781	0.024	188.04	3.16	250
MM	0.0015122	1.5265	1.023	230.32	38.66	2.2	**MKS2**	0.0807396	0.0562	0.019	268.10	17.68	8.8
MSF	0.0028219	0.2902	0.752	193.35	170.11	0.15	**LDA2**	0.0818212	0.0571	0.023	60.50	22.42	6.2
MF	0.0030501	3.0250	0.936	216.80	18.04	10	**L2**	0.0820236	0.2167	0.024	49.39	5.94	84
ALP1	0.0343966	0.0164	0.020	11.99	89.84	0.67	**T2**	0.0832193	0.2317	0.023	117.54	5.85	100
2Q1	0.0357064	0.0372	0.022	44.37	32.79	3	**S2**	0.0833333	2.8189	0.023	111.62	0.44	15000
SIG1	0.0359087	0.0441	0.020	31.04	30.02	5	**R2**	0.0834474	0.1681	0.020	97.55	6.82	72
Q1	0.0372185	0.2111	0.018	318.12	6.16	140	**K2**	0.0835615	0.8336	0.017	111.40	1.21	2500
RHO1	0.0374209	0.0686	0.022	316.98	18.84	9.4	**MSN2**	0.0848455	0.0330	0.022	314.78	46.02	2.2
O1	0.0387307	1.7974	0.023	325.39	0.72	6400	**ETA2**	0.0850736	0.0324	0.014	128.49	23.68	5.5
TAU1	0.0389588	0.0476	0.039	286.44	43.35	1.5	**MO3**	0.1192421	0.0398	0.008	136.00	10.10	22
BET1	0.0400404	0.0177	0.020	288.35	68.22	0.76	**M3**	0.1207671	0.0107	0.008	203.72	47.93	2
NO1	0.0402686	0.1291	0.023	308.99	9.91	31	**SO3**	0.1220640	0.0214	0.007	218.69	17.77	10
CHI1	0.0404710	0.0241	0.024	328.56	52.51	0.99	**MK3**	0.1222921	0.0093	0.007	246.30	41.69	2
PI1	0.0414385	0.0654	0.027	325.97	26.03	5.9	**SK3**	0.1251141	0.0145	0.007	341.31	30.29	4
P1	0.0415526	0.8748	0.031	339.48	1.92	790	**MN4**	0.1595106	0.0050	0.004	123.77	51.59	1.6
S1	0.0416667	0.0867	0.038	235.59	27.28	5.1	**M4**	0.1610228	0.0277	0.005	164.33	8.59	35
K1	0.0417807	2.7244	0.025	339.61	0.45	12000	**SN4**	0.1623326	0.0031	0.004	23.33	80.18	0.72
PSI1	0.0418948	0.0369	0.025	265.95	39.17	2.1	**MS4**	0.1638447	0.0187	0.004	271.14	12.88	18
PHI1	0.0420089	0.0295	0.028	333.83	50.48	1.1	**MK4**	0.1640729	0.0055	0.003	277.55	30.95	2.9
THE1	0.0430905	0.0254	0.025	309.93	61.43	1.1	**S4**	0.1666667	0.0228	0.004	228.64	10.16	42
J1	0.0432929	0.1181	0.021	335.63	10.92	31	**SK4**	0.1668948	0.0031	0.003	298.88	66.13	1.1
SO1	0.0446027	0.0317	0.018	327.92	47.92	3	**2MK5**	0.2028035	0.0094	0.003	205.79	16.91	9.5
OO1	0.0448308	0.0630	0.015	325.41	14.71	17	**2SK5**	0.2084474	0.0021	0.002	173.00	71.18	0.78
UPS1	0.0463430	0.0161	0.015	302.60	55.87	1.2	**2MN6**	0.2400221	0.0085	0.003	356.95	18.13	9.5
OQ2	0.0759749	0.0169	0.018	336.41	77.54	0.87	**M6**	0.2415342	0.0206	0.003	29.54	8.44	60
EPS2	0.0761773	0.0338	0.020	8.05	36.83	3	**2MS6**	0.2443561	0.0203	0.003	111.68	6.83	48
2N2	0.0774871	0.1045	0.021	15.44	11.86	25	**2MK6**	0.2445843	0.0061	0.002	119.61	20.36	9.7
MU2	0.0776895	0.1622	0.023	27.76	8.76	49	**2SM6**	0.2471781	0.0037	0.003	172.19	36.79	2.1
N2	0.0789992	1.0899	0.023	33.75	1.26	2300	**MSK6**	0.2474062	0.0031	0.002	173.50	37.80	2.7
NU2	0.0792016	0.2315	0.023	35.67	6.10	98	**3MK7**	0.2833149	0.0019	0.002	203.54	68.31	0.76
GAM2	0.0803090	0.0187	0.025	106.83	83.02	0.58	**M8**	0.3220456	0.0129	0.002	182.09	10.03	37

C.2 ABPR3

North Pole pressure gauge ABPR3. Location: 89° 14.85' N, 148° 7.54' E. Tidal analysis for 3 continuous years of ABPR3 (tidal amplitude and phase, with 95%

confidence intervals), with two missing days (NaNs) is shown in Table C.2. The tidal analysis is based on matlab program of *Pawlowicz et al.* (2002).

Similarly to the tidal analysis of ABPR1, the SA, SSA tides of ABPR3 were added back fitting annual and semi-annual harmonic function. MSM,MM tides are removed manually using harmonics (tidal signal). The rest of the tides are removed only if the SNR ≥ 2 (marked with stars in Table C.2).

Number of standard constituents used: 68. Points used: 104461 of 104461. Percent of var residual after least square fit/var original: 40.87%.

Greenwich phase computed with nodal corrections applied to amplitude and phase relative to center time. Using nonlinear bootstrapped error estimates.

Generating prediction with nodal corrections, SNR is 2.000000. Percent of var residual after synthesis/var original: 44.68%.

Date of analysis: 29-Oct-2009. Number of observations = 104461, Nunber of good observations = 104461, record length (days) = 1088.14.

Start time: 24-Apr-2005 20:45:00. Rayleigh criterion = 2.0. Greenwich phase computed with nodal corrections applied to amplitude and phase relative to center time.

x0= -0.0231, x trend= 1.39, var(x)= 62.1427 var(xp)= 35.2598, var(xres)= 27.7655. Percent var predicted/var original= 56.7%.

Table C.2: Tidal constituents, amplitude, amplitude error, phase, phase error, signal to noise ratio (snr) for ABPR 3. Units of frequency are cycles per hour, and units of amplitude are cm.

tide	frequency	amplitude	amp err	phase	pha err	snr	tide	frequency	amplitude	amp err	phase	pha err	snr
***SA**	0.0001141	2.4229	1.369	223.76	29.35	3.1	***H1**	0.0803973	0.2335	0.021	231.22	4.60	120
***SSA**	0.0002282	2.1671	1.303	182.08	32.42	2.8	***M2**	0.0805114	5.5223	0.021	63.88	0.21	67000
MSM	0.0013098	1.0663	1.009	171.93	67.88	1.1	***H2**	0.0806255	0.3273	0.021	189.04	3.84	240
MM	0.0015122	1.5723	1.230	240.04	45.37	1.6	***MKS2**	0.0807396	0.0557	0.015	257.27	17.30	13
MSF	0.0028219	0.0661	0.893	156.08	234.10	0.0055	***LDA2**	0.0818212	0.0419	0.020	53.90	27.65	4.3
***MF**	0.0030501	3.1554	1.225	220.76	23.61	6.6	***L2**	0.0820236	0.3013	0.031	76.90	6.87	95
ALP1	0.0343966	0.0291	0.026	350.16	54.41	1.3	***T2**	0.0832193	0.2034	0.021	122.17	6.43	92
2Q1	0.0357064	0.0285	0.023	78.36	52.69	1.6	***S2**	0.0833333	2.4807	0.019	114.07	0.43	16000
SIG1	0.0359087	0.0240	0.025	36.17	58.22	0.94	***R2**	0.0834474	0.1512	0.016	98.37	6.03	95
***Q1**	0.0372185	0.1864	0.025	278.95	7.80	57	***K2**	0.0835615	0.7404	0.015	112.68	1.23	2500
***RHO1**	0.0374209	0.0492	0.024	295.07	29.79	4.2	**MSN2**	0.0848455	0.0230	0.022	288.38	50.96	1.1
***O1**	0.0387307	1.6995	0.024	312.44	0.93	5200	***ETA2**	0.0850736	0.0368	0.013	134.76	19.67	8.5
TAU1	0.0389588	0.0205	0.033	298.75	121.71	0.39	***MO3**	0.1192421	0.0426	0.005	147.55	6.27	74
BET1	0.0400404	0.0097	0.018	266.32	146.59	0.28	***M3**	0.1207671	0.0103	0.006	227.94	34.58	2.8
***NO1**	0.0402686	0.1139	0.019	333.13	9.15	35	***SO3**	0.1220640	0.0201	0.005	222.87	14.16	17
CHI1	0.0404710	0.0197	0.022	342.54	82.97	0.81	**MK3**	0.1222921	0.0072	0.006	240.67	39.81	1.7
***PI1**	0.0414385	0.0498	0.032	314.69	33.21	2.5	***SK3**	0.1251141	0.0140	0.005	341.41	19.33	6.5
***P1**	0.0415526	0.8458	0.033	333.29	2.32	640	***MN4**	0.1595106	0.0075	0.005	141.88	37.37	2.4
***S1**	0.0416667	0.0771	0.046	220.20	31.76	2.8	***M4**	0.1610228	0.0288	0.005	170.35	9.32	36
***K1**	0.0417807	2.6458	0.028	335.34	0.59	8900	**SN4**	0.1623326	0.0028	0.004	273.33	93.74	0.57
***PSI1**	0.0418948	0.0464	0.028	251.19	38.55	2.8	***MS4**	0.1638447	0.0177	0.005	267.62	14.19	13
PHI1	0.0420089	0.0354	0.027	328.45	52.37	1.7	***MK4**	0.1640729	0.0065	0.003	283.75	32.55	3.7
THE1	0.0430905	0.0227	0.023	328.59	67.88	0.97	***S4**	0.1666667	0.0210	0.004	230.52	12.11	26
***J1**	0.0432929	0.1155	0.026	337.52	11.66	20	**SK4**	0.1668948	0.0039	0.003	271.30	43.19	1.6
SO1	0.0446027	0.0189	0.024	327.94	76.81	0.63	***2MK5**	0.2028035	0.0096	0.003	231.58	17.87	11
***OO1**	0.0448308	0.0516	0.016	314.16	17.62	11	**2SK5**	0.2084474	0.0012	0.002	258.82	134.49	0.35
UPS1	0.0463430	0.0097	0.014	292.09	92.65	0.51	***2MN6**	0.2400221	0.0055	0.003	331.21	34.80	2.8
OQ2	0.0759749	0.0100	0.018	18.43	106.04	0.31	***M6**	0.2415342	0.0213	0.003	23.51	8.99	45
***EPS2**	0.0761773	0.0332	0.019	30.14	32.87	3	***2MS6**	0.2443561	0.0205	0.003	115.38	9.11	47
***2N2**	0.0774871	0.1052	0.020	33.16	9.69	27	***2MK6**	0.2445843	0.0056	0.002	116.60	20.72	6.4
***MU2**	0.0776895	0.1363	0.021	36.64	8.32	42	***2SM6**	0.2471781	0.0049	0.003	156.66	37.79	3.2
***N2**	0.0789992	0.9201	0.019	38.70	1.39	2300	***MSK6**	0.2474062	0.0033	0.002	197.79	36.31	2.2
***NU2**	0.0792016	0.1646	0.019	36.77	6.65	74	***3MK7**	0.2833149	0.0040	0.002	149.31	32.25	3.1
GAM2	0.0803090	0.0180	0.017	105.69	54.99	1.1	***M8**	0.3220456	0.0122	0.003	189.87	12.81	23

C.3 ABPR4

North Pole pressure gauge ABPR4. Location: 89° 58.6' N, 178° 13.8' E. Tidal analysis for 1 year of ABPR4 (tidal amplitude and phase, with 95% confidence intervals) is

shown in Table C.3. The tidal analysis is based on matlab program of *Pawlowicz et al.* (2002).

Number of standard constituents used: 67.

Points used: 8819 of 8820. Percent of var residual after lsqfit/var original: 32.83%. Greenwich phase computed with nodal corrections applied to amplitude and phase relative to center time. Using nonlinear bootstrapped error estimates. Generating prediction with nodal corrections, tidal constituents removed have those with SNR larger than 2.00 (marked with stars in Table C.3). Percent of var residual after synthesis/var original: 62.99%.

Date: 25-Jun-2007. Number of observations = 8820, number of good observations = 8819. Record length (days) = 367.50.

Start time: 19-Apr-2006 12:00:00. Raleigh criterion = 1.0. Greenwich phase computed with nodal corrections applied to amplitude and phase relative to center time.

x0= 4.19e+006, x trend= -76.5. var(x)= 7846.2555 var(xp)= 3871.5379 var(xres)= 4942.3546.

Percentage of variance predicted / variance original = 49.3%.

Table C.3: Tidal constituents, amplitude, amplitude error, phase, phase error, signal to noise ratio (snr) for ABPR 4. Units of frequency are cycles per hour, and units of amplitude are cm.

tide	frequency	amplitude	amp err	phase	pha err	snr	tide	frequency	amplitude	amp err	phase	pha err	snr
SA	0.0001141	3.4198	1.974	324.62	39.31	3	***M2**	0.0805114	5.8859	0.059	59.85	0.60	9800
SSA	0.0002282	0.5579	1.870	146.90	160.35	0.089	***H2**	0.0806255	0.4461	0.064	204.92	8.80	48
MSM	0.0013098	1.0248	1.717	199.80	125.12	0.36	***MKS2**	0.0807396	0.0840	0.054	230.30	35.77	2.4
MM	0.0015122	2.1425	2.157	233.82	62.72	0.99	**LDA2**	0.0818212	0.0642	0.069	23.06	64.82	0.85
MSF	0.0028219	0.5696	1.750	265.61	190.87	0.11	***L2**	0.0820236	0.2653	0.097	58.54	23.10	7.3
***MF**	0.0030501	3.1602	2.053	226.71	40.24	2.4	***T2**	0.0832193	0.2212	0.065	139.92	15.70	12
ALP1	0.0343966	0.0363	0.035	337.73	64.02	1	***S2**	0.0833333	2.5817	0.062	111.96	1.47	1700
2Q1	0.0357064	0.0148	0.030	40.17	138.23	0.24	***R2**	0.0834474	0.2065	0.057	114.06	14.69	13
SIG1	0.0359087	0.0525	0.040	27.47	44.35	1.7	***K2**	0.0835615	0.7570	0.049	112.04	3.68	230
***Q1**	0.0372185	0.1978	0.041	309.86	11.60	23	**MSN2**	0.0848455	0.0228	0.052	194.08	154.51	0.19
***RHO1**	0.0374209	0.0840	0.042	323.45	32.25	4	**ETA2**	0.0850736	0.0446	0.042	142.88	56.23	1.1
***O1**	0.0387307	1.7785	0.041	326.10	1.19	1900	***MO3**	0.1192421	0.0536	0.026	137.57	27.01	4.2
TAU1	0.0389588	0.0388	0.051	293.86	101.98	0.56	**M3**	0.1207671	0.0259	0.028	239.93	67.67	0.83
BET1	0.0400404	0.0116	0.027	317.17	154.73	0.19	**SO3**	0.1220640	0.0227	0.023	186.95	64.00	0.98
***NO1**	0.0402686	0.1338	0.028	343.61	12.87	22	**MK3**	0.1222921	0.0230	0.022	221.06	69.15	1
CHI1	0.0404710	0.0130	0.029	315.76	159.82	0.2	**SK3**	0.1251141	0.0228	0.024	324.79	65.15	0.84
PI1	0.0414385	0.0353	0.049	315.50	78.97	0.52	**MN4**	0.1595106	0.0113	0.015	101.37	93.20	0.51
***P1**	0.0415526	0.8634	0.052	341.59	3.73	270	**M4**	0.1610228	0.0246	0.017	162.59	42.06	2
S1	0.0416667	0.0648	0.073	179.37	65.38	0.78	**SN4**	0.1623326	0.0019	0.011	269.10	209.45	0.027
***K1**	0.0417807	2.6736	0.044	342.79	1.01	3600	**MS4**	0.1638447	0.0057	0.011	208.35	153.43	0.27
***PSI1**	0.0418948	0.0739	0.051	175.05	36.53	2.1	**MK4**	0.1640729	0.0035	0.010	242.01	160.64	0.12
***PHI1**	0.0420089	0.0657	0.045	21.69	45.90	2.1	**S4**	0.1666667	0.0073	0.013	186.96	116.71	0.31
THE1	0.0430905	0.0033	0.031	172.54	243.68	0.011	**SK4**	0.1668948	0.0035	0.009	255.33	141.50	0.15
***J1**	0.0432929	0.0899	0.041	344.31	30.53	4.7	**2MK5**	0.2028035	0.0061	0.007	239.75	80.73	0.63
SO1	0.0446027	0.0509	0.041	16.62	48.57	1.5	**2SK5**	0.2084474	0.0031	0.005	104.92	148.95	0.29
***OO1**	0.0448308	0.0642	0.023	330.77	24.41	7.5	**2MN6**	0.2400221	0.0080	0.007	4.60	50.90	1.2
UPS1	0.0463430	0.0155	0.020	3.14	94.52	0.56	***M6**	0.2415342	0.0195	0.007	27.33	23.58	7.5
OQ2	0.0759749	0.0184	0.044	344.22	146.53	0.17	***2MS6**	0.2443561	0.0210	0.007	117.11	18.06	8
EPS2	0.0761773	0.0306	0.051	25.53	106.30	0.36	**2MK6**	0.2445843	0.0044	0.005	104.07	67.91	0.79
***2N2**	0.0774871	0.1295	0.061	36.13	28.50	4.5	***2SM6**	0.2471781	0.0098	0.007	166.59	38.68	2
***MU2**	0.0776895	0.1239	0.068	34.14	31.31	3.3	**MSK6**	0.2474062	0.0041	0.004	207.57	66.62	0.96
***N2**	0.0789992	1.0236	0.066	31.70	3.42	240	**3MK7**	0.2833149	0.0057	0.008	255.47	77.12	0.51
***NU2**	0.0792016	0.2131	0.066	36.53	15.74	10	***M8**	0.3220456	0.0150	0.006	176.31	28.66	4.7
***H1**	0.0803973	0.2116	0.067	267.11	19.03	9.8							

C.4 ABPR5

North Pole pressure gauge ABPR5. Location: 89° 58.71' N, 32° 55.43' W. Tidal analysis for 1 year of ABPR5 (tidal amplitude and phase, with 95% confidence intervals),

with two missing days (NaNs) is shown in Table C.4. The tidal analysis is based on matlab program of *Pawlowicz et al.* (2002).

Location of ABPR1: 89° 15.26' N, 60° 21.58' E. Amplitude units are cm.

All constituents are used to de-tide the pressure record, except SSA tide, which pertain to real oceanographic signal of annual and semiannual cycles.

Number of standard constituents used: 59. Points used: 34887 of 34888.

Greenwich phase computed with nodal corrections applied to amplitude and phase relative to center time.

Using nonlinear bootstrapped error estimates. Percent of var residual after lsq-fit/var original: 40.59%. Percent of var residual after synthesis/var original: 40.73%.

Date of analysis: 06-Apr-2012.

Number of observations = 34888. Number of good observations = 34887. Record length (days) = 363.42.

Start time: 20-Apr-2010 14:00:00. Rayleigh criterion = 1.0.

Greenwich phase computed with nodal corrections applied to amplitude and phase relative to center time.

x0= 0.0521, x trend= 0.468, var(x)= 52.75 var(xp)= 31.41, var(xres)= 21.48.

Percent var predicted/var original= 59.6%.

Table C.4: Tidal constituents, amplitude, amplitude error, phase, phase error, signal to noise ratio (snr) for ABPR 5. Units of frequency are cycles per hour, and units of amplitude are cm. The signal to noise ratio is snr.

tide	frequency	amplitude	amp err	phase	pha err	snr	tide	frequency	amplitude	amp err	phase	pha err	snr
SSA	0.0002282	0.8749	1.422	130.38	103.10	0.38	**MKS2**	0.0807396	0.0441	0.078	312.82	112.29	0.32
MSM	0.0013098	0.4561	1.206	35.39	169.65	0.14	**LDA2**	0.0818212	0.0434	0.076	46.84	124.53	0.33
MM	0.0015122	1.3106	1.829	167.37	74.99	0.51	**L2**	0.0820236	0.1780	0.129	63.54	45.43	1.9
MSF	0.0028219	0.3159	1.258	124.65	194.08	0.063	**S2**	0.0833333	2.5691	0.098	108.97	2.25	690
MF	0.0030501	2.7039	1.587	188.78	36.33	2.9	**K2**	0.0835615	0.7535	0.099	108.99	8.08	58
ALP1	0.0343966	0.0581	0.036	266.46	35.32	2.6	**MSN2**	0.0848455	0.0121	0.073	207.56	231.43	0.028
2Q1	0.0357064	0.0614	0.030	27.87	31.29	4.1	**ETA2**	0.0850736	0.0346	0.066	167.51	129.74	0.27
SIG1	0.0359087	0.0250	0.031	32.28	88.25	0.66	**MO3**	0.1192421	0.0350	0.009	152.09	15.11	15
Q1	0.0372185	0.2215	0.037	341.62	9.86	36	**M3**	0.1207671	0.0048	0.008	148.73	105.06	0.38
RHO1	0.0374209	0.0329	0.037	336.42	71.63	0.79	**SO3**	0.1220640	0.0112	0.009	213.95	51.33	1.7
O1	0.0387307	1.7522	0.033	326.64	1.24	2800	**MK3**	0.1222921	0.0184	0.009	274.75	31.66	3.9
TAU1	0.0389588	0.0325	0.042	248.39	71.98	0.61	**SK3**	0.1251141	0.0118	0.009	47.78	42.80	1.6
BET1	0.0400404	0.0384	0.037	17.93	54.40	1.1	**MN4**	0.1595106	0.0044	0.006	189.45	84.31	0.58
NO1	0.0402686	0.1560	0.025	331.52	10.86	39	**M4**	0.1610228	0.0321	0.007	178.94	11.96	18
CHI1	0.0404710	0.0148	0.028	290.10	132.51	0.29	**SN4**	0.1623326	0.0102	0.006	65.10	33.83	2.6
P1	0.0415526	0.8551	0.037	343.68	2.68	540	**MS4**	0.1638447	0.0175	0.006	298.88	23.96	8
K1	0.0417807	2.7378	0.037	344.46	0.84	5400	**MK4**	0.1640729	0.0068	0.006	25.45	58.61	1.3
PHI1	0.0420089	0.0290	0.033	36.89	73.08	0.75	**S4**	0.1666667	0.0220	0.008	197.56	16.87	8.4
THE1	0.0430905	0.0352	0.037	295.69	66.23	0.93	**SK4**	0.1668948	0.0042	0.006	274.91	91.30	0.45
J1	0.0432929	0.1398	0.038	346.01	17.04	13	**2MK5**	0.2028035	0.0150	0.004	218.55	15.22	18
SO1	0.0446027	0.0212	0.031	300.94	109.64	0.48	**2SK5**	0.2084474	0.0068	0.004	193.54	28.87	3.1
OO1	0.0448308	0.0730	0.028	322.09	25.04	6.6	**2MN6**	0.2400221	0.0035	0.005	308.36	84.31	0.59
UPS1	0.0463430	0.0136	0.031	289.03	106.83	0.19	**M6**	0.2415342	0.0198	0.004	29.57	13.37	20
OQ2	0.0759749	0.0144	0.063	359.60	211.04	0.053	**2MS6**	0.2443561	0.0167	0.005	120.16	17.46	13
EPS2	0.0761773	0.0059	0.070	10.05	246.25	0.0071	**2MK6**	0.2445843	0.0058	0.004	91.42	46.51	1.9
2N2	0.0774871	0.1262	0.094	3.00	52.00	1.8	**2SM6**	0.2471781	0.0061	0.005	142.67	47.82	1.4
MU2	0.0776895	0.1247	0.107	25.18	45.92	1.4	**MSK6**	0.2474062	0.0060	0.005	153.21	43.47	1.7
N2	0.0789992	0.9354	0.103	31.35	6.84	82	**3MK7**	0.2833149	0.0016	0.003	147.77	111.17	0.33
NU2	0.0792016	0.1652	0.092	24.86	31.08	3.2	**M8**	0.3220456	0.0074	0.003	180.66	24.29	6.6
M2	0.0805114	5.7303	0.098	57.39	1.03	3400							

VITA

Ana Cecilia Peralta Ferriz was born and raised in Mexico City. She earned a bachelor of sciences in Oceanography at the Autonomous University of Baja California, in Ensenada, Baja California, Mexico, in 2004. She received a Master of Sciences in Physical Oceanography in 2008 and a PhD in 2012 at the University of Washington.